Characterization of surface plasmon resonances in metallic planar nanostructures by electron energy loss spectroscopy

CHARACTERIZATION OF SURFACE PLASMON RESONANCES IN METALLIC PLANAR NANOSTRUCTURES BY ELECTRON ENERGY LOSS SPECTROSCOPY

BY

EDSON PAZUR BELLIDO SOSA, M.Sc.

A THESIS

SUBMITTED TO THE DEPARTMENT OF MATERIALS SCIENCE & ENGINEERING

AND THE SCHOOL OF GRADUATE STUDIES

OF MCMASTER UNIVERSITY

IN PARTIAL FULFILMENT OF THE REQUIREMENTS

FOR THE DEGREE OF

DOCTOR OF PHILOSOPHY

Doctor of Philosophy (2017) McMaster University

(Doctor of Philosophy) Hamilton, Ontario, Canada

TITLE:	Characterization of surface plasmon resonances in metallic planar nanostructures by electron energy loss spectroscopy
AUTHOR:	Edson Pazur Bellido Sosa M.Sc. Materials Science & Engineering Texas A&M University, College Station, Texas, USA
SUPERVISOR:	Dr. Gianluigi A. Botton
NUMBER OF PAGES:	1, 207

To my parents, Tula and Amador

Abstract

Surface plasmon resonances at the nanoscale hold great potential for applications in many areas, and the characterization of plasmonic nanostructures plays a critical role in the realization of these applications. Electron energy loss spectroscopy (EELS) has emerged as a powerful characterization tool to study the response of plasmonic nanostructures due to its high spatial-resolution and the capability to probe bright as well as dark plasmonic modes. The main limiting factor of EELS is the energy resolution. However, in this thesis, we overcome this limitation using a combination of electron monochromation and the use of the Richardson-Lucy algorithm. We show that the algorithm could be used to obtain effective energy resolutions up to 10 meV. Using EELS we analyze the resonances of planar nanostructures, and we found that the supported resonances can be described as edge and cavity or film modes, behaving as 1D and 2D modes respectively. We also demonstrate that edge modes are unaffected by the presence of bends up to the critical angle of 90° where the modes start self-interacting producing large energy shifts. The interaction of plasmon resonances is also studied, and we show that the coupling can be reduced to three behaviors: coupling through the edge, coupling through a corner, and non-coupling. We propose a method to control the coupling through the edge in offset nanowires, by tuning the nodal alignment and spectral overlap of the edge modes. Finally,

we analyze the plasmon modes supported by Koch snowflake fractal antennas, and we demonstrate that modes present in the fractals are formed by the edge modes supported by their characteristic edges. This thesis provides a complete picture of the surface plasmon resonances supported by planar nanostructures and demonstrates the ability of EELS to probe and image a wide variety of plasmonic resonances.

Acknowledgements

First, I would like to thank my supervisor for his guidance and support throughout the course of my Ph.D. studies. Thanks for the amazing opportunity of being part of your research group. Thanks also go to my friends and colleagues that are or were part of the Microscopy of Nanoscale Materials group. Thank you for all the great memories and all your support, working with you has been a wonderful experience. My gratitude to David Rossouw for his guidance and for training me in the use of the Titan microscope; to Matthieu Bugnet for always lending a helping hand with the experiments and for sharing his knowledge; to Hanshuo Liu, Isobel Bicket, Lis Melo, Samantha Stambula, Steffi Woo, Sagar Prabhudev, Alexandre Pofelski, Fei Yang, Andrew Scullion, and Viktor Kapetanovic for their friendship and for all the fun moments and captivating conversations about research, science, politics, philosophy and more that I will always cherish. My thanks go to my external collaborators: Alejandro Manjavacas, Yue Zhang, Gabriel Bernasconi, Peter Nordlander, and Olivier Martin for all the work and useful discussions. I would like to thank my supervisory committee members John Preston and Harold Haugen for their insights and for their time and effort in being part of my committee. Thanks to the staff at the Canadian Centre for Electron Microscopy for their assistance with the experiments. I also would like to acknowledge the Department of Materials Science and Engineering at

McMaster, the McMaster School of Graduate Studies, and the Ontario Graduate Scholarship program for providing financial support. Thanks go to my family, for all their love and support. Thanks to my fiance Diana for her love, constant support and care, and to my beloved parents and sister, Amador, Tula, and Yemid, for all their love, understanding, guidance and unconditional support. You are my source of strength and inspiration.

Abbreviations

ADF	Annular dark field
EBL	Electron beam lithography
EEL	Electron energy loss
EELS	Electron energy loss spectroscopy
FWHM	Full width at half maximum
HAADF	High angle annular dark field
LDOS	Local density of states
LSPR	Localized surface plasmon resonance
MNPBEM	Metallic nanoparticle boundary element method
NW	Nanowire
PSF	Point of spread function
RL	Richardson-Lucy
SEM	Scanning electron microscope
SPP	Surface plasmon polariton
SPs	Surface plasmon
STEM	Scanning transmission electron microscope
TEM	Transmission electron microscope
ZLP	Zero loss peak

Contents

List of Tables

List of Figures

Preface

Light has fascinated humanity since ancient times, as evidenced by the earliest known lenses, made from polished quartz, which dates back to 700 BC. Since then our understanding of light has increased significantly, thanks to revolutionary work of many scientists. From the first optics treatises of Euclid (300 BC) and Alhazen (11^{th} Century) to the formulation of the classic theory of electromagnetism by James Maxwell (1860s) and the development of quantum optics, we are building our understanding of the nature of light and its interaction with matter.

Richard Feynman's famous talk, entitled *There is plenty of room at the bottom* [17] delivered more than 50 years ago, is considered to be seminal in the conception of nanotechnology. In the talk, he presented his visionary idea of a technological revolution leading towards the atomic scale and the boundaries of the physical laws. Since his talk, nanotechnology has traveled far, unraveling and discovering new properties and phenomena in several areas of knowledge. Optics is no stranger to this technological revolution. In particular, thanks to the advancements in fabrication methods of nanostructures in the last decades the ability to confine light on sub-wavelength scales was achieved using surface plasmons excited on nanoscale structures.

Surface plasmons (SPs) are electron density waves that exist at the interface of a metal and a dielectric akin to the traveling waves that propagate across the surface

of a pond after throwing a pebble into the water. The study of this phenomenon gave rise to the development of the research field called *Plasmonics*. The field of plasmonic is experiencing an exponential growth because of its potential for technological advancement [18]. The range of possible applications is vast, and this *promise of plasmonics* [19] has promoted an explosion of research in this field over the last decade not only for the technological impact but also for the fascinating science behind this phenomenon.

As Feynman himself stated, to study phenomena at the nanoscale, we require high spatial resolution, and to achieve it we required good electron microscopes [17]. As predicted by Feynman in 1959, the advances in electron optics made the rise of Nanotechnology possible. Relatively recently, it was shown that it is possible to excite SPs in the visible range using the fast electrons of an electron microscope and detect the SPs with sub-wavelength resolution [20]. The combination of the very high resolution of electron microscopes and the use of electron spectroscopies in the microscope showed to be more than suitable to study the local optical response of metallic nanostructures. Electron energy loss spectroscopy (EELS) inside a scanning transmission microscope (STEM) stands out among other electron microscopy techniques in the characterization of SPs, not only due to the high spatial resolution that can be achieved but also due to the ability to probe bright as well as dark SPs [21]. In this thesis, a myriad of plasmon resonances modes that complex, as well as simple, planar structures support is shown, studied and analyzed using the high-resolution of STEM-EELS and the improved resolution obtained with the use of computational algorithms. The effects of plasmon coupling and hybridization of plasmonic nanostructures in proximity are also analyzed and studied. The understanding of plasmon

resonances in nanostructures and their coupling mechanism, will not only expand the current knowledge of plasmon resonances in nanostructures, but give us the tools to design plasmonic absorbers required for a variety of applications, including energy harvesting, sensing, therapeutics, catalysis, and nano-optics in general.

This thesis consists of seven chapters. Chapter 1 provides the theoretical framework of the formation of surface plasmon resonances in metallic nanostructures. It also includes a description of the excitation of surface plasmons by fast electrons as well as the background and literature review required to understand the results presented in chapters 3 to 5. Chapter 2 describes the methods used in this thesis including sample fabrication, characterization as well as modeling of plasmonics nanostructures. The use of the Richarson-Lucy algorithm to improve the energy resolution of EELS for the characterization of surface plasmon resonances is presented in Chapter 3. Results and analysis of edge and film (cavity) modes, which are the two types of modes excited on planar nanostructures are shown in Chapter 4. The coupling of planar nanostructures is described in chapter 5 through the study of the offset nanowire dimers, nano-square dimers, and metallic strips. In chapter 6, the results and analysis of the surface plasmon resonances in planar metallic fractal structures are presented. Finally, Chapter 7 provides the conclusion and summarizes the contributions of the research described in this thesis.

Chapter 1

Surface Plasmons

Surface Plasmons are electron density oscillations that occur at the interface between a conductor and a dielectric when the real part of the dielectric function $Re(\epsilon)$ changes sign from positive in the dielectric material to negative in the conductor. These oscillations are associated with electromagnetic fields at the interface, which resemble light waves bound to the surface of metal. When the extent of the metallic surface is smaller than visible light wavelengths, we have electromagnetic fields confined to the nanoscale. The potential applications of surface plasmons promoted the growth of plasmonics as a research area. To mention just a few examples:

- Plasmon resonances can be used to fabricate highly sensitive chemical sensors and could allow identification down to the single molecule level [22].
- The ability to squeeze light down to nanoscale volumes of surface plasmons has the potential to provide unprecedented resolution for optical patterning [23, 24, 25].
- Metal nanoparticles with resonances in the infrared can be used to eliminate

tumors without damaging nearby tissue [26, 27].

- Due to its reduced size, plasmonic nanostructures can be incorporated in photodetectors and photovoltaic devices and potentially increase their performance [28].
- Metamaterials composed of plasmonic nanostructures can have unique optical characteristics such as negative refraction, which is required to realize exotic phenomena such as super-lensing and optical cloaking [29, 30, 31].

In this chapter, the historical development marking key contributions to the field of plasmonic is described briefly, followed by the theoretical background, and the description of surface plasmons on various configurations. Finally, a physical interpretation, as well as a description of the different models to explain the coupling of plasmonic structures, are also given in this chapter.

1.1 Plasmonics a historical perspective

The first plasmonic application dates as far back as the 4^{th} century, where Romans unknowingly used nanoscale metallic particles to fabricate glass. The famous Lycurgus Cup is a relic from this era, which due to the optical dichroism of the metallic nanoparticles in the glass, this cup appears jade green in reflected light but a brilliant red in transmission, as seen in figure 1.1. The first quantitative observation of surface plasmons started back in 1902, when Wood illuminated a metallic diffraction grating with polychromatic light and noticed narrow dark bands in the spectrum of the diffracted light [32], which are known, even today, as Wood Anomalies. Lord Rayleigh suggested a physical interpretation soon after the discovery of the anomalies. However, it is only on 1941 that the anomalies were associated with the excitation of

electromagnetic surface waves by Fano [33]. From the inception of Plasmonics, EELS was a fundamental tool for the study of surface plasmons. In 1957 Ritchie proposed that thin metallic films could support collective electron oscillating modes excited by an inelastic interaction with fast electrons, providing the first theoretical description of surface plasmons. The experimental confirmation of the theory came two years later in experiments of reflection EELS of a 10 nm thick aluminum film by Powell and Swan [34, 35].

Figure 1.1: Lycurgus Cup [British Museum Images].

Surface plasmons excited optically in metal films on a substrate were reported and explained in 1968 almost simultaneously by Otto [36] and by Kretschmann and Raether [37]. In 1974 Fleishman observed an unexpected enhancement of the signal of Raman-scattering from molecules deposited on rough metallic surfaces. Three years later Jeanmaire and Van Duyne explained that the enhancement was caused by the interaction of the high electromagnetic fields of surface plasmons on the metallic surface and the molecules, and the technique now known as surface-enhanced Raman

spectroscopy was born. Another observation that triggered interest in the scientific community occurred on 1989 when Ebbesen fabricated an array of holes in a metal film and observed that the nanoscale holes transmitted more light than expected. But it was only nine years later that the explanation of the enhanced transmission was attributed to surface plasmons [38]. Since then, the field of Plasmonics has expanded tremendously, and a reflection of this growth is the amount of scientific literature related to surface plasmons that since the late 90s has doubled every five years [39].

1.2 Theoretical description of plasmons

1.2.1 The Drude model

In 1900, Paul Drude proposed one of the most simple but at the same time very useful models to describe the interaction of a metallic solid and an electromagnetic field [40, 41]. Drude assumed the description of the interaction was based on the microscopic movement of the electrons in the metal. It considers the metal as a lattice of positively charged ions in which electrons behave as a free gas of non-interacting particles that move in the immobile lattice of ions driven by the force of the external electric field. The model neglects any electron-electron and electron-ion long-range interaction, being instantaneous collisions the only interactions that a free electron experiences. After a collision, the electrons emerge with a random direction, with an average time between collisions τ, as shown in figure 1.2(a). Considering that in average the collisions cause the movement of the electron to be damped, Drude obtained the following equation of motion of an electron in a metal under the influence of an electric field [39, 42]:

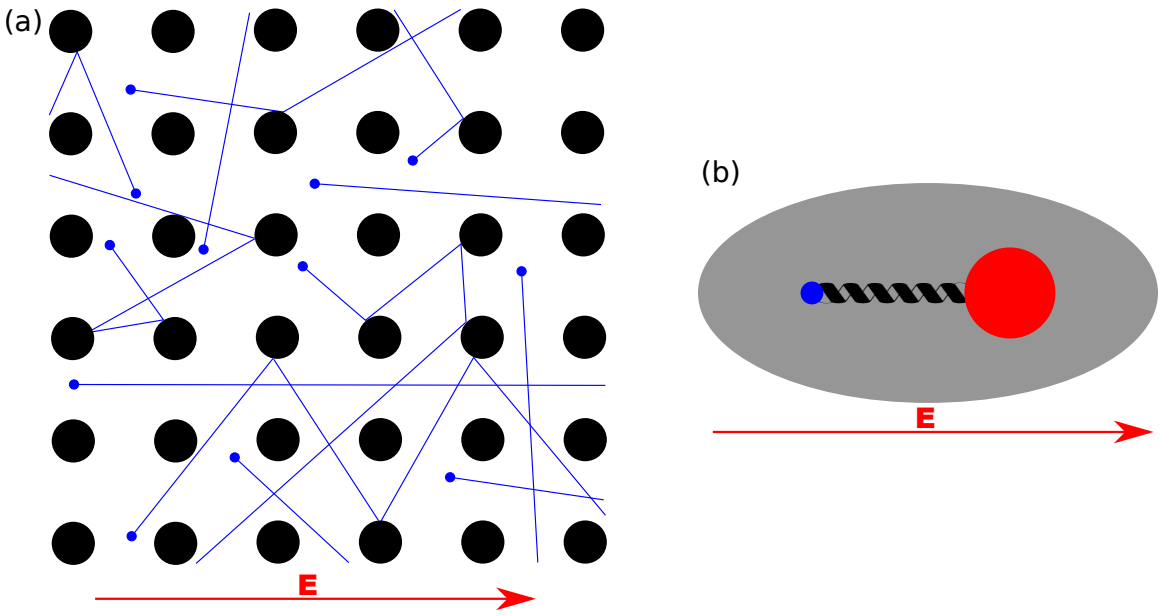

Figure 1.2: (a) In Drude model the metal is formed by a lattice of fixed positive ions (black circles) and the electrons (blue circles) are free to move and only experience instantaneous collisions. The improved Drude-Lorentz model (b) also considers the electrons bound to the atomic nucleus (red circle).

$$m\frac{\partial^2 r}{\partial t^2} + m\gamma\frac{\partial r}{\partial t} = qE \tag{1.1}$$

where r is the position of the electron, m describes the effective free electron mass, γ is the damping term ($\gamma = \frac{1}{\tau}$), also known as the collision frequency, q is the charge of the electron, and $E = E_0 e^{-i\omega t}$ is the external electric field (where E_0 and ω are the amplitude and the frequency of the applied electric field respectively). Assuming a solution of the form $r(t) = r_0 e^{-i\omega t}$ and replacing into equation 1.1, this gives:

$$r(t) = \frac{-qE(t)}{m\omega^2 + i\omega m\gamma} \tag{1.2}$$

This microscopic movement of the electrons in the metal has an effect at the

macroscopic scale which is an induced polarization $P(t) = qn_e r(t)$ that arises when conduction electrons are displaced by a distance r (n_e is conduction electron density). This induced polarization is connected to the external electric field through the dielectric function ϵ of the material:

$$\epsilon(\omega)E(\omega) = \epsilon_0 E(\omega) + P(\omega) \tag{1.3}$$

Replacing the polarization into equation 1.3, we get the Drude dielectric function of a free electron metal:

$$\epsilon(\omega) = \epsilon_0 - \frac{\omega_p^2}{\omega^2 + i\gamma\omega} \tag{1.4}$$

where ϵ_0 describes the ionic background in the metal and ω_p is the bulk plasma frequency of the free electron gas given by:

$$\omega_p^2 = \sqrt{\frac{n_e q^2}{m}} \tag{1.5}$$

It is useful to separate and identify the real and imaginary parts of the dielectric function:

$$Re[\epsilon(\omega)] = \epsilon_0 - \frac{\omega_p^2}{\omega^2 + \gamma^2} \tag{1.6}$$

$$Im[\epsilon(\omega)] = \frac{\omega_p^2 \gamma}{\omega^3 + \gamma^2 \omega} \tag{1.7}$$

With this simple model, we can describe the optical properties of a free electron metal. Assuming $\epsilon_0 = 1$ and zero damping ($\gamma = 0$), the Drude dielectric function

simplifies to $\epsilon = 1 - \omega_p^2/\omega^2$. With this approximation we can distinguish to regimes: One when $\omega > \omega_p$, ϵ is positive, thus the metal has a real refractive index ($n = \sqrt{\epsilon}$). Therefore, the metal becomes transparent because the electrons in the metal are too slow to respond fast enough to the external field. The other regime when $\omega < \omega_p$, then ϵ is negative, and the refractive index becomes imaginary, and this implies that electromagnetic waves cannot propagate inside the medium and are reflected because the electrons in the metal can screen the field.

The validity of the Drude model gives accurate results for metals in the infrared region but starts to break down in the visible region because higher-energy photons can promote electrons from lower energy bands into the conduction band. This inter-band transition lies in the visible part of the spectrum for some metals like gold and copper, thus in this range electrons can be promoted from the d-band to states above the Fermi energy, these transitions are responsible for the particular color in these metals. Figure 1.3 shows a comparison of the Drude and experimental dielectric function for silver.

1.2.2 The Drude-Lorentz model

Five years after Drude model, Lorentz extended the model to include the bound electrons responsible for inter-band transitions using a classical approach [42]. In this approach, we expand the Drude model and consider that the electrons in energy bands below the conduction band are bound to the nucleus. These bound electrons, in the model, are displaced from their equilibrium by the interaction with the electric field but will "bounce" back to their equilibrium position when the field vanishes, as shown in figure 1.2(b). This phenomenon can be described in the equation of motion of the electrons with a spring constant that provides the restoring force that maintains

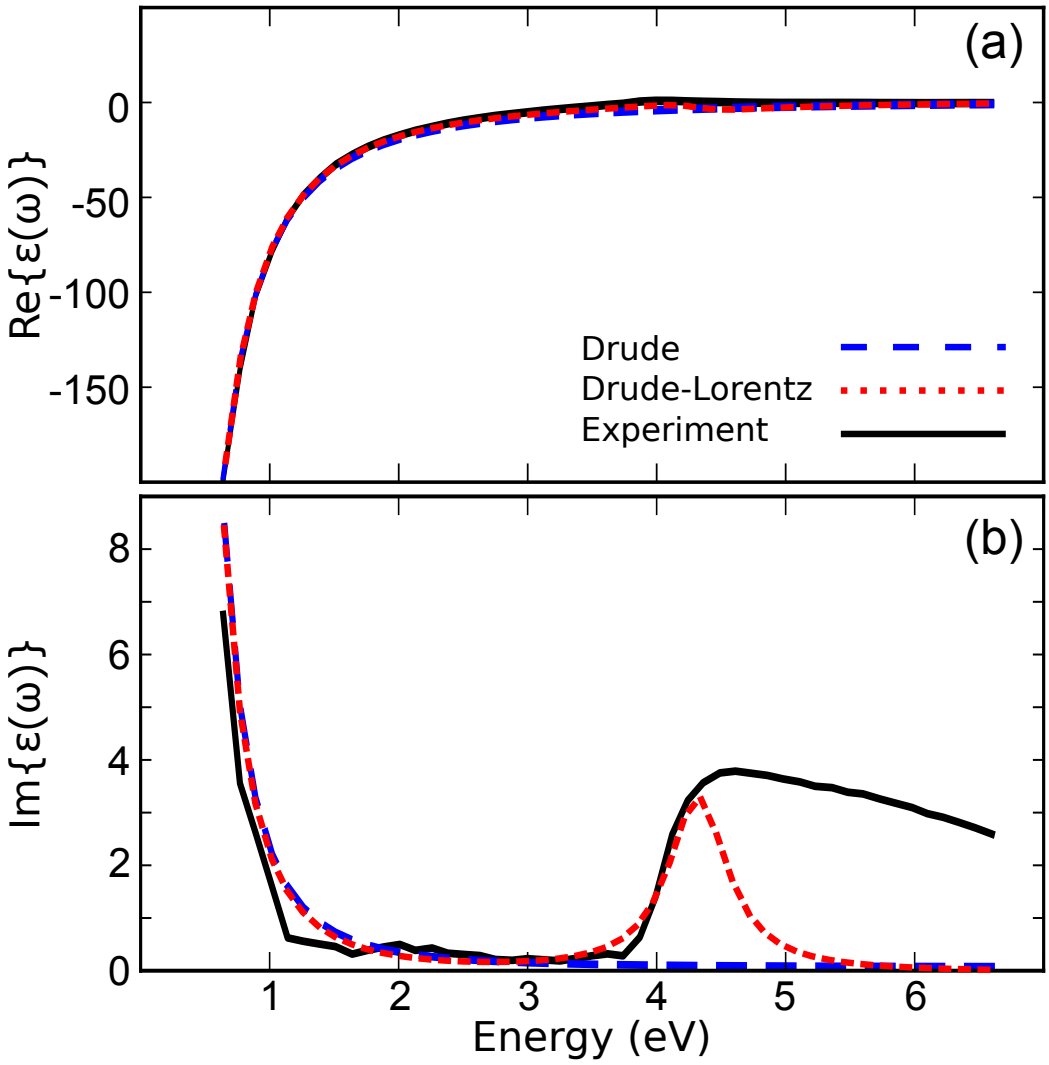

Figure 1.3: (a) Real and (b) imaginary parts of the dielectric function of silver calculated with the Drude model (blue), the Drude-Lorentz model (red), and experimental data (black) from literature [1].

the bound electrons in their equilibrium position as follows:

$$m\frac{\partial^2 r}{\partial t^2} + m\gamma\frac{\partial r}{\partial t} + m\omega_0^2 r = qE \tag{1.8}$$

where the spring constant κ is written in terms of the resonant frequency of the bound electron ω_0 ($\omega_0 = \sqrt{\frac{\kappa}{m}}$). Following a similar procedure than in the Drude's model we have the Drude-Lorentz dielectric function:

$$\epsilon(\omega) = \epsilon_0 + \frac{\omega_p^2}{\omega_0 - \omega^2 - i\gamma\omega} \tag{1.9}$$

Figure 1.3 shows the comparison between the real and imaginary parts of the dielectric function in the Drude model and the Drude-Lorentz model, and the experimental dielectric function of silver [1]. The Drude model has a good agreement at energies below 3.8 eV however it breaks down for higher values. The Drude-Lorentz has a larger range of validity up to approximately 4.2 eV. However, for higher energies, none of the models fits with the experimental dielectric function, this can be improved by adding more inter-band transitions into the model.

1.2.3 Surface Plasmon Polaritons at Interfaces

Surface plasmons present at interfaces between a dielectric and metal are known as surface plasmon polaritons (SPPs). These surface electromagnetic waves propagate along the interface and are coupled to the electron oscillations in the metal. For the physical description of these SPPs, we assume a planar interface with ϵ_2 for the metal at $z < 0$, and ϵ_1 for the dielectric at $z > 0$. The interface located at $z = 0$ defines the coordinate system, with the field propagating along the x direction, as shown in figure 1.4. The wave equation describes the SPPs, and each region can be solved

separately. Assuming that the dielectric function ϵ is uniform and does not change with the position we have the following wave equation:

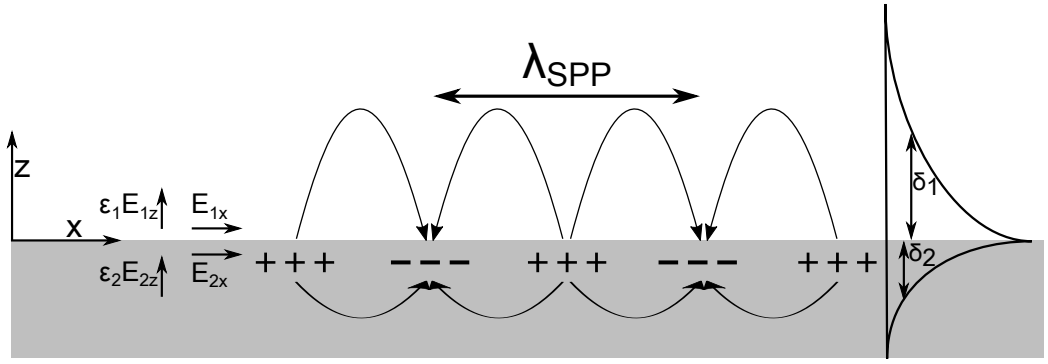

Figure 1.4: Schematic representation of an intensity distribution of an SPP propagating along a metal-dielectric interface (x), where the z component of the electric field decays exponentially

$$\bigtriangledown^2 \hat{E} - \frac{\epsilon}{c^2}\frac{\partial^2 \hat{E}}{\partial^2 t} = 0 \tag{1.10}$$

We know that the SPPs propagate parallel to the surface but decay exponentially into the metal and into space away from the interface, thus we can write a solution of the equation in each region j as:

$$\hat{E}_j = (E_{jx}\hat{x} + E_{jz}\hat{z})e^{i(k_{jx}x-\omega t)}e^{ik_{jz}z} \tag{1.11}$$

Replacing the solution $\hat{E}$ into equation 1.10 we obtain the Helmholtz equation:

$$\bigtriangledown^2 \hat{E} + k^2 \hat{E} = 0 \tag{1.12}$$

where $k^2 = \epsilon(\frac{\omega}{c})^2$.

The phase is continuous at the interface for a wave propagating at the surface, thus

$k_{1x} = k_{2x} = k_x$. The boundary conditions indicate how the solutions from each region match at the interface. The normal component of the displacement is continuous across the interface, thus $\epsilon_1 E_{1z} = \epsilon_2 E_{2z}$. Also the parallel component of the electric field is also continuous at the interface $E_{1x} = E_{2x}$. We know that the wave propagate along x , thus k_x is real. Since the wave is evanescent along z then k_{iz} is imaginary (see figure 1.4). With all this considerations, we obtain the dispersion relation for SPPs:

$$k_x = \frac{\omega}{c}(\frac{\epsilon_1 \epsilon_2}{\epsilon_1 + \epsilon_2})^{1/2} \tag{1.13}$$

$$k_{jz} = \frac{\omega}{c}(\frac{\epsilon_j^2}{\epsilon_1 + \epsilon_2})^{1/2}, j = 1, 2 \tag{1.14}$$

From this dispersion relation we deduce that the condition in which k_x is real and k_{jz} is imaginary can only be satisfied if $\epsilon_1 \epsilon_2 < 0$ and $\epsilon_1 + \epsilon_2 < 0$. If we assume an interface with $\epsilon_1 = 1$ and a metal described by Drude model with no damping, $\epsilon_2 = 1 - \omega_p^2/\omega^2$, the dispersion relation along the interface becomes:

$$k_x = \frac{\omega}{c}(\frac{\frac{\omega^2}{2} - \omega_{sp}^2}{\omega^2 - \omega_{sp}^2})^{1/2} \tag{1.15}$$

where $\omega_{sp} = \omega_p/\sqrt{2}$ is the surface plasmon frequency. Figure 1.5 shows the light line and the dispersion relation for a Drude metal which lie to the right demonstrating the bound nature of the SPPs. The light line does not cross the SPPs dispersion relation at any point. For this reason, is not possible to directly excite SPPs with plane waves and a medium is needed to compensate for the momentum mismatch, to change $\omega = ck_x$ to $\omega = ck_x/n$.

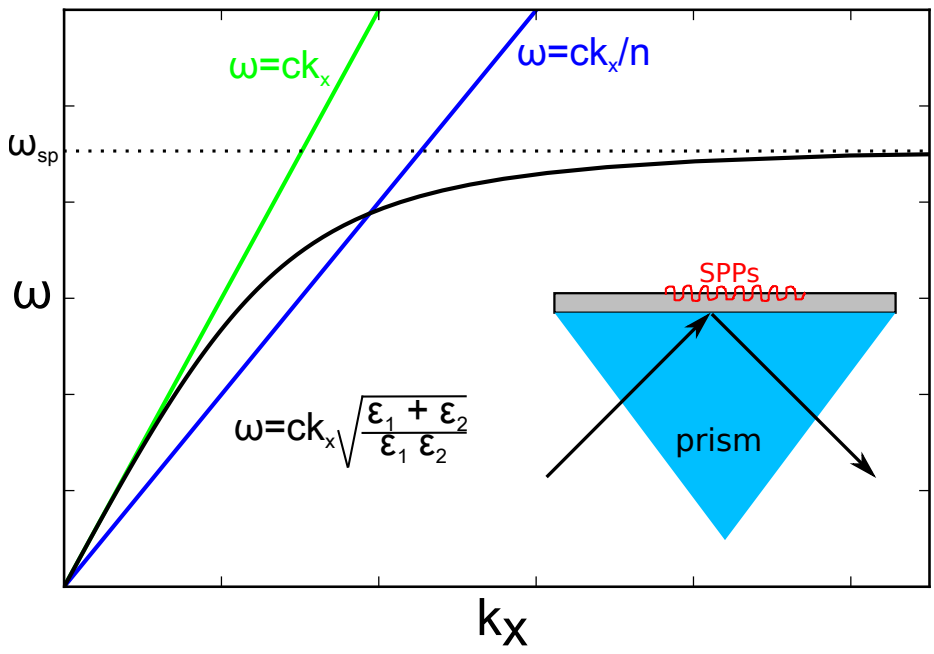

Figure 1.5: The light line on vacuum (green) and on a prism (blue), as well as the dispersion relation for the SPPs at a metal-air (black) is shown, with surface plasmon frequency ω_{sp} indicated. The inset shows the Kretschmann configuration that provides enough momentum to excite SPPs with optical excitation

The dispersion relation displays the properties of the SPPs. We can see that for small wave vectors corresponding to low frequencies (energies) the SPPs are close to the light line. Therefore the plasmon waves are delocalized and extend over many wavelengths into the dielectric space [42]. On the contrary, when the wave vectors are large, the SPPs approach the characteristic surface plasmon frequency. For a Drude metal without damping, the wave vector approaches infinity as the SPP frequency reaches ω_{sp}, and the group velocity goes to zero. In this limit, the SPPs takes an electrostatic character which is known as the surface plasmon. The dispersion relation also explains why it is possible to use a prism to excite SPPs in a metallic film in the Kretschmann configuration [37]. In that configuration, the metal prism interface

creates an evanescent field with enough momentum to excite SPPs at the metal-air interface, as shown in in figure 1.5.

In real metals, damping is not negligible, and losses and energy dissipation occur [43]. These losses are related to the imaginary part of the dielectric function as shown in equation 1.7. In the traveling SPPs, damping creates an attenuation of the wave constraining the distance traveled by the SPPs. The intensity of the wave decreases as $e^{-2Im[k_x]x}$. Thus the characteristic propagation length (L_{SPP}) depends on the imaginary part of the wave vector as follows:

$$L_{SPP} = \frac{1}{2Im[k_x]} \tag{1.16}$$

Losses also affect the penetration of the evanescent wave in the z direction, imposing a limit on the distance the wave can penetrate. This limit is known as skin depth. Considering that the SPPs fields along z fall off as $e^{-|k_{jz}||z|}$. Thus the skin depth is defined as:

$$\delta_j = \frac{1}{k_{jz}} \tag{1.17}$$

Using the theoretical description above, we estimate values of propagation length L_{SPP} in the visible range for silver which goes from approximately 10 μm to 200 μm. Similarly, the total skin depth in the dielectric δ_{air} ranges between 150 nm and 800 nm, while the skin depth inside silver δ_{silver} does not vary much with an average value of 20 nm at visible frequencies.

1.2.4 Localized Surface Plasmons

As we discussed previously, metal surfaces can support propagating plasmon modes that are strongly localized at the surface. When the surface folds up into a discrete structure, the field is quantized into discrete modes. Therefore, the structures instead of propagating waves they form standing waves defined by the geometry of the particle or finite structure. When an electromagnetic wave interacts with a discrete structure, which is smaller than the wavelength of the wave, the electron gas is polarized which creates a restoring force in the structure. This force produces an oscillation of the electron density in the structure. Thus a resonance, which can be excited directly by light, with discrete plasmon modes can arise. These plasmon resonances are called localized surface plasmons. The frequency of the plasmon resonant modes will depend on the geometry of the particle. i.e. the lowest order mode of a spherical particle is illustrated in figure 1.6(a). This mode that shows positive charge accumulation on one side and negative charge accumulation on the opposite side of the particle is the lowest energy mode known as the dipolar mode.

Structures with different shapes will support different modes. For example, a nanorod that is elongated in one direction will support longitudinal modes when an external field is polarized along the long axis of the rod and will support transverse modes when is polarized along the short dimension, as shown in figure 1.6(b). The localized surface plasmons modes occur at discrete frequencies, but they are strongly broadened by the damping in the metal. If damping is significant the plasmon dissipates relatively quickly and the resonances become broad. As we saw before, damping is related to the scattering of electrons that disturbs the coherence of the plasmon oscillation. The time from the scattering event until the moment in which coherence

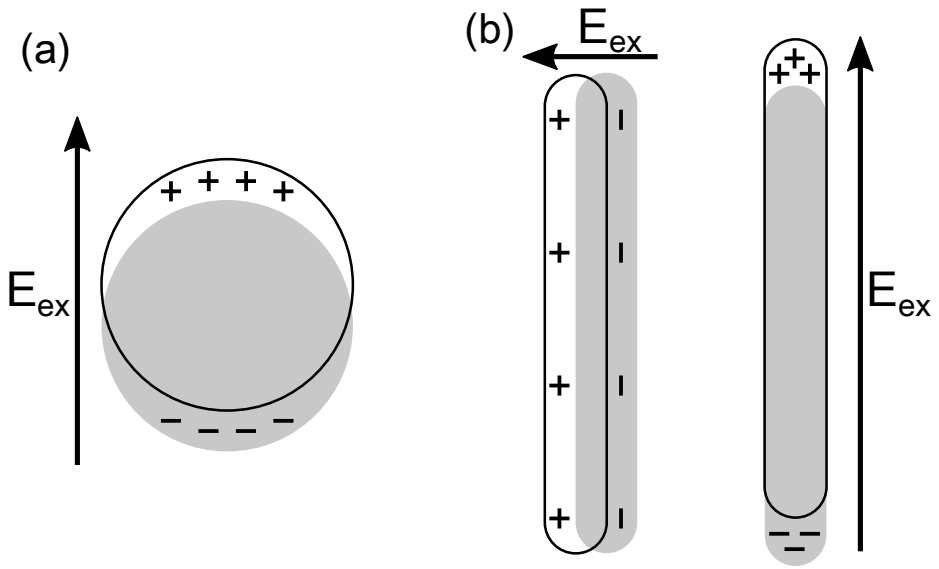

Figure 1.6: (a) Diagram of the dipolar mode of a spherical particle excited by an external field represented by the arrow. (b) Diagram of the lowest order longitudinal (right) and transverse (left) modes of a nanorod (b)

is destroyed is called dephasing time T_d. The dephasing time includes all the different channels in which a plasmon could decay. i.e. radiative decay and non-radiative decay processes that result in hot electrons and holes [43]. The dephasing time of a localized surface plasmon oscillation can be determined from the full width of the spectral resonance of a plasmon Γ, as follows:

$$T_d = \frac{2\hbar}{\Gamma} \tag{1.18}$$

In a finite plasmonic structure, due to the confinement of the plasmon oscillation, multipolar modes can be supported when the structure is larger than the surface plasmon wavelength and also much larger than the skin depth. However, if the structure is smaller than the skin depth, the oscillations are in phase with the external

electric field. In this case, the structure can be approximated to a dipole, and higher order modes are absent. Therefore the far field response of the particle can be modeled by an effective dipole moment. However, the near field response of the particle will vary locally and will strongly depend on the geometry of the particle.

1.2.5 Plasmons in a metallic sphere

The metallic sphere is the simplest structure that can be studied when analyzing finite plasmonic structures. Even though this is the most simple structure, to obtain a relatively simple analytical solution of the optical response of the sphere some approximations have to be made. The initial approximation is that the sphere diameter is much smaller than the wavelength of the field that is exciting the plasmon response, allowing retardation effects to be ignored. This approximation is known as the "quasistatic" approximation because it permits a plane wave to be described as a constant field ($E = E_0$). Therefore, the external electric potential in polar coordinates is $\Phi = -E_0 r\cos(\theta)$. Then, it is possible to arrive at a general solution of the form [42]:

$$\Phi_{in}(r,\theta) = \sum_{l=1}^{\infty} A_l r^l P_l(\cos(\theta)) \tag{1.19}$$

$$\Phi_{out}(r,\theta) = \sum_{l=1}^{\infty} [B_l r^l + C_l r^{-(l+1)}] P_l(\cos(\theta)) \tag{1.20}$$

Where, B_l is determined by the boundary contidions at ∞ where $\Phi_{out} = E_0 r\cos(\theta)$, therefore $B_1 = -E_0$ and $B_l = 0$ for $l \neq 1$ indicating that for a very small particle higher order modes cannot exist in the quasiestatic limit [39], as we mentioned before. A_l and C_l are determined from the boundary conditions at the surface of the sphere,

as was the case in the metallic interface. Thus at $r = R$, the tangential components of the electric field inside and outside are equal, and the normal components of the displacement are also same. With this conditions and with the dielectric function of the metal particle ϵ_{in} and the dielectric function of the surrounding medium ϵ_{out} we have that the potentials become:

$$\Phi_{in} = -\frac{3\epsilon_{in}}{\epsilon_{in} + 2\epsilon_{out}} E_0 r \cos(\theta) \tag{1.21}$$

$$\Phi_{out} = -E_0 r \cos(\theta) + \frac{\epsilon_{out} - \epsilon_{in}}{\epsilon_{in} + 2\epsilon_{out}} \frac{E_0 R^3 \cos(\theta)}{r^2} \tag{1.22}$$

The potential outside the sphere Θ_{out} shows two components one which is the external field ($\Phi = -E_0 r \cos(\theta)$) and the other which has the form of an electric dipole proportional to the external field $\frac{\alpha \vec{E_0} \cdot \vec{r}}{4\pi r^3}$, because $\Phi_{dipole} = \frac{\vec{p} \cdot \vec{r}}{4\pi\epsilon_0\epsilon_{in} r^3}$ and $\vec{p} = \alpha\epsilon_0\epsilon_{in}\vec{E_0}$ where α is defined as the polarizability. Therefore for a metallic sphere in the quasistatic limit we have:

$$\alpha = 4\pi R^3 \frac{\epsilon_{out} - \epsilon_{in}}{\epsilon_{in} + 2\epsilon_{out}} \tag{1.23}$$

From equation 1.23, we can see that the total value of the polarizability will depend on the excitation frequency if ϵ_{in} or ϵ_{out} varies with frequency. Also, the polarizability will reach a maximum value when $\epsilon_{in} + 2\epsilon_{out}$ is at a minimum for a particular frequency; this occurs when $Re[\epsilon_{in}(\omega)] = -2\epsilon_{out}$, indicating that a resonant mode, called the dipole surface plasmon, is present. The magnitude of the resonance will depend on the values of $Im[\epsilon_{in}]$ and $Im[\epsilon_{out}]$, the smaller they are, the stronger the resonant. In the limit when no damping is present, and both values are zero a

singularity exists, and a resonant mode can be excited even for minuscule external fields. For a sphere made of a Drude metal, with a dielectric function as shown in equation 1.9, without damping and in a vacuum environment ($epsilon_{out} = 1$), the polarizability takes the form:

$$\alpha = 4\pi R^3 \frac{-\omega_p^2}{3\omega^2 - \omega_p^2} \tag{1.24}$$

Therefore, for small frequencies ω, the polarizability approaches the static polarizability $4\pi R^3$. For high frequencies, α tends to zero, and the external field does not induce a dipole because the electrons in the sphere cannot react fast enough to the external excitation. At the singularity point, we have the dipole surface plasmon resonance which occurs at a frequency $\omega_{dsp} = \frac{\omega_p}{\sqrt{3}}$.

For our analysis, we have considered that the sphere falls within the quasistatic approximation, which is limited to particles much smaller than the excitation wavelength. For bigger particles, even for particles larger than 10% of the wavelength, the optical response starts to differ from the quasistatic response [39]. The phase of the external field is no longer constant across the volume of the particle, and higher order modes can arise. Therefore a different approach that considers retardation is required. Gustav Mie completed the full electrodynamic solution in 1908 by expanding the fields using Bessel and Hankel spherical functions [44]. The equations of the fully retarded solution for the metallic sphere are not easy to understand intuitively, and their analysis goes beyond the purpose of this chapter. Analytical solutions of the optical response of only simple structures like the ones described here are of practical interest. A numerical approach is preferred to model more complex structures, as will be discussed in Chapter 2.

1.3 Plasmonic coupling

In the previous section, we have described the surface plasmon on finite metallic nanostructures. When these finite structures are in proximity, their near-fields interact changing the optical response of the assembly. This phenomenon was studied using EELS first already in 1982 in the pioneering work of Batson [45] using aluminum nano-spheres. Intuitively, when a nanoparticle is excited, it will have an electric field associated with the surface plasmon, as we saw in the previous section. This electric field is "perceived" by the neighboring nanostructure. Therefore each particle in an assembly of particles will experience a field which is the sum of the external field plus the near-field of the other nanostructures, resulting in a coupled optical response. From this simple picture of the coupling of plasmonic nanostructures, we can already infer that the coupling is strong when the regions of two or more nanostructures with high charge density are next to each other. Also, the coupling strength will increase when the separation between the nanostructures decreases.

For a simple case of two metallic spheres in the quasistatic approximation, we can assume that each particle will behave as a dipole, as illustrated in Figure 1.7. Because of the net field on the two spheres, the restoring force in each particle will increase or decrease depending on the polarization direction of the external field. Therefore, the interaction of the two metallic spheres will produce a different net dipole and optical response than an isolated sphere. For a field transversal to the axis between the two particles, the polarization of the second particle will be out of phase with the plasmon field of the first one. Therefore, the coupled resonance requires higher energy than the single-dipole resonance, so the plasmon resonance blue-shifts. For a field parallel to the axis, the plasmon field of the first particle is in phase with the polarization of

the second one. The in-phase response of the spheres occurs at energies below the resonance of the single dipolar mode. Thus the coupled resonance mode will red-shift. In the coupling of the parallel configuration, the fields across the gap between the particles can be much greater than the fields in isolated particles. This enhanced field so-called "hot spot" can strongly interact with anything in the gap, so nanoparticle dimers are excellent antennas that can couple electromagnetic waves into and out of localized emitters [39]. This effect is used to enhance Raman scattering by molecules adsorbed on hot spots in a technique know as Surface-enhanced Raman spectroscopy (SERS).

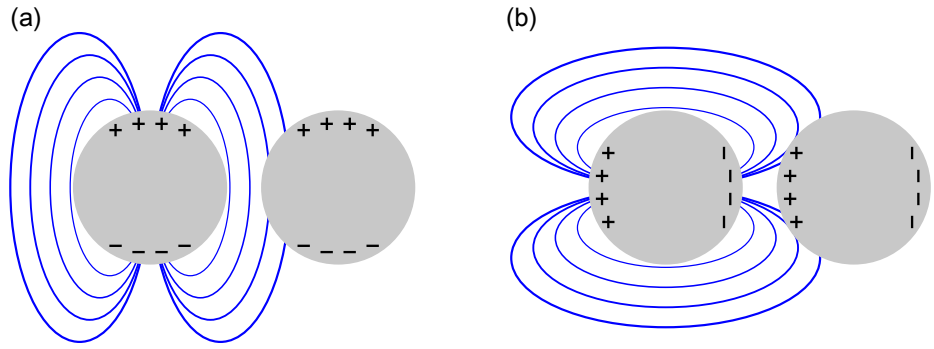

Figure 1.7: Diagram of the coupling of the dipolar modes of two spherical particles excited by external field transversal to the particle-particle axis (a), and excited by a field parallel to the particle-particle axis (b).

1.3.1 The Exciton Coupling model

The simplified description of coupling described above has a strikingly similarity to the spectral changes observed in the dimerization of organic chromophores, which is explained by the exciton coupling model. In the exciton model after dimerization, the excited-state levels of the each isolated chromophore split into two levels, one

lever with higher energy and other with lower energy with respect to the single chromophore excited state. These two possible states correspond to two arrangements of the transition dipoles of the molecules in the dimer, one with the dipoles in-phase or symmetric and the other with the dipoles out-of-phase or anti-symmetric [46]. In this approximation, the Coulombic interaction between the molecular dipoles determines the energy splitting. The energy of the interaction "$U_{splitting}$", in this model, is given by [47]:

$$U_{splitting} = -\frac{\kappa|\mu|^2}{4\pi\epsilon_0 r^3} \tag{1.25}$$

where $|\mu|^2$ is the module of the transition dipole, r is the distance between dipoles, and κ is a dipole orientation parameter given by:

$$\kappa = 3\cos(\theta_1)\cos(\theta_2) - \cos(\theta_{12}) \tag{1.26}$$

with θ_{12} the angle between the transition dipoles, θ_1 the angle between dipole 1 and the axis connecting the two dipoles, and θ_2 the angle between dipole 2 and the axis of the dipoles. In the limit where the particle size is much smaller than the wavelength of the incident field, and the interparticle distance r is much smaller than the particle size, the exciton-coupling model can describe the plasmonic interaction of metallic particles[46]. Thus, for the coupling of LSPR in nanoparticles, we can consider the four relative orientations of the dipoles as shown in figure 1.8.

For an external field polarization along the interparticle axis, we have an end-to-end alignment of the two dipoles. Figure 1.8 shows the angles between the dipoles, thus $\kappa = 2$. This value of κ results on a negative value of the interaction energy

$U_{splitting}$, suggesting that in the end-to-end symmetric configuration of dipoles the interaction is attractive. Hence, the resonant energy of the dimer red-shifts with respect to the single particle resonance. When the dipoles are aligned anti-symmetrically in the longitudinal configuration, the angular distribution as shown in figure 1.8 results in $\kappa = -2$ and a positive interaction energy. This indicates that the interaction is repulsive and the resonance energy is higher that the one of the isolated particle. However, this mode is optically forbidden because the dipoles have an equal magnitude and opposite orientation, so the net dipole cancels out. This mode is called a "dark mode" because in the quasistatic limit it cannot be directly excited by free propagating light, however, can be excited by local probes such as electron beams. "Dark modes" are not truly dark in larger structures were retardation is not negligible, however these modes are very difficult to excite with photons under normal incidence making them even more difficult to detect with optical spectroscopies. Single nanostructures can also sustain high order dark modes when the net dipole of the resonance is zero. For the case where the external field polarization is transversal to the interparticle axis, and both dipoles are parallel to each other, $\kappa = -1$, resulting in a positive interaction energy. Therefore the interaction is repulsive and the resonance energy blue-shifts, however, the magnitude of the shift is half of the energy of the longitudinal modes. Finally, for the transversal configuration with the dipoles anti-symmetrically aligned $\kappa = 1$, so the resonant energy is lower. This mode is also a dark mode because the dipoles cancel out the net dipole moment in the dimer.

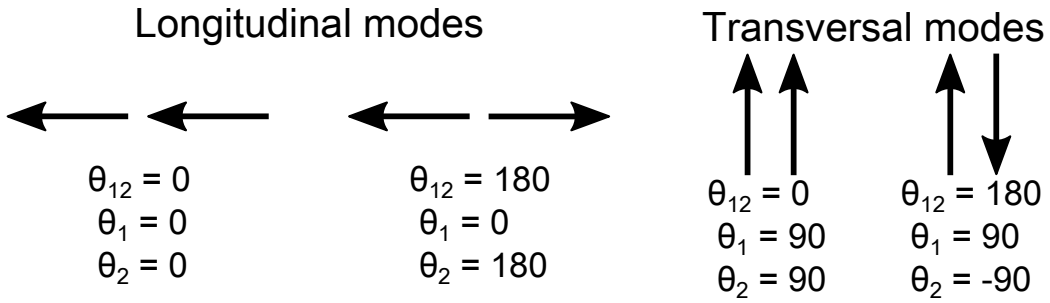

Figure 1.8: Schematic of the four possible dipole configurations of the coupling of two metallic particles and their respective angular orientations (see text)

1.3.2 Plasmon Hybridization

The plasmonic coupling of more complex nanostructures that cannot be approximated to a dipole and in which higher order modes are not negligible can be described by the "hybridization" of the plasmons resonances supported by the individual nanostructures or resonant modes of more simple shapes. This mathematically intensive model can be used to understand the response of particles with very complex geometries as well as structures formed by multiple particles.

One of the first described examples was the plasmonic response of a nanoshell, that can be understood by the plasmon hybridization between surface plasmons supported by a nanosphere and nano-cavity [2] as shown in figure 1.9(a). The nanoshell support plasmons with surface charges in their inner and outer surfaces that can be modeled as charges on a cavity and a sphere respectively. These charges can interact due to the finite thickness of the shell, and the strength of the interaction is controlled by the thickness of the shell. The hybridization results in a splitting of the plasmon resonances into two new resonances: A symmetric bonding plasmon and an antisymmetric antibonding plasmon. Adapting the formalism of molecular orbital

theory and using a linear combination of atomic orbitals (LCAO) that in this case were spherical harmonics to describe the electron density of a sphere and a cavity, Prodan *et. al.* demonstrated that interactions of their plasmons resonances give rise to the hybridized plasmon modes shown in figure 1.9(a). Although quantitively the hybridization model can be mathematically demanding and depending on the geometry can require expensive numerical calculations, as is the case of the atomic hybridization model. The concept of mode splitting into bonding and antibonding modes can be intuitively used to understand plasmonic coupling.

Another example of plasmon hybridization is the coupling of metallic nanorods [3]. In this example, the coupling strength depends on the distance between the structures, the mode order and the distance between the resonance and the neighboring structures. As in the previous example, the coupling of the plasmons leads to splitting of modes in two modes, one with higher energy and another with lower energy and, as seen in figure 1.9(b), the hybridization depends on the relative orientations of the nanorods. With hybrid modes emerging when the nanorods are aligned either in parallel or series. When the nanorods are aligned perpendicular to each other, they do not couple. Thus they do not form hybrid plasmon modes. The hybridization model provides an intuitive way of analyzing the plasmonic response of complex nanostructures as well as the coupling between nanoparticles, making possible to predict the splitting of resonant modes in ensembles of nanoparticles.

1.3.3 Fano Resonances

In the models discussed above, coupling promotes the formation of new modes with resonances shifted in energy and nature. In the examples we showed, we have the

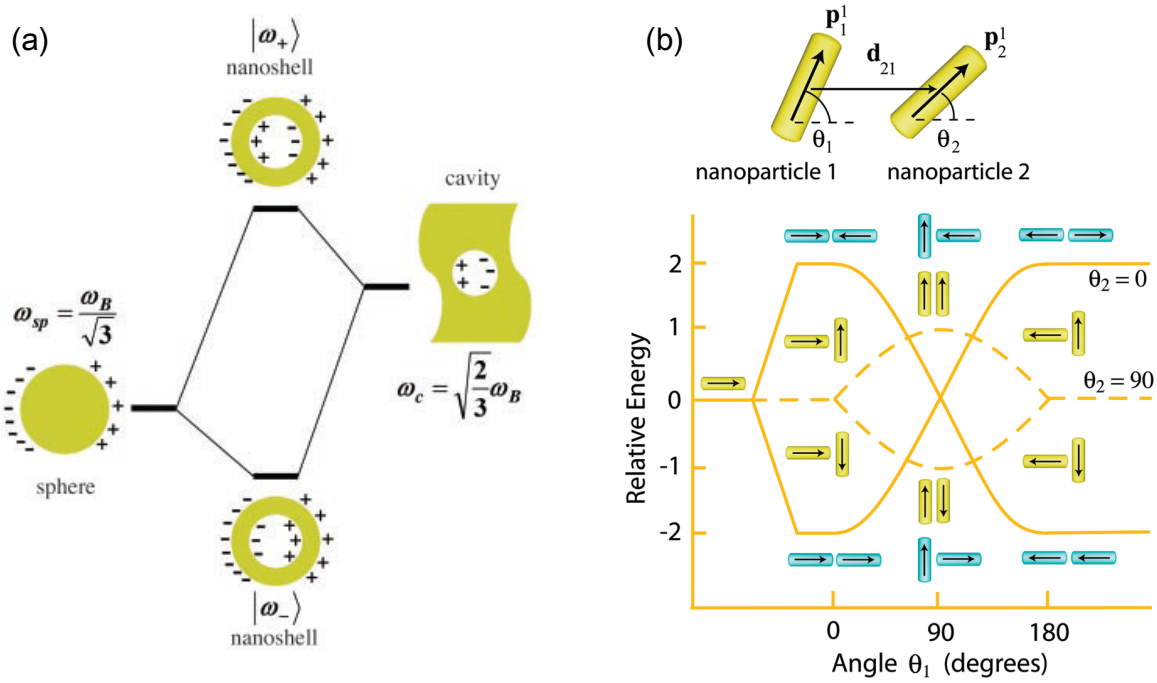

Figure 1.9: Energy-level diagram describing the plasmon hybridization in a metallic nanoshell resulting from the interaction between an sphere and cavity plasmons (a). The two nanoshell plasmons are an antisymmetrically coupled (antibonding) ω_+ plasmon mode and a symmetrically coupled (bonding) ω_- plasmon mode. Diagram of the plasmon hybridization arising from the interaction of two nanorods (b). Top Panel: the relative geometry of two nanorods showing the direction their dipole moments. θ_1 and θ_2 are the angles formed by the nanorods with the horizontal line. Bottom panel: the hybridization diagram for the nanorods showing the relative shift in energies for different orientations. The solid curve is for nanorod 2 horizontal ($\theta_2 = 0$) and the dashed curve is for nanorod 2 vertical ($\theta_2 = \pi/2$). Adapted from [2] and [3].

coupling of equivalent modes, i.e. dipole-dipole coupling, where the modes have similar decay rates. However, when multiple resonant modes of a metallic nanostructure system are excited simultaneously, interference between resonant modes with very different decay rates can occur leading to a spectral response that differs from the usual mode splitting. Specifically, if a narrow dark mode interferes with a broad bright mode, the spectral response can take and asymmetric shape known as a Fano resonance [48]. This definition is an adaptation of the original definition of Fano resonance which is the interference between a continuum state and a discrete state that resonantes in the same energy range of the continuum state.

An example of resonance interference in a plasmonic system is the case of a symmetric nanodisk clusters or plasmonic oligomers. Figure 1.10 shows the experimental extinction as well as the numerical results of the gold oligomers of various configurations, shown in the SEM images in the central panel. The spectrum of a single gold disk (monomer) in the last row of the figure shows the dipolar mode. When we put together a group of seven monomers (forming an heptamer), as shown in Figure 1.10, they couple. The coupling strength depends on the interparticle gap distance. For a 130 nm gap, the coupling is weak, and only one peak is observed. However, as gap decreases, a "dip" appears, which becomes more pronounced as the gap is further reduced. This dip is characteristic of a Fano interference. The coupling of the dipolar modes of the disks in this structure forms a bonding mode that consists of all the individual modes oscillating in-phase. This in-phase oscillation also produces an enhanced broad radiation making the bonding mode super-radiant [4]. As we saw above, coupling also creates an antibonding mode in the heptamer. In this antibonding mode, the dipolar mode of the central disk oscillates out of phase with the dipolar

plasmons of the neighboring disks. The out of phase oscillation considerably reduces the net dipole moment of the antibonding mode inhibiting radiation resulting in a subradiant plasmon mode [4]. The interference of the broad super-radiant bonding mode and the narrow subradiant antibonding mode induces the sharp Fano resonance shown in Figure 1.10. As in the case of the heptamer, other structures can support Fano resonances [49]. Structures in which coupling produces a broad super-radiant mode and a narrow subradian mode in an energy range where the two plasmon modes can interfere will support Fano resonances.

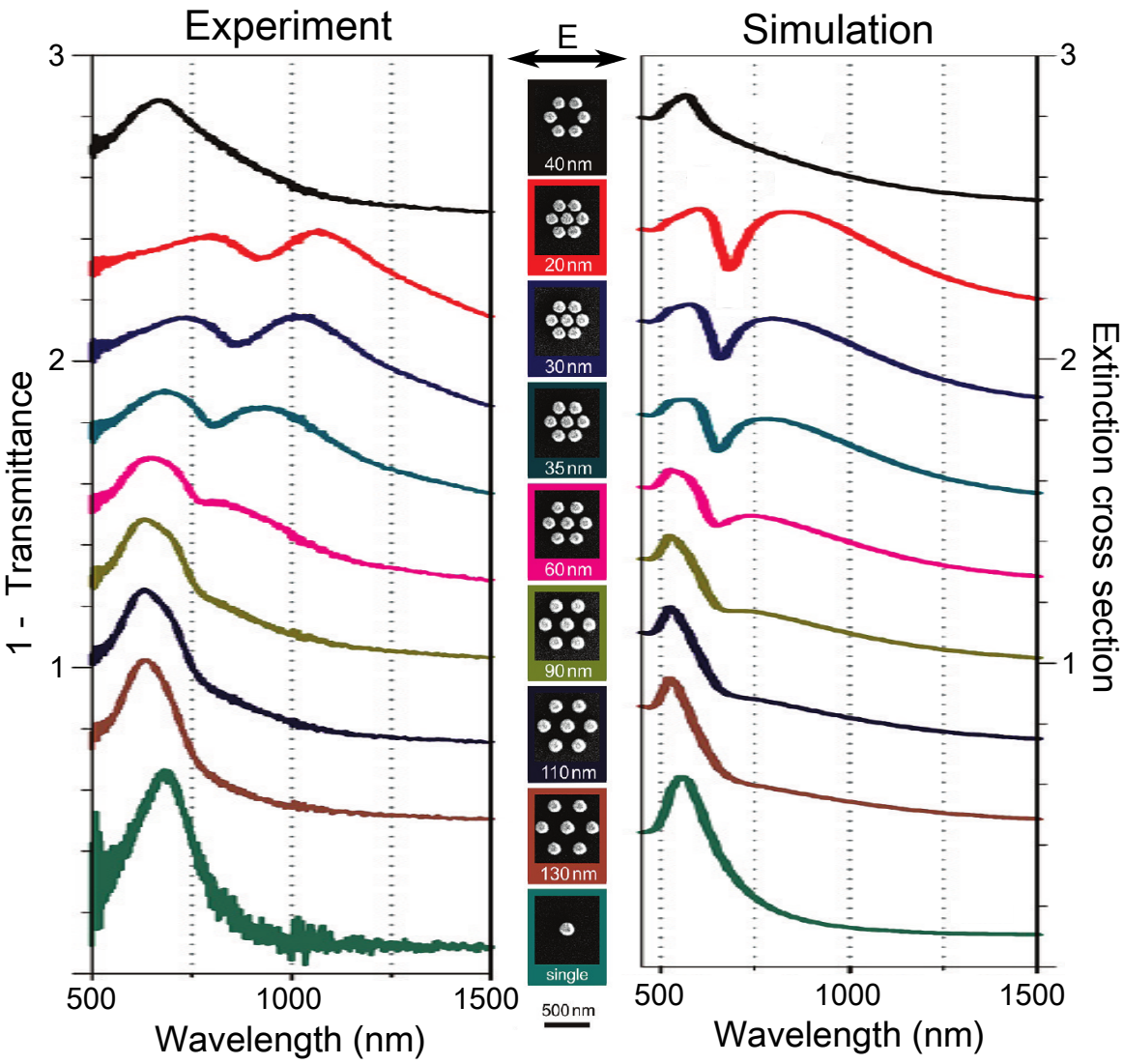

Figure 1.10: Experimental and simulated extinction spectra of a gold disk or monomer, a hexamer, and heptamers with different interparticle gap distances. The middle column shows SEM images indicating the gap separation. As the gap separation decreases in the heptamers, we observe the formation of a Fano resonance due to the coupling of a super-radiant mode and a subradiant mode (see text). Adapted from [4].

Chapter 2

Modelling, Fabrication, and Characterization of Plasmonic Nanostructures

In this chapter, we describe the methodology we followed for the study of the plasmon resonances in planar structures starting by the modelling of the finite structures we used in our study. A brief description of the software use and the theory behind it is given. The structures used in this work were fabricated following a top-down approach know as electron beam lithography. The details and parameters of the fabrication procedure of the silver planar strucutres are also described in this chapter. The characterization of the plasmonic structures, in this work, was done by STEM-EELS. Here we provide a general description of STEM and EELS, followed by a description of the excitation of surface plasmons by fast electrons, the physical interpretation of the EELS signal, and a comparison with optical spectroscopy. Finally, the chapter closes with a summary of the relevant literature on the characterization of surface

plasmons by EELS.

2.1 Modelling of surface plasmons

In this work, some of the experiments are complemented by numerical modeling performed using the Metallic Nanoparticle Boundary Element Method (MNPBEM) Matlab toolbox. This software package simulates finite metallic nanostructures, using the boundary element method (BEM) developed by Trugler *et. al.* [50, 51]. This toolbox solves Maxwell's equations for particles with homogeneous and isotropic dielectric functions in a dielectric environment. The package works best for metallic nanoparticles with sizes in the range of a few to few hundreds of nanometers, and for energies in the optical and near-infrared regime.

In the BEM the nanoparticles are described by frequency dependent dielectric functions separated by abrupt boundaries, and the fields in each region are described in terms of interface sources that are calculated by imposing the continuity of the potential and the electric displacement as boundary conditions [52]. The advantage of this method is that requires less computational effort since it only involves calculations at the boundaries and not of the whole volume. This method can be used to solve fully retarded and non-retarded (quasistatic approximation) Maxwell's equations that describe surface plasmons excited by plane waves, dipoles or electron beams of any arbitrary finite shape that can be discretized in a three-dimensional mesh as shown in figure 2.1. Some of the limitations of MNPBEM are that it was not designed to model large structures, it requires large amounts of memory to run optimally, and the commands to build a 3D model are limited making the construction of complex structures difficult. In this thesis, I model silver structures using tabulated dielectric

functions, and unless otherwise stated the structures are not supported and instead effective dielectric functions were used. Some simulations presented in this thesis are performed by collaborators that did not use MNPBEM. The methods and details of theses simulation are described in the corresponding chapters.

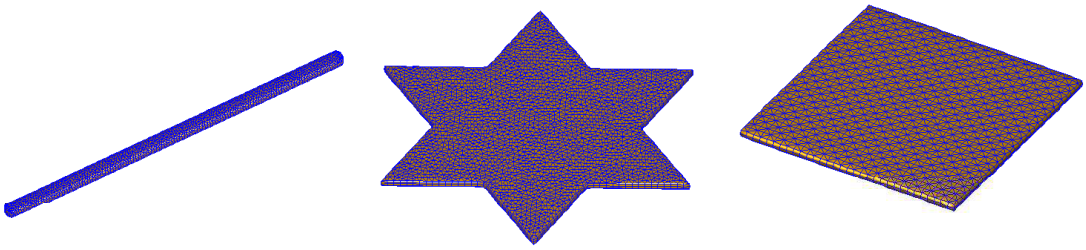

Figure 2.1: Discretized particle boundaries created on the MNPBEM toolbox.

2.2 Electron beam lithography

The growth of the field of plasmonics was sparked in part by the ability to fabricate nanostructures. Two main types of fabrication methods exist, top-down that in general involves depositing or removing material to form a pattern; and bottom-up that involves chemical synthesis. The early works on EELS mapping of plasmonic structures relied almost exclusively on structures fabricated by a bottom-up approach. However, the level of complexity of the structures, and the degree of morphology and arrangement control that can be synthesized by this approach is limited compared with top-down methods. Lithography, as well as other top-down methods, is versatile in the sense that you can fabricate different structures without changing the experimental procedure as is the case of top-down methods. For these reasons in this work, I fabricate the structures studied in this thesis exclusively by electron beam

lithography a well known top-down method.

The samples are fabricated on silicon nitride TEM grids. We have to use thin membranes as the substrate for our nanostructures because the sample must be electron transparent to be analyzed using STEM-EELS. For the 80keV accelerating voltage of our experiments and electron transparent sample is a several tens of nanometers depending on the material. The fabrication process starts by cleaning the silicon nitride grids. First, we gently rinse the grid with acetone and with isopropyl alcohol. We dry the grid with a N_2 gun and secure it on a stub. Then, we plasma clean the grid for 2 minutes. After the cleaning we proceed to deposit the resist, which in our cases is polymethyl methacrylate (PMMA) 950 000 molecular weight at 3 % anisole, on a 3 mm diameter and 30-50 nm thick silicon nitride TEM grid (Norcada) by spin coating at 4000-6000 rpm for 90 seconds. The TEM grid is supported on a transparent Gel-Pack^{TM} film on a glass cover slip [53]. This arrangement prevents the rupture of the silicon membrane by the vacuum suction of the spin coater. After the thin film is formed, the sample then is baked at 175 °C for 5 minutes.

The samples are patterned using energetic electrons on a JEOL JSM-7000F SEM equipped with Nano Pattern Generation System (NPGS). Scanning coils in the SEM allow the point by point exposure of the resist, by scanning a focused electron beam across the sample. Together with the scanning coils, the high-speed beam blanker allows full 2D control of the beam allowing the patterning of any 2D shape into the resist. The patterning is performed with a 30-40 pA beam current at the highest allowed electron beam energy in our system (30 keV) to reduce undesired scattering events and increase resolution. The beam dosage is adjusted according to the type of pattern we want to write. NPGS allows you to choose between point, line, and area

dosage. It is recommended to run a test sample such as the one shown in figure 2.2 to obtain optimum writing dosages for the three types of dosages. As a practical rule for line dosages, it is recomended to use values between 0.5 and 5 μC/cm, and for area dosages values between 240 and 600 μC/cm^2, and trying to keep the dosage low when writing structures with gaps.

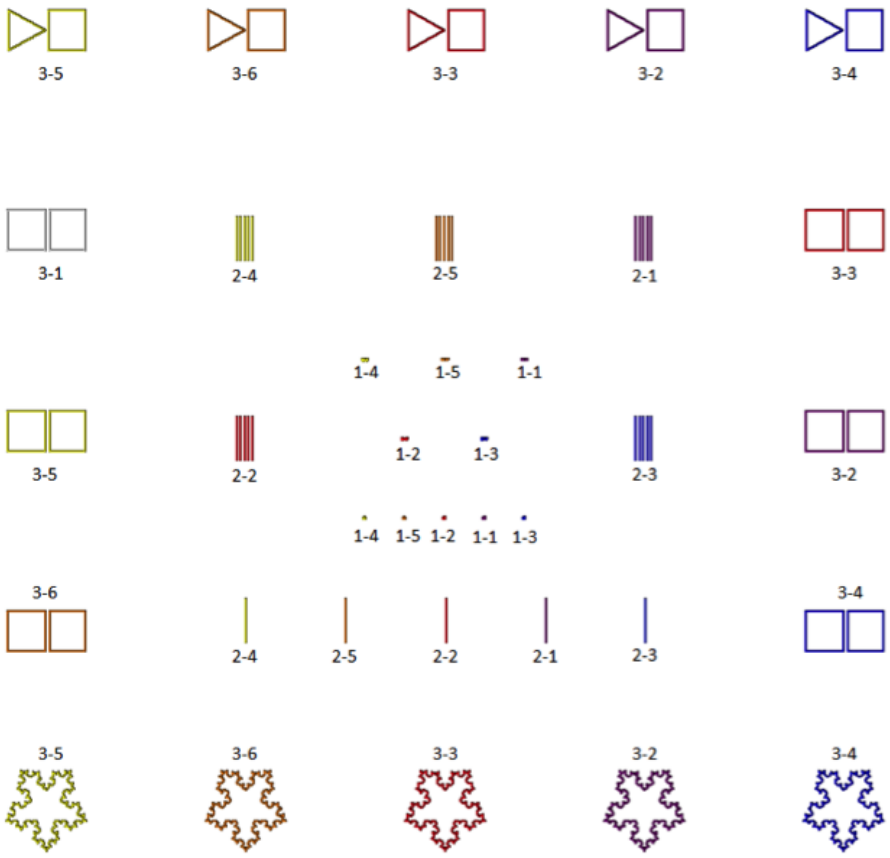

Figure 2.2: Example of a test pattern to obtain optimal dosages for a particular EBL system. The pattern has points, single lines, group of lines, polygons, polygon dimers with small gaps, and fractal structures to test all possible types of 2D patterns.

After exposure, the high-energy electrons have broken the long polymer chains of

PMMA into short fragments which are removed by soaking the sample in a 3:1 isopropyl alcohol : methyl isobutyl ketone developer solution for 70 seconds. The sample is the rinsed in isopropyl alcohol and dried with N_2 steam. After developing, 30 to 50 nm Ag film is deposited on the samples in an electron beam evaporator system, with a 6 keV and 250 μA electron source. After the Ag film is deposited all over the surface of the sample, we remove the excess metal by lift-off. The sample is soaked under agitation in acetone, which dissolves the resist and the metal that was on top of the resist is removed, leaving behind the desired metal pattern on the substrate. Finally, after the excess metal is removed we rinse the sample in isopropyl alcohol and blow dry with the N_2 gun. Figure 2.3 shows a scheme of the fabrication procedure.

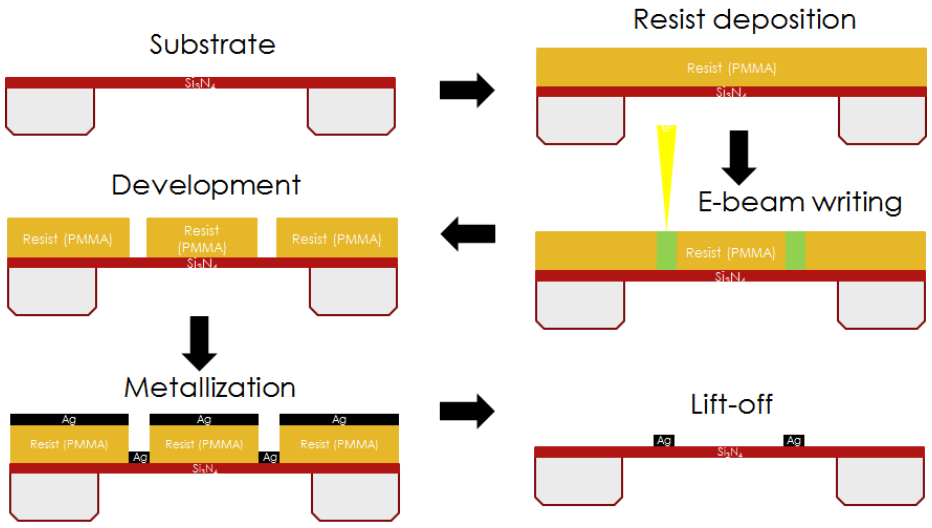

Figure 2.3: Diagram of the procedure for electron beam lithography of silver structures in silicon nitride membrane

2.3 Scanning Transmission Electron Microscopy

Our study of the SP resonances is performed in an STEM-TEM (FEI Titan 80-300) equipped with an electron monochromator and operated in STEM mode. A schematic of a generic TEM is shown in figure 2.4. The electrons are extracted from the emitter in the gun, which in our case is a field emission operating in the Schottky mode, by the anode which is held at a potential between 1.8 and 5.5 keV. The emitter is a single crystal tungsten, covered with a thin layer of zirconia. The zirconia lowers the work function of the emitter when the emitter is heated to approximately 1800 K [5]. Two main characteristics of an electron gun to consider are the brightness and the energy spread. Brightness is a measure of the current density per unit of solid angle normalized to the acceleration voltage. For an S-FEG the brightness is in the order of 0.5 to 2.0 10^7 [A/m^2 Sr V], and for an X-FEG is typically around 0.7 to 1.5 10^8 [A/m^2 sr V] [5]. The energy spread determines the energy resolution in EELS (see below) and can limit spatial resolution in the STEM. The electrons exit the gun with an energy spread in the range of 0.5 to 0.8 eV. To improve this energy spread the microscope is equipped with a monochromator, which is positioned right below the gun. The monochromator is a Wien filter which disperses the electrons by energy into a line, part of the line is selected using a slit, which allows electrons with a much narrower energy spread to pass. Under optimal conditions, the monochromator can reduce the spread below 100 meV. In this work, the monochromator was operated under accelerating conditions with a potential of 800 V. After the monochromator, the electrons are accelerated to 80 keV in most of our experiments, unless otherwise indicated.

After the accelerator, the electrons go through a series of electromagnetic lenses.

The lenses create strong magnetic fields in the path of the electrons that forces the electrons to stay in the optic axis inducing a focusing effect. The main purpose of the lenses in STEM mode is to form a very small probe on the sample. Two sets of lenses are used to form the beam: the condenser lenses, and the objective lenses. The condenser lenses (C) that are in principle used to converge the electrons from the source to the objective lenses. A condenser aperture is inserted between condenser lenses to define the convergence angle which is the angular size of the beam. The objective lenses (Obj) play a critical role in the quality of the probe and size of the probe in the STEM, and under optimal conditions, the lenses can form a sub-nanometer electron beam. The objective lenses are typically symmetrical, with two pole pieces separated by a small gap, which can be as small as 1 mm and can support magnetic fields higher than 1 T [8].

In the STEM the focused beam is deflected by scanning coils in a raster fashion over a two-dimensional region of interest in the sample. After the beam has interacted with the sample, a set of projector lenses allow us to manipulate the transmitted beam that reaches the detectors. In our experiments two signals are acquired simultaneously: The high angle scattered electrons in a high angle annular dark field (HAADF) detector, which is sensitive to the atomic number of the scattering atoms, and provides morphological information of the sample; and the low angle scattered electrons that are collected in the electron energy loss spectrometer. The two signals are collected at each pixel position in the scan, forming an HAADF image and EELS spectrum image, as shown in figure 2.5. The spectrum image is a 3D data array, in which two axes correspond to the spatial position of the beam and the third axis correspond to the energy loss spectrum. A slice of this 3D data set at a particular

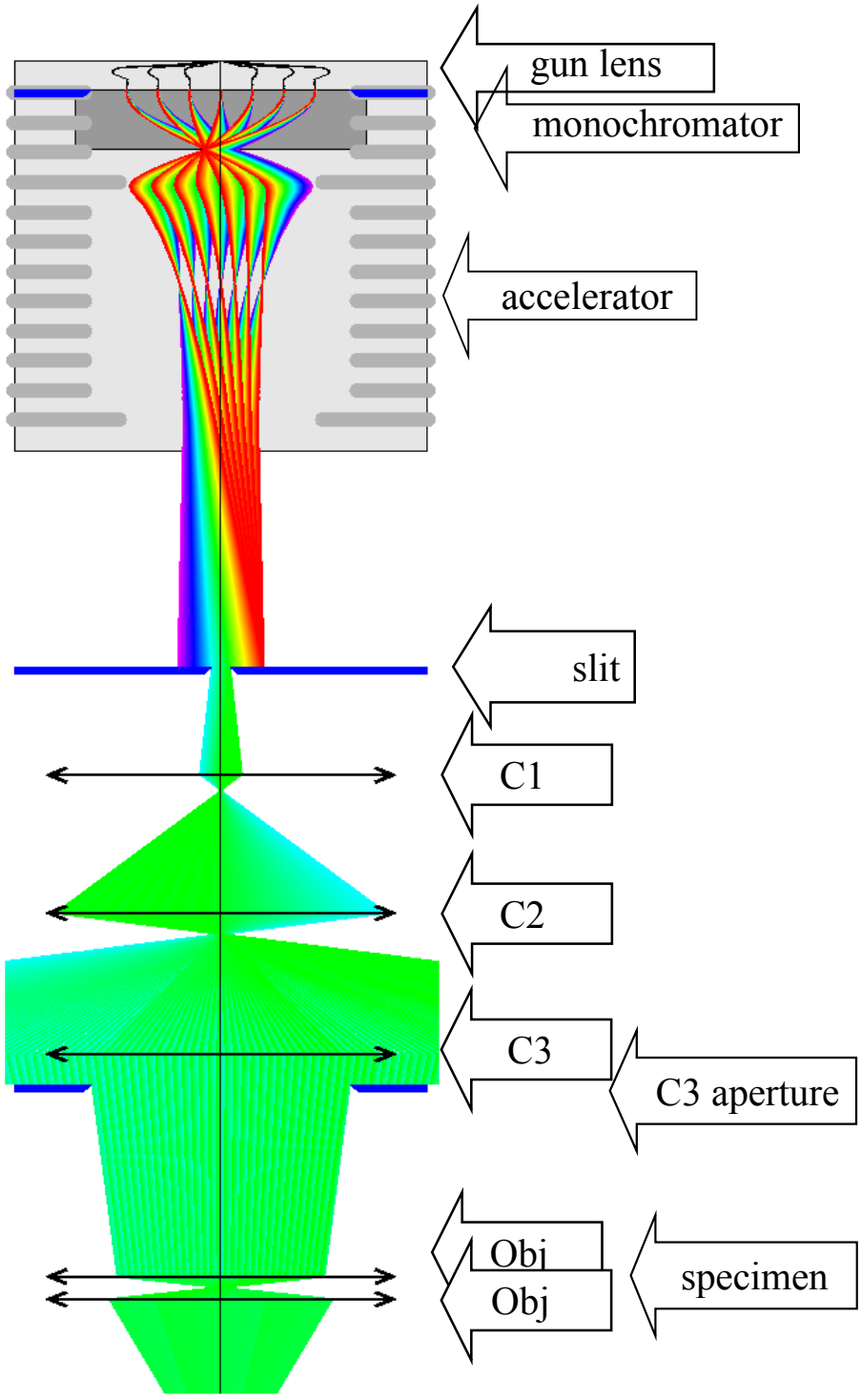

Figure 2.4: Schematic of a monochromated STEM [Adapted from [5]]

energy of interest can be extracted forming energy filtered maps. Also spatially resolved spectra can be extracted by selecting a column of the data set at the pixel of interest, see figure 2.5.

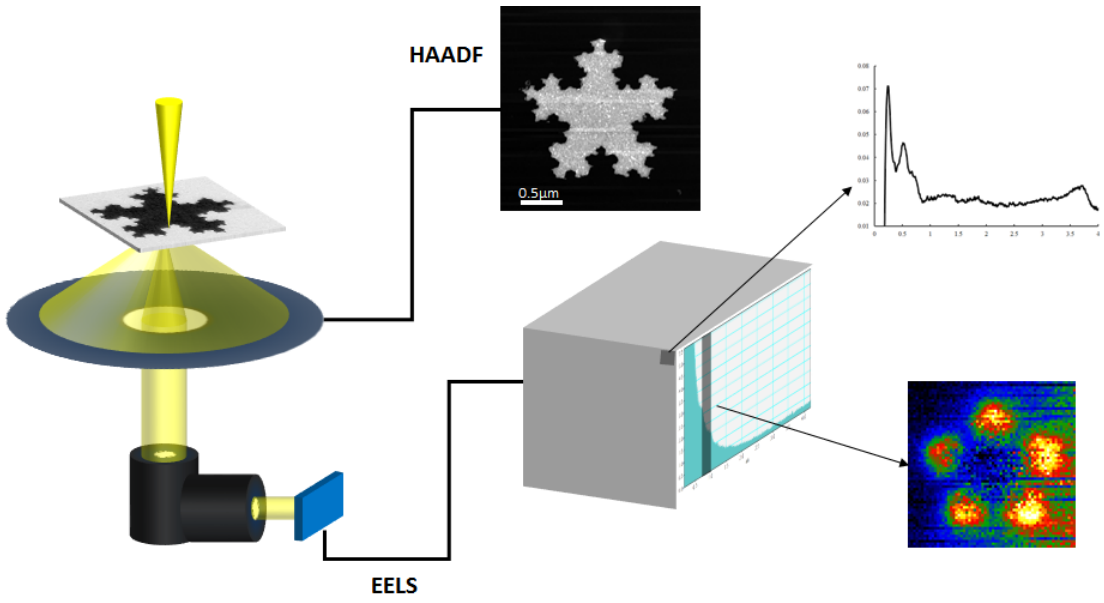

Figure 2.5: Diagram of STEM-EELS showing the HAADF and EELS simultaneous acquisition. The 3D spectrum image can be divided into energy filtered maps and spatially resolve spectra.

2.4 Electron Energy Loss Spectroscopy

Electron energy loss spectroscopy (EELS) is a technique that measures the energy that an electron, in an incident beam of electrons, has lost due to the interaction with a sample. This interaction causes various inelastic processes in the sample. These processes can be divided in two by the amount of energy lost in the interaction. In the region called core loss, the electrons from the beam interact with electrons in the core energy levels. The EELS signals acquired in these excitations, known as core

edges, are generally in the region above 50 eV and are related to the binding energy of the excited electrons in an atom. The edges are labeled according to the atomic energy shell from which the excited electron emerged. Signals from this region are used routinely to identify elements in a sample. What is more, the chemical state and bonding environment of the atoms in a compound is also identifiable by the analysis of fine modulations, known as energy loss near-edge structure (ELNES). In the valence or low-loss region, electrons have interacted with the weakly bound electrons in the outer energy levels, usually with energies below 100 eV. In this energy region, the energy loss reflects the dielectric response of the material, and information about intraband transitions, interband transitions, plasmons, band gaps, excitons, and the specimen thickness can be drawn. Also, it is in this region that excitation of SPs occur and can be studied. Therefore this work is entirely focused on this region.

Figure 2.6 shows the three types of signals that can be collected by the spectrometer in an EELS experiment: The core loss region, the valence loss or low loss region, and the zero loss region. The zero loss region, as its name indicates, constitutes all the electrons that have not interacted inelastically with the sample. In an ideal case, the zero loss signal will be a delta-function. However, in reality, the zero loss signal has a width and forms a peak called the zero loss peak (ZLP). The width of this ZLP is a good measure of the energy broadening (intrinsic and instrumental), for this reason, it is used to determine the spectral resolution of an EELS experiment. The long energy tails of the ZLP overlaps with the low-loss region. Considering that the low-loss signal can be significantly smaller than the tails of the ZLP, the SP spectral can be difficult to retrieve, and techniques such as ZLP subtraction and deconvolutions are used.

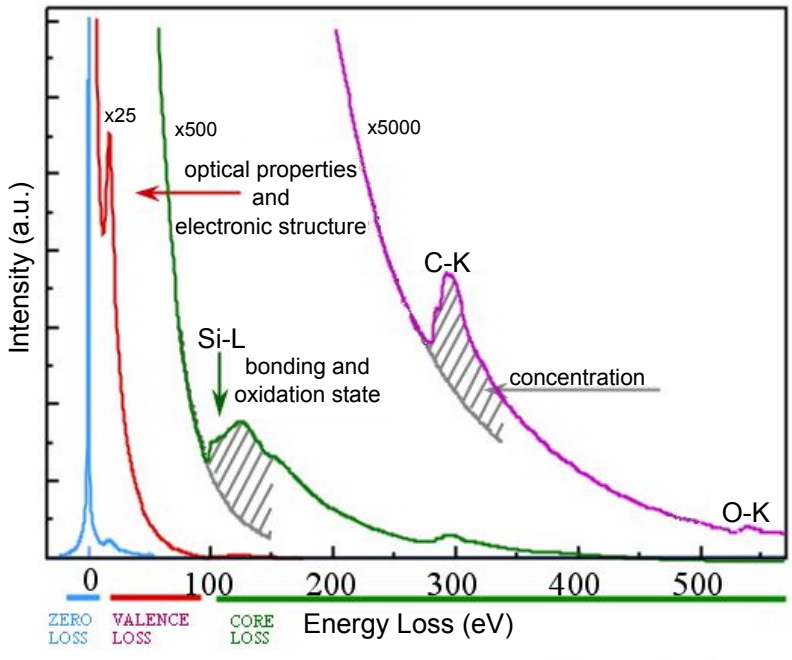

Figure 2.6: EELS spectrum showing the zero-loss, valence loss, and core loss regions (from [6]).

After the electron beam interacts with the sample, the low angle scattered electrons are collected in a post-column prism spectrometer. The range of angles collected by the spectrometer or collection angle is controlled by the EELS entrance aperture and the camera length. The projector lenses adjust the camera length. Figure 2.7 shows a diagram of the components of a prism spectrometer, which two primary functions are to disperse the beam into components of different energies and to detect or image the dispersed electrons. At the entrance of the spectrometer, a series of correction coils compensate for aberrations in the beam before the electrons reach the electron prism. In the electron prism, the electrons are dispersed according to their energies. Then, the dispersed beam is magnified and focused by a series of multipole lenses to form a spectrum in the dispersion plane located at the scintillator. If the

lenses of the spectrometer are misaligned the signal from one particular energy might spread over multiple CCD pixels, and the energy resolution might degrade considerably, for this reason, careful tuning of the spectrometer lenses is required. In the scintillator, the electrons forming the spectrum are converted into photons. Then the photons travel in an optical fiber to finally arrive at the CCD camera where the signal is read.

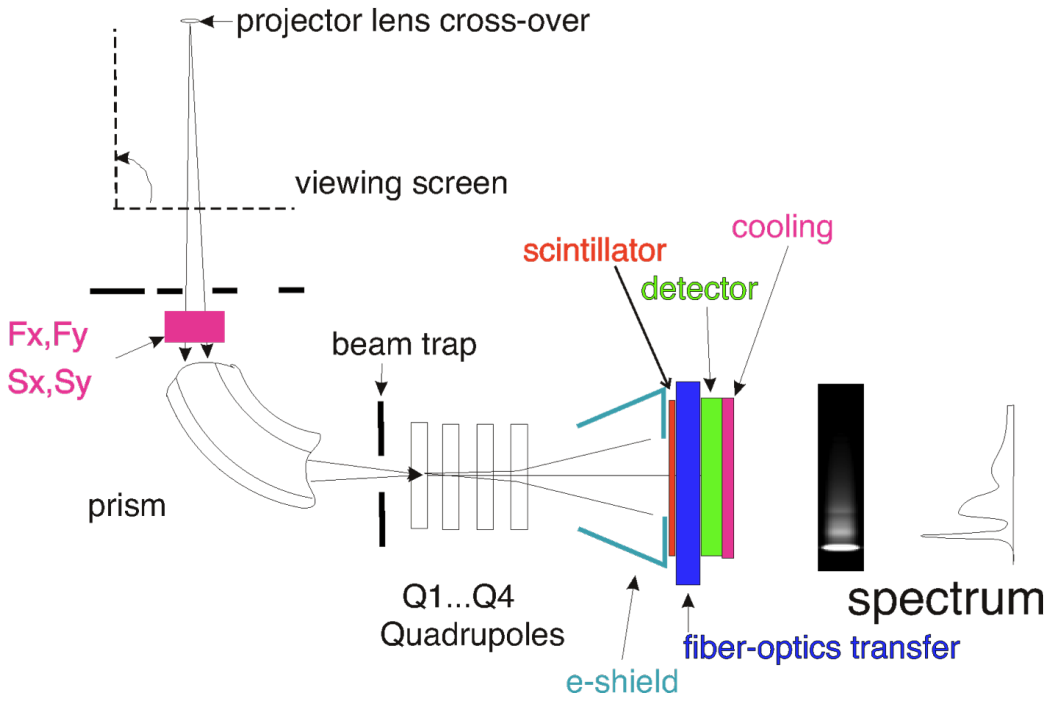

Figure 2.7: Diagram of a post-column prism spectrometer (from [7]).

2.5 EELS of Surface Plasmons

SPs in an electron microscope are excited by the electrons traveling at very high speeds. To describe an electron in the beam, we can assume that the electron is a point charge that follows a straight-line trajectory with constant velocity v. Thus

the charge density of the electron would be $\rho_e(\hat{r}, t) = -q\delta(\hat{r} - \hat{v}t)$. These electrons have an electromagnetic field associated that can be described as evanescent radiation because its intensity decays exponentially away from the electron trajectory. Also, the electrons can also be considered a source of super-continuum light because due to their δ function charge density, they can excite in all frequency ranges, and it has a momentum that can lie outside of the light cone [52]. This is an important fact because it means we can excite surface plasmons directly without the need of a momentum matching element. Because of the local nature of the electron beam, the electric field associated with the electron can polarize a nanostructure locally exciting a resonant mode. Due to this locality it is possible to excite non-dipolar modes and dark modes in finite structures.

When the swift electron interacts with a structure the energy loss experienced by the electron moving with constant velocity $\hat{v}$ is related to the force applied by the induced electric field ($\hat{E^{ind}}$) acting back on the traveling electron [54].

$$\Delta E = q \int \hat{v} \cdot \hat{E^{ind}}[r_e, t] \, \mathrm{d}t = \int_0^\infty \hbar\omega \Gamma_{EELS}(\omega) \, \mathrm{d}\omega \tag{2.1}$$

where r_e is the position of the electron travelling down the column along z, and Γ_{EELS} is the energy loss probability is given by:

$$\Gamma_{EELS}(\omega) = \frac{q}{\pi\hbar\omega} \int \Re(e^{-i\omega t} \hat{v} \cdot \hat{E^{ind}}[r_e, \omega]) \, \mathrm{d}t \tag{2.2}$$

From both equations, we can see that the problem is reduced to calculate the electric field induced by the traveling electron. Several approaches have been taken to obtain this electric field for many geometries, from a single isolated sphere, as we

discussed in the previous chapter, to complex structures, using analytical expressions as well as numerical methods. It is important to point out, from equation 2.1, that an energy loss probability occurs when the electron trajectory is parallel to the induced electric field lines. This does not mean that EELS will not be able to measure modes with a dipole oriented perpendicular to the beam trajectory. It means that, while the net dipole orientation might lie in a plane perpendicular to the beam direction, this is not necessarily true for the lines in the induced electric field. Thus, an energy loss can occur as long as there are induced field lines parallel to the electron beam trajectory. Which implies that all modes can be measured, not only the dipolar modes as is the case in the far field optical experiments. This is because the electric field induced by the incoming electron is local in nature, in contrast with plane wave excitation.

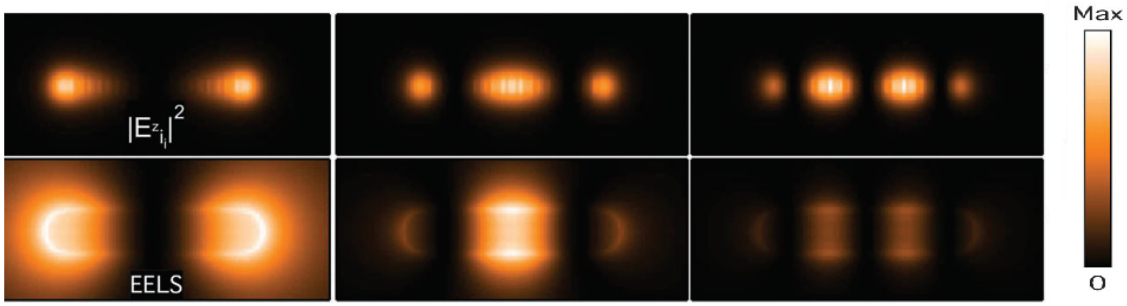

Figure 2.8: Top panel: Example of the square of the z component of the electric eigenfield taken 6 nm away from a 50 nm length and 10 nm diameter nanorod. Bottom panel: EELS maps for electron trajectories parallel to the z axis (accelerating voltage 200 keV). For each quantity, the intensity scale is the same. Adapted from [8]

Figure 2.8 as well as equation 2.2 show the link between the EELS probability and the induced field in the sample. This helps us understand the relationship between the spectral maps we obtain in this work and what is physically happening in the sample. However there is another description that is useful to explore, this is

the electromagnetic local density of states (EMLDOS). This quantity represents the density of optical modes for a given energy at a given point in space. EMLDOS indicates the positions in the sample where electromagnetic energy is concentrated, and there is a high probability of exciting a mode. Calculating the EMLDOS can be as complex as calculating the induced electric field. But for simplicity let's assume that the modes can be defined by an eigen-field $E_i(\hat{r})$ in the quasistatic approximation, and we project the EMLDOS along an arbitrary axis z, then we have [8]:

$$\rho_z(\omega) = \frac{1}{2\pi^2\omega} \sum_i \Im[f_i(\omega)]|E_i^z(\hat{r})|^2 \tag{2.3}$$

where $f_i(\omega) = \frac{\Lambda_i+1}{\Lambda_i-\Lambda(\omega)}$, with $\Lambda(\omega) = \frac{1+\epsilon(\omega)}{1-\epsilon(\omega)}$, and $\Lambda_i = \Lambda(\omega_i)$.

From the equation we can recognize two main components, $f_i(\omega)$ which has the spectral component and $|E_i(\hat{r})|^2$ has the spatial component associated with the local field strength. If we apply the same approximations to calculate the EELS probability assuming the electrons are moving in a straight direction along the z axis, we have [8, 55]:

$$\Gamma_{EELS}(\omega) = \frac{q^2}{\pi\hbar\omega^2} \sum_i \Im[f_i(\omega)]|E_i^z(\hat{r})|^2 \tag{2.4}$$

We can see that the $\Gamma_{EELS}(\omega) \propto \rho_z(\omega)$, and as an example, figure 2.8 shows EELS probability and the square of the z-component of the electric field for the first three modes of a nanorod. The EELS and electric field variations have the same nodes and antinodes positions; however, their total amplitudes are not comparable. For the case of solutions of fully retarded cases, the link between EELS probability and the z component of the EMLDOS is still valid, as was shown by Kociak for a silver disk

[9](figure 2.9), and there is a qualitative agreement between the two quantities.

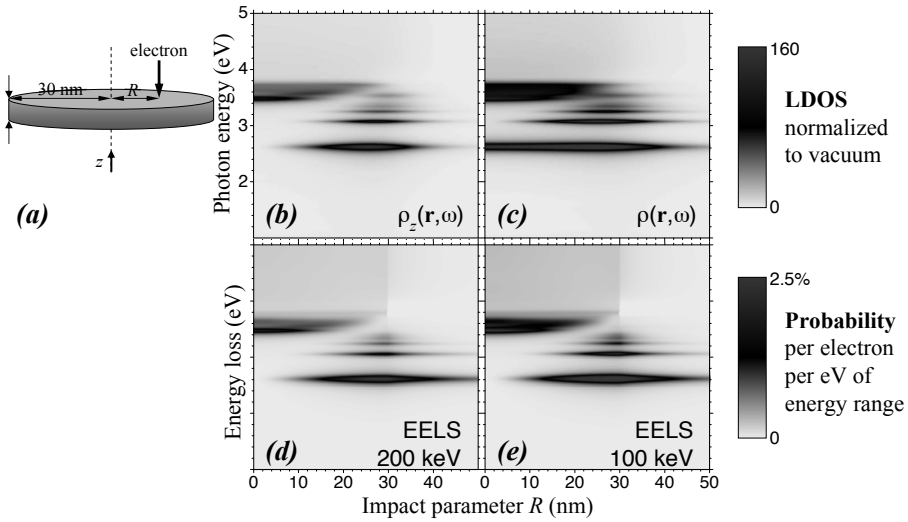

Figure 2.9: Relation between EELS and LDOS in planar geometries. (a)Diagram of an Ag disk of height 10 nm and radius 30 nm, where the electrons move along z, perpendicular to the disk. The EELS probability for 200-keV (c) and 100-keV (d) electrons mimics closely the LDOS (c) projected along the z axis in a plane 10 nm above the disk (b). Adapted from [9]

In EELS experiments all the energy absorbed or scattered by the sample is provided exclusively by the incoming electron. Therefore, intuitively, the energy loss spectra should correspond to the extinction of the field the electron carries. We can use the modal description under the quasistatic approximation, described above, to compare EELS measurements with optical spectroscopy. In this formalism, the extinction cross sections takes the form [55]:

$$\sigma_{ext}(\omega) = \sum_i A_{ext,i}\omega\Im[f_i(\omega)] \tag{2.5}$$

with $A_{ext,i}$ are frequency independent prefactors. Comparing equation 2.5 and 2.4, we can see that for a given mode i the spectral components of EELS and optical

extinction are proportional to $\Im[f_i(\omega)]$. This direct proportionality obtained from the approximation suggest that is possible to compare EELS and extinction spectra qualitatively.

2.6 Imaging of Surface plasmons by EELS in the literature

Although EELS and electron spectroscopies in general played a very important role in the study of plasmons, as we saw in the previous chapter, the interest in the field declined considerably during the 90's and early 2000's. In 2001 the work of Yamamoto *et. al.* demonstrated that it was posible to excite and image optical excitations with fast electrons at nanoscale using cathodoluminesce [20]. However, It is not until 2007 that the EELS scientific community regains interest in the field thanks to the work of Nelayah *et. at.* and Bosman *et. al.* [10, 56]. Nelayah was able to map surface plasmon modes in triangular silver nanoprims, as shown in figure 2.10, using EELS in a STEM, and the ability to image localized surface plasmons with an unprecedented resolution was demonstrated. In 2008 Garcia de Abajo *et. al.* found and mapped dark modes of elongated particles that cannot be excited by optical techniques, providing further insight into the potential of EELS as a technique to study surface plasmons [21].

Since then, several structures have been investigated including particles[15, 57, 58], cubes [59, 60, 61, 62], disks [63, 64], wires[12, 11, 16, 65, 66], including more complex structures [53, 67, 68, 69, 70, 71, 72, 73, 74]. Botton's group has been actively involved in the advancement of this area of research. Silver nanorod antennas were studied, and the presence of multiple Fabry-Perot-like resonances was confirmed, as shown in figure

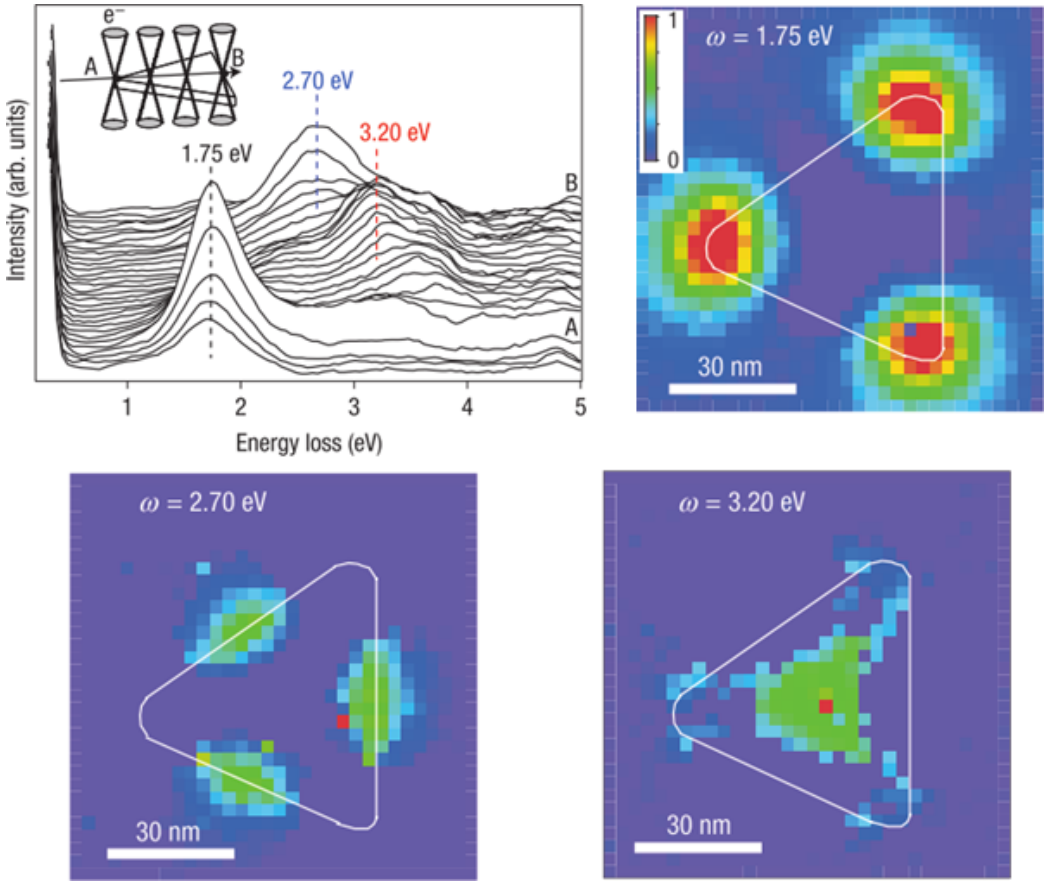

Figure 2.10: Top left panel: A series of STEM EEL spectra acquired along an axis (A to B) of the nanoprism illustrated in the inset. Dotted lines mark the energy of the three main resonances. Top right and bottom panel: Energy filtered maps of the resonant modes. The contour of the particle is shown as a white line. Adapted from [10]

2.11 [12]. The formation of plasmon resonances that remain unaffected, despite the presence of sharp kinks and corners in bent nanowires, was also demonstrated (Fig. 2.11)[11]. Finally, the Babinet's principle was also studied in a nano-slot fabricated by FIB in a silver film [75]. This work is a continuation of the efforts of Botton's group to study and understand the formation of plasmonic resonances in nanostructures.

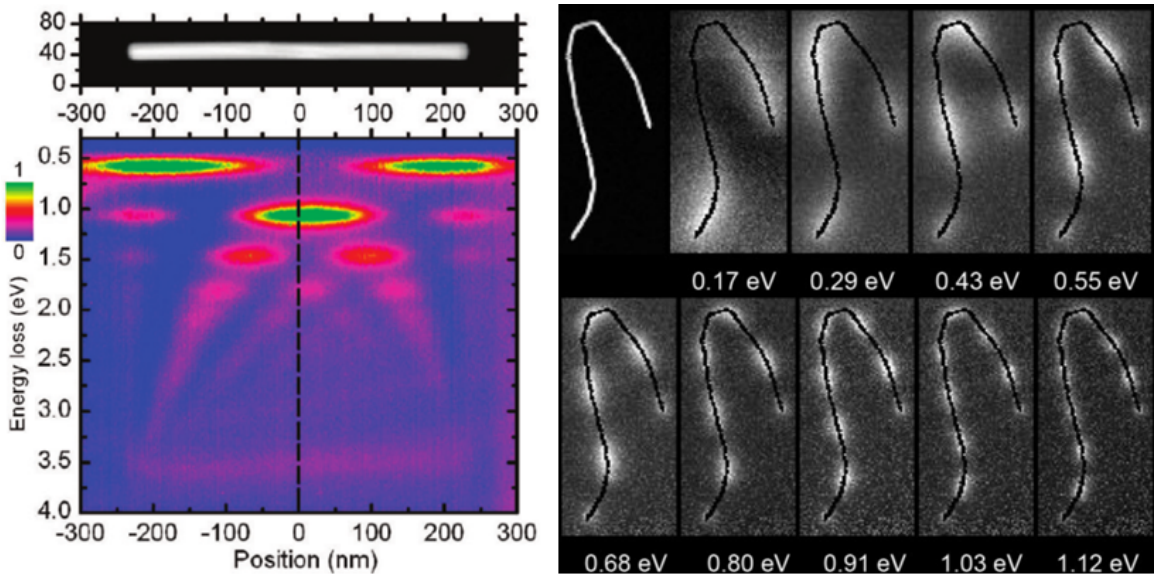

Figure 2.11: Left panel: HAADF image of a silver nanorod (top) and multiple resonance modes imaged in along the length of the nanorod (bottom). Right panel: energy filtered maps of bent nanowires that support surface plasmon resonances. Adapted from [11, 12]

2.6.1 Edge and film modes in planar nanostructures

The mapping of planar nanostructures by EELS showed that SPs resonances were located at the edges, corners and the center of the particles and a dependence of the energy and intensity of the modes on their size remained identified [13]. As shown in figure 2.12 the dependence in the edge length as well as in the aspect ratio of

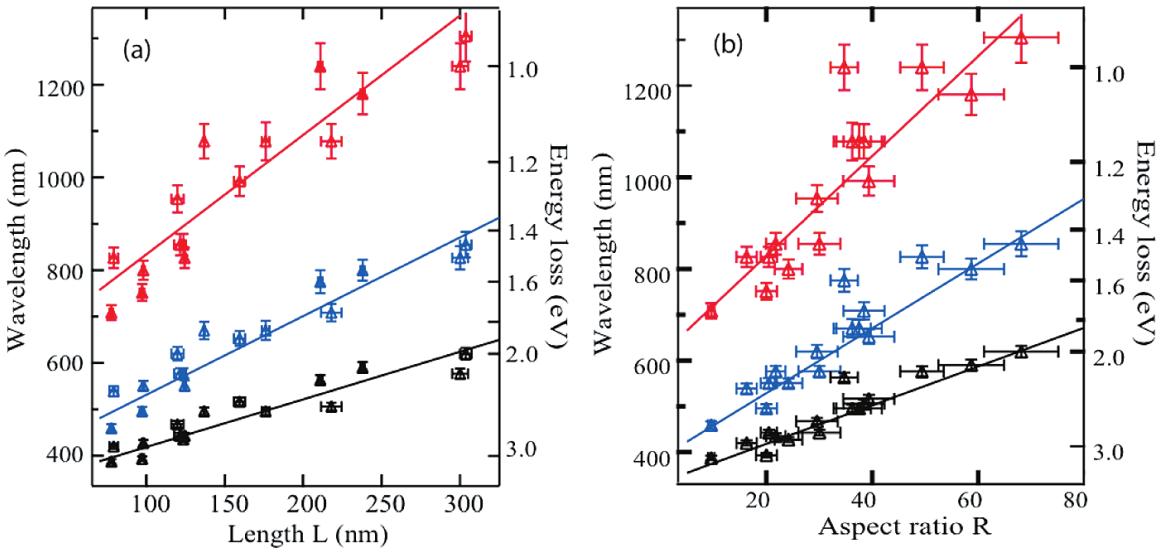

Figure 2.12: Energy dependence of the surface plasmons of silver nanoprisms as function of (a) the edge length (b) and the aspect ratio. Corner mode (red), edge mode (blue), and center mode (blue) of a prism as shown in figure 2.10 (from [13]).

the structure with a clear blueshift for smaller particles. Studying the resonances presented at the edges of platelets of different shapes and dimensions, it was shown that the dispersion of this plasmons follow the same trend despite their different geometry, indicating that these plasmons might be similar in nature [73]. It was demonstrated that modes sustained by the edge of a silver thin film with a finite size in one dimension can sustain plasmon resonances that can be well described in a one-dimensional standing wave framework [14]. Figure 2.13 shows energy filtered maps of these edge modes that were used to calculate the dispersion relation of the edge modes. All these reports demonstrate that quasi-1D modes can describe modes presented at the edges of continuous planar nanostructures.

Similarly, a spectroscopy study of the central or cavity modes on planar disks shows that there is a dependence of the energy of the modes and the radius of the

disks [63]. It was also shown that thin films sustain modes due to the plasmon coupling between the surfaces caused by the reduced thickness. As in the case of the edge modes, it would be natural to assume that these film modes will also extend to the case of finite particles. We have confirmed this assumption by mapping high order cavity or film modes of nano-squares [76]. Also, Schmidt *et. al.* used the geometrical and spectroscopic data of silver nanodisks to calculate the dispersion relation and showed that it follows the dispersion of an extended film, as shown in figure 2.13 [14]. These works provide an indication that SPs resonances in planar structures can be separated and identified as edge modes and cavity modes with 1D and 2D dimensionality respectively. What is more, it was shown that edge modes within a single rectangular particle can couple to each other and form bonding and antibonding modes [77].

2.6.2 Resonances in particle assemblies

A little more than one year after the first demonstration of surface plasmon mapping, the first study of coupled particles was published, showing the local behavior of two elongated particles in proximity [21]. The splitting of modes into bonding and antibonding in particles dimers was demonstrated spectroscopically [15], as shown in figure 2.14, confirming the hybridization theory explained in Chapter 1. The coupling of nanowire dimers was also studied, showing that the mode splitting is also possible for modes of high order [16], where the probability maxima of the bonding modes are localized at the gap, while in the antibonding modes are located toward the dimer ends. These modes couple in such a way that resembles a continuous nanowire as shown in figure 2.15.

As discussed in the previous chapter, the strength of the coupling depends on

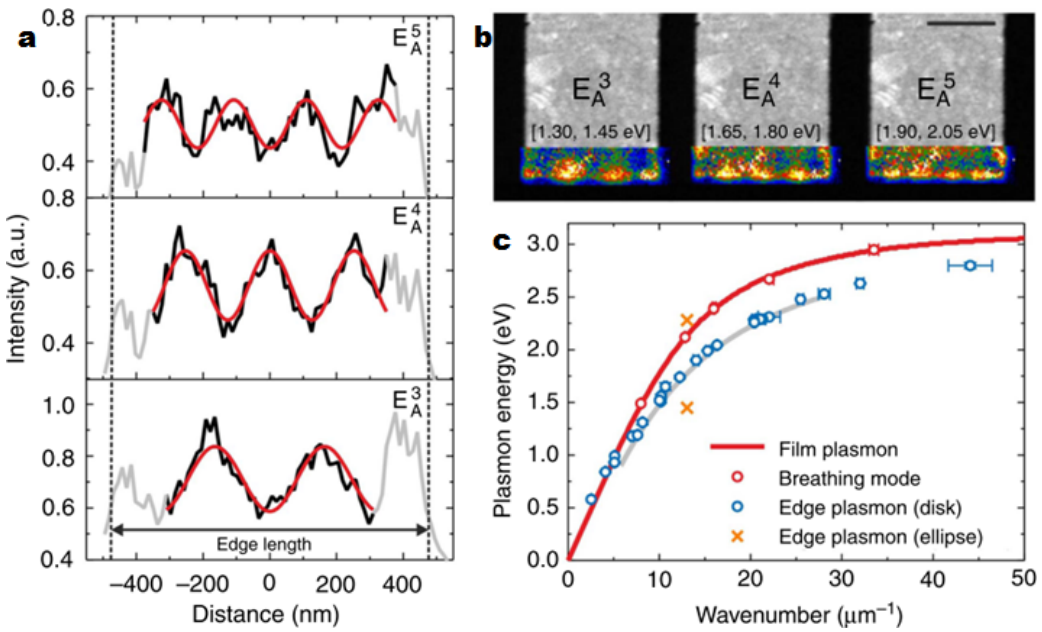

Figure 2.13: (b) HAADF image of a 30-nm-thick silver film with a 0.95 mm long side superimposed with EELS maps acquired in the indicated energy ranges. The maps show standing wave patterns corresponding to edge plasmons. (a) Intensity line profiles extracted from the edge modes in (b). The experimental data (black lines) are fit by a sinusoidal describing a standing wave (red lines). (c) Dispersion relation retrieved from resonant plasmon modes of nanodisks 30 nm high with diameters of 100 - 800 nm (red and blue symbols). The red curve is the calculated dispersion relation of the film mode of a 30-nm-thick silver film on a 15-nm-thick Si_3N_4 substrate. Adapted from [14].

the distance of between the nanostructures. The closer the structures the larger the splitting. When the separation is as small as 5 nm, the plasmon coupling is such that the particles act as building blocks to form resonances of more complex structures [78]. In arrangements with such small gaps the arrays behave like a single structure and the array nature of the structure is lost, which demonstrates the extreme case of coupling without entering in the quantum mechanical regime. For particles with separations below 2 nm quantum mechanical effects start to emerge. Bosman *et.*

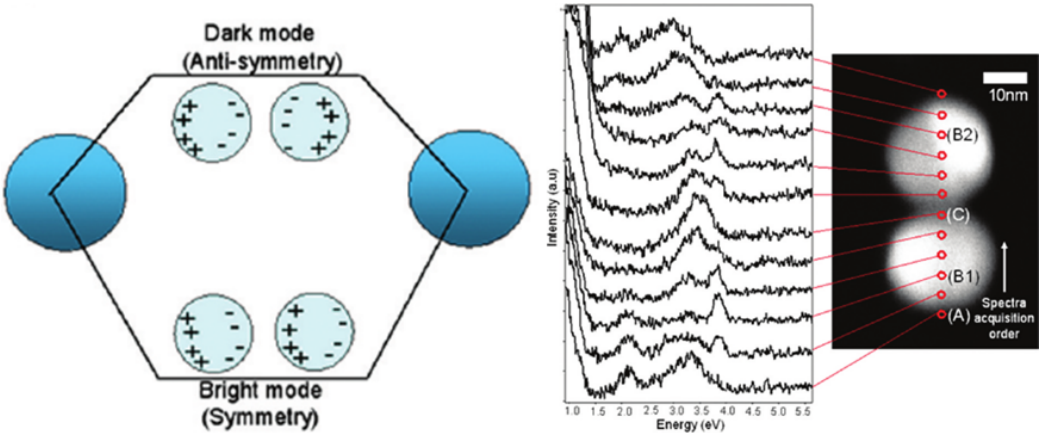

Figure 2.14: Left panel: Hybridization model of a symmetric dimer. Right panel: EELS data a silver nanoparticle dimer, showing plasmon energies as a function of electron probe position. Adapted from [15]

al. observed a tunneling charge transfer mode in molecular tunnel junctions made of two nano-cubes bridged by self-assembled monolayers [62]. For the case of small particle chains, the number of particles determines the number of possible modes. A chain containing N particles supports N modes, in addition to the transverse mode, resembling multipolar nanowire modes [79].

This succinct summary of some of the reports on the characterization of plasmon resonances by EELS is a small example of the capabilities of EELS as a tool used for the in-depth analysis of plasmonic structures, materials, and devices. Thanks to EELS mapping the localization of modes at the edges, and at the center of planar nanostructures was shown to be more than arbitrary descriptions of the modes and to be a description of the physical origin of the modes. In Chapter 4, we describe our contribution towards the understanding of the origins of edge modes and film or cavity modes. In chapter 6, we go beyond simple structures by discussing the surface plasmon resonances in planar fractal structures, and we describe how simple edge

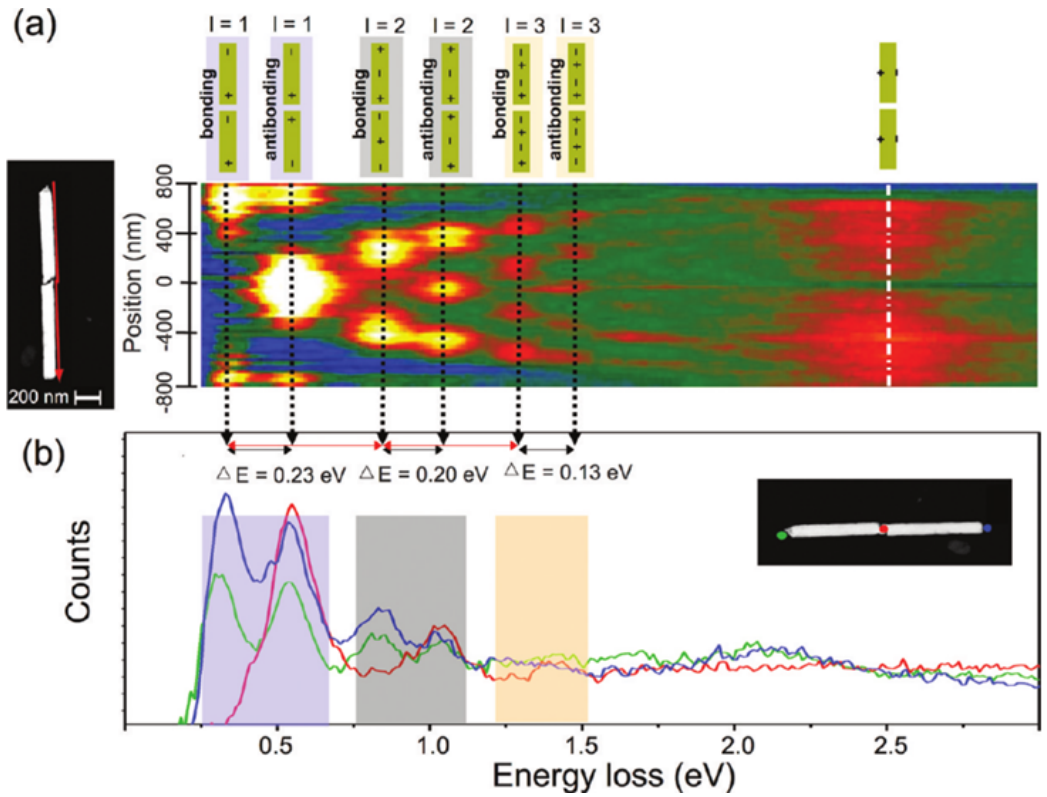

Figure 2.15: (a) Plasmonic field intensity map measured along a nanowire dimer (red arrow). The wires are separated by a small gap of 8 nm. The schematics on top represent the electric field distribution along the dimer. (b) Electron energy-loss spectra measured at the two ends of the dimer (blue and green lines) and a spectrum measured in the dimer gap (red line). The colored dots in the image inset specify the measurement positions for each spectra. From [16].

modes give rise to the complex spectral response of a fractal geometry. Also, much has been learned about plasmonic coupling through EELS, as we described above, from the confirmation of the splitting and field localization of bonding and antibonding modes to the analysis of quantum effects in small gaps. However, most of the work focused on hybridization of dipolar modes or formation of larger plasmonic structures by strong coupling, while studies of high order edge or cavity modes coupling have

remained marginal. In Chapter 5, we analyze the coupling of planar nanostructures focusing on higher order modes through the study of offset nanowire dimers, nanosquare dimers, and metallic strips. In this work, we show that the high spatial resolution, the ability to excite surface plasmons locally, and the broad range of energies that can be analyzed, due to improvements in energy resolution shown in Chapter 3, make EELS a unique tool for nanophotonics.

Chapter 3

Improving EELS Energy Resolution

One of the challenges in electron energy loss spectroscopy (EELS) is to improve the energy resolution without compromising spatial resolution [80]. In modern electron microscopes, as we described in previous chapters, the energy resolution is improved by the use of gun monochromators. The monochromator filter and select the electrons of the source based on their energy and reduce their spread to a range between 70 - 200 meV [81], and with more recent hardware improvements up to 30 meV [82], and very recently to values around 10 meV [83, 84]. This new efforts are being made with the aim to obtain high spectral resolution and current for a high spatial resolution given by the electron optics. A different way to approach the challenge of improving the energy resolution is by the use of post-acquisition computer algorithms [85, 86]. Fourier-log and Fourier ratio procedures are available in commercial software (Gatan's Digital Micrograph EELS package) and are used to remove plural scattering and sharpen spectral peaks. However, spectral sharpening is limited with these methods by noise

amplification [81, 85]. Other numerical approaches are based on the use of Bayesian methods of deconvolution. These methods treat the spectral noise separately from the data and have been successfully implemented to reconstruct EELS measurements. Overwijk *et al.* [87] and Kuzuo *et al.* [88] have used the maximum entropy method to improve the resolution in spectra of carbon K-edge. The same algorithm has also been used to improve the resolution of the cobalt L_{23}-edge [81], boron K-edge [89], and aluminum L_{23} ELNES of alpha-alumina[90].

Another Bayesian method is the iterative Richardson-Lucy (RL) algorithm [91, 92], which has been used extensively in a variety of fields, ranging from optical microscopy to astronomy [92, 93, 94, 95, 96]. The RL algorithm has also been previously implemented to increase the resolution of EELS spectra. To the best of our knowledge, Zuo was the first to apply the algorithm in this field and use it to reconstruct EELS measurements of nickel L-edges [97]. Gloter *et al.* also used the RL algorithm to reconstruct carbon K-edges, iron L_{23}-edges and oxygen K-edges; after deconvolution, they obtained energy resolutions of 0.2 - 0.3 eV [98]. The use of the RL algorithm of spectra acquired with a monochromated beam has also been explored by Botton *et al.* who tested the efficiency of the deconvolution in silicon L_{23}-edges [99]. Also, Kimoto *et al.* used RL deconvolution on monochromated EELS spectra to reconstruct aluminum L_{23} ELNES of alpha-alumina [90]. The RL algorithm has also been successfully implemented in the low loss regime. Egerton *et al.* used the algorithm to extract the spectrum of individual components in a bilayer film [86], Aguiar *et al.* applied the deconvolution to resolve peaks related to the valence electronic structure and optical response of silicon [100], and Lazar used it to measure the band gap in GaN and silicon [99]. The RL deconvolution has also been used to resolve surface

plasmon resonances (SPR) of pure gold and Au-Ag alloy nanoparticles [101], and to improve the resolution of SPR measurements in triangular silver nanoparticles [10].

As mentioned in Chapter 1, the study of surface plasmon resonances in metals has attracted great interest because of their ability to confine electromagnetic energy down to nano-scale dimensions [102]. The study of plasmon resonances at nano-scale requires a high spatial resolution and the ability to analyze a wide energy range of the electromagnetic spectrum with high energy resolution. STEM-EELS, because of the very high spatial resolution [52], is one of the best techniques for imaging surface plasmon resonances. It can reach the ultimate spatial resolution, thanks to recent advances in electron sources and developments in electron optics [103, 104], limited only by inelastic delocalization [105]. To obtain accurate images of low energy surface plasmon resonances, the energy resolution is crucial, because even with an energy resolution of 1 eV is difficult to observe energy losses below 5 eV, due to the high intensity of the zero loss peak (ZLP) tail compared with low loss signal intensity [81].

In this Chapter, published here [106], we implement and assess the limits of the Richardson-Lucy algorithm [91, 92], in an in-house MATLAB script as shown in figure 3.16, in an effort to further improve the energy resolution of low loss spectra acquired with a monochromated electron beam. In particular, we use the RL algorithm to improve further the resolution of EELS maps of surface plasmon resonances from a lithographically patterned silver nanowire acquired with a monochromated beam. We also apply the RL deconvolution to simulated spectra and measure the signal-to-noise ratio of the deconvolved spectra as a function of the number of iterations to test the effectiveness of the deconvolution and to obtain optimal deconvolution parameters. To find an optimal number of iterations, we implement and test two algorithms. The

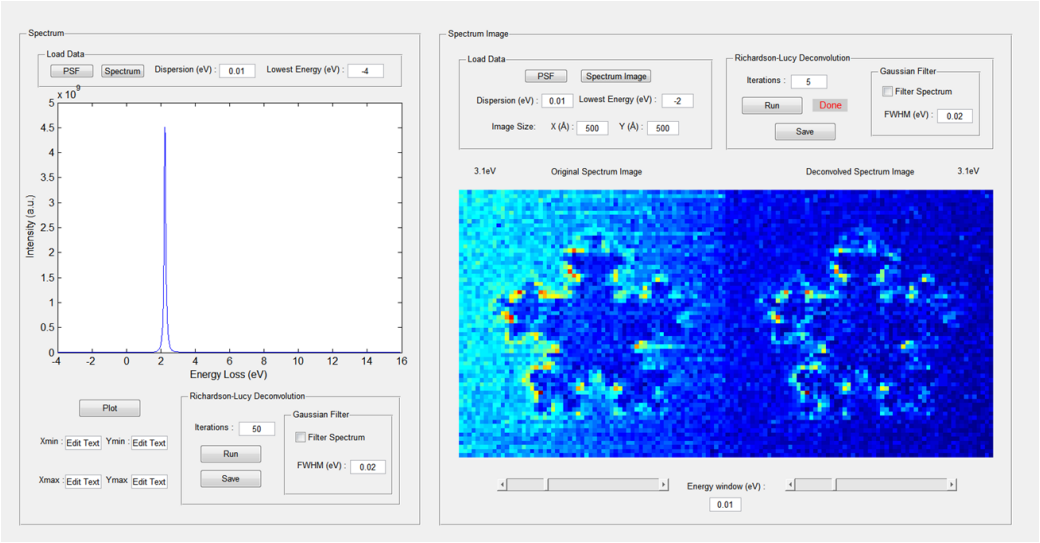

Figure 3.16: Screenshot of the RL GUI implemented in MATLAB.

first is a very simple noise control algorithm, and the second is the stopping criterion suggested by Van Kempen [94].

3.1 The Richardson-Lucy Algorithm

In the spectrometer, the signal from electrons with the same energy should reach only one channel of the CCD camera. However, in reality, this is not the case because of optical aberrations in the spectrometer, beam spreading in the detector, and the finite energy width of the electron source cause cross channeling, in which a point representing a specific energy is spread over multiple channels forming a blurred point. We represent this phenomenon with the following equation:

$$I(i) = \sum_j P(i/j)O(j), \tag{3.6}$$

where $P(i/j)$ represents the point of spread function (PSF) of the spectrometer, $O(j)$ represents the "expected" spectra and $I(i)$ represents the blurred spectra.

In STEM-EELS we detect electrons by converting the signal from the electrons into photons, and we read this photon signal on a CCD camera. All these processes of converting and reading the signal are statistical processes that originate from the particle nature of electrons and photons. Moreover, before reaching the detector, the signal has a statistical variation that follows a Poisson distribution. For this reason, when we record a spectrum, we cannot be sure we measure the expected intensity due to the presence of Poisson noise in the signal. The Poisson distribution in the detector can be described by:

$$P(D(i)/I(i)) = \frac{e^{-I(i)} I(i)^{D(i)}}{D(i)!}, \tag{3.7}$$

where $D(i)$ represents the measured signal and $P(D(i)/I(i))$ represents the probability of measuring $D(i)$ given a signal $I(i)$.

By maximizing the joint likelihood of the Poisson distribution, it is possible to estimate $I(i)$ given the measured spectra $D(I)$. Through deconvolution, we can calculate the "expected" spectra $O(i)$ given the PSF of the spectrometer, which has to be normalized. This procedure can be done by applying the Richardson-Lucy algorithm, which is a Bayesian iterative procedure described by:

$$O_{(j)}^{k+1} = O_{(j)}^{k} \sum_{i} \frac{P(i/j) D(i)}{\sum_{l} P(i/l) O_{(l)}^{k}}, \tag{3.8}$$

where k is iteration number, $P(i/j)$ is the PSF, and $O_{(l)}^{k}$ is the estimation of the expected spectra or image at k iterations.

When applying the RL algorithm to EELS measurements, the deconvolution has two main advantages. The first one is that it considers the Poisson noise in the original data. The second advantage is that the restored spectrum is robust against small errors in the PSF. However, the main inconvenience of the algorithm is that it might introduce artifacts and amplify noise at large number of iterations, especially for noisy spectra. The solution to prevent the creation of these artifacts is to limit the number of iterations as also suggested by Gloter *et. al.* [98]. In this work, we implement and test two simple algorithms in MATLAB to limit the iterations before artifacts are created on the reconstructed spectrum.

The first criterion is to monitor the noise at each iteration, in an area where we expect the spectra should have no peaks, and limit the number of iterations when the noise in this area reaches a threshold value. In our case, we set a threshold value which is equal to the original noise of the data set or a multiple of this original noise level. We define the noise, in a spectrum, as the variance of the signal every five measurements as follows:

$$Noise = \frac{1}{N}\sum_{j}^{N}\sigma_j, \tag{3.9}$$

where $\sigma_j = \frac{1}{5}\sum_{i}^{5}(x_{i+j} - \mu_j)^2$ and $\mu_j = \frac{1}{5}\sum_{i=j}^{j+4} x_i$.

As mentioned by Van Kempen *et al.* [94], the likelihood of an RL estimate increases logarithmically as a function of the number of iterations. Therefore, if we monitor the change of the reconstructed spectrum with respect to the reconstructed estimation, we can estimate how close to the maximum likelihood solution we are. As

a second stopping criterion, we impose a threshold value on the change of the reconstructed spectrum to limit the number of iterations. The change of the reconstructed spectrum (δO) is defined as [94]:

$$\delta O = \frac{\sum_i O(i)^{k+1} - O(i)^k}{\sum_i O(i)^k}. \tag{3.10}$$

3.2 Results and Discussion

When we define the EELS resolution of a system, we use the FWHM of the ZLP. This has been done historically in the literature and represents the system resolution [87, 98, 89, 82]. In addition, in an EEL spectrum, the PSF is well described by the ZLP. Similarly, the deconvolved ZLP is a good estimate of the PSF in the deconvolved spectra; hence, by analyzing the deconvolved ZLP, we can determine the effective resolution in the system. In the literature, to assess the resolution of the reconstructed spectrum when no experimental data obtained with higher energy resolution systems is available for comparison (as in the case here), the energy resolution of the system after reconstruction is based on the FWHM of the reconstructed ZLP [87, 89]. For example, Ishizuka et al. (2003) measured the energy resolution by the FWHM of the ZLP before and after drift correction, and they considered the energy resolution of the corrected spectrum as the FWHM of the reconstructed ZLP. Also, Overwijk and Reefman (2000) stated that the energy resolution is well described by the FWHM of the deconvoluted ZLP and indicated it as the "effective" energy resolution. We thus use here the same terminology to define the energy resolution of the deconvolved spectrum and effective resolution.

3.2.1 Deconvolution of simulated data

To evaluate the performance of the RL deconvolution, we apply the algorithm to a blurred spectrum generated from simulated EELS plasmon resonance peaks obtained at the tip of the nanowire geometry (figure 3.17). The zero loss peak of the simulated spectrum is modeled as a Gaussian function centered at 0 eV with a standard deviation of 10 meV. This accounts for the ideal case where the width of the ZLP is equal to dispersion per channel of the EELS spectrometer, and an intensity 100 times larger than the most intense plasmon peak. To generate the blurred spectrum, we need to include noise and effects of the PSF on the spectrum (figure 3.18a). First, we include the PSF by convolution of the ideal spectrum with the PSF, which in our artificial spectrum is a ZLP extracted by the reflected tail method from the experimental spectrum image. The noise considered in the artificial spectrum is a Poisson additive noise with a measured standard deviation of the fluctuations in the signal of $9.5\ x\ 10^{-5}$. The resolution of the artificially blurred spectrum is 70 meV as measured by the FWHM of the ZLP.

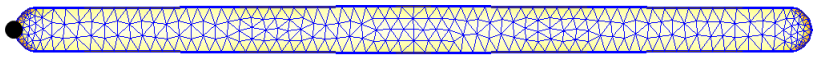

Figure 3.17: Nanowire showing the mesh used it for the simulation. The black dot indicates the position where the simulated spectrum is obtained.

Using the same PSF we used to generate the artificial spectrum, we perform the RL deconvolution on the spectrum after 50, 125 and 1000 iterations as shown in figure 3.18a. The ZLP after deconvolution is very close to the simulated data even after only 50 iterations and there is not much difference as the number of iteration increases. After 50 iterations we can see that the reconstructed spectrum matches very well with

the ideal spectrum for peaks below 1.6 eV. Between 1.6 eV and 2.9 eV, the peaks can be clearly identified. However, some artifacts that might be confused with shoulders and small peaks are also identifiable. For energies above 2.9 eV, the peaks cannot be clearly identified and fall within the noise level, and the deconvolution induces significant artifacts, including changes in peak positions and splitting of peaks. After 125 iterations, there is not much change for peaks below 1.6 eV compared with peaks after 50 iterations. However, for peaks above 1.6 eV the amplitude of the small artifacts increases. After 1000 iterations the amplitude of the artifacts at energies above 1.6 eV is comparable with the peaks, and we cannot clearly distinguish between signal and artifact. As we can see from figure 3.18a, the RL deconvolution is very sensitive to noise, and it is prone to noise amplification and the creation of artifacts that can be confused with real peaks at large number of iterations.

As suggested in the literature [94, 98], a method to reduce the sensitivity to noise is through suppression of parts of the signal where the noise contribution is larger than the signal contribution. These noisy parts of the signal can be suppressed by convolution of the spectrum with a Gaussian function. In our case, we filter our data using a 0.02 eV wide Gaussian function centered at 0 eV, which corresponds to a width of two energy channels. We convolve the artificial spectrum and the PSF with the Gaussian function to suppress the noisy part of the data.

Figure 3.18a shows the deconvolution of the filtered data after 90, 125 and 1000 iterations. It can be seen that the formation of artifacts is reduced. For energies below 1.6 eV, the reconstructed spectrum fits reasonably well with almost no artifacts even after 1000 iterations. For peaks between 1.6 eV and 2.9 eV, the artifacts are only visible for the reconstruction after 1000 iterations. For energies above 2.9, artifacts are

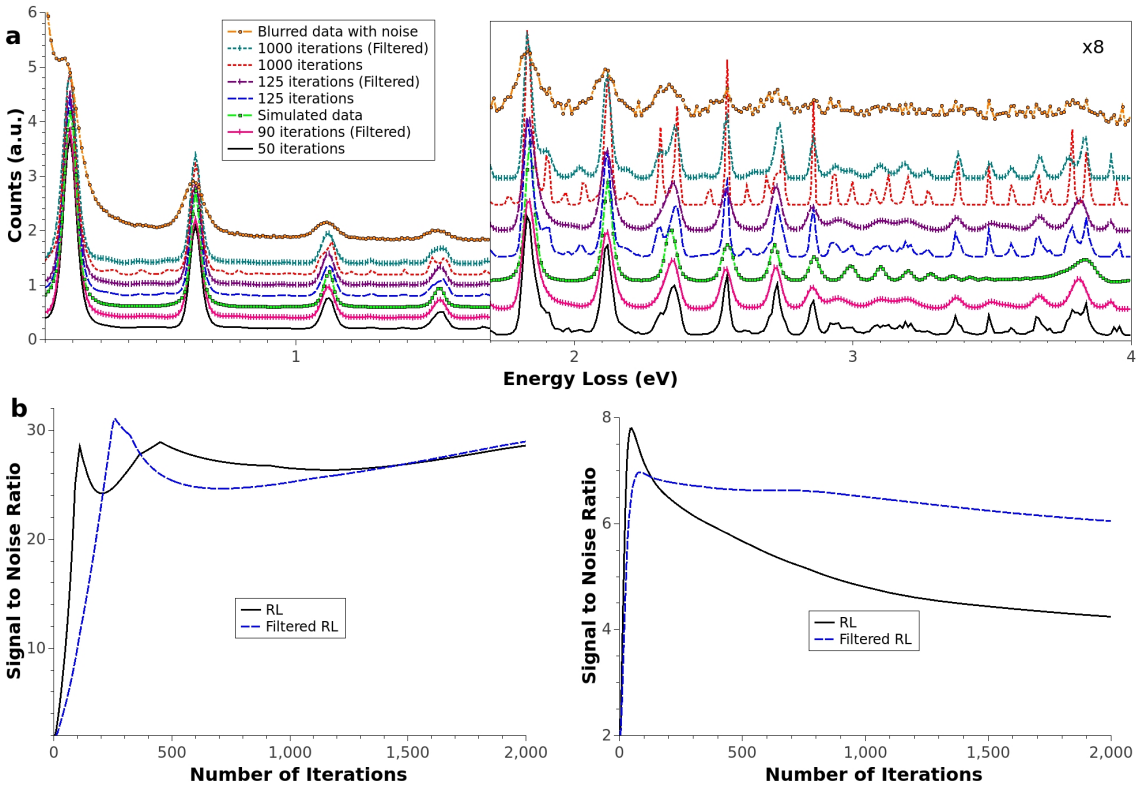

Figure 3.18: Spectra showing simulated data, blurred simulated data, and the deconvolved spectra after 50, 125 and 1000 iterations, as well as the filtered deconvolved spectra after 90, 125 and 1000 iterations (a). Signal-to-noise ratio of the zero loss peak for filtered and unfiltered deconvolution (b). Signal-to-noise ratio of filtered and unfiltered deconvolution of surface plasmon resonance peaks (c).

induced, but their amplitude is smaller compared with the unfiltered reconstruction. However, the original signal has also been suppressed, and the only peak that can be distinguished corresponds to the bulk plasmon of silver at 3.8 eV, which appears red-shifted in the reconstructed spectrum.

The performance of the RL algorithm can be described with respect to energy loss peaks in three different regimes: peaks that are almost noiseless and can be clearly distinguished from noise, peaks that are noisy but can be distinguished from noise,

and peaks with amplitudes comparable to the noise level. The RL algorithm can handle the deconvolution of the first two cases readily by increasing the resolution of the measurement and removing the tail of the ZLP, allowing identification of the surface plasmon peaks at very low energies. However, in the third regime, where noise amplification can be confused with real peaks, the user should exercise care when interpreting reconstructed spectra. In cases where the noise in a spectrum is small throughout the entire range of measured energies, the deconvolution is expected to have an optimal performance in an extended energy range. It is also worth pointing out that the major improvements with the deconvolution appear near the zero loss as observed in the first peak at 0.19 eV, which initially is only visible as a shoulder of the zero loss peak and then is very quickly resolved after only 50 iterations.

Visually, the filtered deconvolution gives better results with less amplification of noise. In order to quantify the efficiency of the filtered and unfiltered deconvolutions, we calculate the signal-to-noise ratio of the reconstructed spectrum as a function of the iteration number (k) [98]:

$$\frac{S}{N}(k) = \frac{1}{\sum_i |O_n(i) - O_n^{(k)}(i)|}, \tag{3.11}$$

where $O_n(i)$ is the simulated data at energy i normalized by the sum of the simulated spectrum ($O_n(i) = \frac{O(i)}{\sum_i O(i)}$), and similarly $O_n^k(i)$ is the reconstructed spectrum after k iterations at energy i normalized by the sum of the reconstructed spectrum in the energy range where the signal-to-noise ratio is calculated.

For the analysis of the signal-to-noise ratio of the deconvolved spectrum, we divide the spectrum into two parts: One is the ZLP (energies below 0.1 eV), and the other part is formed by the plasmon resonances peaks. We make this distinction because

the intensity of the ZLP is larger compared with the intensity of the plasmon peaks. Therefore, the ZLP dominates the values of the signal-to-noise ratio. As seen in figure 3.18b and 3.18c, the signal-to-noise ratio of the two parts of the spectrum is completely different. In the case of the ZLP (Figure 3.18b), we have two maxima for the unfiltered deconvolution and only one maximum for the filtered. In the reconstructions, we observe a small monotonic increase of the signal-to-noise ratio after 1,200 and 700 iterations for the unfiltered and filtered deconvolution, respectively. This increase in the signal-to-noise ratio of the ZLP indicates that no artifacts are created in this region as the number of iterations increases. In the plasmon peak region (Figure 3.18c) we have a maximum value of the signal-to-noise ratio which corresponds to the optimal value of the reconstruction. For the unfiltered deconvolution, the optimal value occurs at 50 iterations, after this maximum the signal-to-noise decreases rapidly, which indicates that more iterations will not improve the spectrum. For the filtered deconvolution the optimal value of iterations is 90, after this value, the signal-to-noise decreases relatively slowly as a function of the number of iteration. From these results, we can see that the filtered deconvolution does not perform better than the unfiltered deconvolution. However, if we do not know the optimal number of iterations, which is in general the case, the filtered deconvolution is a good alternative because the signal-to-noise ratio does not decrease significantly if we overestimate the number of iterations. The lower value of the maximum signal-to-noise ratio of the unfiltered deconvolution is expected because when we filter the spectrum, we are suppressing part of the signal that might lie within the noise level, and this lost signal cannot be recovered by the deconvolution.

We have implemented two criteria to limit the number of iterations and to obtain

a restored spectrum without artifacts. In the first criterion, we monitor the noise level in a range of energies where we know there are no peaks and stop the deconvolution when the noise level is equal to the noise level of the blurred spectrum. We implemented this stopping criterion for the reconstruction of the artificially blurred spectrum and monitor noise in three energy ranges. The first energy range is between -0.4 and -0.2 eV since we measure energy loss of plasmon resonances we should not have peaks in this range of energies and the only variations in signal value comes from noise. In this range, the noise stopping criterion failed because the RL deconvolution does not amplify the noise because no peaks are expected in this range, and only pure Poisson noise is present, that the algorithm is designed to handle. This means no artifacts are created as the number of iterations increases, therefore the deconvolution will continue indefinitely. In the second energy range (between 1.2 and 1.4 eV), the deconvolution stops after 1913 iterations. In this case, the deconvolution introduces artifacts but only after a large number of iterations, for this reason, the control algorithm "concludes" that the RL deconvolution is converging to a better estimate, and only after small artifacts are introduced the algorithm stops. In the third energy range (between 3.0 and 3.2 eV), we know beforehand that there are plasmon peaks present. However, the noise amplitude is comparable to the signal amplitude; therefore, in this range, it is likely that we will introduce artifacts during the RL deconvolution. The control algorithm limits the number of iterations to 60 in this range of energies, which is consistent with the maximum value of the signal-to-noise ratio (50 iterations) shown in figure 3.18c. The noise monitoring criterion for limiting the number of iterations performs much better in this range of energies because in this range more artifacts were introduced and the algorithm monitors the formation

of these artifacts and stops the deconvolution when the amplitude of these artifacts is larger than the noise of the original spectrum.

For the filtered deconvolution in the first range (-0.2 to -0.4 eV) we obtain the same result as in the unfiltered reconstruction, the algorithm fails and the deconvolution continues indefinitely. In the second range (1.2 to 1.4 eV) the algorithm limits the number of iterations to 6932 iterations. In this energy range, a large number of iterations is expected, because most of the noise is filtered in the convolution with the Gaussian function, and is only detected by the control algorithm after a large number of iterations. In the third range, the number of iterations is limited to 44. The advantages of this method of limiting the number of iteration are that it is not computationally expensive, it is simple to implement, it provides a measure of the quality of the reconstruction, and it could limit the number of iterations close to the optimal reconstructed spectrum. The main disadvantage is that we need to choose and appropriate range to monitor the noise amplification to obtain an optimal reconstructed spectrum.

As a second criterion, we monitor the change of the reconstructed spectrum as a function of the number of iterations in the entire spectrum. We impose a threshold value on the change of the spectrum, Van Kempen suggested a value of 0.001, at this value the number of iterations is 86 for our simulated spectrum. When the threshold value is 0.0025 the number of iterations is limited to 52, which is close to the maximum signal-to-noise ratio (figure 3.18c). When we monitor the change of the deconvolved ZL peak, we find that the number of iterations at which the RL algorithm stops, for a fixed threshold value, is the same as when we monitor the whole spectrum. However, when we monitor the change of the deconvolved SPR peaks, the algorithm is stopped

after fewer iterations. For example, with threshold values of 0.001 and 0.0025, the number of iterations is 74 and 42 respectively; and for a threshold value of 0.002, the algorithm stops after 48 iterations, close to the optimum number of iterations. For the filtered deconvolution, when the threshold value is 0.001, the deconvolution stops at 117 iterations, but with a value of 0.0015, the number of iterations is 91, which is close to the maximum signal-to-noise ratio. Monitoring the change of the ZL peak and imposing threshold values of 0.001 and 0.0015, the number of iterations is limited to 118 and 92 respectively. When we monitor the change of the SPR peaks, we obtain 69 iterations for a threshold value of 0.0015 and 89 iterations, which is close to the optimum, for a threshold value of 0.001. The advantage of this method is its simplicity and ease of implementation, and it saves computation time because it stops the deconvolution when the change in the spectrum is small. However, the main disadvantage is that this criterion does not provide a direct measurement of noise amplification in the reconstruction.

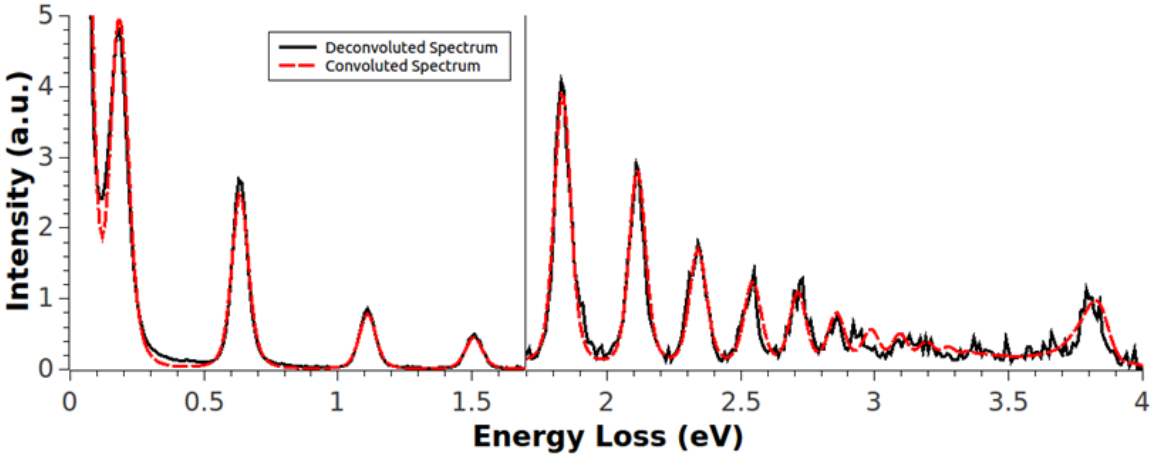

Figure 3.19: Deconvoluted spectrum (black solid line) and convoluted spectrum, which is the convolution of the simulated spectrum (expected spectrum) and the ZLP extracted from the deconvoluted spectrum (red dashed line).

To complement the discussion on energy resolution in a deconvolved spectrum we performed a test to demonstrate that the deconvoluted ZLP is a good estimate of the PSF in the deconvolved spectra, from which we can extract the effective resolution. We applied the RL algorithm and deconvolved the simulated blurred spectrum stopping the RL algorithm after five iterations (called deconvolved spectrum). Then, we extracted the deconvoluted ZLP by the "2 Gaussian" method in Digital Micrograph. The convolution of the simulated spectrum (expected spectrum) and the extracted deconvolved ZLP (called convolved spectrum) reproduces the deconvolved spectrum, as shown in Figure 3.19. The deconvolved and convolved spectra present some differences that can be attributed mainly to the noise in the deconvolved spectrum (which is not considered in the convolved spectrum) and to errors in the extraction of the ZLP from the deconvolved spectrum. Figure 3.19 shows that the width of the plasmon peaks in the deconvolved spectrum is well reproduced by the convolved spectrum. Therefore, we can state, therefore, with confidence that the ZLP of the deconvolved spectrum is the PSF; therefore the FWHM of the deconvolved ZLP is a good representation of the effective energy resolution of the deconvolved spectrum.

3.2.2 Deconvolution of experimental data

We acquired experimental low loss EELS data of a lithographically patterned silver nanorod. As previously described, we obtain the EELS data by scanning the sample with an electron beam and acquiring a spectrum at each pixel position in the scan obtaining a 3D dataset. Figure 3.20 shows the sum of the raw data spectra acquired over the scanned region (illustrated in figure 3.21), where up to four peaks are resolved. The peaks correspond to multipolar surface plasmon-polariton resonances. Also, we can identify the surface plasmon at 3.5 eV and the bulk plasmon at 3.8 eV. The

number of counts in the experimental ZLP is 1.3 x 10^9 electrons, considering the sum of all the spectra in the spectrum image. On average, the number of counts of the experimental ZLP in each pixel position is 2.5 x 10^5 and 4.2 x 10^4 electrons outside and inside the silver nanorod, respectively. In addition, from the sum of all spectra in the spectrum image, the number of counts at the energy of the most intense plasmon peak, before deconvolutions, is 8.8 x 10^6 electrons, which is 144 times smaller than the height of the integrated ZLP over the spectrum image.

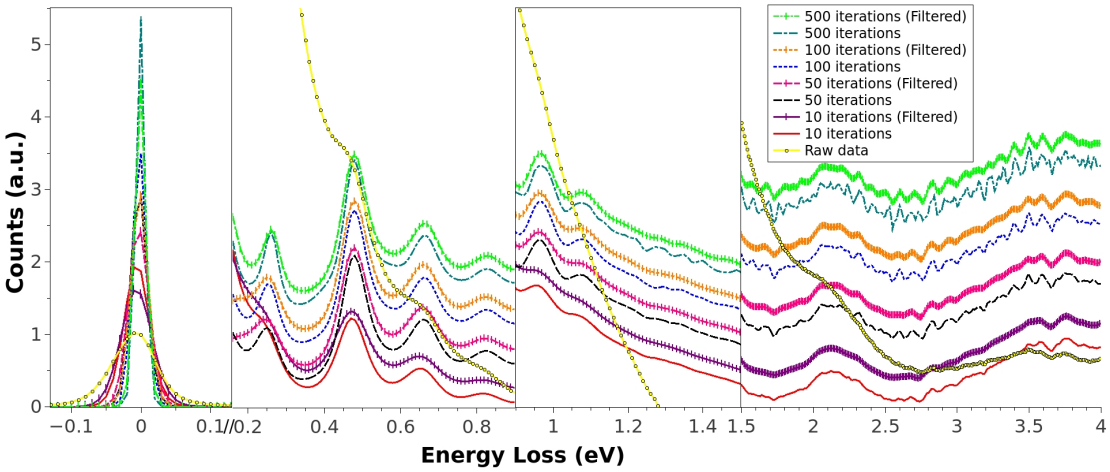

Figure 3.20: Spectra showing experimental raw data, and the filtered and unfiltered deconvolved spectra after 10, 50, 100 and 500 iterations.

We apply the RL deconvolution to each spectrum in the spectrum image. The PSF of the instrument was obtained by extracting the ZLP from the EELS data by the reflected tail method. Figure 3.20 shows spectra which are the sum of reconstructed spectra after 10, 50, 100 and 500 iterations. The reconstructed experimental spectrum shows noise amplification after a large number of iterations, in this case after 100 and 500 iterations, as was also observed in the simulated spectrum reconstruction. This amplification is only evident at energies above 1 eV where the noise amplitude is close

to the signal amplitude. If we compare the raw data with the reconstructed spectra, we can see that the plasmon peaks are buried on the tail of the zero loss peak and are barely distinguishable in the raw data. However, after deconvolution, we can clearly distinguish the surface plasmon resonance peaks from the ZLP tail at a low-energy loss. The first resonant peak, which corresponds to the dipolar surface plasmon mode, is a shoulder of the ZLP after 10 iterations, but it is clearly distinguishable after 50 iterations. As demonstrated in the deconvolution of simulated data, we can see that the most dramatic improvement in the experimental data is in the region below 1eV.

At energies below 1 eV where the noise level does not dominate the signal, we can see that as the number of iterations increases the peaks are sharper and more defined. This allows the detection of peaks at very low energies where noise is not a limiting factor. For peaks above 1 eV, the noise amplitude is close the signal amplitude and only some peaks can be resolved. The peak at 1.08 eV can be seen as a shoulder after ten iterations and can be clearly visible after 50 iterations. The next peaks at 1.2 and 1.32 are only visible after 50 iterations as small shoulders. As the number of iterations is increased, the resolution of the spectra improves from 70 meV to 40 meV after ten iterations (measured by the FWHM of the zero loss peak). After 50 and 100 iterations the FWHM of the zero loss peaks is 30 meV, and after 500 iterations the FWHM is 10 meV, but we have also amplified the noise by increasing the number of iterations. To effectively improve the resolution of our EELS measurements, we need to limit the number of iterations to an optimal value where both the FWHM of the zero loss peak and the noise amplification is minimized. The final limit at which we can successfully deconvolve a spectrum will depend on the acquisition conditions. We could increase the exposure time to increase the signal-to-noise ratio. However,

the initial energy resolution of the spectrum might be degraded depending on the stability of the electron gun and monochromator. As always, there is a trade-off between signal-to-noise ratio and energy resolution. By increasing the exposure time to achieve higher signal-to-noise ratio the stability of the entire acquisition system will eventually limit the initial energy resolution.

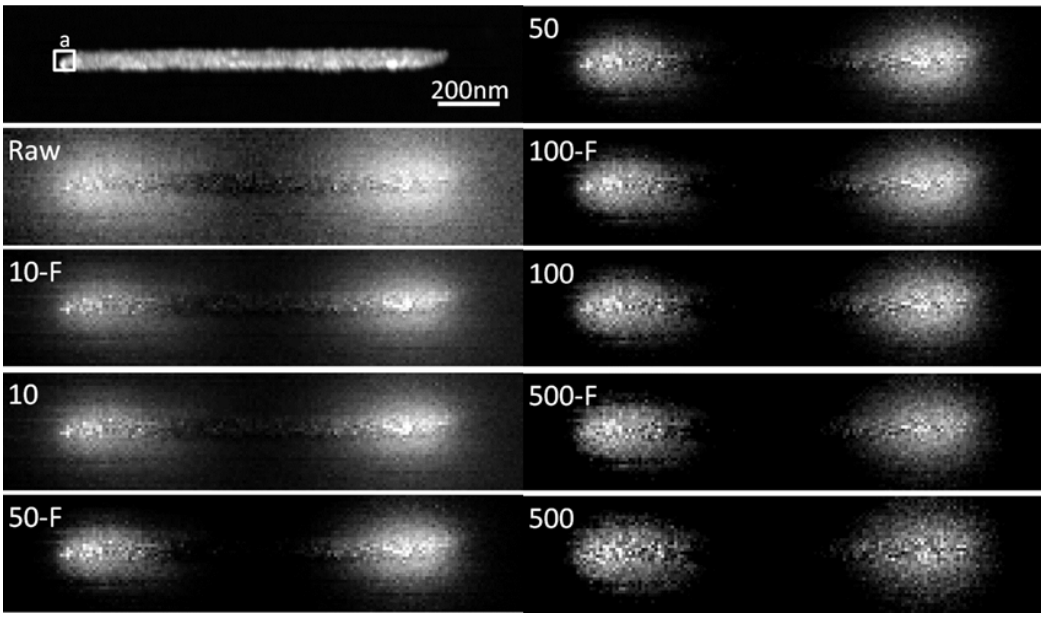

Figure 3.21: The top left panel shows an annular dark field image of a lithographically patterned silver nanowire. The subsequent panels represent the normalized raw, filtered (F) and unfiltered deconvolved energy filtered maps after 10, 50, 100 and 500 iterations of the first multipolar plasmon resonance of the nanowire at 0.265 ± 0.005 eV energy loss.

We have also applied the RL deconvolution on filtered data, where convolution of the spectrum with a Gaussian function suppresses noisy parts of the signal [94]. In our case, we filter the spectrum at each pixel position, and we filter the PSF using a Gaussian function centered at 0 eV and with a 0.02 eV width. Figure 3.20 shows the reconstructed data using the Gaussian filter. As in the case of the simulated

data, the filtered reconstruction is less noisy compared with the non-filtered data as clearly seen between 1.5 and 4 eV. We also notice that the deconvolution is less efficient for the filtered data. This can be seen in the deconvolved zero loss peak, where the amplitude of the peak after 100 iterations has the same amplitude as the filtered deconvolved peak after 500 iterations. This loss of efficiency is expected since we are broadening the original spectra by convolution with a Gaussian function and we are introducing an extra PSF that needs to be deconvolved. From inspection of the deconvolved spectra we could infer that the optimal number of iterations of the unfiltered deconvolution is between 10 and 50, and this ideal deconvolution will have an energy resolution of 30 meV. The optimal number of iterations for the filtered deconvolution lies between 50 and 100, and will also have an energy resolution of 30 meV. However, if the features of interest in the spectrum are localized at energies below 1 eV, we could obtain an energy resolution up to 10 meV after 500 iterations, which is the minimum value of dispersion per channel in our spectrometer.

Table 3.1: Normalized raw, filtered and unfiltered deconvoluted energy filtered maps after 10, 50 and 100 iterations of multipolar plasmon resonances on a lithographically patterned nanowire. The maps are formed with an energy window of ± 0.03 eV

Energy (eV)	**Raw data**	**10 it.**	**10 fil. it.**	**50 it.**	**50 fil. it.**	**100 it.**	**100 fil. it.**
0.25	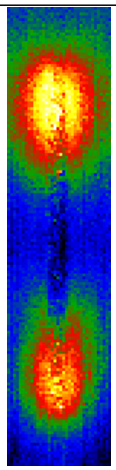	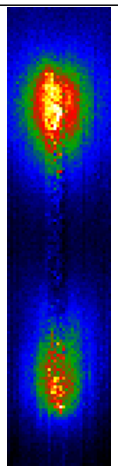	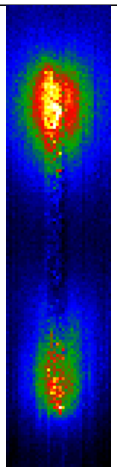	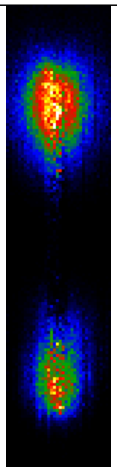	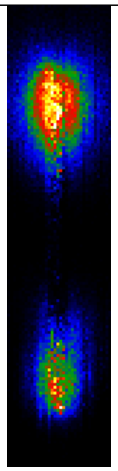	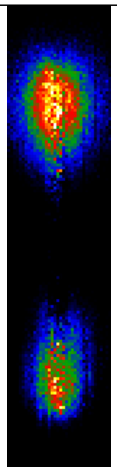	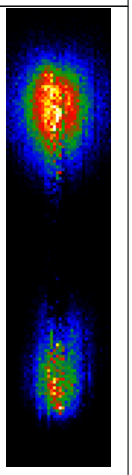
0.48	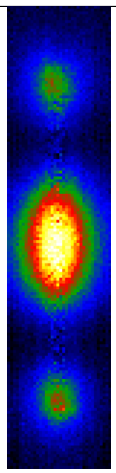	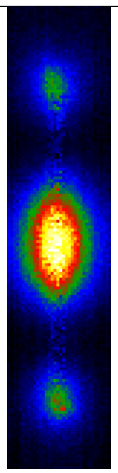	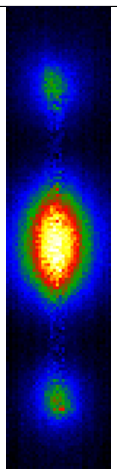	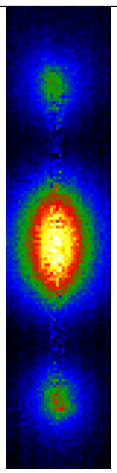	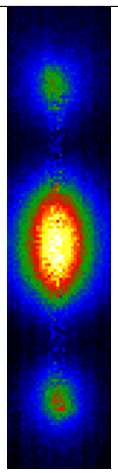	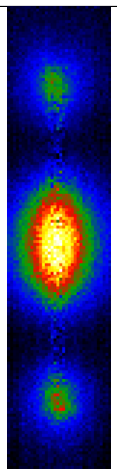	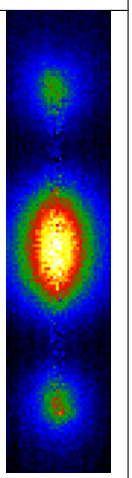

Continued on next page

Table 3.1 – *Continued from previous page*

Energy (eV)	**Raw data**	**10 it.**	**10 fil. it.**	**50 it.**	**50 fil. it.**	**100 it.**	**100 fil. it.**
0.67	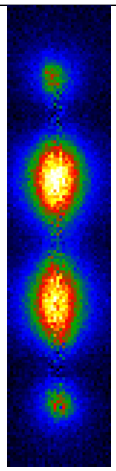	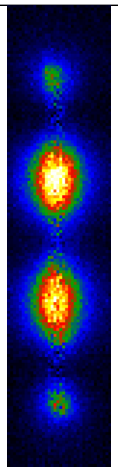	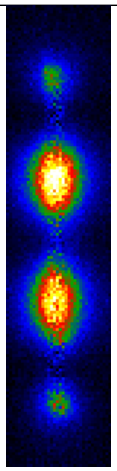	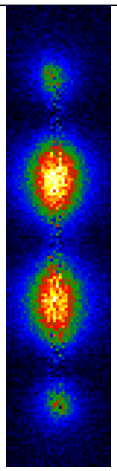	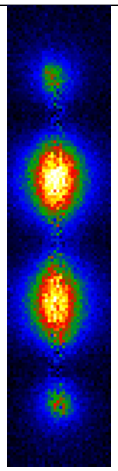	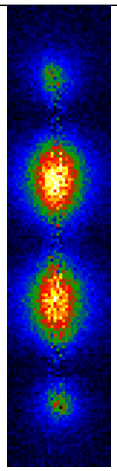	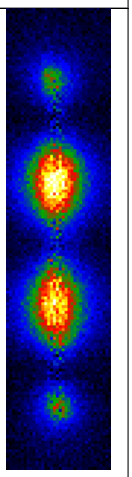
0.83	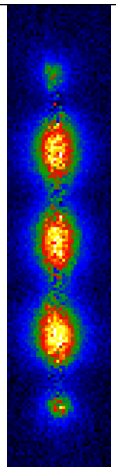	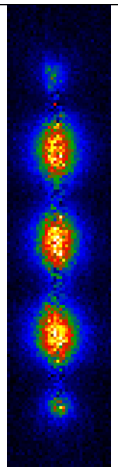	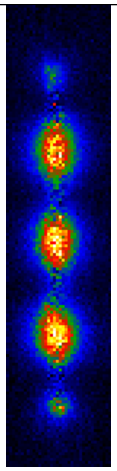	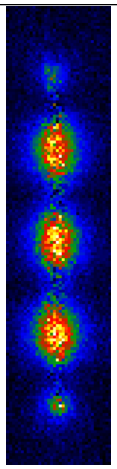	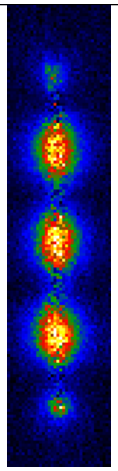	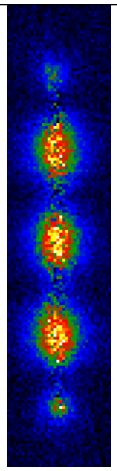	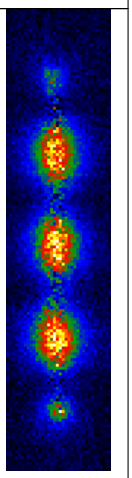

Continued on next page

Table 3.1 – *Continued from previous page*

Energy (eV)	**Raw data**	**10 it.**	**10 fil. it.**	**50 it.**	**50 fil. it.**	**100 it.**	**100 fil. it.**
0.97	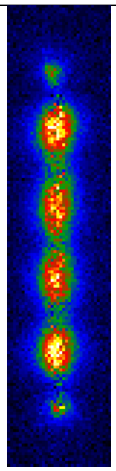	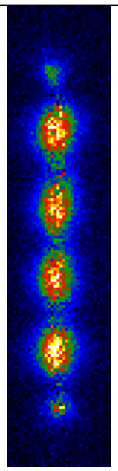	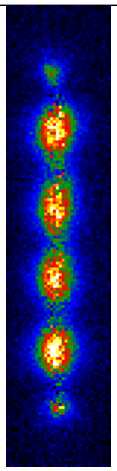	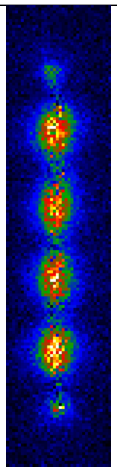	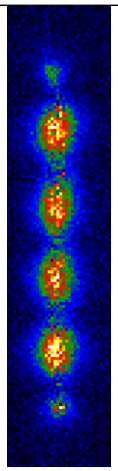	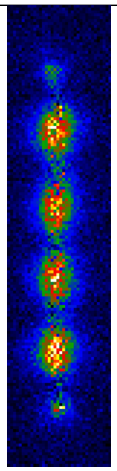	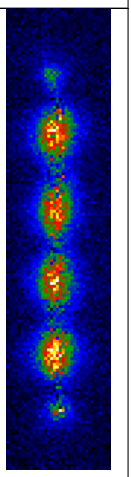
1.08	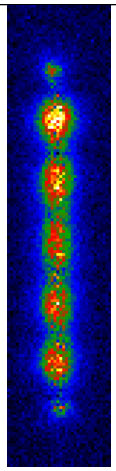	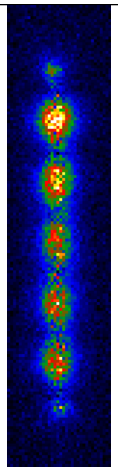	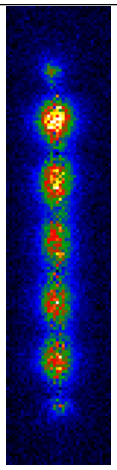	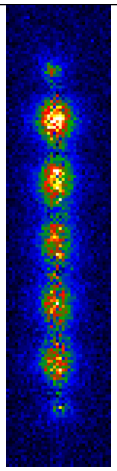	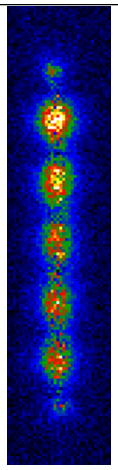	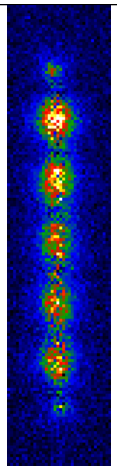	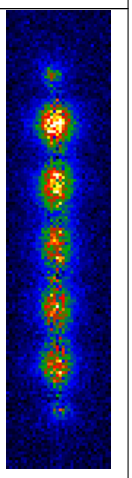

Continued on next page

Table 3.1 – *Continued from previous page*

Energy (eV)	**Raw data**	**10 it.**	**10 fil. it.**	**50 it.**	**50 fil. it.**	**100 it.**	**100 fil. it.**
1.20	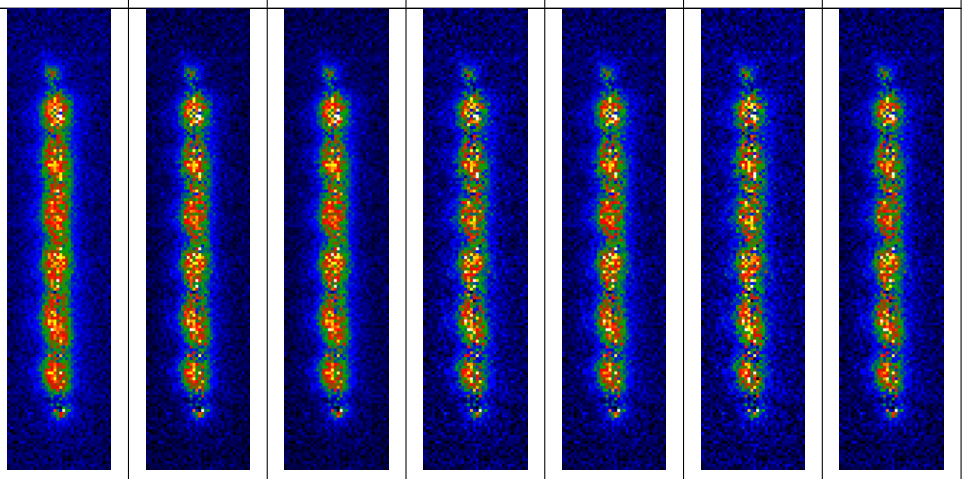						
1.32	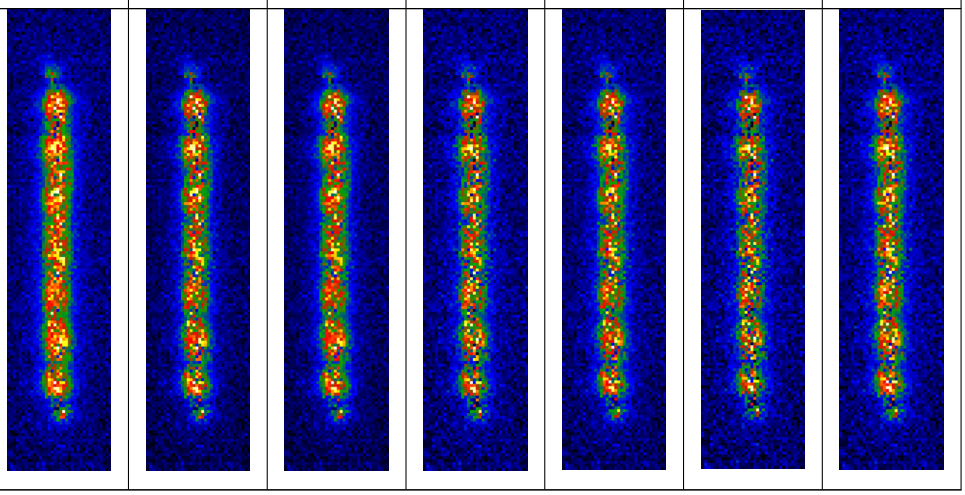						

We have so far shown that the effective energy resolution in recorded spectra can be improved using the RL deconvolution. However, we have not shown the effects of the improvement of the spectral energy resolution in energy filtered maps. Figure 3.21 shows the effect of the filtered and unfiltered reconstruction on energy filtered

maps. As seen in the reconstructed spectra, noise amplification is also seen in the energy filtered maps as we increase the number of iterations. We also observe that the deconvolved plasmon modes are more locally defined than the modes on the original energy filtered maps, this can be clearly seen after the 6^{th} resonance (table 3.1). However, for maps after 100 iterations, this improvement in the localization of the plasmon modes is no longer visible due to the increase in noise. Table 3.1 shows energy filtered maps of eight multipolar surface resonant modes of the silver nanowire after 10, 50, and 100 iterations. This improvement in the apparent localization is due to the substantial decrease in the background due to the zero-loss peak intensity drop, and consequently the reduction in the zero-loss tails. This effect can be visualized from local spectra extracted from the tip of the nanowire (area inside the square), shown in the annular dark field image in figure 3.21, which demonstrates the dramatic drop in the intensity of the tail of the zero-loss after 10 and 50 iterations (figure 3.22). The effect results in both the improved contrast in the energy filtered maps and also the apparent localization as the background due to the zero-loss tails are extended over the entire field of view.

The improved spectral resolution also improves the contrast in the energy filtered maps as shown in figure 3.21. To quantify this increase in contrast, we define contrast as:

$$Contrast = \frac{I_{max}-I_{min}}{I_{max}+I_{min}},$$

where I_{max} and I_{min} is the maximum and the minimum intensity of the energy filtered map respectively. Table 3.1 shows the contrast of the multipolar resonance energy filtered maps. After ten iterations the contrast is improved up to a factor of three. After 50 and 100 iterations there is a diminishing improvement in the contrast, and

after 500 iterations the improvement is negligible.

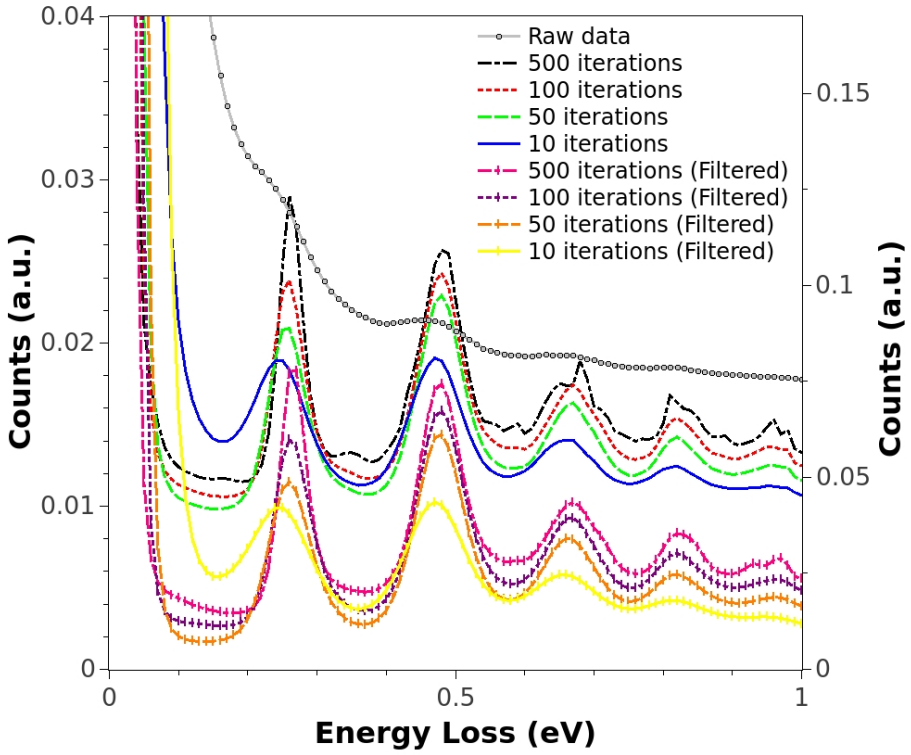

Figure 3.22: Deconvolved and raw spectra obtained from the tip of the nanowire as shown in figure 3.21. The scale of the raw and deconvolved data is shown in the right and left axis respectively.

The effect of filtering the spectrum at each individual pixel position with a Gaussian function on the energy filtered maps is shown in figure 3.21 and table 3.1. The effect is very subtle, but two effects can be identified: One is that the maps are less noisy than the maps formed by unfiltered deconvolution. This effect is expected since the convolution with Gaussian function suppresses noise amplification in the spectrum, which is reflected on the energy filtered maps. A second effect is the reduction of contrast compared with the unfiltered reconstructed maps after the same

Table 3.2: Contrast of the normalized surface plasmon energy filtered maps

	0.25 (eV)	**0.48 (eV)**	**0.67 (eV)**	**0.83 (eV)**	**0.97 (eV)**	**1.08 (eV)**	**1.20 (eV)**	**1.32 (eV)**
0 it.	0.28	0.49	0.49	0.55	0.57	0.63	0.64	0.65
10 fil. it.	0.91	0.93	0.89	0.93	0.90	0.93	0.92	0.93
10 it.	0.92	0.93	0.91	0.94	0.92	0.94	0.93	0.94
50 fil. it.	1.00	0.98	0.94	0.98	0.96	0.97	0.95	0.96
50 it.	1.00	0.99	0.95	0.99	0.98	0.98	0.97	0.97
100 fil. it.	1.00	0.99	0.94	0.99	0.97	0.98	0.96	0.98
100 it.	1.00	0.99	0.96	0.99	0.99	0.99	0.98	0.98
500 fil. it.	1.00	1.00	0.96	1.00	0.99	1.00	0.99	0.99
500 it.	1.00	1.00	0.99	1.00	1.00	1.00	1.00	1.00

number of iterations. This reduction in contrast might be explained by the reduction in efficiency of the filtered deconvolution introduced by the Gaussian function convolution.

We apply the two criteria to limit the number of iterations to the experimental data. Since the data is formed by spectra at each position of the beam raster, we apply the stopping algorithm to the sum of the spectra to obtain an optimal number of iterations. Once the optimal number of iterations from the total spectra is found, we can apply it to the each spectrum in the data set. We could apply the stopping criterion to each spectrum in the data set, but each spectrum in the data would have different number of iterations, and it would generate irregular energy filtered maps.

In the first criterion, we monitor the noise level by considering four ranges of energy, where no plasmon peaks are identified. If we impose the noise threshold as the noise level of the original spectrum, the deconvolution stops after the first iteration, for this reason, we analyze the number of iterations as multiples of the original noise level. Figure 3.23 shows the number of iterations as a function of the multiples of the original noise level for filtered and unfiltered deconvolutions and for

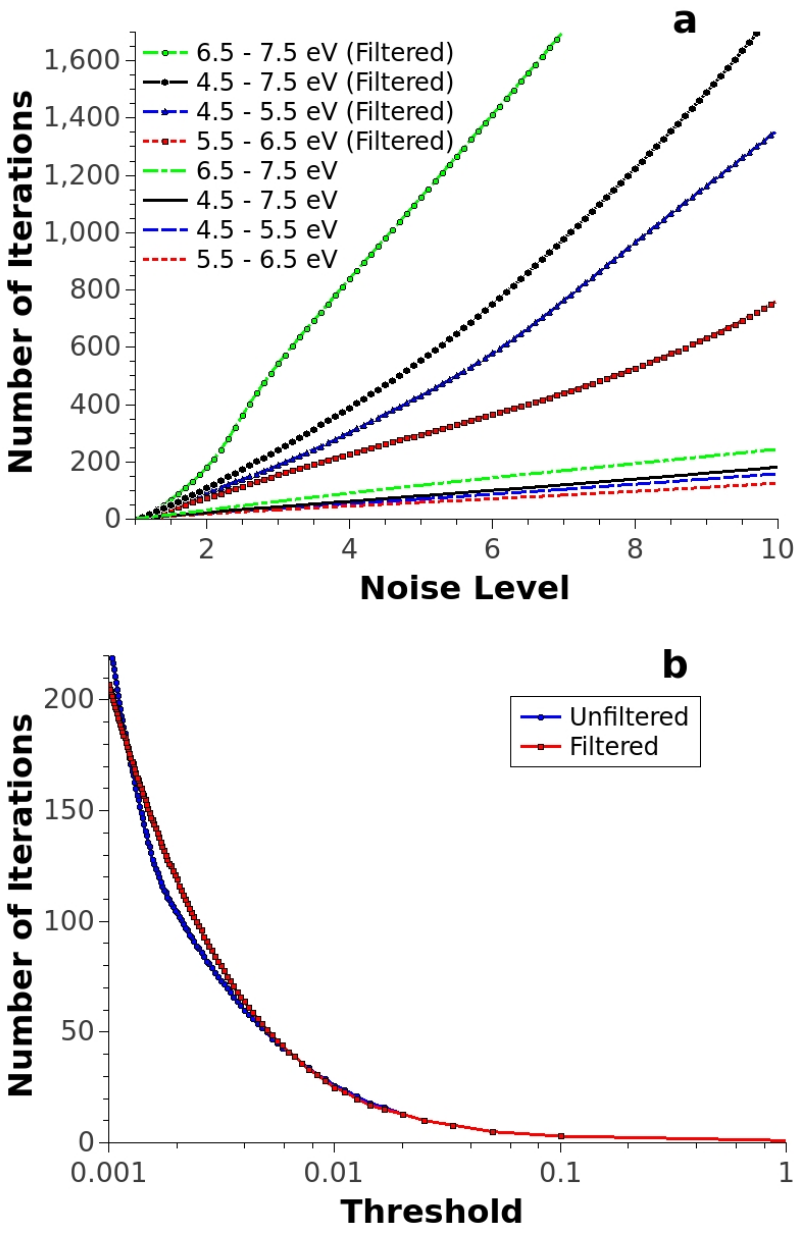

Figure 3.23: Optimal number of iterations versus noise level obtained monitoring noise in four energy ranges: 4.5 to 5.5 eV; 5.5 to 6.5 eV; 6.5 to 7.5 eV; and 4.5 to 7.5 eV for unfiltered and filtered devoncolution (a). Number of iterations versus threshold value of the slope of the change of the deconvolved spectrum for unfiltered and filtered deconvolution (b).

the four energy ranges: 4.5 to 5.5 eV, 5.5 to 6.5 eV, 6.5 to 7.5 eV, and 4.5 to 7.5 eV. The optimal number of iterations in this stopping criterion depends on the range of energy we chose for the noise monitoring. We observe that if we choose a larger energy range, the optimal number of iterations is close to the average value of the smaller ranges within. For the filtered deconvolution, we observed that the number of iterations to obtain the same noise amplification as in the unfiltered deconvolution increases considerably. This occurs because the filtering removes part of the noise, preventing its amplification during the deconvolution. This method is a simple way to limit the number of iterations controlling the quality of the reconstruction. We do not monitor noise level on the negative side of the spectrum because the deconvolution removes the noise effectively in this range, which means no artifacts are created as the number of iterations increases, therefore the deconvolution will continue indefinitely.

We also apply the second criterion proposed above and monitor the change of the reconstructed spectrum with respect to the reconstructed estimation. We varied the imposed threshold value and found the optimal number of iterations as shown in figure 3.23. We can see that the number of iterations increases rapidly as we decrease the threshold value. We also observe a small difference between the filtered and unfiltered deconvolution which implies that the rate of change is intrinsic of the deconvolution. For the threshold value of 0.001 suggested by Van Kempen [94], the number of iterations for the unfiltered spectrum is 228 and for the filtered case is 207. The noise level after the same number of iterations is between eight and ten for the unfiltered case and between two and five in the filtered case, which suggests that this threshold value might not be recommended if we want to maintain low noise levels in the reconstruction. An appropriate threshold value would be between 0.0025 and

0.01 for the unfiltered reconstruction and between 0.0015 and 0.005 for the filtered reconstruction.

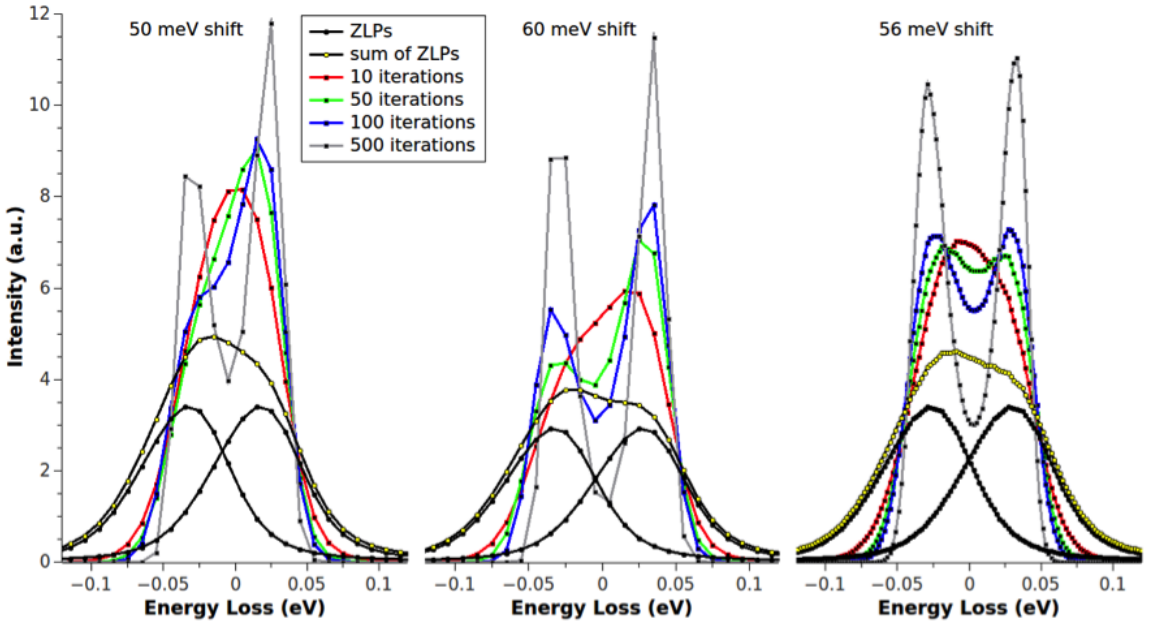

Figure 3.24: Deconvolution of two zero-loss peaks (ZLPs) separated by 50 meV (left) and 60 meV (center), the ZLPs have an energy dispersion of 10 meV. Deconvolution of two ZLPs separated by 56 meV (75% of full-width at half-maximum), the ZLPs have an energy dispersion of 2 meV (right).

The studied cases show successful examples of how the RL algorithm can improve the effective energy resolution of a system, and how the algorithm can extract information at lower energies by reducing the PSF of the system. However, the algorithm also present limitations; as shown by Lazar et al. the algorithm could not readily resolve two peaks that were separated by less than the FWHM of the ZLP [99]. To test our deconvolution algorithm, we performed the test done by Lazar et al., in which the sum of two identical ZLPs shifted in energy by 75% of the ZLP FWHM are deconvolved. For the test, we use an experimental ZLP with an FWHM of 74 meV.

Since the energy dispersion we used for the acquisition is 10 meV, we shifted the two ZLPs by 60 and 50 meV, which are 81 and 68% of the ZLP FWHM, respectively. Figure 3.24 shows that, for the 60 meV shift, the deconvolution can differentiate the two peaks after 50 iterations, and sharpen the FWHM of the peaks to ∼24 meV after 500 iterations. For the 50 meV shift, the deconvolution can properly differentiate the two peaks after only 500 iterations and we obtain an FWHM of ∼32 meV. We can notice that the spectrum has been affected after deconvolution because of the close proximity of the two peaks. We also see a relatively large discrepancy in the intensities of the deconvoluted peaks with respect to the original intensity ratio. But this difference might be influenced by the energy dispersion of the spectrum considering that, for a shift of 60 meV, we have only five channels between the peaks and only four channels for the 50 meV. To test this hypothesis, we have done extra tests. We numerically increased the dispersion in our test to 2 meV per channel by linear interpolation of the experimental ZLP acquired with 10 meV energy dispersion, and shifted the two peaks by 75% (56 meV) as in the test performed by Lazar et al.. In these conditions, as seen in Figure 3.24, we can already differentiate the two peaks after 50 iterations. After 500 iterations the FWHM of the peaks is 26 meV, and the discrepancies in the intensity of the two peaks are considerably reduced, with an intensity ratio of 0.95 compared with 0.77 and 0.72 for 60 and 50 meV shifts, respectively. This shows that, although the RL algorithm requires a larger number of iterations to deconvolve two peaks in proximity to each other, it is possible to resolve these features if deconvolution is done carefully, and the acquired spectrum has low noise levels.

3.3 Conclusions

We implemented the Richardson-Lucy algorithm and used it to reconstruct surface plasmon resonance peaks measured by EELS. We tested the performance of the reconstruction in a blurred simulated spectrum and in experimental EELS spectra from a lithographically patterned silver nanorod. We found that for high signal-to-noise ratio spectra, the deconvolution improves the resolution of the spectra without introducing artifacts, even for a relatively large number of iterations. However, for low signal-to-noise ratio spectra, noise is amplified, and artifacts are created after a large number of iterations.

In the blurred simulated spectrum, we analyzed the effectiveness of a filtered and unfiltered deconvolution and found that the former deconvolution is a better choice when the number of iterations is close to the optimal number. However, if the number of iterations deviates from the optimal, the accuracy of the deconvolution decreases considerably. In the filtered deconvolution, we found that the accuracy has a smaller deviation from the optimal value, compared with the unfiltered deconvolution, if the number of iterations deviates from the optimal. For this reason, the filtered deconvolution is recommended in cases where no information of the optimal number of iterations is known, which is in general the case.

In the deconvolution of the experimental data, we observed a considerable reduction of the zero loss peak tail, allowing the identification of low energy plasmon peaks. We were also able to identify several peaks that were not visible by inspection in the original spectra after ten iterations and even more peaks were identified after 50 iterations. We have obtained a record energy resolution of 30 meV after 50 iterations with small noise amplification; and a resolution of 10 meV after 500 iterations

with negligible noise for spectral features below 1 eV. After spectral reconstruction, we obtained surface plasmon energy filtered maps, where we observed an increased localization of the modes due to the reduced background arising from the tails of the zero-loss peak. As expected, we also observed that noise amplification in the spectral reconstruction at large iteration numbers can be seen in the energy filtered maps. Finally, a considerable increase in contrast of the energy filtered maps, even after only ten iterations, is observed.

We have implemented and tested two methods to limit the number of iterations. In one, we monitor the noise level over an energy range where no peaks are expected. In the other, we monitor the change of the deconvolved spectrum at every iteration. In the first stopping criterion, we recommend a noise level less or equal to two times the noise of the original spectrum to obtain a good reconstruction. In the second criterion we recommend a threshold value between 0.01 and 0.002 for the unfiltered reconstruction and between 0.005 and 0.001 for the filtered reconstruction.

In summary, we demonstrated the use of the Richardson-Lucy algorithm to the deconvolution of surface plasmon resonances measured by EELS, and we show that the algorithm can be used to obtain resolutions up 30 meV with optimal signal-to-noise ratios, and 10 meV for signals below 1 eV. In addition, we show that the deconvolution of EELS spectra enhances the contrast of the EELS energy filtered maps by a factor of three. These results show that the RL algorithm can be used as a powerful post-processing tool of EELS spectra and can be used in the analysis of surface plasmon resonances in nanostructures for plasmonic and photonic applications.

Chapter 4

Edge and Film plasmon modes

Before achieving the full technological potential of plasmonics, we need to understand the basic mechanisms in which nanostructures form plasmonic resonances. For this reason, this chapter focuses on understanding the types of resonances present in simple planar structures and their properties. We start analyzing the plasmon resonances present in nano-squares and metallic strips. The simplicity of these structures makes them a good model for the study of planar structures that supports edge and cavity or film modes. In this chapter, we show our published work [76] with the collaboration of Prof. Nordlander group, which performed the simulations of the nano-squares. Finally, to investigate further the properties of edge modes, we analyze the modes present in bent wires and edges and how the bending angle affects the properties of the edge modes.

4.1 Edge and film modes of nano-squares

In this section, we analyze the plasmonic response of silver nano-squares of sizes ranging from 230 nm up to 1 μm. We find that in even a simple nanostructure can support

a large variety of multipolar modes. In particular, we were able to map high order edge as well as low probability high order cavity modes with energies in the interval from 2.36 eV down to 0.33 eV. We take advantage of the high energy and spatial resolution of EELS to study the character of these modes, most of which, due to their low excitation probability, low resonance energy, or the fine spatial features, have not been previously mapped. Rigorous theoretical modeling supports the experimental results. Furthermore, by comparing electron energy loss (EEL) spectra with the scattering cross-section of the nanostructures under study, we show that most of the observed plasmonic modes cannot be detected in optical measurements under normal illumination. These results not only emphasize the well-established versatility of this technique for the study of plasmonic resonances but show that simple structures can exhibit a rich variety of resonances well suited to test theoretical models and challenge the limits of experimental techniques.

4.1.1 Experimental EELS measurements

A cartoon of the experimental system under analysis is sketched in figure 4.26. We study silver nano-squares with a lateral size L and 40nm of thickness as shown in the high angle annular dark-field (HAADF) images of two of the fabricated nano-squares with L = 230 nm and L = 430 nm (Fig. 4.25). We use an 80 keV electron beam (with a beam current of 1 nA), which is focused on the sample and scanned over the region of interest. The spectrometer (Gatan Imaging Filter, Tridiem model 865) is set to a dispersion of 10 meV per channel, 8 binning in the nonenergy-dispersive direction, and an exposure time of 1 ms per spectrum. To improve the energy resolution of the spectral images, we apply the Richardson-Lucy algorithm described in Chapter 3,

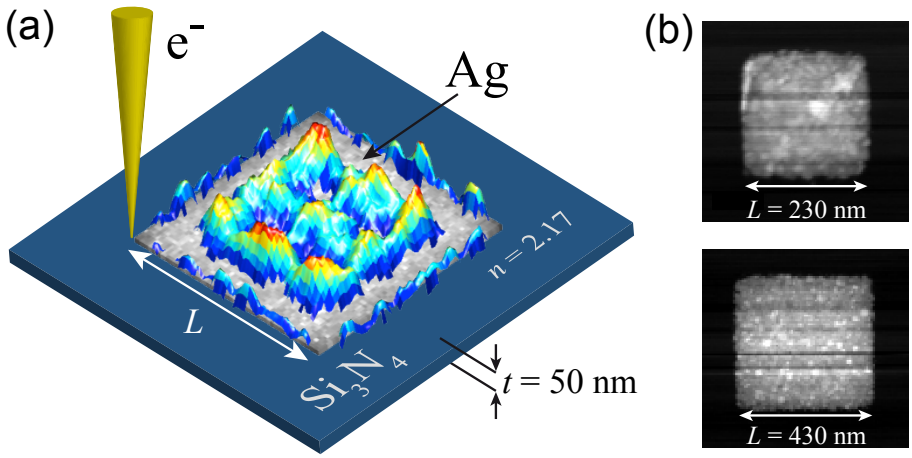

Figure 4.25: Description of the experimental setup and the system under study. (a) We consider a silver nanosquare of lateral size L and 40nm of thickness, fabricated on a silicon nitride membrane of thickness t = 50 nm. We use an 80 keV electron beam to excite the different plasmon resonances of this system. (b) Annular dark-field images of two of the silver nanosquares considered in this work.

obtaining effective energy resolutions down to 50 meV measured from the full-width-at-half-maximum of the zero loss peak. We acquire the spectral images using electron beam step sizes as small as 4 nm.

Figure 4.26 (a) shows the EEL spectra of silver nano-squares of different lateral sizes L measured using electron beams passing close to the edge of these systems (red-shadowed area in the inset). These spectra show a collection of different plasmon modes. As the size of the square increases, the modes shift to lower energies, and higher-order modes become visible. Interestingly, the redshift occurs at different rates for different modes. This can be noticed by looking at the energy difference between modes #1 and #2, which clearly decreases with increasing size. Remarkably, we are able to resolve these two peaks even for the nano-square with L = 1 μm, for which the energy difference is only 90 meV. We determine the nature of these plasmon modes

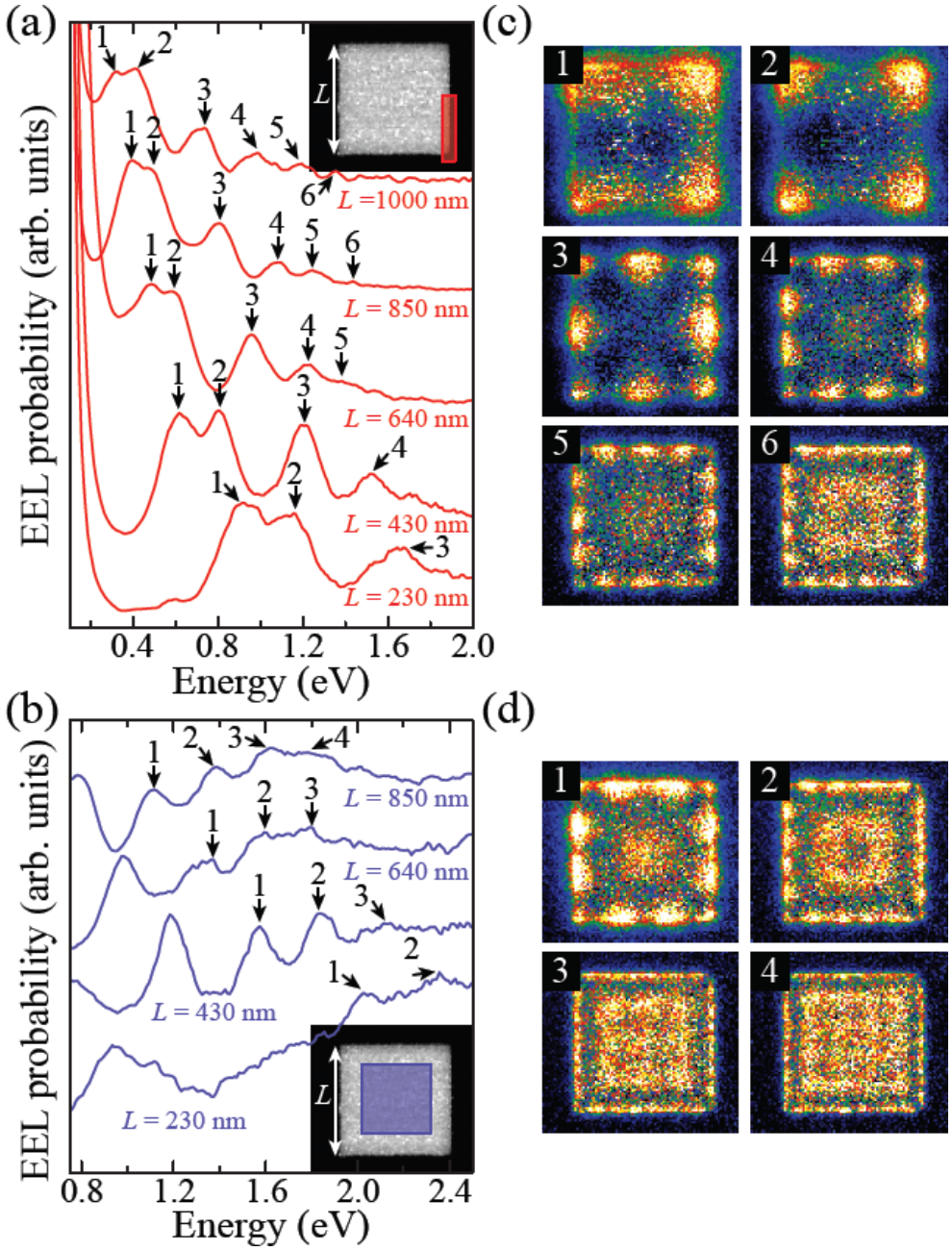

Figure 4.26: Edge and cavity plasmon modes of silver nanosquares. EEL spectra measured at the edge (a) and at the center (b) (see insets) of silver nanosquares with different lateral sizes L. EEL maps for the L = 850nm nanosquare corresponding to the edge (c) and cavity (d) plasmon modes shown in (a) and (b), respectively.

from the corresponding EEL maps, which are plotted in figure 4.26 (c) for the case of a nano-square with L = 850 nm and in Figure 4.29c,d and 4.27 for nano-squares of other lateral sizes L.

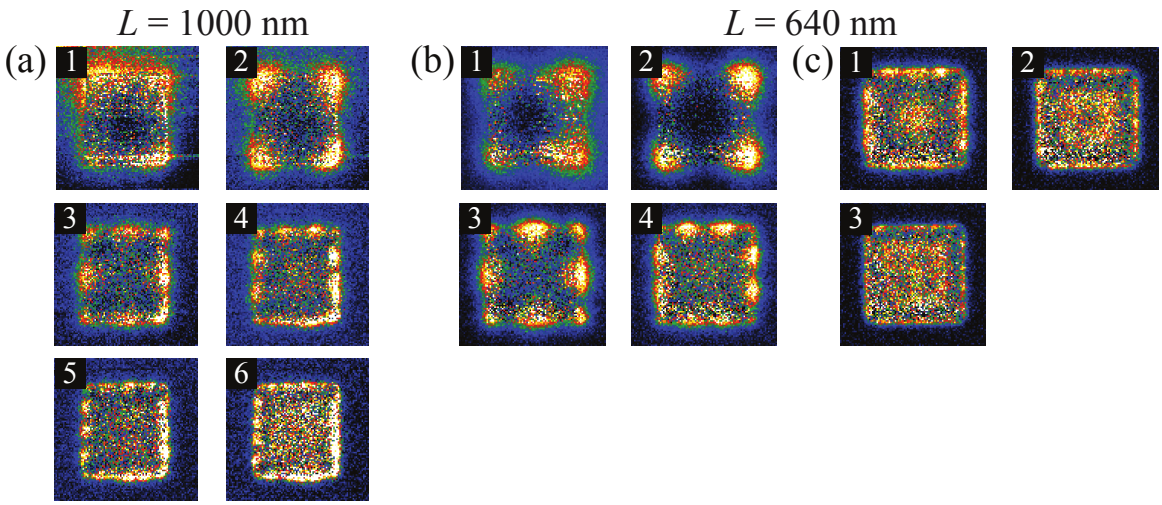

Figure 4.27: (a) EELS energy filtered maps for nanosquare with L = 1000 nm showing the edge modes of figure 4.26a, and energy filtered maps for nano-square with L = 640 nm displaying the edge (b) and cavity (c) modes of the spectra in figure 4.26a,b.

We obtain these maps by integrating over an energy window of ± 30 meV around the corresponding resonance peaks. As seen in figure 4.26 (c) we are able to clearly identify six different modes. The EEL probability of the first four modes is concentrated at the edge of the nanostructure. For that reason we label them as edge modes, each of them having a different multipolar character determined by the number of nodes of the EEL probability along the edge: mode #1 has no node and thus correspond to a dipolar pattern, mode #2 has one node as expected from a quadrupolar distribution, while modes #3, #4 and #5 have two, three, and four as they correspond to the next multipolar orders. Similar modes have been observed in the EEL maps of nanotriangles [73], nanocubes [78], and nanostrips [14].

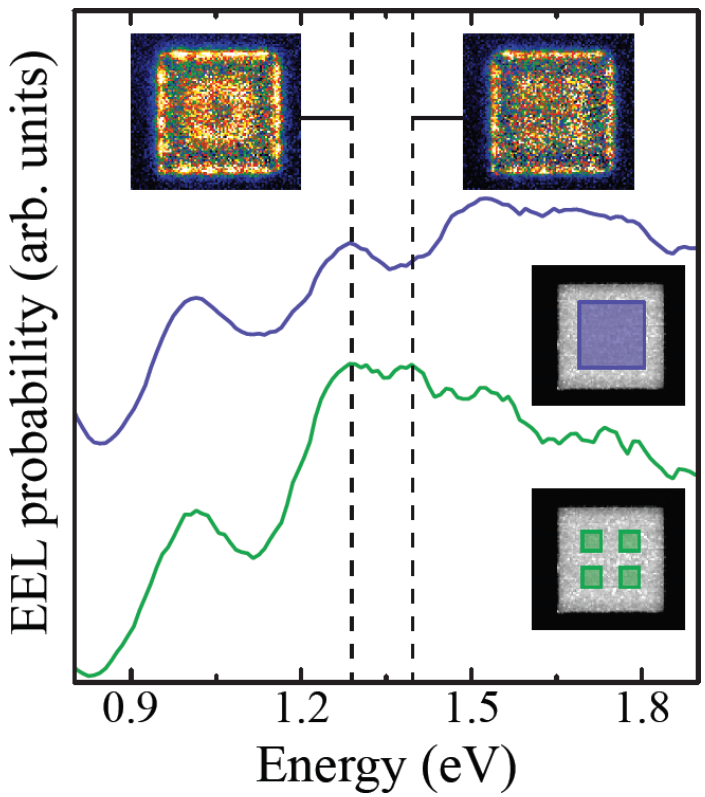

Figure 4.28: EEL spectra for the silver nanosquare with L = 850nm obtained from the integration of the EEL signal acquired at two different regions of the nanosquare (blue- and green-shadowed areas of the lower insets). The upper insets show the EEL probability maps corresponding to the energies indicated by the dashed lines.

As the number of nodes increases, the EEL maps start to display some probability in the central region of the nano-square. This can be noticed for mode #5, whose EEL probability map shows a circular spot at the center, although it is more evident for mode #6. In this case, due to the large number of nodes the EEL probability along the edge becomes almost constant and a square pattern becomes visible at the center of the nanostructure. We refer to the modes displaying a strong EEL probability at the center of the nanostructure as cavity modes because they resemble the three-dimensional plasmon modes present in ring-shaped cavities [107]. Low order cavity

modes, also referred as film and breathing modes, have been observed in nanodisks [14, 63]. As expected from their EEL probability maps, these modes are more efficiently excited when the electron beam passes through the center of the nanosquares. This is the case of the EEL spectra shown in figure 4.26 (b), which are obtained by integrating the EEL signal acquired within the blue-shadowed area shown in the inset. As in figure 4.26 (a) we observe a collection of different modes that shift to lower energies as the size of the square increases. We investigate the character of these modes by analyzing their associated EEL probability maps obtained by integrating the signal over a $\pm$ 60 meV energy window centered at the peak. We plot these maps in figure 4.26 (d) for the four plasmon resonances of the L = 850nm nano-square. As expected, all modes have a significant EEL probability at the center.

We can exploit the analogy of this system with a two-dimensional cavity and label these resonances using a pair of numbers (n,m) corresponding to the number of antinodes that the mode displays along the two axes of the square. Using this notation, the mode #1 in Figure 4.26 (b), which displays a spot at the center, corresponds to the (1, 1) mode of the nanocavity. Mode #2 is then identified as the superposition of modes (2, 1) and (1, 2), which, due to the symmetry of the square geometry, are degenerate and therefore are excited simultaneously in our measurements. Exactly the same happens with mode #3, which results from the superposition of modes (3, 1) and (1, 3). Interestingly, modes with n = m and n > 1, such as mode (2, 2) cannot be clearly identified from the spectra showed in figure 4.26 (b). However, as shown in figure 4.28, this mode becomes visible in the EEL spectrum if instead of integrating the signal of the whole central region (blue-shadowed area in the lower inset of

figure 4.28), we integrate only the part acquired at the corners of that region (green-shadowed area in the lower inset of figure 4.28), where we expect to find the antinodes of the (2, 2) mode. This is clearly confirmed by the analysis of the corresponding EEL maps, which are also plotted as insets in figure 4.28. Mode #4, which appears as a broad resonance in the spectrum, can be identified from the corresponding EEL map as the superposition of modes (4, 1) and (1, 4). In contrast, modes (2, 3), (3, 2), and (3, 3) do not appear in the spectrum. These modes, as was the case for mode (2, 2), have a smaller EEL probability compared with modes (n, 1) when the signal from the whole central region is integrated and are therefore obscured by modes (4, 1) and (1, 4). It is worth emphasizing that the high energy resolution achieved due to the reduction on the tails of the zero loss peak, and the relatively high beam currents employed, are the necessary conditions that allow the study of these high-order modes, which, before this work [76], have not been previously mapped in such detail.

4.1.2 Theoretical EELS simulations

To complete our analysis of the multipolar edge and cavity plasmon modes, and to obtain a deeper understanding of the plasmonic response of these nanostructures, we compare our EELS measurements with theoretical simulations based on the rigorous solution of Maxwell's equations using a finite-difference-time-domain (FDTD) EELS solver developed by our collaborators [108]. Figure 4.29a,b show the comparison between the experimental and the simulated EEL spectra of silver nano-squares with L = 230 nm and L = 430 nm for electron beams passing through different positions. More specifically, we measure the experimental spectra by integrating over the shadowed areas shown in the insets, which are color coded (red for the corner, green for the edge center, blue for 1/4 of the edge, and yellow for the central part of

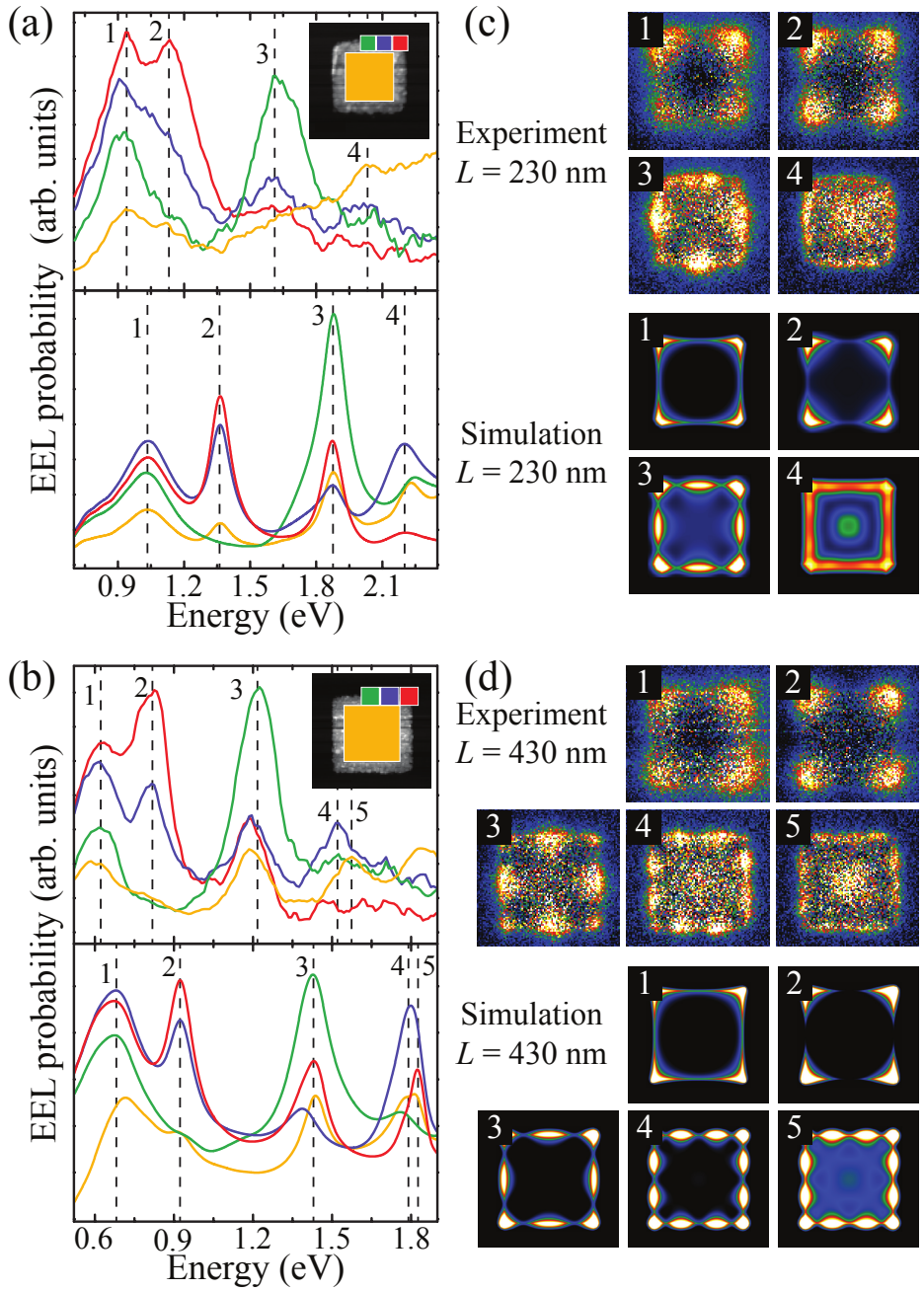

Figure 4.29: Comparison between EEL measurements and theoretical simulations. (a,b) Experimental (top) and simulated (bottom) EEL spectra for silver nanosquares of L = 230 nm and L = 430 nm. (c,d) Experimental EEL maps (top) and simulated LDOS maps (bottom) for the different plasmon modes shown in (a) and (b).

the nano-square). The same integration area is also used for the simulated spectra, which are calculated using electron trajectories passing through the same areas of the nanostructure. The agreement between the measured and simulated EEL spectra is very good. We attribute the small discrepancies in the peak position to geometrical defects on the fabricated structures as compared with the perfect shapes used in the simulations. Another possible source of discrepancy are the differences between the values of the thickness t and refractive index n of the substrate (see Figure 4.25a) used in the simulation and the actual experimental values. A change on those magnitudes can shift the position of the resonances, as shown in Figure 4.30. Similarly, we attribute the differences in the peak widths to the polycrystalline character of the fabricated nanostructures, which results in broader resonances when compared with the simulations. We also compare the measured EEL probability maps with theoretical simulations of the local density of photonic states (LDOS) performed by our collaborators. More specifically, we considered the component of the LDOS parallel to the electron trajectory calculated on a plane parallel to the silver nano-squares and situated 5 nm above them (Figure 4.29c,d). This quantity contains information on the near-field intensity distribution and is therefore related to the EEL probability maps [9, 109], as confirmed by the good agreement with the experimental results.

Examining the EEL spectra in Figure 4.29 obtained at different positions, we observe that the dipolar edge plasmon (mode 1) is more homogeneously distributed along the edge of the nano-square than the quadrupolar edge plasmon (mode 2). This is seen from the faster decay of the EEL intensity associated with the latter as we move away from the corner (red, blue, and green curves in Figures 4.29a,b) and is consistent with our previous analysis based on the number of nodes along the edge.

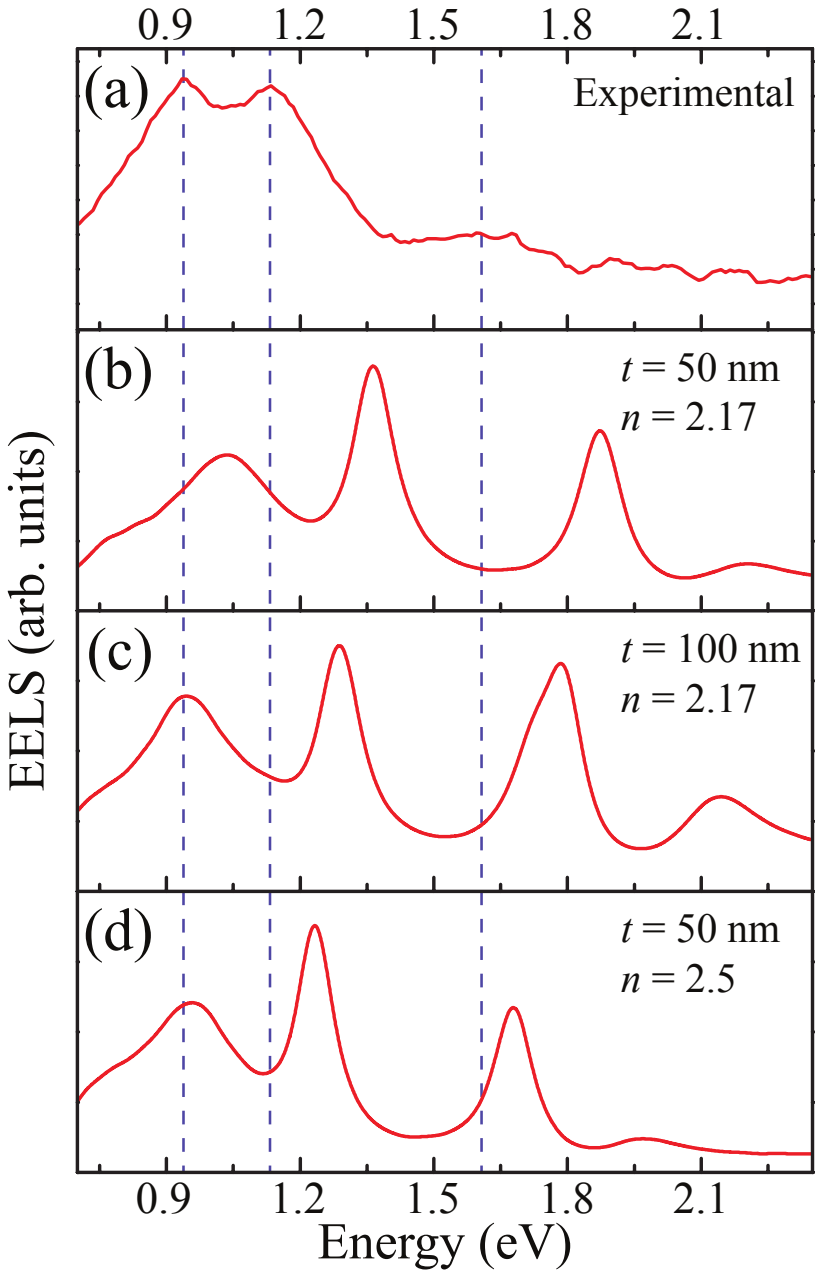

Figure 4.30: Effect of the thickness t and refractive index n of the substrate on the EEL probability. (a) Experimental EEL spectrum for a nanosquare with L = 230 nm. (b-d) Simulated EEL spectra for the same nanostructure assuming t = 50 nm and n = 2.17 (b), t = 100 nm and n = 2.17 (c), and t = 50 nm and n = 2.5 (d). All spectra correspond to excitation at the corner of the nanostructure.

In a similar way, mode 3 has a strong peak at the center of the edge, as expected from the number of nodes associated with this mode. However, the measured EEL probability at the corner is smaller than what is predicted theoretically, something that we attribute to the departure of the fabricated nanostructure from a perfect square shape. The theoretical simulations also demonstrate the formation of the cavity plasmon modes, as seen from the increase of the relative intensity of the EEL spectra at the center of the nanostructure (yellow curves), which is also corroborated by the simulated LDOS maps (mode 4 in Figure 4.29c and mode 5 in Figure 4.29d). Again, the higher intensity at the edges in the simulated results as compared with the experimental data can be attributed to imperfections on the experimental geometry.

4.1.3 Comparison with scattering cross-section

We can complete the characterization of the plasmonic response of the silver nanosquares by analyzing theoretical simulations of their optical scattering cross-sections. The results of the calculation of the scattering cross-section for normal incidence are shown in figure 4.32 (gray curves) along with the EEL spectra obtained for electron beam trajectories passing through the center (yellow curves) and the corner (red curves) of the nanostructure. Interestingly, the scattering spectrum only shows one large peak, which corresponds to the dipolar edge plasmon supported by the nanosquares. The reason is that higher multipolar modes couple more weakly to light than the dipolar mode and because of that are commonly known as dark modes, as we discussed in Chapter 1. This is the case for the quadrupolar edge plasmon, which is clearly visible in the EEL spectra, does not show up in the optical spectrum. It is important to notice that the large size of the nanostructures studied here makes possible the excitation of the dark modes using tilted illumination thanks to the

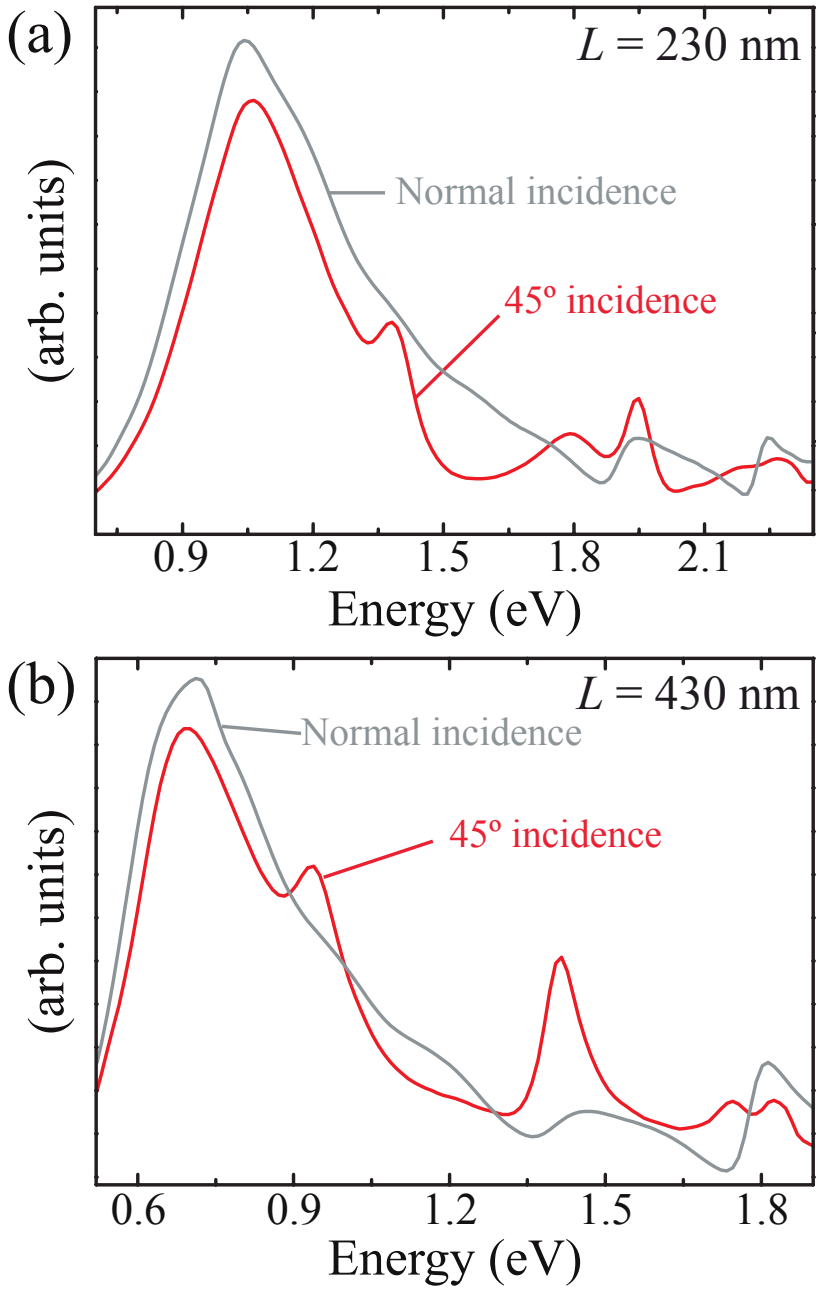

Figure 4.31: Scattering cross-section of the silver nanosquares with lateral size L = 230 nm (a), and L = 430nm (b). The grey curves correspond to normal incidence, while the red curves stand for the case of unpolarized light impinging at 45 degrees.

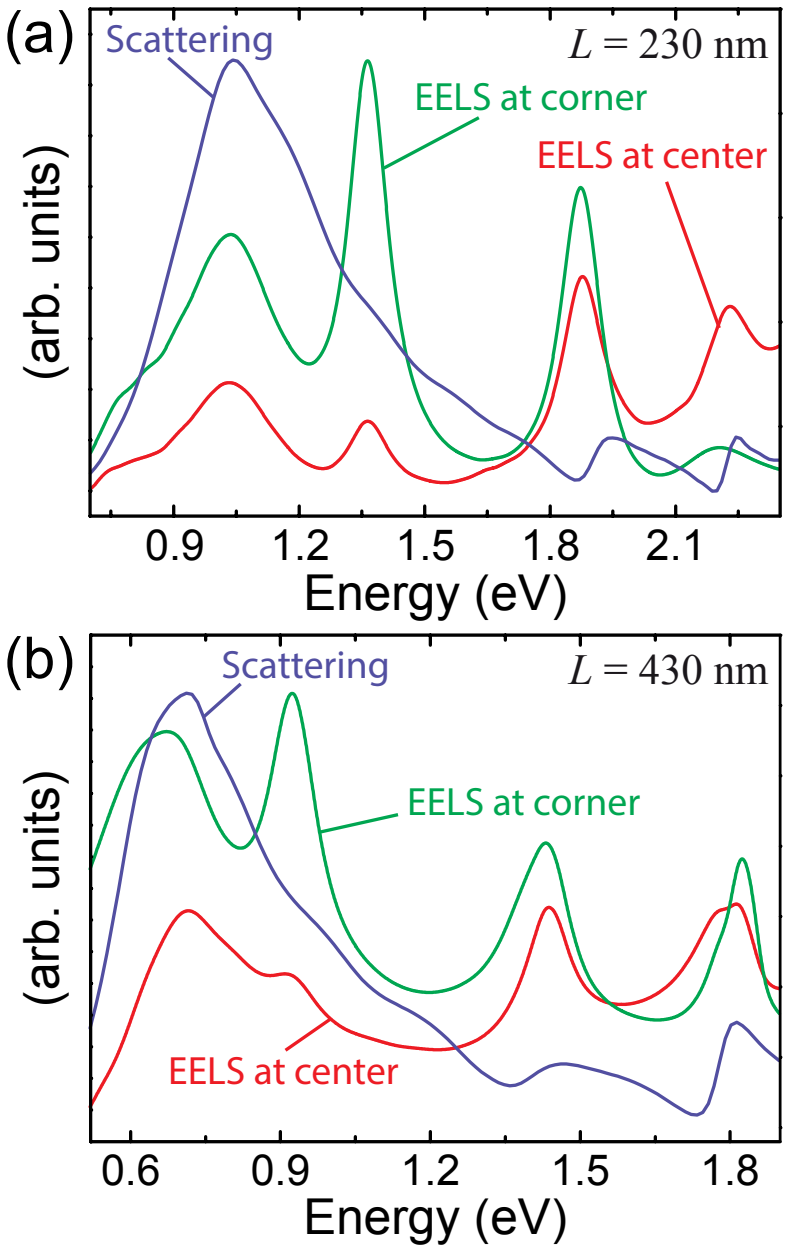

Figure 4.32: Comparison between EEL and optical spectra. We consider silver nanosquares with lateral size L = 230nm (a) and L = 430nm (b). The grey curves correspond to the optical scattering cross-section of the silver nanosquares, while the EEL spectra are calculated for electron trajectories passing through the center (yellow curves) and the corner (red curves) of the nanostructure.

symmetry-breaking caused by retardation [110]. This is shown in Figure 4.31, where we compare the cross-section calculated for light impinging at normal and 45 incidence. Interestingly, the next two modes appear in the scattering spectra in the form of weak Fano resonances [48, 49]. These resonances are the result of the interaction between a bright superradiant mode with a broad line shape and a dark subradiant mode displaying a narrow line shape. In our case, the dipolar edge plasmon acts as the bright mode, while the dark modes are the higher multipolar modes (modes #3 and #4 in figure 4.26). The interaction between these modes is facilitated by symmetry breaking provided by the presence of the substrate and retardation. Dark modes, due to their reduced radiative losses, have significantly narrower lineshapes than bright modes.

4.2 Edge modes on bent structures

4.2.1 From nano-square to nanowire

As described in the previous section, edge modes can be described as one dimensional resonances [14, 76, 111, 112]. Where an edge mode of order n is denoted as E_n, n being the number of nodes along the edge. The canonical one dimensional structure that supports one dimensional modes is a nanowire. Therefore, it is logical to think that the modes in a nanowire are related to the edge modes. To test this principle, we transform a nano-square into a nanowire by changing the width of the nanosquare. Figure 4.33a shows simulated EELS spectra calculated at the center of one edge of the nanosquare as we transform it into a nanowire, as indicated by the stars in Figure 4.33b. We observe how the E_2 mode splits into two modes as we reduce the width of the 200x200x6 nm^3 nano-square in order to transform it into a 20x200x6

nm^3 nanowire. As the distance between edges shortens the edge modes interaction enhances resulting into the formation of a bonding and an antibonding mode as described by the hybridization theory [2]. The charge distribution of the modes, shown in Figure 4.33b, confirms that the E_2 modes splits into a lower energy mode or bonding E_2 mode (E_{2B}), with both edges displaying equal charges, and an higher energy mode or antibonding E_2 mode (E_{2A}), with the edges displaying opposite charges [77]. If the width of the nano-rectangle keeps decreasing evolving into a nanowire, we observe that the E_{2B} mode shifts to lower energies and becomes what we know as the second one dimensional mode of the nanowire. Also, the E_{2A} mode shifts to higher energies outside of the analyzed energy range and it does not appear among the nanowire modes. From Figure 4.33 we observe the presence of the E_{4B} mode which, as was the case of the E_{2B} mode, shifts to lower energies as the width decreases and becomes the fourth one dimensional mode of the nanowire. We also notice the presence of a dipolar mode (shown in the charge distribution in Figure 4.33b) that, as the distance between edges is reduced, becomes the transverse mode found in nanowires. The coupling of edges modes within a single structure is different to the coupling of modes in multiple structures where no charge transfer is possible, as we explained in chapter one, in the multiple particle case case what defines which mode has a lower or higher energy is the electrostatic interaction between particles, and in general equal charges produce repulsion and have higher energies; and opposite charges produce attraction an have lower energy. In the case of coupling of edge modes within the same particle the antisymmetric charge distribution in both edges (antibonding mode) has a higher energy and the symmetric charge distribution (bonding mode) has a lower energy. Intuitively, we can say that in order to have antisymmetric charges at opposite edges

of a structure we need to polarize the structure, therefore the more polarized the structure the more energy is required to maintain the polarization, and the higher the resonant energy of the mode. Also, the smaller the polarization of the structure the lower the energy required, and the lower the resonant energy of the mode.

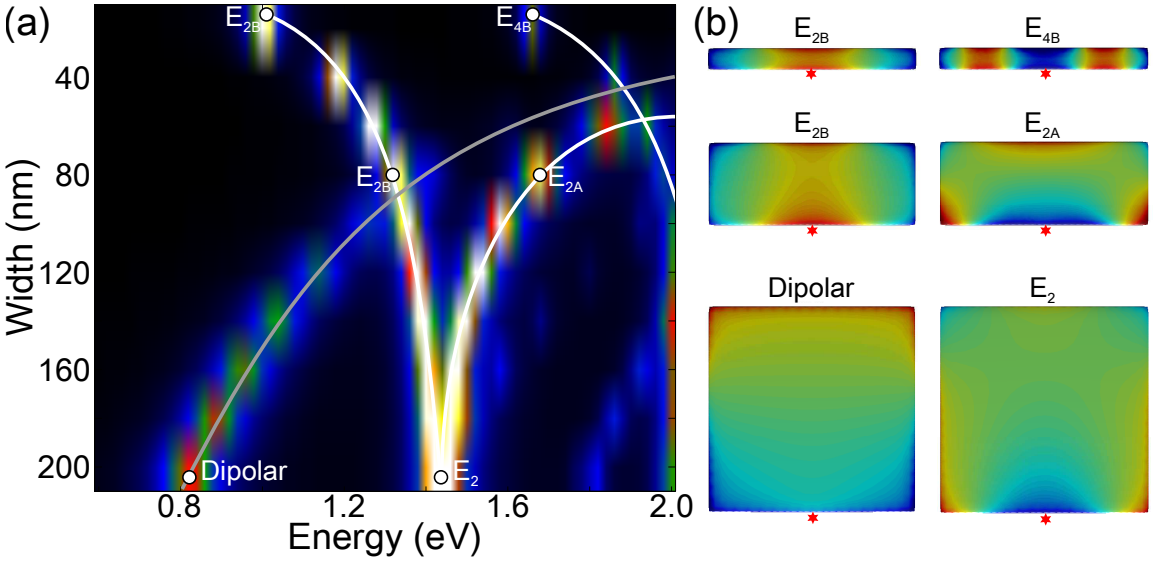

Figure 4.33: Evolution of simulated EELS spectra (shown in a temperature scale) as a function of the width of a rectangular structure (a) that transforms from a nano-square (200 nm) to a nanowire (20 nm), calculated at center of one edge indicated by a red star in (b). Charge distribution of the edge modes indicated by the white dots in (a) in the rectangular nanostructure of a width of 20 nm (top panel), 80 nm (central panel), and 200 nm (bottom panel) (b).

In this section, we have demonstrated that the one dimensional modes present in nanowires are formed by the coupling of edge modes within the nanowire [77]. This explains why there is a dependence of the the resonant energy of the modes on the aspect ratio of the nanowire. The larger the aspect ratio the lower the resonant energy of the modes. Alternatively, the larger the aspect ratio of the nanowire the stronger the coupling between edges and the larger the red-shift of the bonding edge modes.

4.2.2 Energy shifts and the critical angle of edge modes

Now that we have stablished the relation between the edge modes and the modes in a nanowire, we will focus on how these edge modes change as an edge bents and is no longer straight. To study the effect of bending on edge modes we will study the bending of nanowires. A previous work showed that the presence of kinks in a nanowire did not affected the localized plasmon resonances [11]. However, in that work the investigated bending angles were larger than 90°. In this section, we will analyze the evolution of the nanowire modes for several bending angles. For this analysis 2μm long 30 nm thick and 70 nm wide silver nanowires with bending angles from 30° to 180° are fabricated by electron beam lithography in 50 nm silicon nitride TEM membranes as we described in Chapter 2. The EELS spectra are acquired in a monochromated microscope and the data was post-processed by applying the Richardson-Lucy deconvolution and a normalization procedure as explained in Chapters 2 and 3.

Figure 4.34 shows EELS spectra acquired at three distinct locations, indicated in the annular dark field (ADF) images, for nanowires with different bending angles. In the straight wire we have seven modes identified as bonding edge modes E_{nB} with $n =$ 2 to 8 the number of nodes along the wire. Figure 4.36a shows the EELS intensity profile of the straight nanowire displaying the nodal distribution of its edge modes. As we decrease the bending angle we can see that mode E_{7B} and E_{8B} converge from 0.9 eV and 1.01 eV respectively in the 180° nanowire to join in energy at 0.96 eV in the 30° nanowire, the same trends follow modes E_{5B} and E_{6B} converging from 0.66 eV and 0.81 eV respectively to 0.78 eV at 30° bending angle. Modes E_{2B}, E_{3B}, and E_{4B} do not appear to follow the same trend as the higher order modes, and only mode

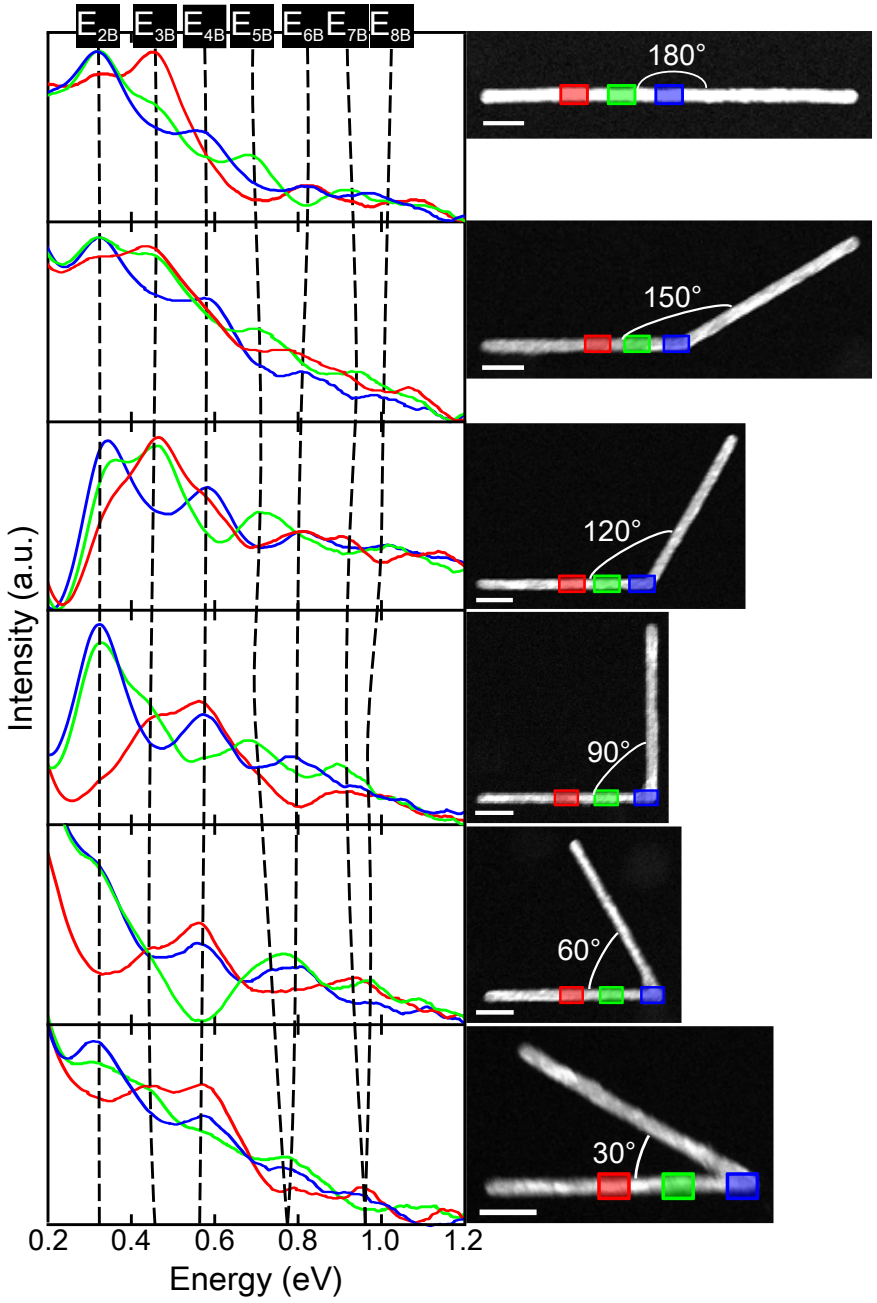

Figure 4.34: Evolution of EELS spectra of nanowires as a function of bending angle (left) acquired at three color-coded locations shown in the anular dark field (ADF) images (right). The scale bar in all ADF images is 200 nm.

E_{2B} experiences a very small blue shift from 0.43 eV to 0.45 eV as we decrease the bending angle. To further support the experimental results we performed numerical simulations of bent nanowires using the MNPBEM Matlab toolbox [50, 51] as explained in Chapter 2. Because the fabricated structures are fairly large (2 μm long) it is computationally expensive requiring a large memory, for this reason we simulate nanowires at a scale five times smaller than the fabricated nanowires. The 400 nm long 6 nm thick and 14 nm wide silver nanowires are simulated using a tabulated experimental dielectric function [113] for silver and the effect of the silicon nitride substrate is modeled using an effective dielectric function of 2 for the surrounding environment.

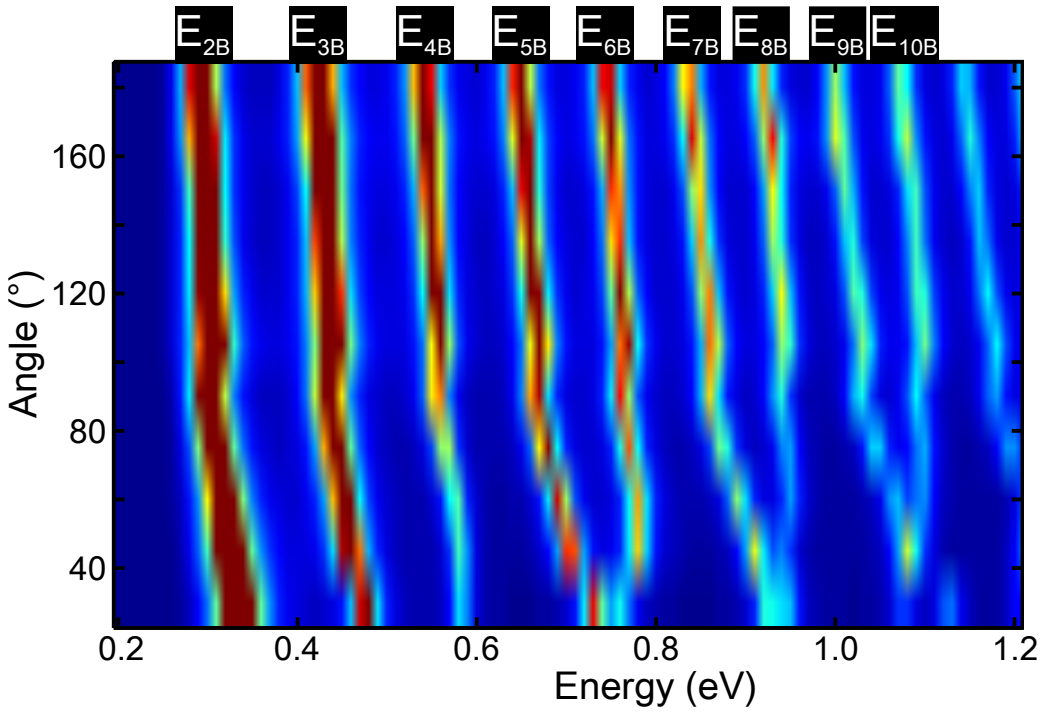

Figure 4.35: Evolution of simulated EELS spectra as a function of bending angle in silver nanowires

The simulated spectra in Figure shows the same trend that we found in the experimental EEL spectra with modes E_{5B} and E_{6B} converging from 0.65 eV and 0.75 eV respectively in a straight nanowire to 0.74 eV in a 30° nanowire. The same trend is found in modes E_{7B}-E_{8B} and E_{9B}-E_{10B} with the modes converging at 30° angle. Mode E_{3B} experiences a blue shift, as we saw experimentally, from 0.42 eV at 180° to 0.48 eV at 30° in two stages a low rate shift of 0.11 meV/deg between 180° and 90°, and a faster shift rate of 0.83 meV/deg between 90° and 30°. For the case of modes E_{5B}, E_{7B}, and E_{9B}, they blue shifts with low rates of 0.11, 0.22, and 0.22 meV/deg respectively between 180° and 90°, however their shift rate increases to 1.3, 1.2, and 1.0 meV/deg between 90° and 30° which is more than five times the shift rate of angles above 90°. A different phenomenon is observed in modes E_{4B}, E_{6B}, E_{8B}, and E_{10B}, although they experience a low rate blue shift of 0.11, 0.11, 2.2, and 2.2 meV/deg at angles between 180° and 90°, for angles below 90° the modes blue shift first to later red shift before converging with modes E_{3B}, E_{5B}, E_{7B}, and E_{9B} respectively. In mode E_{2B} we notice that there is not shift from 180° to 90°, however for angles below 90° the mode experiences a blue shift with a rate of 0.66 meV/deg. These results indicate that although there is a very small shift for angles above 90° the change is negligible and very difficult to detect experimentally with current energy resolutions, explaining why Rossouw et. al. did not find any change in the modes they analyzed [11]. However, for angles below 90° the energy shift is not negligible particularly for high order modes where edge modes even intersect. Therefore, we can infer that the edge modes in bent edges are unaffected by the presence of bends up to the critical angle of 90° where the modes start self-interacting producing large energy shifts and modes can eventually converge.

4.2.3 Antinode clustering and self-interaction of edge modes

Now that we have analyzed the energy shifts produced by the bending of the edges in nanowires, we can analyzed how the nodal distribution of the edge modes is affected by the presence of a bend. Figure 4.36 shows the experimental and simulated EELS intensity profile of a straight nanowire and a 30° bent nanowire acquired from the gray regions displayed on the ADF images. From the figure we observe the typical nodal distribution of an straight nanowire with nodes moving away from the center of the nanowire as the mode order and energy increase. This typical nodal distribution changes considerably for the 30° bent nanowire. We notice that the modes E_{5B} and E_{6B} have merged, as well as the modes E_{7B} and E_{8B}, and their antinodes have clustered due to the presence of the kink at the middle of the nanowire. When the two modes coincide in energy, it is not a simple mode overlap, but the antinodes of the modes merge. In modes E_{5B} and E_{6B} antinodes that are up to 28 nm apart in the 180° nanowire shift to become only one antinode in the 30° nanowire. Similarly, in modes E_{7B} and E_{8B} antinodes that are 22 nm apart at 180° become one antinode at 30°. Even in the case of modes E_{3B} and E_{4B} that do not merge at 30°, the antinode distance between the modes is reduced from 36 nm in the 180° nanowire to only 10 nm in the 30° nanowire. This is a clear indication of antinode clustering produced by the presence of a bend in the nanowires. Because of this antinode clustering, the nodal distribution of the edge modes in the 30° nanowire, shown in Figure 4.36b, resembles more the distribution of a nanowire half the size of the actual nanowire. This effect is expected if we realize that in the limit when the bending angle is 0°, we have a nanowire half the size of the original nanowire.

Figure 4.37 shows the eigenmodes E_{5B} and E_{6B} for several bending angles. Modes

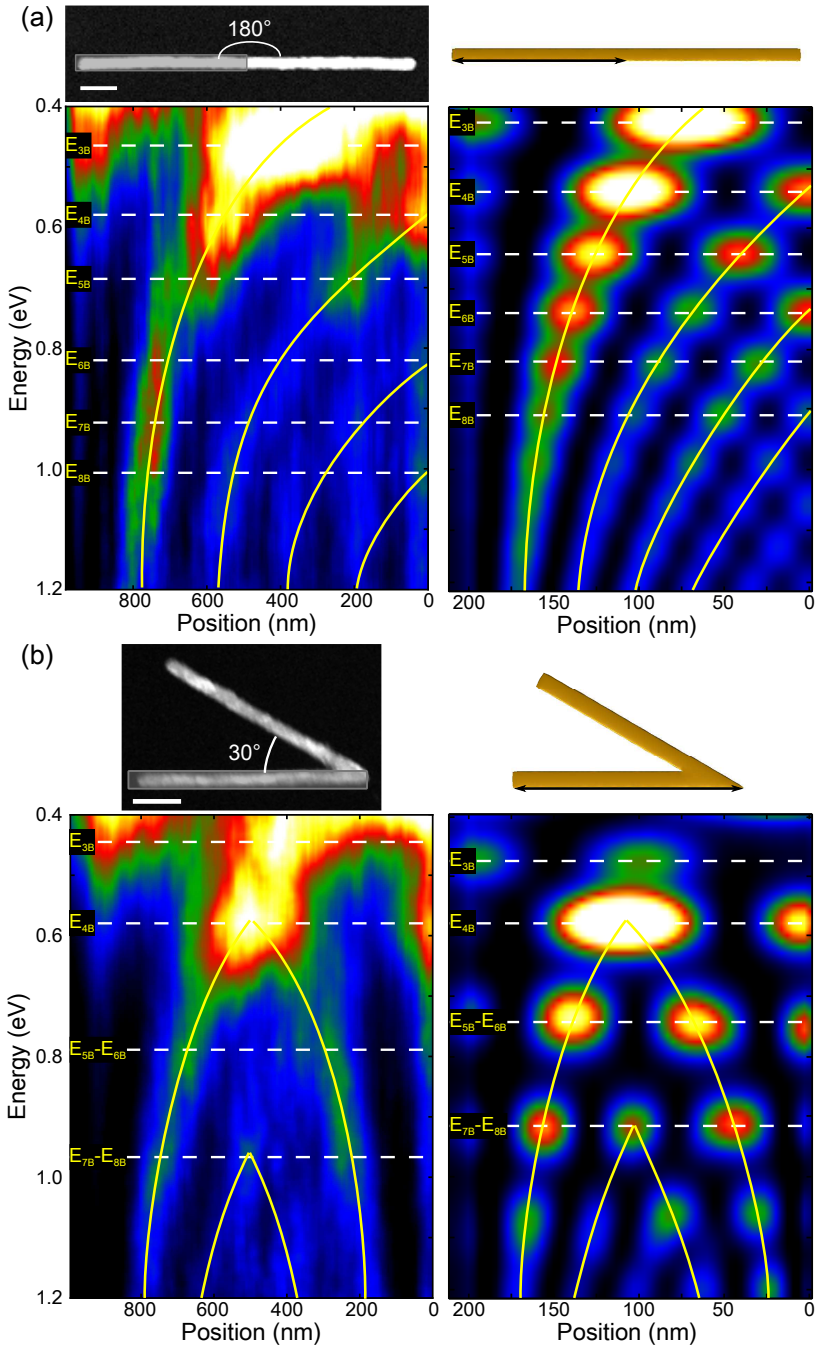

Figure 4.36: Experimental and simulated EELS intensity profile of a straight nanowire (a) and a 30° bend nanowire (b) showing how the nodal distribution of the edge modes changes due to the presence of a kink. The profiles were acquired in the gray regions shown in the ADF images. The scale bars are 200 nm

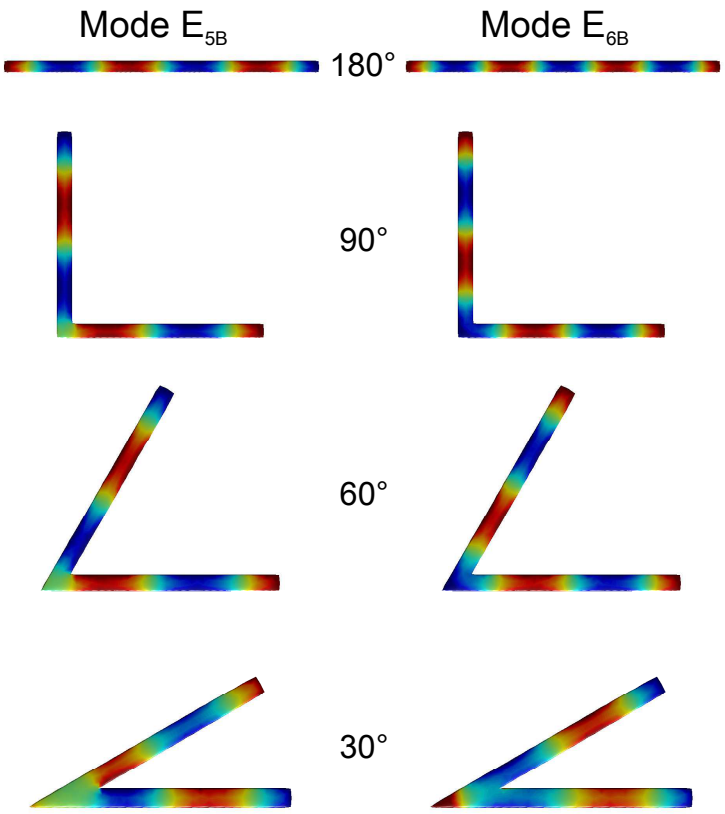

Figure 4.37: Evolution of the Eigenmodes E_{5B} and E_{6B} as the bending angle changes showing the charge distribution of the edge modes.

E_{5B} and E_{6B} are a good example to explain the effect of self-interaction of the modes within a bent nanowire. As we explained above, between 180° and 90° all the modes experience a small blue shift. From the eigenmodes we observe that, at those angles, the antinode distribution does not experience a significant change and there is very little interaction between antinodes. Below 90°, we observe that, as we reduce the bending angle, the antinodes closer to the bend in mode E_{5B} the interaction between antinodes of opposite charge becomes stronger. This proximity produces the rapid blue shift we saw in Figure 4.2.2. In mode E_{6B} we observe that as the bending angle

reduces the central antinode gets confined over the kink in the outer edge of the wire. Also when the bending angle is sufficiently small (i.e. 30° for mode E_{6B}) the antinodes closer to the bend merge as seen in Figure 4.37. The merging of these antinodes produces the red shift we saw in in Figure 4.2.2 that eventually causes the intersection of even and odd modes. For the particular case of modes E_{5B} and E_{6B} the intersection occurs around 30° where the eigenmodes become degenerate. Based on this example we can notice that the higher the mode order the larger the number of antinodes close to the bend, and the stronger the effect that causes the modes to shift. For this reason we see that higher order modes are more strongly affected by the angle change than lower order modes.

4.3 Conclusions

In summary, we have used EELS and rigorous modeling to characterize the plasmonic response of silver nano-squares of several sizes supported by silicon nitride substrates. We have found that these nanostructures support a collection of multipolar edge and cavity modes, whose nature we have investigated through the analysis of the corresponding EEL probability maps. The characterization of these modes, which have not been previously detected in smaller structures, has only been possible by pushing the detection to the current limits of this technique. Furthermore, by comparing the EEL spectra with optical scattering cross-section calculations, we have confirmed that most the modes supported by the nanosquares are dark and cannot be detected using optical measurements due to their high multipolar nature. The results emphasize, yet again, the well-established versatility of EELS and the sensitivity of this technique to probe both bright and dark plasmon resonances.

We have demonstrated the relationship between edge modes and the one dimensional modes in nanowires. We showed that the modes supported by a nanowire are bonding edge modes produced by the coupling of the edges in the nanowire. We also showed that there is negligible change on the edge modes in nanowires bent by angles larger than the critical angle of 90°. However, for angles smaller than 90° the modes shift significantly. These shifts are caused by the interaction of the antinodes of an edge modes as the angle decreases, this interaction is stronger for high order modes. For small angles the even modes red shift and the odd modes blue shift causing the modes to converge. Due to this convergence the nodal distribution of highly bent nanowires resemble the nodal distribution of a nanowire half the size of the original nanowire. In this Chapter, by analyzing a range of simple structures, we have shown that the combination of EELS experiments and theory provides a fundamental understanding of the plasmon physics necessary to improve the design and optimization of new nanostructures for nanophotonic applications.

Chapter 5

Coupling of Plasmonic nanostructures

Tailoring the LSPR that provides extra flexibility is the coupling of plasmonic nanostructures due to the interaction between the LSPR of the individual structures. The optical response is modified when the distance between nanostructures is smaller than their lateral size and a splitting of modes can be induced, as was explained by Prodan et al. [2] in their hybridization model. The interaction of plasmonic nanostructures also induces other unique effects, such as tunneling charge transfer plasmons [62], and Fano resonances [114], expanding the toolset to modify the optical properties of nanostructures. Even in the simplest case of nanoparticle dimers, a hybridization of the dipolar mode that is dependent on the inter-particle distance is observed [115, 15]. This phenomenon has been used in the concept of plasmon rulers [116, 117]. In structures where the excitation of higher order modes is efficient, a richer modal spectrum can be obtained by plasmonic coupling of higher order modes, and phenomena such as intermodal coupling [118] can be observed. However, most of the investigation on

plasmonic coupling has been mostly focused on the interaction of dipolar modes, or in small structures where higher order modes are difficult to detect [119], and not much attention has been devoted to the coupling of high order modes.

As we saw in Chapter 4, we can describe the modes present in planar nanostructures as edge and film or cavity modes. In this Chapter, we explore the interaction between edge modes in multiple configurations, including the coupling of edge modes in nano-squares, slot waveguides, and offset nanowires. Taking advantage of the high resolution of EELS and its ability to excite dark modes we study not only the coupling of low order modes but we also pay particular attention to the coupling of high order modes. From the analysis of the structures, we show how versatile is the use of coupling for the tuning of the optical properties of plasmonic nanostructures, and we also show the wide variety of modes that can be excited by coupling of edge modes. The section about the coupling of edge modes in nano-squares and slot waveguides, has been published here [112] and was done in collaboration with Prof. Nordlander from Rice University and Prof. Manjavacas from University of New Mexico.

5.1 Edge mode hybridization in nano-square dimers

In this work, we present a detailed study of the plasmonic coupling of edge modes with a special emphasis on the interaction of high order modes and the formation of gap modes. Through the investigation of the response of a number of nano-squares dimers 40 nm thick with lengths from 420 nm to 1 μm separated by gaps ranging from 50 nm to 100 nm, we study the coupling of these dimers by separating them into low order and high order modes. To further understand the coupling of edge modes and the formation of gap modes, we investigate structures composed of two

50 μm long and 40 nm thick silver strips with widths ranging from 470 nm to 1150 nm separated by gaps with sizes from 95 nm to 115 nm (slot waveguides). The dispersion relation of the modes formed by the coupling of edge modes in the nano-square dimers is also analyzed and compared with the dispersion of the modes in the planar slot waveguides. In this section, the experimental results are complemented with numerical simulations of EELS using the MNPBEM Matlab toolbox [50, 51] described in chapter 2. The effect of the silicon nitride substrate is modeled using an effective dielectric function of 2.5 for the surrounding environment, and the silver structures are modeled using a tabulated dielectric function [113].

5.1.1 Coupling of low order modes in nano-square dimers

Figure 5.38 (a) shows the EEL spectra acquired in six different areas of a 420 nm nano-square dimer with 50 nm gap as indicated in the inset of the figure. Due to the high effective energy resolution of the spectra (60 meV), measured from the full-width-at-half-maximum of the zero loss peak, we can identify ten LSPR with peaks in multiple positions. The plasmon resonances present in the nano-square dimer can be separated into two groups for their analysis: One group formed by the first five LSPR consisting of the lower order modes, and a second group integrated by the next five resonances, corresponding to the higher order modes.

The experimental, as well as the simulated, EELS maps of the first five resonances, are shown in figure 5.38(b-d). To extract the EELS maps, corresponding to each surface plasmon resonance mode, we isolate the contribution from each peak in the plasmon maps using the non-linear least squares fitting tool of the "DigitalMicrograph" software, which fits Gaussian peaks to a spectrum image [120]. From the

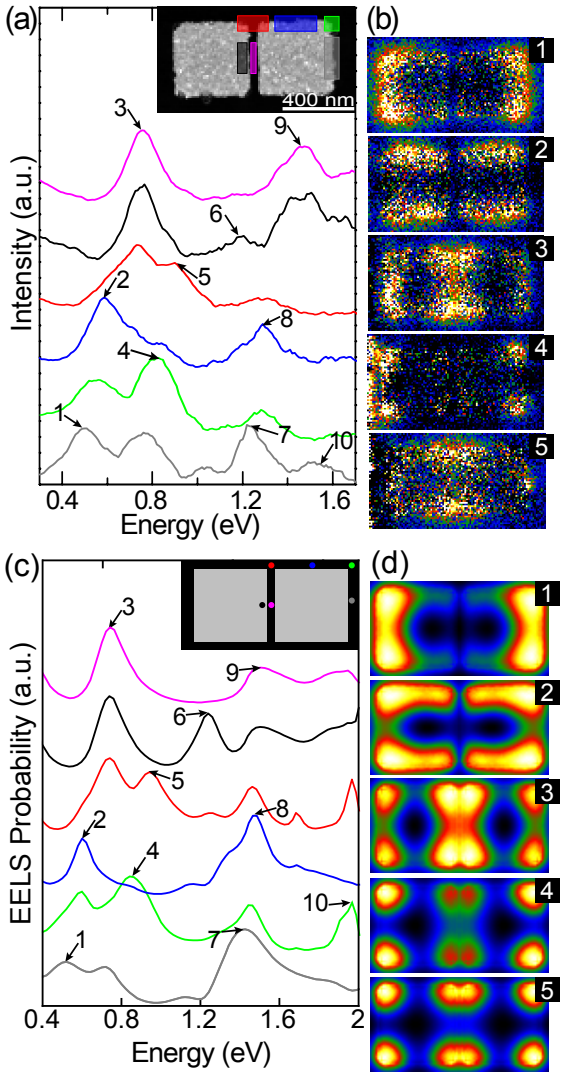

Figure 5.38: (a) EEL spectra of a 420 nm nano-square dimer with 50 nm gap acquired at the color-coded positions indicated in the annular-dark-field (ADF) image in the inset. Ten peaks corresponding to LSPR modes, indicated by the arrows, are identified. (b) EELS maps of the first five resonant modes. (c) Simulated EEL spectra of the nano-square dimer with its resonant modes indicated by the arrows. (d) Simulated EELS maps of the first five plasmon modes. The first three modes are formed by coupling of the dipolar modes in each nano-square, while the next two modes are formed by the coupling of the quadrupolar modes.

EELS maps, we can identify the nature of the different modes supported by the nano-square dimer. The first three modes correspond to the coupling of the dipolar mode of a single nano-square. Two of these new modes can be identified as bonding (mode 1) at 0.50 eV, where charge carriers of opposite sign are accumulated at each edge near the gap, and anti-bonding (mode 3) at 0.76 eV, where charge carriers of the same sign are localized at the edges near the gap. These type of modes have been described previously in particles and wires [16, 59, 15, 69]. Mode 2 at 0.60 eV is a dipolar transversal mode similar to the modes found in wires and rods [16, 12]. The formation of this transversal mode can be explained by the lifting of the degeneracy in the nano-square dimer between the dipolar mode with opposite charges at the top and bottom sides of the square and the dipolar mode with opposite charges at the left and right sides. In the dimer, the left-right dipole modes couple creating the aforementioned bonding and anti-bonding modes, while the top-bottom dipoles form this transversal mode. In the structures we analyze, we did not find a strong enough interaction of the top-bottom dipoles that will lift the degeneracy of the transversal bonding and anti-bonding modes. Thus they appear as a single transversal mode. Mode 4 and 5 are generated by the coupling of the quadrupolar modes in each square. As it is the case in the coupling of the dipolar modes, the quadrupolar mode also splits into a bonding mode at 0.83 eV, where the charges of opposite sign are localized in the corner close to the gap, and an anti-bonding mode at 0.95 eV, where the charges of equal sign are concentrated in the corners close to the gap. Figure 5.40 shows an energy diagram summarizing the coupling of lower order modes. The formation of the five modes by the coupling of the dipolar and quadrupolar modes is an evidence of the wide range of modes that can be excited by coupling of plasmonic structures.

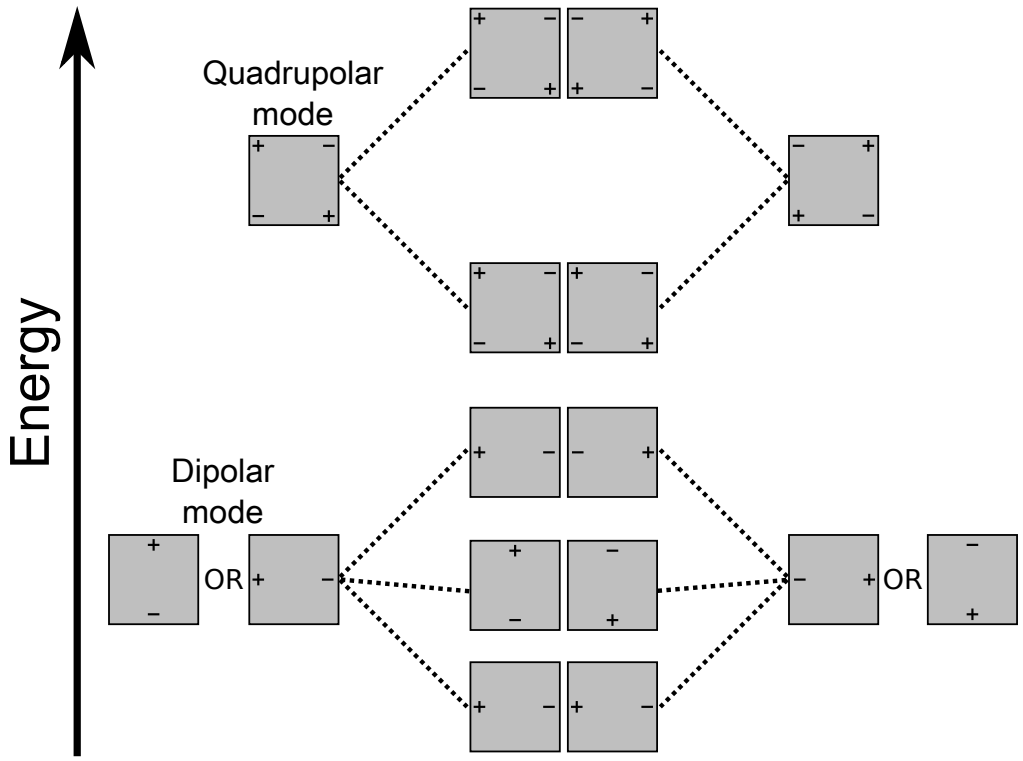

Figure 5.39: Energy diagram summarizing the coupling of the dipolar and quadrupolar modes in nano-square dimers. The diagram depicts the five modes generated by the coupling of lower order modes. The relative energy positions are not to scale since the energy splitting will be determined by the coupling strength.

5.1.2 Edge modes and the coupling of high order modes in nano-square dimers

Besides the coupling of low order modes, the spectra in Figure 5.38(a) and (c) also exhibits several peaks corresponding to the coupling of high order modes. The intensity distribution of these modes supported by the 420 nm nano-square dimer is displayed in Figure 5.41. The figure shows the experimental EELS intensity and the simulated EELS probability as a function of electron energy loss (EELS profile) acquired from

three different edges: edges of the gap (region "i"); an edge on the side of the dimer (region "ii"); and an edge on the base of the dimer (region "iii"), as illustrated in the annular-dark-field (ADF) image and diagram. The experimental EELS profiles are slightly different from the simulated ones because the fabricated structure has very rough edges that affect the formation of the plasmon resonances. The modes formed by the coupling of the nano-square are identified with white dashed lines and a mode number that correspond to the peaks in the spectra in Figure 5.38(a). To understand the origin of these modes let's first analyze the high order modes in a single square. Figure 5.39 shows the EELS intensity profile acquired at one edge of a 430 nm long silver nano-square, and indicates the high order modes supported by the structure. These modes with their EELS intensity concentrated at the edge, observed on planar nanostructures, can be described as quasi 1-D edge modes (E_n) [14, 76, 77] with the number of nodes "n" representing the order of the resonance. In Figure 5.39 edge modes of order two (E_2), three (E_3) and four (E_4) are observed.

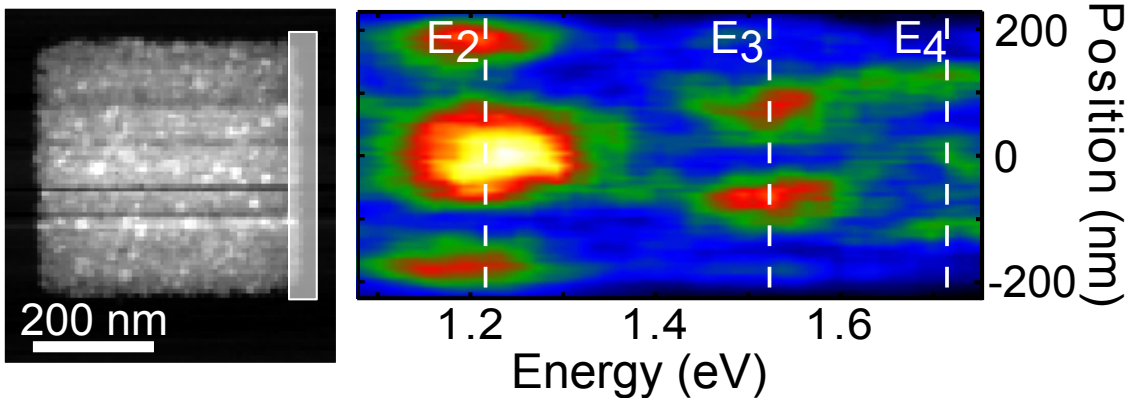

Figure 5.40: Electron energy loss spectroscopy (EELS) intensity profile (right) obtained from the region indicated in the annular dark field (ADF) image of a 430 nm nano-square (left). The profile shows the presence of three edge modes E_2, E_3, and E_4, marked by the dashed lines.

When two planar structures, such as the nano-squares are in proximity, these edge modes can couple. This coupling is responsible for the presence of peaks 6 to 10 in the spectra in Figure 5.38(a). In a nano-square, this second group of peaks could also be described as edge modes. To explain this premise, we can analyze the modes by region: In region "iii" (base of the dimer), we can distinguish two modes: mode 7 and 10, based on their number of nodes, correspond to second (E_2) and third (E_3) order edge modes at 1.25 eV and 1.53 eV respectively. In region "ii" (side of the dimer), we can only distinguish clearly one peak (mode 8) at 1.30 eV with two nodes, thus corresponding to a second order edge mode (E_2). In these two regions ("ii" and "iii") we observe two second order modes at different energies (mode 7 and 8). This difference in energy is caused by the coupling of edge mode E_2 through the corner of each nano-square on the side of the dimer (region "ii"). This weak coupling causes the apparent shift in energy with respect to the edge mode E_2 in the base of the dimer (region "iii"), which does not couple. As we will discuss later in the manuscript and in Figure 5.42, this shift in energy is an indication of mode splitting due to the coupling of modes.

A different behavior is observed in the gap of the dimer (region "i"), in this case, we observe the presence of two modes: mode 6 and 9 with node distribution that corresponds to a second order edge mode at 1.18 eV and 1.46 eV respectively. This similar node distribution indicates coupling of the second order mode of the individual squares that split into these two modes, a bonding and an antibonding mode. We will designate these modes as bonding gap edge ($BG-E$) mode and antibonding gap edge ($AG-E$) mode due to their charge distribution similar to the low order modes. Charges of opposite sign are accumulated at each edge in the gap in the

$BG - E$ mode, and charges of the same sign are localized at the edges of the gap in the $AG - E$ mode. The black line and magenta line spectra, acquired in the gap region of the nano-square dimer and shown in Figure 5.38 (a) and (c), provide more insight into the nature of these gap edge modes. We notice that mode number 6, or the bonding gap edge mode order two ($BG - E_2$), only appears in the black-line spectra, which indicates that this mode can only be excited when the electron beam is positioned over the metal on the edge of the nano-square. On the other hand, mode number 9, or the antibonding gap edge mode order two ($AG - E_2$), appears in both the black line and the magenta line spectra, which indicates that this mode is more delocalized.

In order to further understand the coupling of edge modes, we simulate the EELS response of the 420 nm nano-square dimer varying the coupling strength by changing the gap size. Figure 5.42 shows the change of the EELS spectra as a function of gap size, plotted in a temperature scale where the peaks appear as "warmer color" bands, at three different positions of the nano-square dimer. Each position, indicated by color-coded dots in black, blue and gray in Figure 5.38(c), is at the center of an edge. The spectrum at each position, as we described before, captures the three different behaviors observed in the coupling of edge modes in a nano-square dimer. The strongest coupling of edge modes is through the edges within the gap in nano-square dimers (black dot Figure 5.38(c) and region "i" Figure 5.41). Figure 5.42(a) shows how this strong coupling splits mode E_2, present in a single square, into gap modes $BG - E_2$ and $AG - E_2$, splitting that is still present for gaps as large as 150 nm in the 420 nm nano-square dimer. As the gap decreases the splitting is stronger, and we observe how the bonding modes experience a significant red shift, and that even

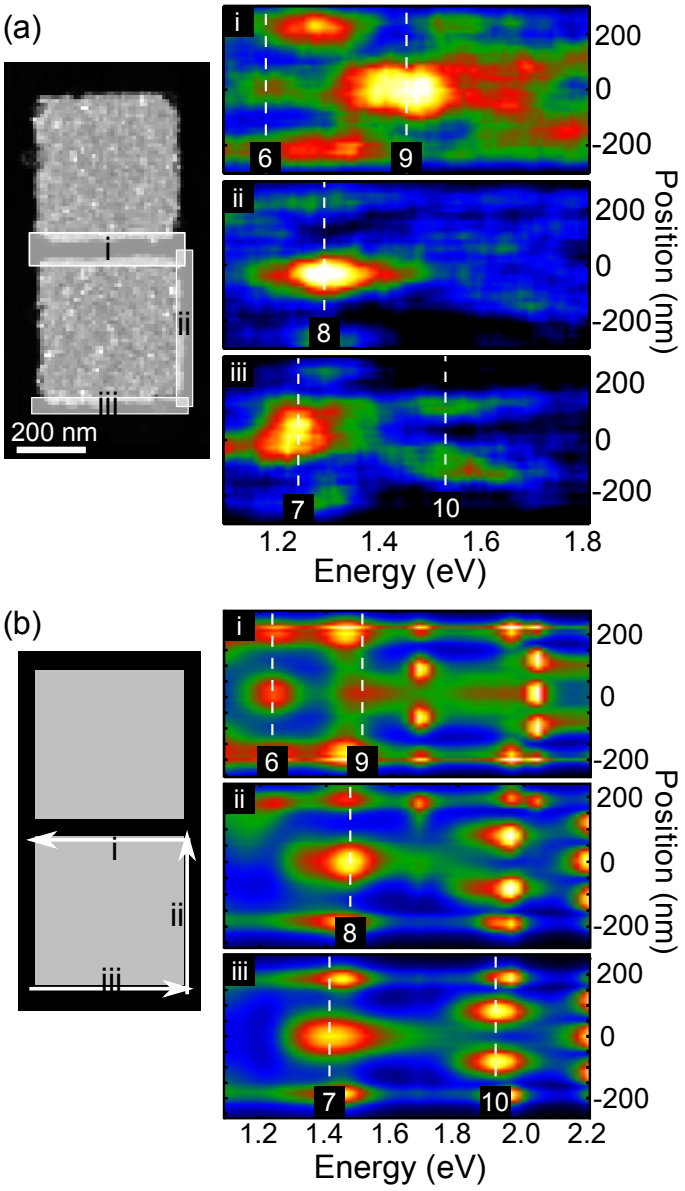

Figure 5.41: a) Experimental EELS intensity profile taken from three regions: the gap ("i"), the side of the dimer ("ii"), the base of the dimer ("iii") as shown in the ADF image of the 420 nm nano-square dimer, and (b) simulated EELS probability line profile taken from the lines (i,ii,iii) indicated in the diagram. The plasmon resonance peaks are indicated by their corresponding mode number from the spectra in Figure 5.38 and by the dashed lines. The intensity in all the EELS profiles is normalized to their maximum value.

higher order bonding modes can be observed in the analyzed energy range. Modes similar to the gap edge bonding modes were also observed in flat gap antennas and nanocubes and were denoted as transverse cavity plasmon (TCP) modes [121, 122]. Unlike the gap edge bonding modes, the antibonding modes blue shift slightly as we decrease the separation. Interestingly, the shift saturates and no change in energy is observed for small separations, as seen in Figure 5.42(a).

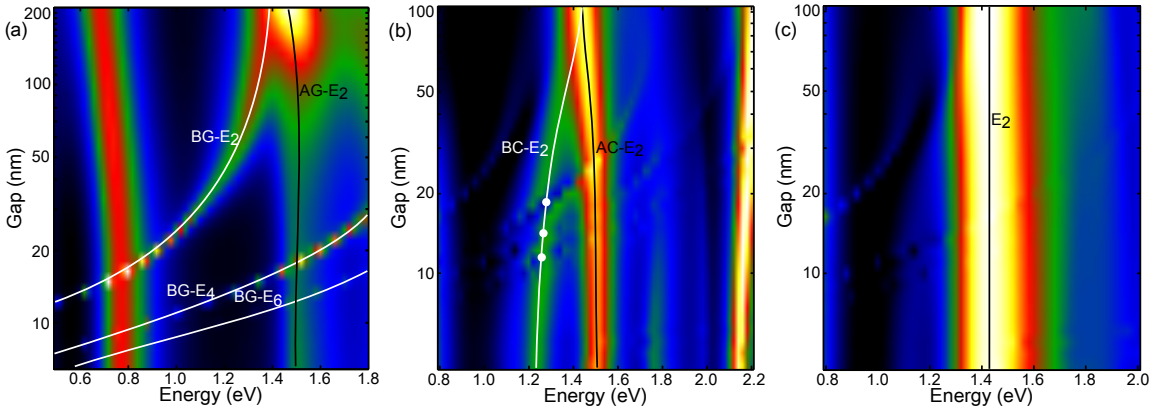

Figure 5.42: Evolution of simulated EELS spectra (shown in a temperature scale) as a function of gap size at the color-coded positions in black at the gap of the dimer (a), blue at the side of the dimer (b), and gray at the base of the dimer(c) shown in Figure 5.38(c). The three different behaviours lead to a general scheme of the coupling of edge modes in planar structures: Coupling through the edge that forms bonding gap edge ($BG-E$) modes and antibonding gap edge ($AG-E$) modes (a); coupling through the corner that forms bonding corner edge ($BC-E$) modes and antibonding corner edge ($AC-E$) modes (b), and no-coupling edge mode (E)(c). The mode around 0.75 eV in panel (a) is the anti-bonding mode formed by the left-right dipole modes in each square (aqua line). The white dots in panel (b) show the anticrossings of mode $BC-E_2$ with high order $BG-E$ modes.

A second coupling behavior is observed at the side of the dimers in the position indicated by the blue dot in Figure 5.38(c) and region "ii" in Figure 5.41. In this region, the edge modes couple through a corner. As seen in Figure 5.42(b), this

coupling is much weaker than the coupling through the edge. For the 420 nm nano-square, we can only see the effects of the coupling at gap separations under 100 nm. For gap separations above 50 nm, the coupling can only be identified as a shift to higher energies due to the higher EELS probability of the antibonding corner edge ($AC - E_2$) mode compared to the bonding corner edge ($BC - E_2$) mode, as we noted from our results in Figure 5.41. Only when we decrease the gap size below 50 nm, we can clearly distinguish the two modes, with the bonding mode red shifting and the antibonding mode blue shifting. As we continue decreasing the gap size, the resonant energy of both modes saturates. This coupling behavior is similar to the coupling of longitudinal modes in nanowires dimers [16], and the longitudinal antenna plasmon modes in nanorods [121]. In Figure 5.42(b) we can also observe the anticrossing (white dots) formed by the interaction between mode $BC - E_2$ and high order bonding gap edge modes ($BG - E$), the interaction weakens as the order of the bonding gap edge modes increases. A similar anticrossing behavior is found in gap plasmons in nanocube dimers where TCP modes interact with bonding modes [122].

The third behavior found in nano-square dimers is identified as "non-coupling", observed at the base of the dimers in the position indicated by the gray dot in Figure 5.38(c) and region "iii" in Figure 5.41. As seen in Figure 5.42(c) in this region the edge modes do not couple and behave as if the edge were isolated, and no change as a function of gap separation is observed. The three different coupling behaviors of the high order edge modes found in nano-square dimers are summarized in Figure 5.43. The identified behaviors demonstrate that coupling of edge modes in nano-squares can be analyzed by studying the coupling of neighboring edges independently, as is shown in Figures 5.41, and 5.44. Due to this independence of the coupling edge

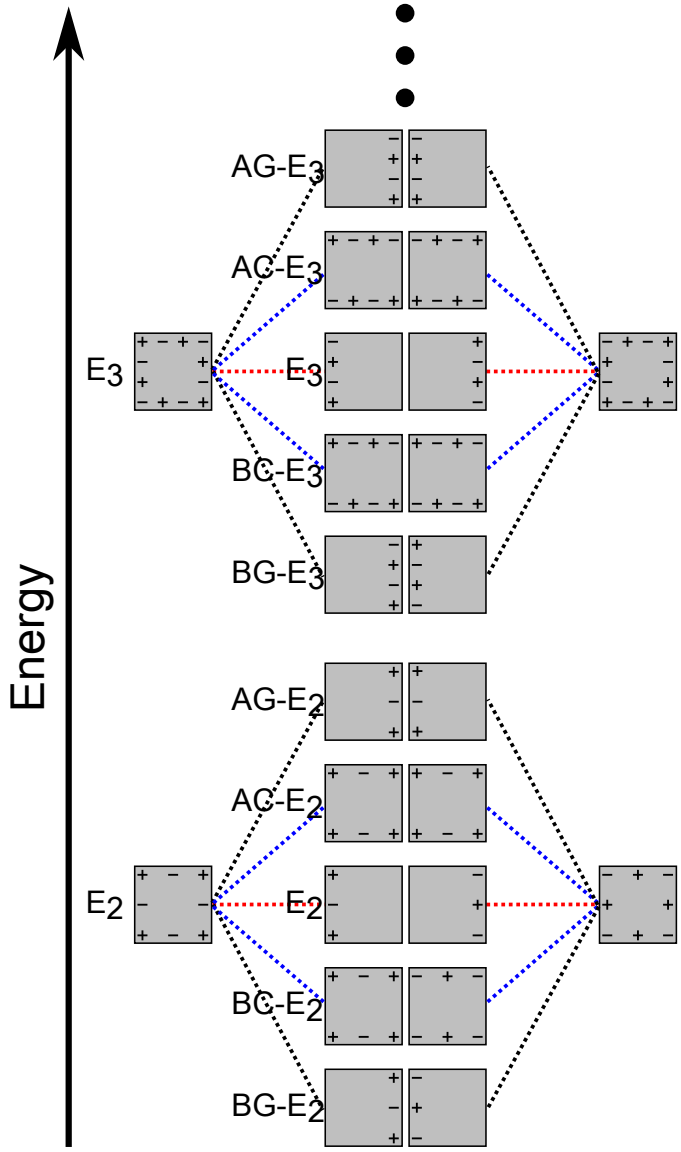

Figure 5.43: Energy diagram summarising the coupling of the high order modes or edge modes in nano-square dimers. The diagram shows the three behaviours: 1) coupling through the gap generating bonding gap edge ($BG-E$) and antibonding gap edge ($AG-E$) modes (black lines); 2) coupling through the corner generating bonding corner edge (BC-E) and antibonding corner edge ($AC-E$) modes (blue lines); 3) non-coupling in the non-interacting edge of the dimer (red lines). The relative energy positions are not to scale since the energy splitting will be determined by the coupling strength, as shown in figure 5.46.

modes, the three behaviors depicted in Figure 5.42 lead to a general scheme of the plasmonic coupling mechanisms of edge modes in planar structures.

5.1.3 Coupling of edge modes and the formation of gap modes

To test the generalization of this proposed scheme for the formation of gap edge modes found in nano-square dimers to other planar nanostructures, we investigate the coupling of edge modes supported by silver strips, which form the so-called slot waveguides. The spectrum (green curve) of a single 50 μm long, 40 nm thick, and 700 nm wide silver strip displayed in Figure 5.46 (a) shows the presence of three edge modes in this metallic slot waveguide. The first mode is identified as edge mode of order one (E_1) or the dipole mode as seen in its EELS map in Figure 5.46 (b). The second and third modes, previously studied [14], are identified as edge modes of order two (E_2) and three (E_3) as confirmed by the intensity distribution in the EELS profile measured along the edge of the strip in Figure 5.46(c)i. The features are similar to the ones found in an isolated nano-square, as seen in Figure 5.39. When two such very long metallic strips interact, their plasmon modes couple and split forming hybrid modes as indicated by the dashed lines in Figure 5.46 (a). Here, the modes present in each one of the two 50 μm long, 40 nm thick, and 700 nm wide silver strips separated by a 100 nm gap splits into two new modes.

From the spectra measured along the edge of one of the strips and over the gap, areas "iii" and "ii" in the inset in Figure 5.46(a) respectively, we observe five peaks. The first and second peak correspond to the modes formed by the coupling of mode E_1, the dipolar edge mode. The EELS map of the first peak (Figure 5.46(b) lower left panel) shows a significant localization of the intensity, proportional to the component of the electric field amplitude perpendicular to the plane of the sample [8], in each one

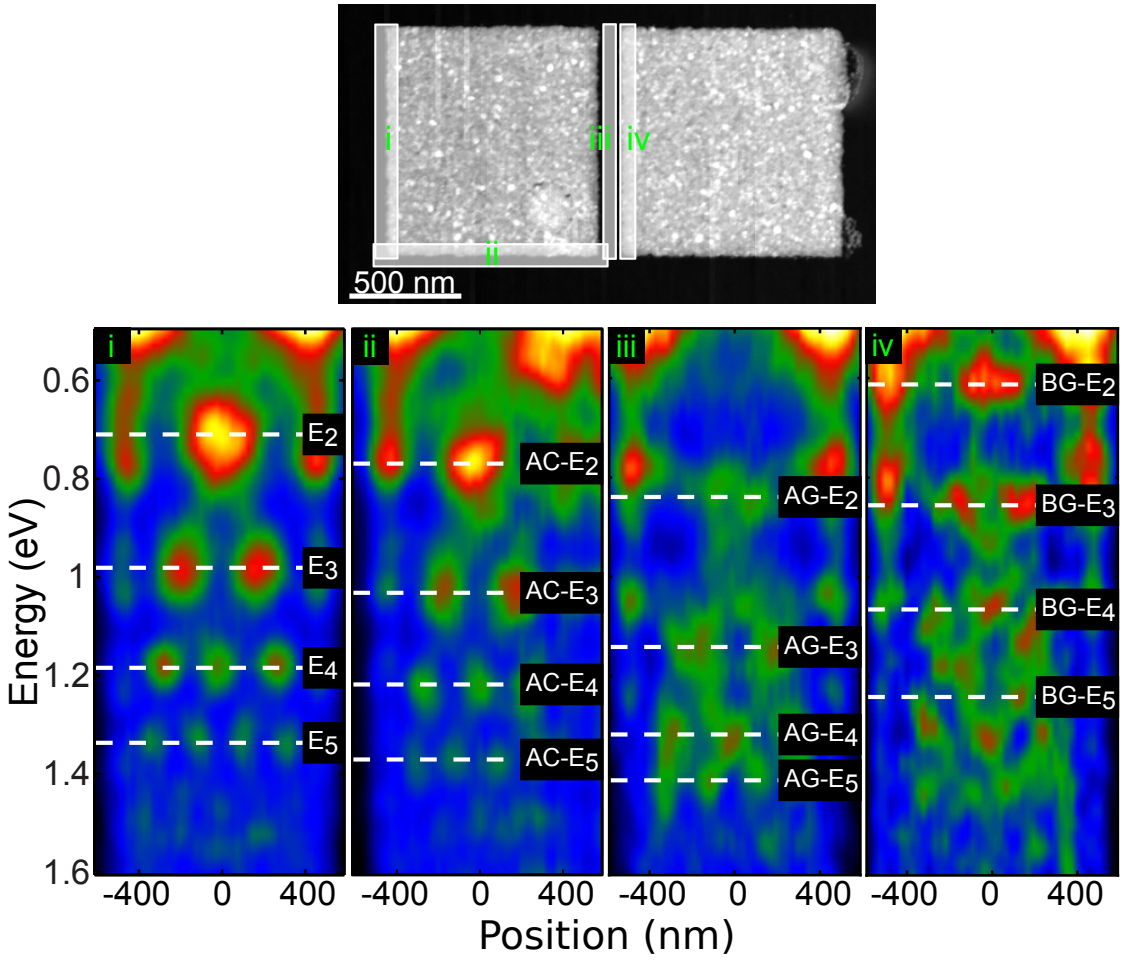

Figure 5.44: EELS intensity profile taken from the areas (i,ii,iii, and iv) shown in the ADF image of a 1 μm long and 100 nm gap square dimer on the top. The dashed lines and their corresponding mode type and order indicate the plasmon modes. We can identify the three types of behaviours found in the coupling of edge modes: the non-coupling edge in area "i"; coupling through the corner in area "ii" where only the $AC-E$ modes are observed due to the weak coupling through the 100 nm gap; and coupling through the edge or gap coupling in areas "iii" and "iv", where high order $BG-E$ and $AG-E$ modes are observed.

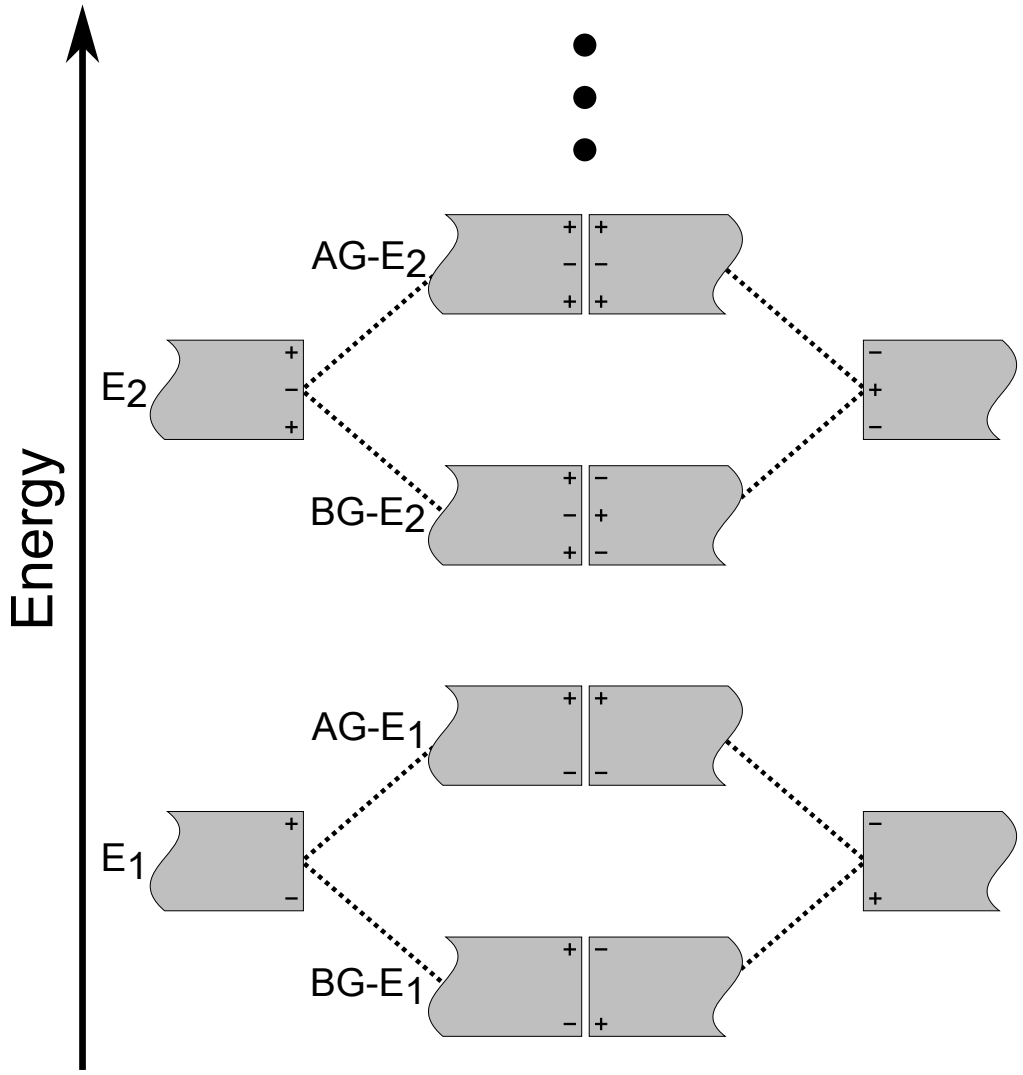

Figure 5.45: Energy diagram summarising the formation of gap edge modes in planar nanostructures. The coupling of the edge modes in slot waveguides through the gap splits an edge mode into an $AG-E$ or symmetric mode and a $BG-E$ or asymmetric mode. The relative energy positions are not to scale since the energy splitting will be determined by the coupling strength.

of the corners of the strips, with a low intensity across the gap. The map of the second mode, however, shows a significant intensity across the gap of the slot waveguide between the corners of the strips. This intensity distribution is topologically identical to the one found on the gap edge modes of the nano-square dimers. We can, therefore, recognize the first peak as the $BG - E_1$ mode and the second peak as the $AG - E_1$ mode. Similar modes were found in metal-semiconductor-metal nanorods and named gap-localized transverse modes. In that particular case, were the plasmon modes of the metal nanorods couple through the semiconductor, the order one gap edge modes are excited spectrally isolated from the other lower order modes due to the asymmetry introduced by the semiconductor in the gap [123]. Mode E_2 also splits into two modes: 1) mode $BG - E_2$, with two nodes along the edge, that can only be excited over the surface of the strip edge (area "iii" in Figure 5.46(c)); and 2) mode $AG - E_2$ that has one very intense antinode at the center of the gap as seen in the EELS profile taken from area "ii" in Figure 5.46(c). Examining the EELS profile at the same energy of mode $AG - E_2$ over the surface of the strip edge in area "iii" we note a very different intensity distribution, with three nodes, indicating the presence of mode $BG - E_3$. The two different intensity distributions indicate that two modes are overlapping at this energy range, and under our experimental conditions (35 meV effective energy resolution and large background) we cannot separate the two modes. These two modes with different field distributions can be excited due to the locality of the electron probe. They appear independently and do not interact, suggesting a strong near-field enhancement due to the overlap[121]. The coupling of mode E_3 in the strips, besides mode $BG - E_3$, also hybridize into mode $AG - E_3$ that can be excited in the gap and presents three nodes along the gap shown in the EELS

profile from area "ii" in Figure 5.46(c). The coupling of the edge modes in the slot waveguides and the formation the gap modes is summarized in Figure 5.45.

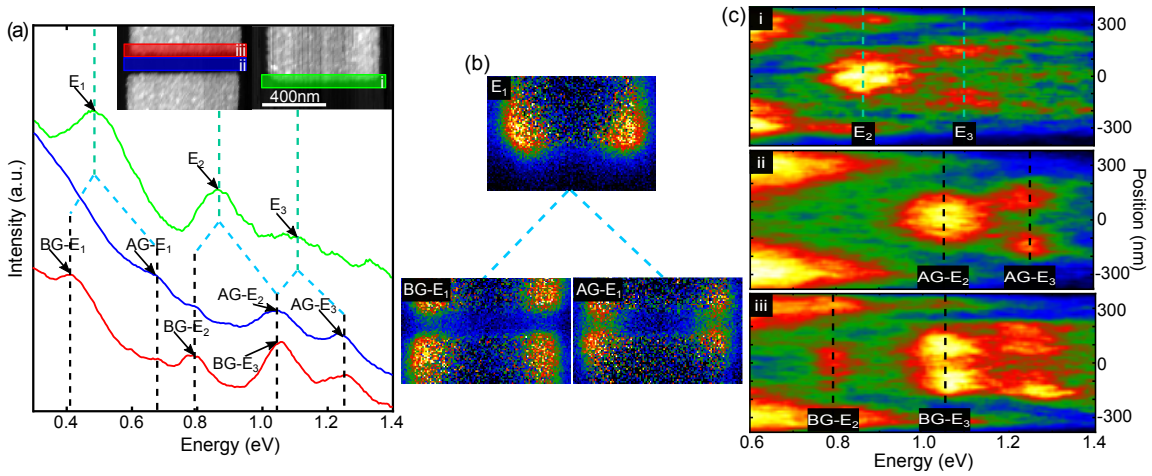

Figure 5.46: (a) Color coded EEL spectra of a 50 μm long, 40 nm thick and 700 nm wide silver strip and a slot waveguide consisting of two silver strips of similar dimension acquired in the areas marked in the ADF image in the insets. Three peaks corresponding to edge modes (E_1, E_2, E_3) are identified in the single strip. After coupling of these modes in a slot waveguide, six modes are identified as indicated by the black arrows. (b) EELS maps of the dipolar mode of the single strip and the bonding and anti-bonding modes formed by the coupling of the dipolar modes in the slot waveguide. (c) EELS profiles of the silver strip and the slot waveguide extracted from the areas indicated in the insets in (a). The maps show the localization of the modes and demonstrate the splitting due to the coupling of the edge modes.

The results from the slot waveguides, as well as from the square dimer, are consistent with the following trend: The coupling of edge modes of the same order through the edge form two types of hybridized modes. One mode with a higher probability of excitation in the gap region (antibonding) and another with a high probability of excitation in the region over the metallic surface of the structure (bonding). The field distribution of the two types of plasmon resonances, which is proportional to

the EELS intensity, resembles the field distribution of the resonances found on infinite slot waveguides with the field concentrated in the gap on the symmetric mode (antibonding mode) and the field localized on the metallic surface on the asymmetric mode (bonding mode) [124].

5.1.4 Dispersion of coupled modes in planar nanostructures

Taking advantage of the high spatial and energy resolution of EELS-STEM measurements, we can gain further insight into the nature of the bonding and anti-bonding gap edge modes and measure their dispersion relation (energy *vs* wavenumber). The dispersion relation is essential to evaluate the physical properties of the surface plasmons and to design structures with tailored properties. To measure the energy of a resonance mode, we fit a Gaussian function to the LSPR peak in the EEL spectra, and determine the wavenumber (k) by measuring the wavelength of the mode (λ_{sp}). In EELS measurements $\lambda_{sp} = 2\lambda_{EELS}$, where λ_{EELS} is the distance between antinodes in EELS profiles and maps, therefore $k = \pi/\lambda_{EELS}$ [125, 65].

Figure 5.47 shows the dispersion relation for the two types of plasmon resonances formed by coupling of edge modes obtained by measuring the energy and wavenumber from ten slot waveguides, fabricated with widths ranging from 470 nm to 1150 nm and gap sizes from 95 nm to 115 nm. We can clearly observe two distinctive dispersion relations, one for the symmetric or antibonding gap edge modes with the EELS probability confined over the gap (red symbols), and one for the asymmetric or bonding gap edge modes with the EELS probability localized on the edge of the structures (blue symbols). The dispersion of the antibonding gap edge modes is closer to the light line (gray line). Therefore these resonances are less confined and have lower propagation losses than the bonding gap edge modes, which are further away from

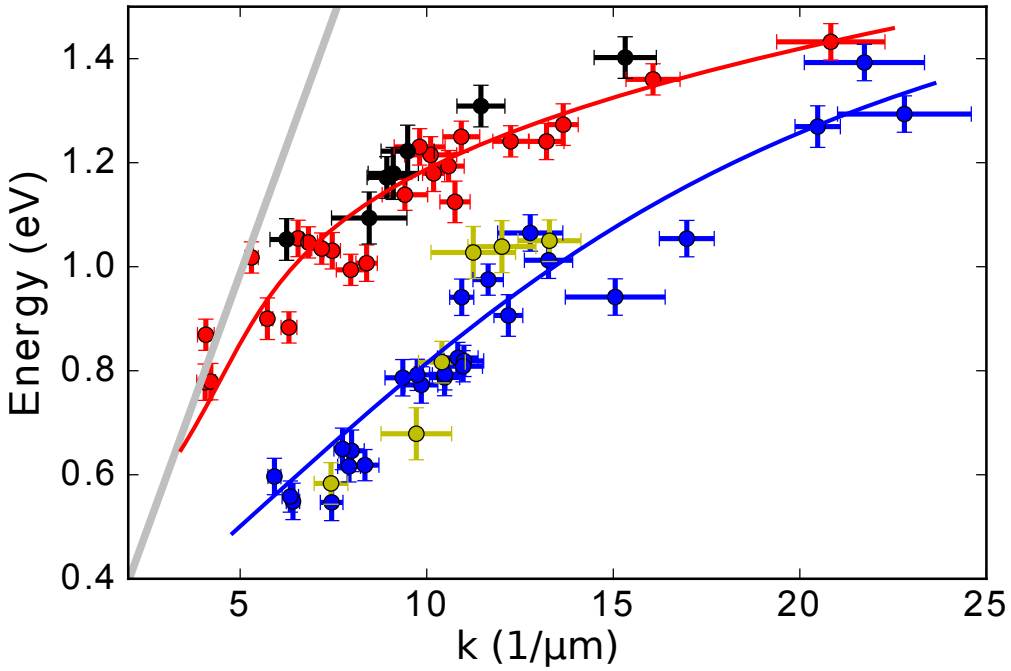

Figure 5.47: Dispersion relation of the plasmon resonances obtained from ten slot waveguides with widths ranging from 470 nm to 1150 nm. The red and blue symbols indicate the dispersion of the symmetric or $AG-E$ modes and asymmetric or $BG-E$ modes on the slot waveguides respectively. The gray line is the light line in vacuum, and the red and blue lines are guide-to-the-eye trend lines for the dispersion of the symmetric and asymmetric modes respectively. The black and yellow symbols show the dispersion relation of the symmetric or $AG-E$ modes and asymmetric or $BG-E$ modes found on the gap of three square dimers with side lengths from 630 nm to 1 μm that follows the same trend as the resonances in the slot waveguides.

the light line. The bonding gap modes are, hence, more bound to the surface of the structures exhibiting higher confinement and higher losses due to larger penetration of the field into the metal. Figure 5.47 also shows the dispersion relation of the plasmon resonances found in the gaps of three nano-square dimers with 630 nm, 850nm, and 1 μm side lengths and gap sizes from 90 nm to 100 nm. As we discussed previously, the square dimers exhibit two types of gap modes similar to the ones found in the slot waveguides: antibonding modes, which are equivalent to the symmetric modes in slot waveguides (black symbols) and bonding modes equivalent to asymmetric modes (yellow symbols) that follow the dispersion of the slot waveguides. This agreement confirms the generality of our proposed coupling scheme.

5.2 Coupling of offset parallel nanowires

In the previous section, we saw coupling of the quasi 1D edge modes for three cases: the non-coupling case, coupling through a corner and coupling through the gap. As we demonstrated in the previous section, coupling through the corner is similar to the coupling of nanowires (NWs) aligned end-to-end [16]. In a similar manner, coupling through the gap would be analogous to the coupling of parallel NWs [112]. However, one configuration remains to be analyzed: the coupling of offset edge modes. Thus, in this section, we investigate the plasmon coupling in laterally offset parallel silver NWs using STEM-EELS and complement it with simulations. Two classes of parallel overlapping NW arrays are investigated: symmetric arrays in which parallel NWs of length L that overlap by βL (Figures 5.48 and 5.51); and asymmetric arrays where one NW of length L and another of length βL are aligned at one end (Figures 5.52 and 5.54). We analyzed two values of β: 1/2 and 2/3. These two values are motivated

under the hypothesis that the coupling of a resonant plasmon mode of a selected order will be preferentially favored according to the nodal alignment of the modes in each wire. For $\beta = 1/2$ modes of an even order would be favored, and for $\beta = 2/3$ modes multiples of the 3rd order mode will be favored, as we will discuss next. The EELS spectrum images of the offset NWs are acquired with an energy dispersion of 10 meV/channel, and after deconvolution, we obtain an average effective energy resolution of 50 meV. All the energy filtered maps are integrated into energy with a window of 20 meV. Simulations of EELS spectra, energy filtered maps, and charge distributions are carried on the MNPBEM Matlab toolbox [50, 51]. The silver NWs are modeled using a tabulated dielectric function [113]. An effective dielectric function of 1.8 was used to model the dielectric environment to account for the substrate effects. The small differences between simulation and experiments are due to the absence of a fully modeled substrate in the simulation and imperfections in fabrication with wire dimensions differing from the ones of the simulations.

5.2.1 Coupling of symmetric offset nanowires

The simulated and experimental EELS spectra of the 1/2-overlapping symmetric NW array for an NW spacing d of 43 nm in the experiment and 50 nm in the simulation is shown in Figure 5.48a. The simulated NWs are 1160 nm long and 40 nm wide, while the fabricated NWs are 1148 nm long and 44 nm wide. Overlaid for comparison are the experimental and simulated spectra of a single NW (black lines). The simulated single wire has the same dimensions as the ones in the simulated array, while the fabricated single wire is 1186 nm long and 63 nm wide. Despite the difference in dimensions between the fabricated single wire and the wires in the array, the non-hybridized 2nd, 3rd and 4th order resonance modes of the single wire, shown in the spectra, serve as a

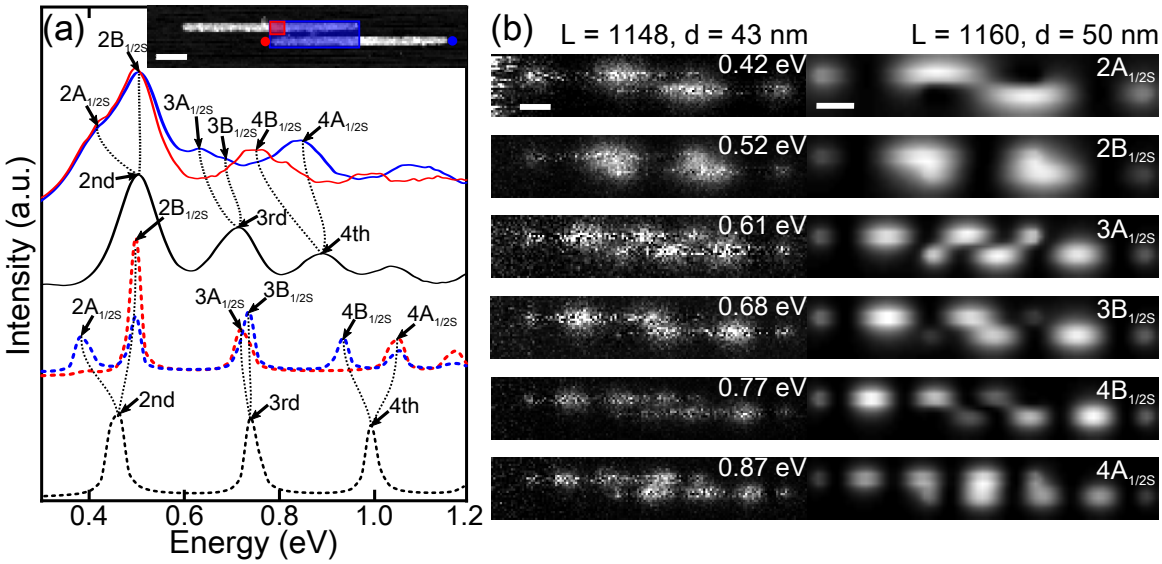

Figure 5.48: (a) Experimental (solid lines) and simulated (dashed lines) EEL spectra of 1/2-overlapping parallel NWs of length L and spaced by d (blue and red lines). The experimental spectra are acquired from the areas indicated in the HAADF image in the inset. The simulated spectra are calculated at two positions indicated in the inset. For comparison, experimental and simulated spectra of a single NW (black lines) of similar dimensions is also shown in the spectra in (a). The spectra display how the modes of order n in each NW couple and split when the offset NWs are close to each other (dotted lines), forming bonding ($nB_{1/2S}$) and antibonding ($nA_{1/2S}$). (b) Experimental (left) and simulated (right) energy filtered maps of the resonant modes supported by the 1/2 overlapping symmetric parallel NW (scale 200 nm).

reference to analyze how the modes change as they start interacting in an offset NW configuration. As we saw in the previous section [112], when a 1D mode (i.e. modes in edges of planar structures and modes in nanowires) couples through a gap, the coupling produces two modes: a bonding (B) mode with opposite or antisymmetric charge in both NWs and an antibonding (A) mode with equal or symmetric charge distribution in both NWs, as shown in Figure 5.49 for two parallel wires. To identify the modes present in the 1/2-overlapping symmetric NWs, we will follow the same description in which symmetric charge distribution between NWs corresponds to an

A mode and antisymmetric charge distribution between NWs corresponds to an B mode. In the experimental EELS spectra in Figure 5.48a we observe six hybridized modes at 0.42, 0.52, 0.61, 0.68, 0.77, and 0.87 eV with their corresponding EELS experimental and simulated energy filtered maps in Figure 5.48b. The modes at 0.42 eV and 0.52 eV can be identified as a 2nd order antibonding ($2A_{1/2S}$) and bonding ($2B_{1/2S}$) modes respectively, because of their charge distribution shown in Figure 5.50a. This is opposite to the case of hybridization of parallel NWs where the bonding mode has a lower energy than the antibonding mode [126]. The $2A_{1/2S}$ mode has a lower energy than the $2B_{1/2S}$ in the 1/2 overlapping symmetric NW array. This reversal of energy can be explained in a simplified and intuitive way if we remember from the plasmonic coupling section in Chapter 1 that the Coulombic interaction determines the energy splitting. If we analyze the induced dipoles in mode $2A_{1/2S}$, we see in Figure 5.50a that in the overlap region the dipoles are antisymmetrically aligned therefore the dipole interaction is attractive, and the resonant energy red-shifts with respect to the single NW resonance. For the $2B_{1/2S}$ the dipoles in the overlap region are symmetrically aligned, therefore the resonant energy blue-shifts. This is the opposite of what happens in parallel NWs, as shown in Figure 5.49. In the parallel wires, the dipoles are antisymmetrically aligned in the bonding mode and symmetrically aligned in the antibonding mode.

In a similar fashion, we can identify the modes at 0.61 and 0.68 as a third order antibonding ($3A_{1/2S}$) and bonding ($3B_{1/2S}$) modes respectively. Because these modes are formed by the coupling of the 3rd order mode in each NW, the geometry of the 1/2 overlapping NWs does not favor coupling as in the case of the 2nd order modes. This

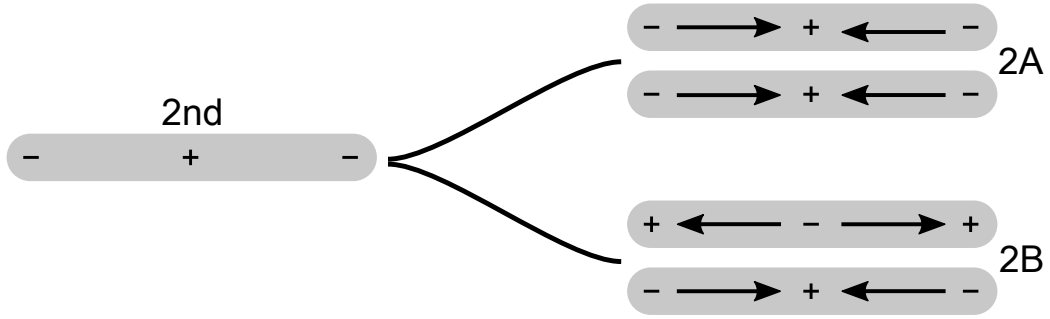

Figure 5.49: Schematic diagram of the formation of hybrid modes in parallel nanowires by coupling of plasmon resonances. The figure shows the symmetric charge distribution in the wires of the antibonding mode A mode and the antisymmetric charge distribution of the bonding mode B mode. The arrows indicate induced dipoles, which indicates if the interaction between modes is attractive or repulsive.

less favorable condition for coupling of the 3rd order modes is evidenced by the lower splitting energy of 70 meV compared to the 100 meV of the coupling of 2nd and 4th order modes in the experiment. This is even better illustrated in the simulations with a 3rd order mode energy splitting of only 20 meV compared with the 120 meV splitting for the 2nd and 4th order modes. Also, the geometric disadvantageous condition is demonstrated by the suppression in amplitude of the hybrid 3rd order plasmon resonance peaks seen in Figure 5.48a. This contrasts the expected monotonic decay in EELS plasmon resonance spectral amplitude with increasing mode order in both single and coupled wires [11, 16, 12, 65]. The resonant modes at 0.77, and 0.87 eV can be identified as bonding ($4B_{1/2S}$) and antibonding ($4A_{1/2S}$) respectively. In this case, the bonding mode is at a lower energy than the antibonding mode, which is the opposite of what we had in modes $2A_{1/2S}$ and $2B_{1/2S}$. To explain this phenomenon, the same simplified static Coulombic interaction can be applied. Analyzing the induced dipoles in mode $4B_{1/2S}$ (see Figure 5.50a), we notice that in the overlap region, the dipoles are antisymmetrically aligned and therefore the interaction is attractive resulting in

a lower energy resonant mode. For the $4A_{1/2S}$ the dipoles in the overlap region are symmetrically aligned, therefore we have a higher energy resonant mode.

The experimental and simulated EELS spectra of the 2/3-overlapping NWs is shown in figure 5.51a displaying the evolution of the modes from the independent modes in a single wire to the coupling and splitting of modes at $d = 58nm$. From the spectra we can identify six hybridized resonant modes at 0.47, 0.52, 0.63, 0.76, 0.84 and 0.92 eV. Figure 5.51b shows the experimental and simulated energy filtered maps of these modes. Following the same description used above, we can identify the modes present in the 2/3-overlapping symmetric NWs. The modes at 0.47 eV and 0.52 eV can be identified as a 2nd order antibonding ($2A_{2/3S}$) and bonding ($2B_{2/3S}$) modes respectively, as shown on their charge distribution in Figure 5.50b. The geometry of the structure, in this case, does not favor the coupling of 2nd order modes as indicated by the low splitting energy of only 50 meV. What is more, to be able to detect the first peak at 0.47 eV, we have to integrate the signal over the green region in the inset. Also, in the blue-line spectra, we cannot readily separate the peak at 0.47. To clearly separate this peak we fit two Gaussians to the integrated spectra on the blue region. After the fitting, we are able to confirm the second peak at 0.52 eV. We can also classify the modes at 0.63 and 0.76 as 3rd order antibonding ($3A_{2/3S}$) and bonding ($3B_{2/3S}$) modes respectively. Here, the geometry facilitates the coupling by direct antinode alignment of the 3rd order mode in each NW. This is reflected in a high splitting energy of 130 meV. Conversely to the hybridized 3rd order modes in the 1/2-overlapping NWs, in this case, the modes do not experienced suppression, indicating that by changing the alignment of the NWs we can control which modes are suppressed or enhanced. For the case of the 4th order modes, the disadvantageous

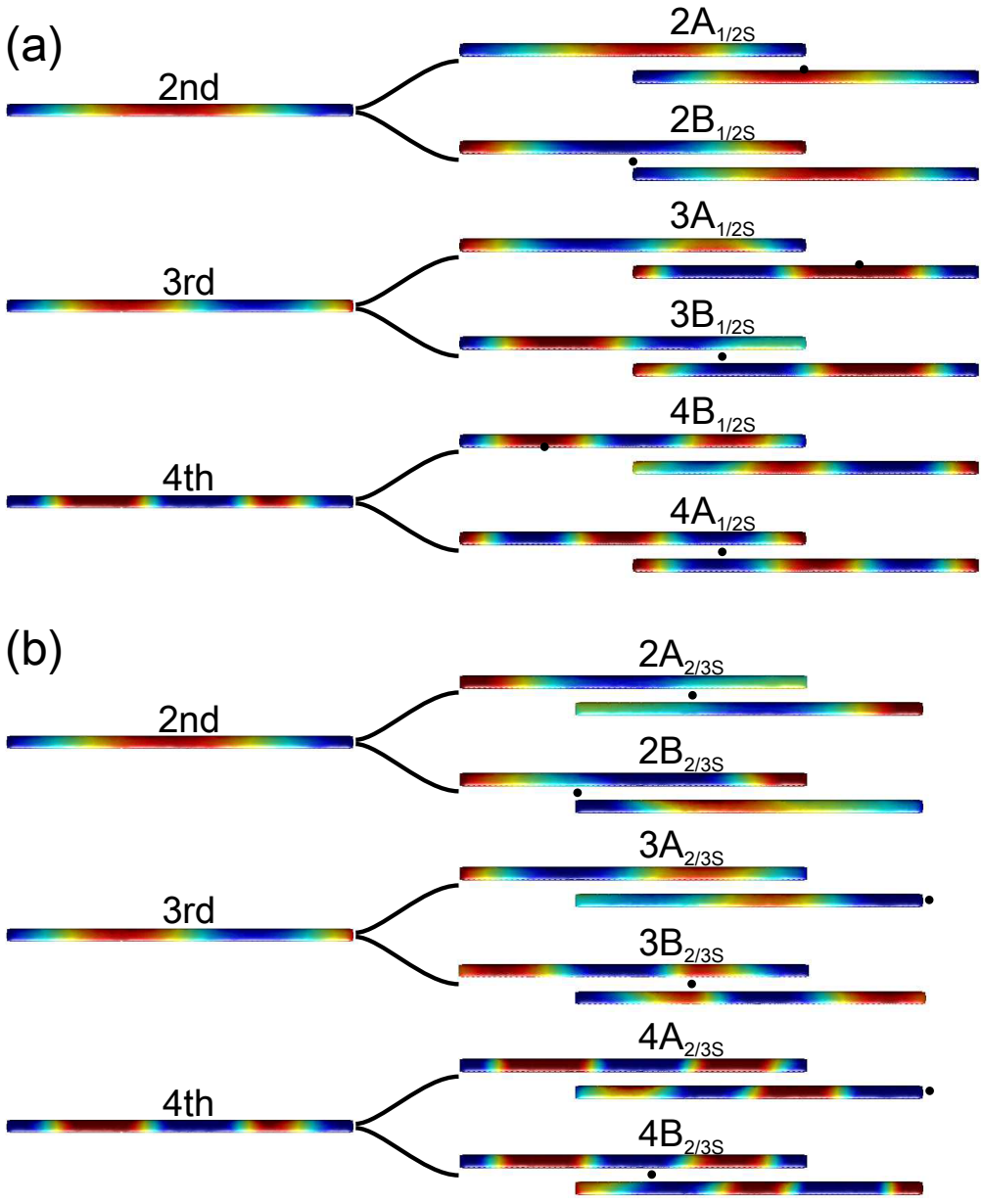

Figure 5.50: Simulated charge distribution of the modes depicting the plasmonic coupling of modes in the 1/2 overlapping symmetric NW array (a) and in the 2/3 overlapping symmetric array (b).

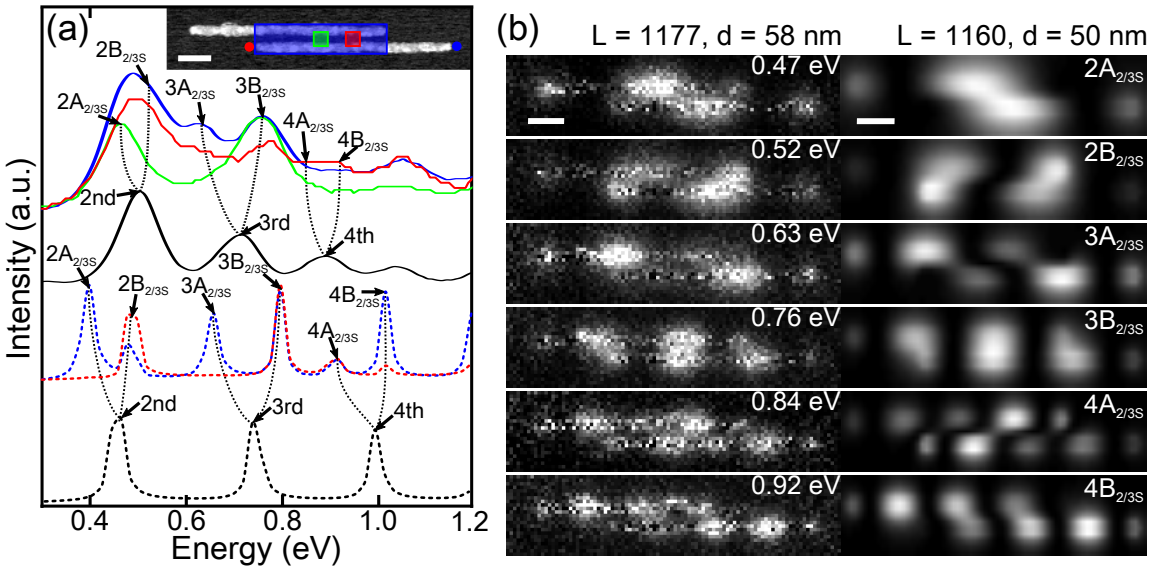

Figure 5.51: (a) Simulated (dashed lines) and experimental (solid lines) EEL spectra of the 2/3-overlapping symmetric NWs of length L and spaced by d (blue and red lines). The experimental spectra are acquired from the areas indicated in the HAADF image in the inset. The simulated spectra are calculated at two positions indicated by the dots in the inset. For comparison, experimental and simulated spectra of a single NW (black lines) of similar dimensions is also shown in (a). The spectra shows how the modes of order n in each NW couple and split when the offset NWs are close to each other (dotted lines), forming bonding ($nB_{2/3S}$) and antibonding ($nA_{2/3S}$). (b) The experimental (left) and simulated (right) energy filtered maps of the resonant modes supported by the 2/3 overlapping symmetric NWs are also shown (scale 200 nm).

geometry that suppress these modes makes it difficult to identify the peaks from the spectra in 5.51a. We are able to detect these peaks separated by 80 meV by Gaussian fitting on the signal integrated over the red region. In this way, we can identify the 4th order resonant modes as antibonding ($4A_{2/3S}$) and bonding ($4B_{2/3S}$) at 0.84, and 0.92 eV respectively. These results suggest that it is possible to promote or suppress the coupling of a particular mode by changing the overlapping length. What is more, it is feasible to reverse the energetic order of the bonding and antibonding modes.

5.2.2 Coupling of asymmetric offset nanowires

Figure 5.52a shows the experimental and simulated EELS spectra of the asymmetric 1/2-overlapping array comprised of two NWs with dimensions specified in in Figure 5.52b. The experimental spectra are acquired over the two regions shown in the inset, while the simulated spectra are calculated at the positions indicated by the dots in the inset. For comparison the figure includes the simulated spectrum of two isolated NWs with lengths of 1160 nm (black line) and 580 nm (gray line).The fabricated isolated long wire is 1186 nm long and 63 nm wide, while the short isolated wire is 595 nm long and 55 nm wide. As in the case of symmetric arrays, we will describe the modes as bonding B and antibonding A according to their charge distribution. However, in this case, the interaction is not between equal modes, as was the case of the symmetric array. Here the coupling is between a high order mode in the long wire and a low order mode in the short wire. Therefore, for the designation of bonding or antibonding, we will use as a reference the charge distribution of the short wire. If the charge distribution in the long wire is equal or symmetric to the short wire we have an antibonding mode, if the charge distribution is opposite or antisymmetric we have a bonding mode. In addition, because we have interaction of modes of different

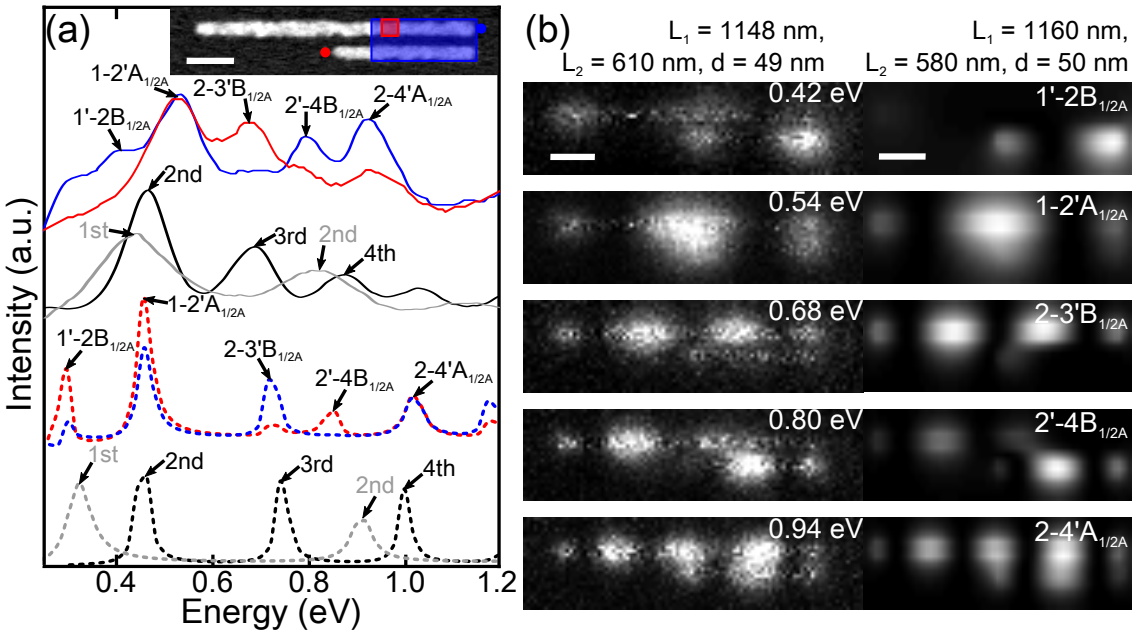

Figure 5.52: (a) Simulated (dashed lines) and experimental (solid lines) EEL spectra of the 2/3-overlapping asymmetric NWs spaced by d (blue and red lines). The experimental spectra are acquired from the areas indicated in the HAADF image in the inset, and the simulated spectra are calculated at two positions indicated by the dots in the inset. For comparison, experimental and simulated spectra of isolated long (black lines) and short (gray line) NWs of similar dimensions as the ones in the array are also shown in (a). (b) Experimental (left) and simulated (right) energy filtered maps of the resonant modes supported by the 1/2 overlapping asymmetric NWs (scale 200 nm).

orders, the coupling does not only depends on the geometrical alignment but also in the spectral overlap of the modes. In the asymmetric 1/2-overlapping array the geometry is chosen such that the 2nd order mode in the longest NW and the 1st order modes of the adjacent NW, and multiples there of, will be aligned and the coupling promoted. However, due to retardation effects, the spectral overlap is not guaranteed, hindering the coupling. Considering this, we can identify the five modes at 0.42, 0.54, 0.68, 0.80 and 0.94 eV shown in the spectra and the energy filtered

maps in Figure 5.52. From the simulated and experimental energy filtered map of the first mode at 0.42 eV, we can see that the mode is dominated by 1st resonant mode of the short wire. However, in the simulation, the presence of the long wire produces a 20 meV red-shift of the mode compare to the 1st resonance in the isolated small wire, which is evidence of coupling between wires. This coupling is also illustrated in the charge distribution in Figure 5.53. In the experiment, we cannot quantify the shift due to coupling reliably since we do not have isolated wires with exactly equal dimensions as the ones in the fabricated array. The geometrical imperfection of the fabricated NWs might enhance or hinder the interaction of the modes in the array. For example, if the alignment is kept by fabricating the small wire exactly half the length of the large wire and spectral overlap is increased by changing the width of one of the wires, the coupling strength would increase. Despite the small coupling strength, the charge distribution of this mode displays an asymmetric alignment of the 1st mode of the small wire and the 2nd mode of the long wire, as seen in Figure 5.53. Based on this description of the mode at 0.42 eV we will denote it $1' - 2B_{1/2A}$. The first number describes the coupling mode in the short wire, the second number is the coupling mode in the long wire, the apostrophe indicates the dominant mode, the letter represents the charge distribution, and "$1/2A$" indicates the 1/2-overlapping asymmetric geometry.

Following the nomenclature from above, we can identify the mode at 0.54 eV as $1 - 2'A_{1/2A}$, indicating that the second mode of the long NW is the dominant mode and the alignment of the charge distribution is symmetric. In the simulation, the effect of coupling in this mode is negligible with no energy shift experienced by the dominant mode in the array compared to the isolated wire. Since we do not know the

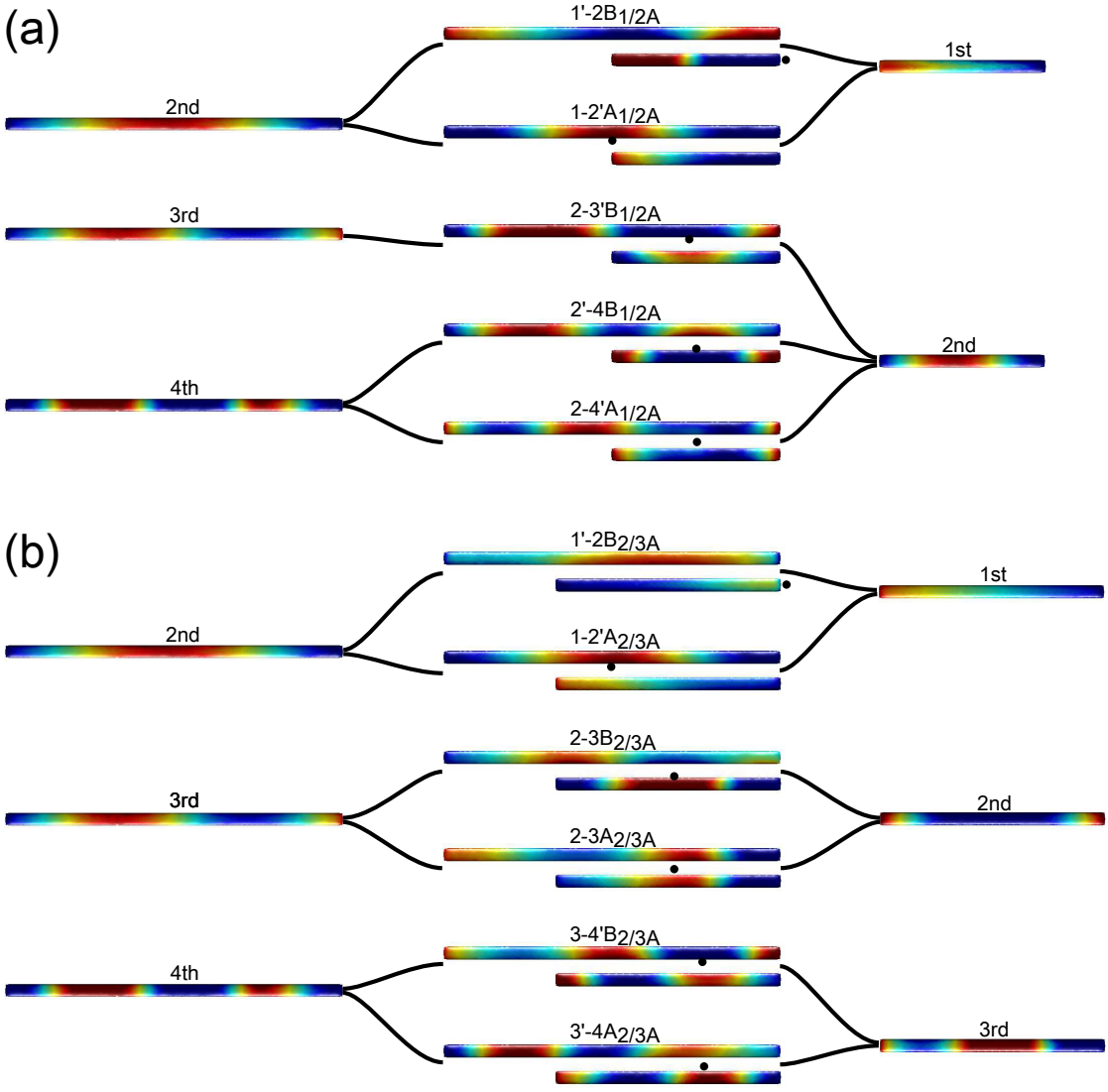

Figure 5.53: Simulated charge distribution of the modes depicting the plasmonic coupling of modes in the 1/2 overlapping asymmetric NW array (a) and in the 2/3 overlapping asymmetric array (b).

exact value of the resonant energy of the isolated structures in the experiment, we cannot comment on the coupling strength of this mode. However, even with no energy shift present in the simulation, the charge distribution of this mode corresponds to an antibonding mode when the electron probe is located on a high probability position, as shown in Figure 5.53. The mode at 0.68 eV is identified as the $2-3'B_{1/2A}$. This mode is formed by the very weak interaction of the dominant 3rd mode of the long wire and the 2nd mode of the short wire. This weak coupling is a result of the geometric misalignment of the structure and the lack of spectral overlap between modes. The modes at 0.80 and 0.94 eV can be identified as $2'-4B_{1/2A}$ and $2-4'A_{1/2A}$ respectively, as shown by the charge distribution in Figure 5.53. Although there is a dominant mode in each one this $2-4$ modes, the coupling strength is much stronger than in the other analyzed modes in this structure. This stronger coupling can be attributed to the nodal alignment between the 2nd mode of the short wire and the 4th mode of the long wire created by the geometry, and to the greater spectral overlap between these modes compared to the overlap of the other modes. The stronger coupling can also be measured by the energy shift of the coupled modes. In the simulation, mode $2'-4B_{1/2A}$ experiences a red-shift of 60 meV compared with the 2nd mode of the isolated short wire and mode $2-4'A_{1/2A}$ is blue shifted by 30 meV compared with the 4th mode of the isolated long wire. The modes analyzed in the 1/2 overlapping asymmetric structure can be considered intermediate states between a fully hybridized mode as the ones shown in the symmetric geometry and an independent mode in isolated wires.

In the asymmetric 1/2 overlapping array, the geometry facilitated the coupling of even modes. In the asymmetric 2/3 overlapping arrays, the geometry favors the

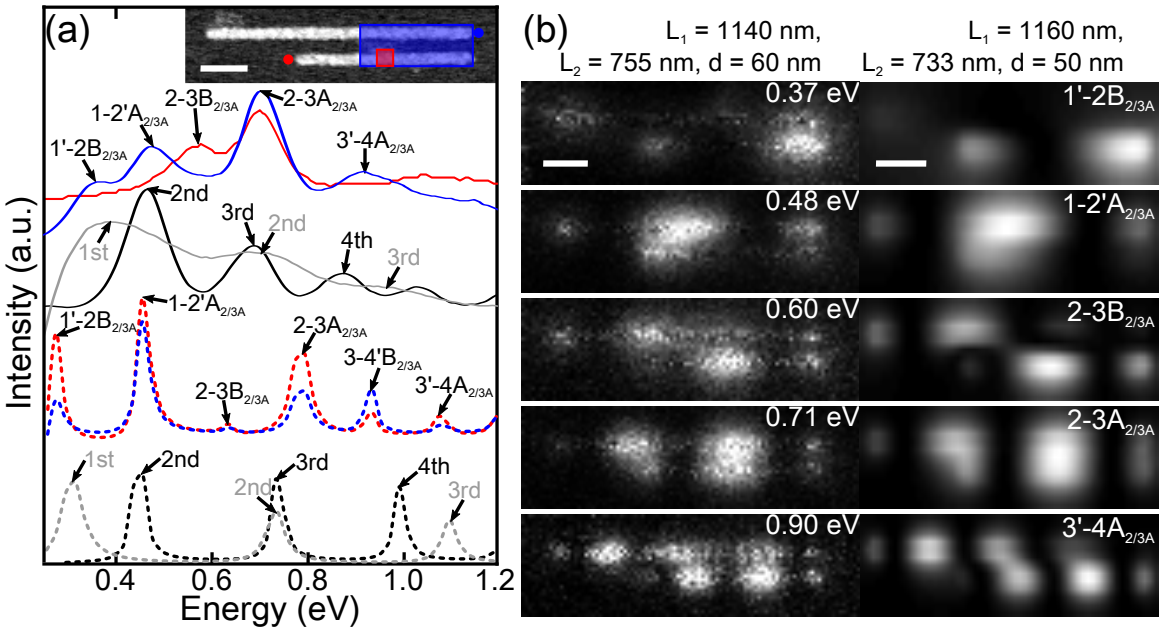

Figure 5.54: (a) Experimental (solid lines) and simulated (dashed lines) EEL spectra of the 2/3-overlapping asymmetric NWs spaced by d (blue and red lines). The experimental spectra are acquired from the areas indicated in the HAADF image in the inset, and the simulated spectra are calculated at two positions indicated by the dots in the inset. For comparison, experimental and simulated spectra of isolated long (black lines) and short (gray line) NWs of similar dimensions as the ones in the array are also shown in (a). (b) Experimental (left) and simulated (right) energy filtered maps of the resonant modes supported by the 2/3 overlapping asymmetric NWs (scale 200 nm).

alignment of the antinodes of the 3rd resonance in the long NW with the 2nd order mode of the short wire. The simulated and experimental EELS spectra of the 2/3 asymmetric array are shown in Figure 5.54a for NWs spaced by 60 nm. From the spectra we can identify five peaks at 0.37, 0.48, 0.60, 0.71, and 0.90 eV corresponding to plasmon resonances with their experimental and simulated energy filtered maps shown in Figure 5.54b. Following the nomenclature described above, we identify the first mode at 0.37 eV as $1' - 2B_{2/3A}$. This mode is dominated by the 1st mode of the short NW which is weakly interacting with the 2nd mode of the long NW. Although the geometry and the spectral overlap are disadvantageous for the coupling, a small interaction is still present inducing an antisymmetric alignment of the charges in the NWs, as shown in Figure 5.53. The coupling also creates a red-shit of 30 meV in the simulation of this mode compared to the 1st mode of the isolated short wire. The mode at 0.48 eV is identified as $1 - 2'A_{2/3A}$ and no energy shift with respect the 2nd mode of the isolated long NW is observed due to coupling in the simulation. The modes at 0.60 and 0.71 eV are identified as $2 - 3B_{2/3A}$ and $2 - 3A_{2/3A}$. Notice that in the denomination of these modes we have not included an apostrophe indicating a dominance of one particular mode. This lack of dominance of one particular mode is produced by the favorable antinodal alignment of the asymmetric 2/3-overlapping geometry and the perfect spectral overlap, shown in the simulated spectra, with equal resonant energies of the 2nd and 3rd modes of the short and long NWs respectively. This lack of dominance can be seen in the energy filtered maps in 5.54b, where we notice that the loss probability of these modes is localized in both NWs and there is not a preferential excitation of one particular NW as was the case of modes $1' - 2B_{2/3A}$ and $1 - 2'A_{2/3A}$. The advantageous configuration of this asymmetric array that favors

the formation of the $2-3B_{2/3A}$ and $2-3A_{2/3A}$ modes is also reflected in the coupling strength which can be quantified by the energy shift of these modes compared with the energies of the resonant modes in the isolated wires. From the simulations, we obtain an energy shift of 120 meV for mode $2-3B_{2/3A}$ and an energy shift of 40 meV for mode $2-3A_{2/3A}$ which amounts to a total energy splitting of 160 meV. These values are comparable with the energy shifts in the symmetric arrays, for example, in the 2/3 overlapping symmetric array the coupling of 3rd order modes causes an energy splitting of 140 meV, and in the 1/2 overlapping symmetric array, the coupling of 2nd order modes produces an energy splitting of 120 meV. This result shows that by careful tuning of the nodal alignment and spectral overlap of the modes it is possible to enhance the coupling of selected modes on NWs of different lengths. Finally, the peak at 0.90 eV is identified as mode $3'-4A_{2/3A}$. In the simulation, the interaction of the 3rd mode of the short wire and the 4th mode of the long wire creates two modes $3-4'B_{2/3A}$ and $3'-4A_{2/3A}$. However, in the experiment, we did not find the $3-4'B_{2/3A}$ mode that in the EELS simulated map is strongly dominated by the 4th mode of the long wire (not shown). The absence of this mode might be caused by further misalignment in the fabricated structures, considering that the short wire is larger than 2/3 of the long wire. The results show the level of control that is possible to obtain by the coupling of plasmonic structures. Such a level of control can also be found in plasmonic heterodimers [127], however the fabrication of structures with multiple materials requires multi-step lithography, and in comparison the proposed approach is done with structures of the same material simplifying the fabrication process.

5.3 Conclusions

The coupling of plasmon resonances is a promising method for tailoring plasmonic properties of nanostructures. In this Chapter, we have used the high spatial and energy resolution of an STEM-EELS system to analyze, in depth, the coupling mechanism of edge modes in planar nanostructures including nano-squares, slot waveguides, and offset nanowires. We have shown that the coupling can be understood by a simple and intuitive scheme based on three distinct behaviours: 1) A strong coupling through the edge of the nanostructure that forms modes denominated bonding gap edge modes and that experience a significant red shift as the gap size decreases, and antibonding gap edge modes that blue shift until convergence for small gap separations; 2) a weaker coupling through a corner, that forms bonding and antibonding corner edge modes similar to the ones found in coupling of nanowires; 3) a non-coupling behaviour where the edge of the nanostructure behaves independently of the rest of the structure and no coupling is observed.

We further studied the formation of gap edge modes in offset nanowires. We have shown that by careful tuning of the nodal alignment by changing the overlapping length in offset nanowires of equal length, it is possible to promote or suppress the coupling of a particular mode. We have also shown that by the adjustment of the offset we can control the energy of the bonding or antibonding modes to the level where we can even reverse the energetic order of this modes. In this Chapter, we have also demonstrated that the coupling of edge modes in NWs of different lengths is possible. In this asymmetric NW arrays, two factors play a role in determining the coupling strength: the nodal alignment and spectral overlap of the interacting modes. The results indicate that it is possible to enhance the coupling of selected modes by

tuning these two parameters. The analysis of the asymmetric NW arrays also showed that it is feasible to control the coupling in order to create modes in which a mode of a selected wire dominates the optical response. This study proves that plasmonic coupling is a very versatile tool to modify the optical response of plasmonic systems. What is more, here we showed a complete picture of plasmonic coupling on planar structures, and provide simplified design rules to aid in the design of future plasmonic devices compatible with planar industrial fabrication methods.

Chapter 6

Surface Plasmons on Fractal Structures

The use of fractal geometries has significantly impacted many areas of science and engineering. One such area is antenna design, where fractal geometries are often utilized in portable communication devices for their compact, broadband characteristics [128]. The term fractal, that was popularized by the work of Mandelbrot [129], is used to describe curves (most commonly in 2 dimensions) that present repeating patterns (exact, quasi or statistical self-similarity), at all scale, often obtained by iteratively applying some transformation on a system. This particular property as well as their ability to compactly fill space makes fractals ideal candidate for broadband antennas and they have indeed inspired the design of several macroscopic antennas that exhibit broadband behavior and improved performance in the GHz regime [130, 131, 132, 133, 134, 135].

In recent years, interest in a new type of antenna based on surface plasmon resonances, designed to operate at visible light frequencies, has been motivated by potential applications in sensing [136], imaging [137], energy harvesting [28], and disease prevention and cure [138], as we saw in previous chapters. These so-called "optical antennas" have characteristic dimensions at nanometer-length scales, requiring nanometer precision for their fabrication and characterization. With improved nanofabrication tools, including focused ion beam and electron beam lithography (EBL), nano-fabrication is becoming increasingly feasible. Early prototype structures studied include dipole [139], gap [122, 140], bowtie [141] and Yagi-Uda [142] antennas. The nanoscale dimensions of optical antennas call for demanding characterization requirements, and experimental techniques that can image beyond the optical diffraction limit are necessary for the detailed study of sub-wavelength field confinements in optical antenna structures. Electron energy loss spectroscopy (EELS), performed in a scanning transmission microscope (STEM), is one of the few techniques which meets these requirements, capable of sub-nm spatial resolution and a spectral resolution exceeding 100 meV [82, 143]. The STEM-EELS technique has been used successfully to map optical excitations in a variety of nanostructure geometries, including triangular prisms [10], rods [12, 60], wires [11], cubes [60], among others [144, 75, 79, 67, 76, 145, 64, 127].

Early studies of optical fractal antenna designs, including the Cayley tree [146], Sierpinski fractals [147, 148, 149] and other fractal geometries [150, 151], suggest that broadband absorption can be achieved in fractal plasmonic nano-antennas. In this work, we study the Koch snowflake fractal geometry. A Koch fractal is constructed

by starting with an equilateral triangle (iteration 0) and repeating the following procedure iteratively: Divide each line segment of the structure into three segments of equal length, then, place an equilateral triangle pointing outward in the central segment in each line (the central segment is the base of the triangle). The fractals are organized by the number of times the described procedure was applied (iteration). We use EBL to fabricate a set of nanoscale fractal antennas on 50 nm thick silicon nitride membranes, and STEM-EELS is used to image the optical excitations supported by the structures. The high spatial resolution achieved with STEM-EELS allows us to visualize the multiple plasmonic modes supported by the fractal structures, to analyze structural origin of the modes present, and to study the effect of self-similarity by comparing the response of different fractal geometry iterations. The experimental results are complemented with numerical calculations of both EELS spectra and eigenmode using a full wave surface integral equation method [152, 153] performed by collaborators at the Nanophotonics and Metrology Laboratory in the École Polytechnique Fédérale de Lausanne - Switzerland. The simulations consider a homogeneous medium surrounding the structure, with a permittivity of $\epsilon = 1.8$ to account for the substrate influence. A Drude model was used for the permittivity of Ag with a plasma frequency of 9.3 eV, losses of 0.03 eV and $\epsilon_\infty = 4.3$. In this Chapter, we show that resonances in a complex geometry such as the Koch snowflake fractal follow simple scaling rules based on the number of characteristic edges found in the structure. These scaling rules can be used in the design of fractal antennas for applications in sensing and compact nanophotonic architectures.

To analyze the effect of self-similarity on the spectral response of metallic nanoantennas, we fabricated silver Koch snowflake fractal antennas of iteration 0, 1 and

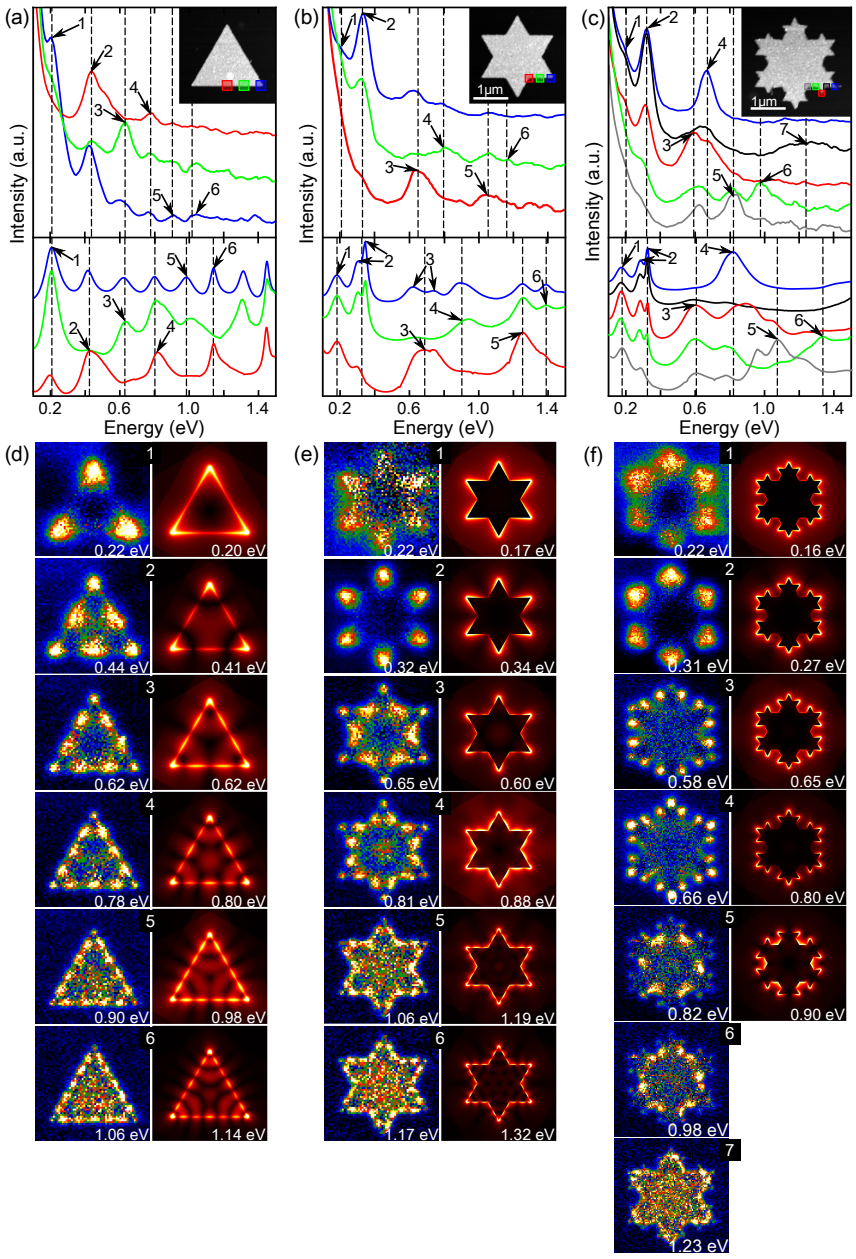

Figure 6.55: Experimental (top) and simulated (bottom) EEL spectra of Koch fractal antennas of iteration 0 (a), 1 (b), and 2 (c) acquired at the color-coded positions indicated in the ADF image in the insets. The arrows indicate the peaks corresponding to resonant edge modes. Experimental EELS maps and simulated nearfield intensity distribution of the modes found in the Koch fractals of iteration 0 (d), 1 (e), and 2 (f). The energy indicated in the nearfield intensity map is the one of the eigenmode, not the energy of the peak in the EEL spectra.

2, as shown in the insets in Figure 6.55. The iteration 0 structure has a side length of 2 μm, and all iterations have a thickness of 30 nm. The spectral response is characterized using an FEI-Titan system equipped with a monochromator and EELS spectrometer as described in Chapter 2. To further improve the energy resolution we performed the deconvolution procedure described in Chapter 3 [106], achieving an effective energy resolution of up to 30 meV in our spectrum images. EELS simulations of the Koch fractal structures are performed to correlate the experiments. Figure 6.55a,b,c shows the experimental (top) and simulated (bottom) EELS spectra of the fractal structures obtained at several positions indicated by the color-coded boxes in the insets. Overall, although the background in the experiment is high due to the tails of the zero-loss peak, we observe a good agreement between the simulation and the experiment with plasmon peaks and energies well reproduced. The increasing difference of the peaks energy between experiment and simulation is assumed to be due to the absence of the substrate in the simulations, whose influence can change with increasing mode energy, as well as possible deviations of the actual Ag permittivity from the Drude model used. The spectral response of each structure shows several surface plasmon resonances with a first resonant peak shown as a shoulder of the zero-loss peak tails at approximately the same energy (0.22 $\pm$ 0.04 eV) for all the iterations of the Koch fractal behavior. The presence of these peaks is confirmed in the well-resolved simulations.

6.1 Edge modes and Koch fractal iteration zero

As previously described, the resonances in a planar structure can be described as quasi one-dimensional resonances (edge modes) along the edge of a structure [76, 14,

77, 111]. An edge mode of order m is noted E_m, m being the number of nodes along the edge. Also, edge modes can be designated odd and even to describe odd or even number of nodes m (or equivalently opposite or identical charges at extremities). In a nanostructure, the edge modes will form eigenmodes according to the symmetry of the structure. Based on the symmetry of the Koch fractal structures, we will designate the eigenmodes symmetric or antisymmetric depending on their charge distribution having symmetric or antisymmetric mirror symmetry with respect to the vertical axis. Due to the structure symmetry, each eigenmode having only the mirror symmetry (symmetric or antisymmetric) will implicitly exist 3 times. Since it does not bring any additional information, this "degeneracy" will not be mentioned further on, and the term degeneracy will only refer to eigenmodes having the same energy but different charge distribution that cannot be matched by mirror or rotation operation. EELS maps also follow the structure symmetry because the signal is obtained by exciting and probing at the same location, the simplest example being the resonances of a nanodisk that appear like concentric rings [63], thus for Koch snowflake fractals EELS maps always appear C_3 symmetric. To be able to better identify the eigenmodes to the EELS map, the electric nearfield intensity of each eigenmode is "symmetrized" by adding itself three times with rotation of 0°, 120° and 240°. Interestingly we observe that degenerated eigenmodes give the same symmetrized nearfield map.

Following this description, we can identify the modes present in the equilateral triangle (Koch fractal iteration 0). Figure 6.55(d) shows energy filtered EELS maps and the simulated, symmetrized, electric nearfield intensity distribution of the eigenmodes of iteration 0. The first resonant peak at 0.22 ± 0.03 eV and its associated

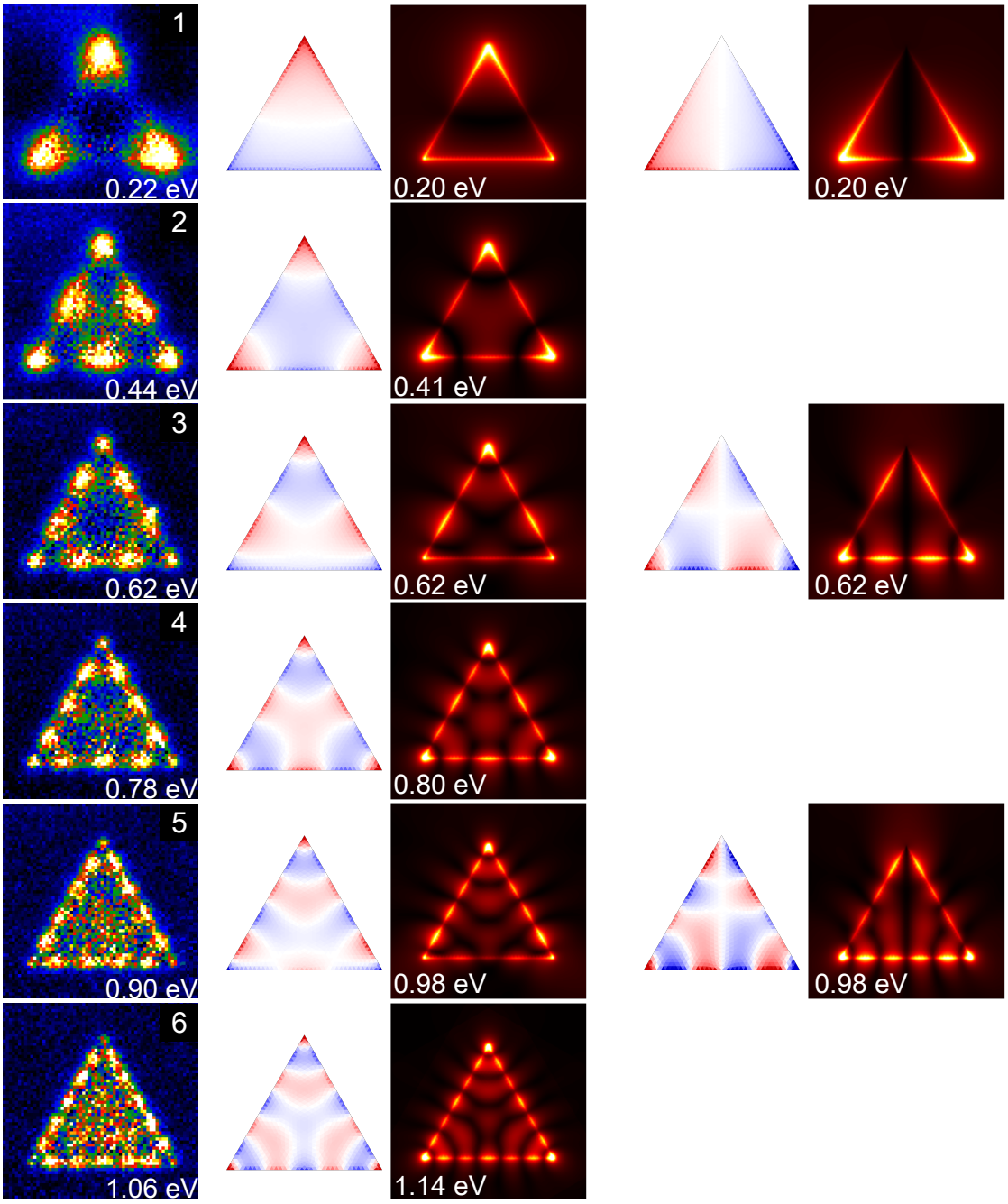

Figure 6.56: Measured energy filtered maps of the Koch snowflake fractal iteration 0 and their corresponding calculated eigenmodes and their near-field distribution. The numbers correspond to the EELS peaks in Figure 6.55a.

map correspond to a dipolar eigenmode or edge mode order one (E_1), as the surface charge distribution of the eigenmodes associated to this peak shows in Figure 6.56. The higher order eigenmodes display the characteristic node distribution of quasi one-dimensional edge modes, and they can be identified as edge modes order two (E_2), three (E_3), four (E_4), and five (E_5) at 0.44 eV, 0.62 eV, 0.78 eV, 0.90 eV, and 1.06 eV respectively (with an effective energy resolution of 30 meV). In the surface charge distribution of the eigenmodes shown in Figure 6.56, we observe that all three edges of the triangle in eigenmodes E_2, E_4 and E_6 (even edge modes) display a charge distribution corresponding to a one dimensional mode of the same order. For the case of E_1, E_3 and E_5, two degenerate eigenmodes are present: one in which two edges have the same charge distribution (symmetric eigenmode); and another mode in which only one edge exhibits the charge distribution corresponding to a one dimensional edge mode. We note that the two other edges have opposite charge distribution sign relatively to each other (antisymmetric eigenmode). Equivalently we can observe that eigenmodes E_2, E_4 and E_6 follow the same C_3 symmetry as the triangle, whereas other eigenmodes only have the mirror symmetry with degeneracy two (antisymmetric and symmetric respectively to the vertical axis). Based on the symmetry of the triangle, the formation of two degenerate eigenmodes for odd edge modes is understandable. Because in all odd edge modes the charge at the extremities of the edge (the triangle corner) must be opposite, and in a triangle only two edges at maximum can fulfill this constraint at the same time, the odd edge modes therefore split into the symmetric and antisymmetric degenerate edge modes. The surface charge distribution of the eigenmodes of iteration 0 confirms that it is possible to describe them as quasi one-dimensional edge modes.

6.2 Characteristic edges and Koch fractal iteration one

As is the case in the Koch fractal iteration 0, the first mode in the fractals of iteration 1 is also identified as dipolar mode with the aid of the simulations. We also notice that, although the geometry modification from iteration 0 to 1 is large, the energy of the dipolar mode shifts only slightly in the simulation, shift that is below our detection limit. Figure 6.58 show the surface charge distribution for the modes of the fractal iteration 1, and we observe that for the dipolar mode two degenerate eigenmodes are supported, one with a top-bottom dipole and the other with a left-right dipole, equivalent to what we found in the dipolar modes in iteration 0. However, the higher order modes of the Koch snowflakes of iteration 1 display complex EELS intensity and charge distributions as observed in figures 6.55 and 6.58. To understand these complex modes, we divided the edges of the fractal structure into characteristic edges, composed of two segments with a 120 degrees angle between them (i.e. "V" shape), as shown in Figure 6.67 and in the inset of Figure 6.57a. To isolate the characteristic edge of the Koch fractal iteration 1, we reproduced this "V" shape at the end of a 50 μ m long silver strip. Figure 6.57(a-b) shows the EELS spectra and energy-filtered maps of the silver strip representing the edges of the Koch snowflake fractal iteration 1. Here we are able to identify four resonant peaks that correspond to edge modes, in a similar manner to the modes found in straight edges on silver strips [14, 112], despite the fact that the characteristic shape of the Koch fractal is formed by two edges at an angle. The EELS intensity distribution corresponds to edge modes of order one (E_1), two (E_2), three (E_3) and four (E_4). As we saw in Chapter 4, bent

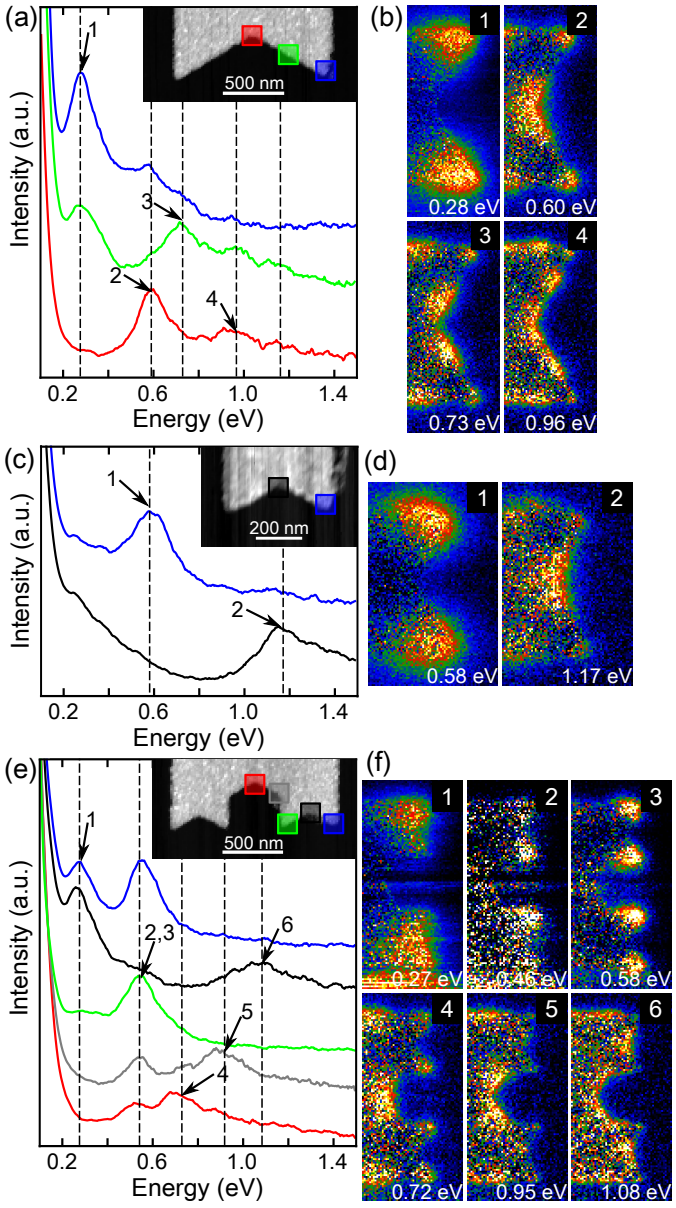

Figure 6.57: Experimental EEL spectra of the characteristic shapes of Koch fractal antennas of iteration 1 (a) and 2 (c, e) reproduced at the very end of a 50 μm long silver strips acquired at the color-coded positions indicated in the annular-dark-field (ADF) image in the insets. The arrows indicate the peaks corresponding to resonant edge modes. EELS maps of the plasmon modes found in the characteristic shapes of Koch fractal antennas of iteration 1(b) and 2 (d, f).

edges will maintain the same quasi one-dimensional modes than the ones found in straight edges. A similar behaviour was found in bent silver nanowires in which the plasmon modes were unaffected by the presence of kinks and corners [11],

A side-to-side comparison of the maps of the isolated characteristic shape and the snowflake fractal iteration 1 is shown in Figure 6.59. Comparing the spectra in figures 6.55(b) and 6.57(a), we observe that the peak corresponding to the E_1 mode in the isolated edges is red-shifted by 70 meV with respect to the second mode in the snowflake. If we align these peaks by red shifting the spectra in the Koch snowflake iteration 1, as shown in figure 6.59(a), we observe an excellent match between the peaks present in the Koch snowflake fractal and the modes of the isolated edge in the 50 μm silver strips. The small energy difference between the modes present in both structures can be attributed to the interaction between the edge modes within the Koch snowflake [77].

Based on the observation that bent edges can support edge modes equivalent to the ones in straight edges, we can now compare the EELS maps of the isolated edges with the ones of the Koch snowflake iteration 1. From the energy filtered maps shown in Figures 6.55(e) and 6.57(b), we can recognize that the second mode in the snowflake corresponds to an edge mode of order one (E_1) or an edge dipolar mode of the "isolated characteristic edge". In the simulated EELS spectra of the Koch snowflake iteration 1 (Figure 6.55b), we notice that the second peak at 0.32 eV is actually formed by two close resonant peaks separated by only 46 meV. Due to the intrinsic width, the experimental EEL spectra cannot resolve those two peaks and thus only one peak appears. Based on these simulations, we know that the second resonant peak, observed experimentally, is formed by three eigenmodes with two degenerate

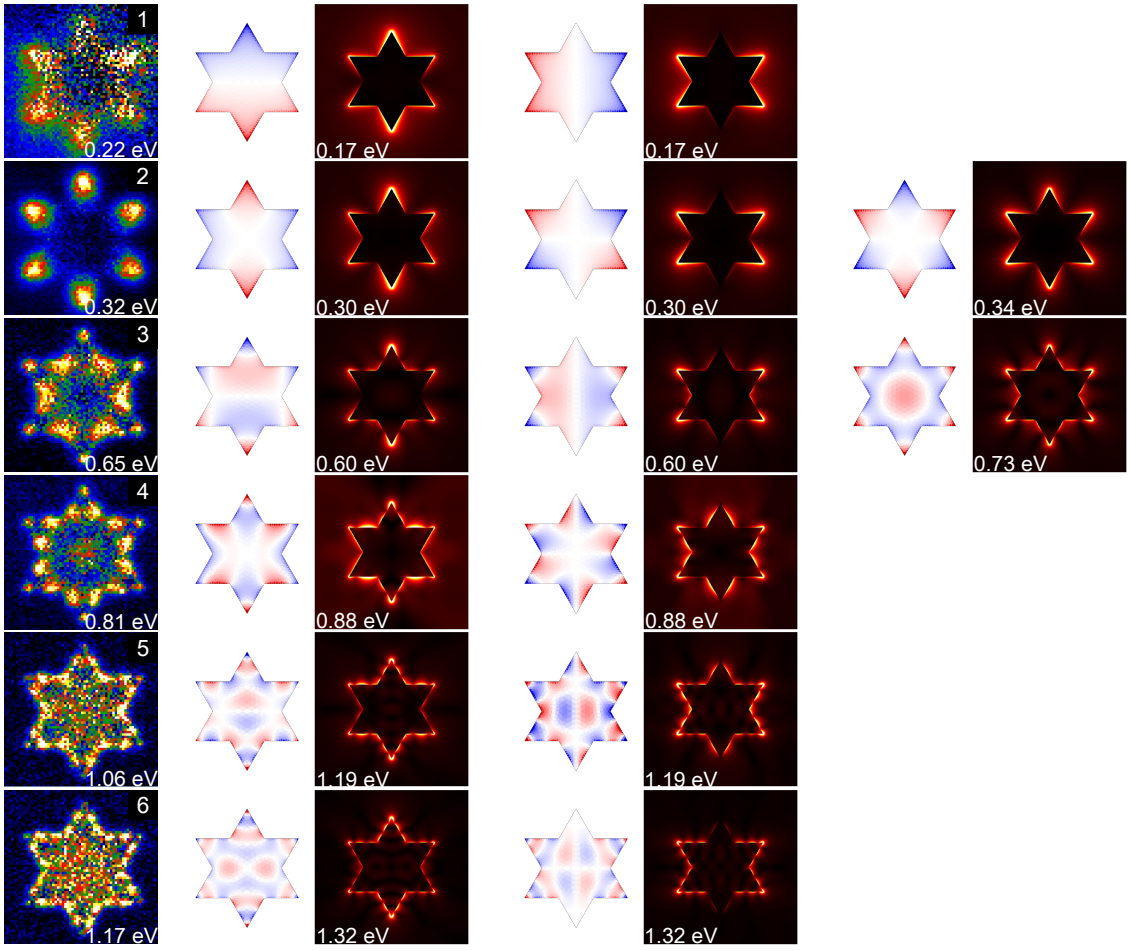

Figure 6.58: Measured energy filtered maps of the Koch snowflake fractal iteration 1 and their corresponding calculated eigenmodes and their near-field distribution. The numbers correspond to the EELS peaks in Figure 6.55b.

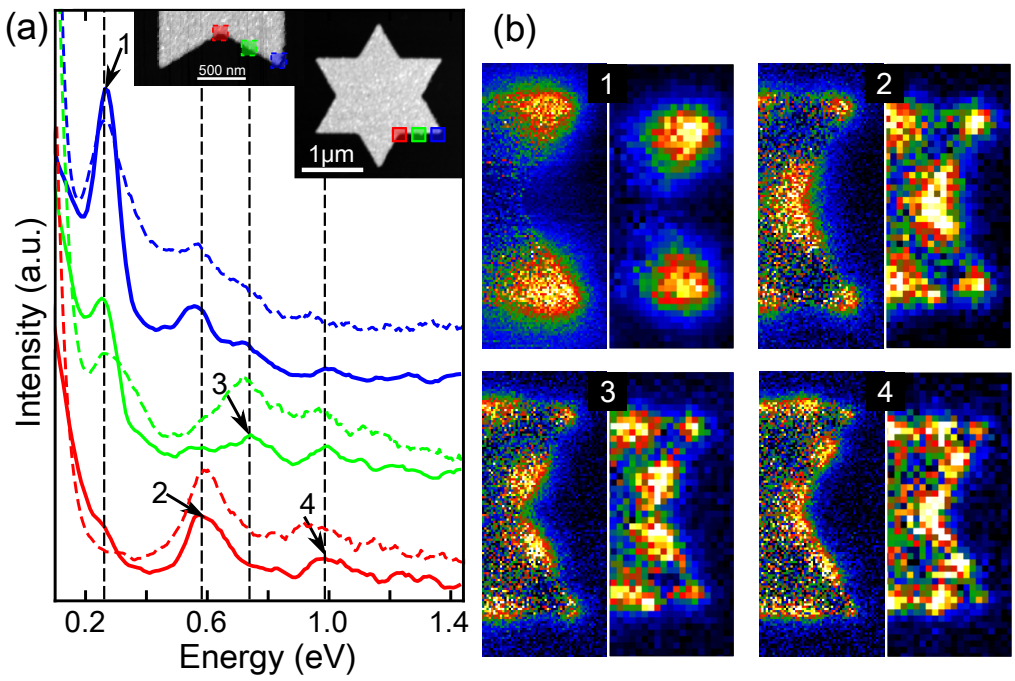

Figure 6.59: Side-to-side comparison of the modes in the isolated edges in the 50 μm silver strips (dashed lines) and in the full Koch snowflake fractals (solid lines) of iteration 1. (a) EELS spectra acquired at the positions marked on the insets. The spectra of the full Koch snowflake fractal is red shifted 70 meV to align the E_1 modes of both structures. (b) Comparison of the EELS energy filtered maps of the isolated edges (left) and of the full snowflake (right) showing that the modes on both structures are equivalent.

modes as shown in Figure 6.58. Due to the symmetry of the structure, the eigenmodes are formed by three different distributions of the E_1 mode formed in the characteristic "V" edges. In one degenerate eigenmode, the charge distribution of the E_1 mode is localized in the top and bottom "V" edges in a symmetric configuration (four times), in the other degenerate eigenmode, it is localized in the left and right "V" edges in an antisymmetric configurations (two times). In the non-degenerate eigenmode, each one of the characteristic edges displays the charge distribution of the E_1 mode.

In a similar manner, the third peak at 0.65 eV is formed by edge mode order two (E_2), and it also has three eigemodes, two generate modes, one with a top-bottom symmetric configuration and the other with a left-right antisymmetric configuration. Equivalently, for the case of resonant peak four, five and six in Figure 6.55b, they are formed by edge modes of order three, four and five respectively by comparison with the isolated characteristic "V" shape.

6.3 Eigenmodes and coupling of edge modes

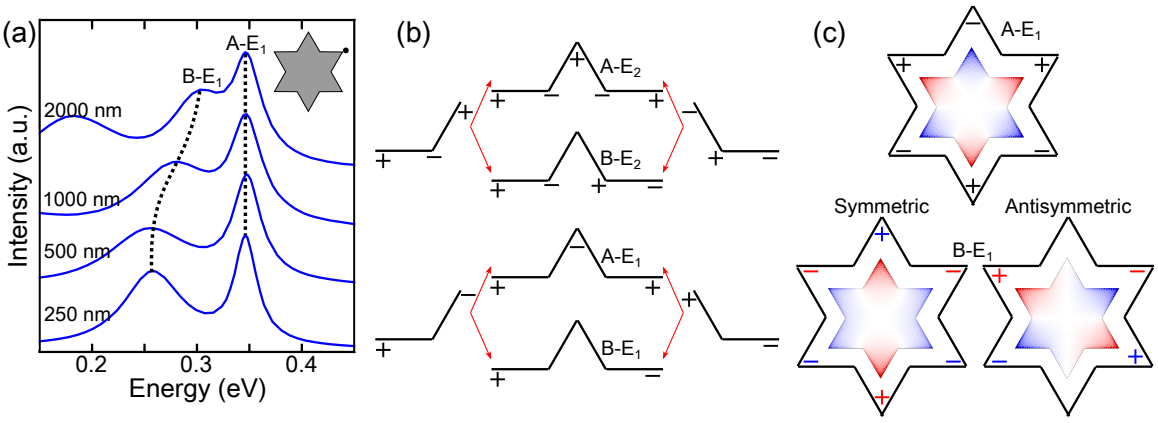

Figure 6.60: (a) Simulated spectrum of Koch fractal iteration 1 for several fractal sizes. The size displayed is the initial length of each side in iteration 0 of the fractal. The two peaks show the evolution of the interaction of the bonding (B) and antibonding (A) E_1 edge modes, as the structure gets smaller a stronger interaction between E_1 modes results in larger splitting energy of these peaks. The inset shows the position where the spectra were calculated. (b) Energy diagram (not to scale) showing the formation of bonding and antibonding modes due to coupling of edge modes E_1 and E_2. (c) Charge distribution diagrams of the bonding and antibonding E_1 modes in Koch fractal iteration 1. Due to the symmetry of the structure the bonding mode supports two degenerate eigenmodes; the calculated eigenmodes are displayed inside the diagrams.

Although the experimental results could be explained neglecting the formation

of three eigenmodes with charge distribution corresponding to edge modes in each characteristic edge, the formation of these eigenmodes might indicate interaction of edge modes within the fractal structure, as shown in the work of Schmidt et al. in rectangular structures [77]. To further analyze the formation of these eigenmodes, we simulate the EELS spectra of Koch snowflake fractals iteration 1 of several sizes while maintaining the thickness of the structure as shown in Figure 6.60a. We want to examine the energy splitting of the peaks formed by E_1 edge modes and not the shift in energy due to the different fractal size; therefore, we align the second peak of each fractal to the second peak in the fractal of initial length of 2 μm. The spectra of the fractals of initial length 1 μm, 500 nm, and 250 nm were red shifted by 0.27 eV, 0.69 eV, and 1.2 eV respectively. We observe that, as we increase the size of the fractal, the energy splitting reduces. This behavior might suggest that interaction of the E_1 edge modes is responsible for the formation of these two peaks. As the size of the fractal increases the distance between edges increases and interaction between edge modes is weaker, thus the energy splitting is reduced.

Also, we can use the hybridization model [2] to explain the charge distribution of the eigenmodes in the Koch fractal iteration 1. For the case of edge modes and one-dimensional modes, when the interaction is through a corner or tip [112, 16], as seen in Chapter 5, the hybridization model dictates the formation of a bonding and an antibonding mode. In the case of the Koch fractal formed by connected characteristic edges, the hybridized modes become bonding (B) and antibonding (A) charge transfer hybridized modes [69], as shown in Figure 6.60b for modes E_1 and E_2. From this results we can observe that the antibonding modes have equal charges at the extremities, while bonding modes have opposite charges. The C_3 symmetry

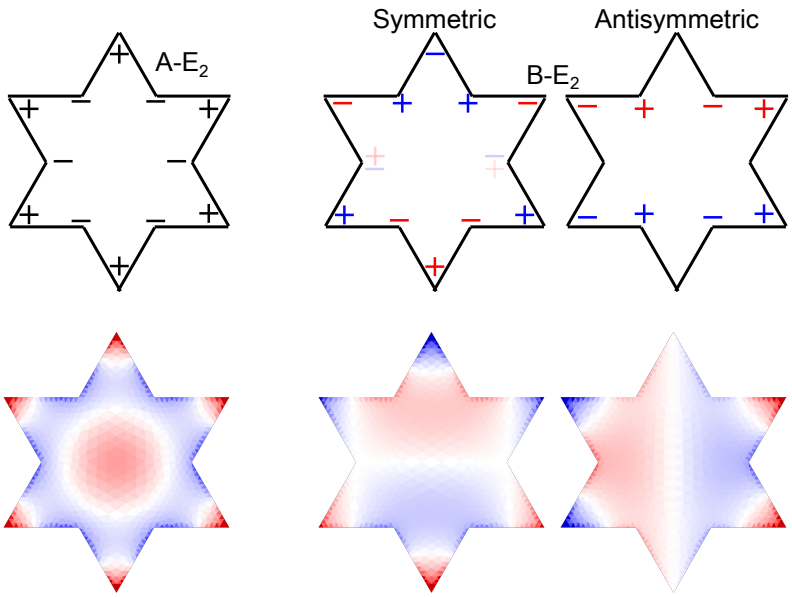

Figure 6.61: Charge distribution diagrams and calculated eigenmodes of the bonding (B) and antibonding (A) E_2 modes in Koch fractal iteration 1. Due to the symmetry of the structure the bonding mode supports two degenerate eigenmodes, and the antibonding mode one non-degenerate eigenmode.

of the Koch fractal would allow a configuration in which all the edges can display the antibonding modes as shown in Figure 6.60c and 6.61 for edge modes E_1 and E_2 respectively. However, for the case of the bonding modes in which the charges at the extremities are opposite, the symmetry only allows two sides of the structure to fulfill this constrain. As was the case for the edge modes in Koch fractal iteration 0, this constraint promotes the formation of a symmetric and an antisymmetric degenerate eigenmodes. In the symmetric eigenmode we have two groups of bonding edge modes (blue and red in Figure 6.60c and 6.61), each group formed by two sides on the fractal displaying bonding edge mode charge distribution symmetrically. In the antisymmetric eigenmode we have two bonding edge modes (blue and red in Figure 6.60c and

6.61) at opposite sides of the fractal displaying an antisymmetric charge distribution. This description of the formation of eigenmodes in the Koch fractal order 1 based on the hybridization of edge modes suggest that there is coupling within the fractal structures. However an in-depth analysis of edge coupling that goes beyond the purpose of this work is required to confirm this hypothesis.

6.4 Koch fractal iteration two

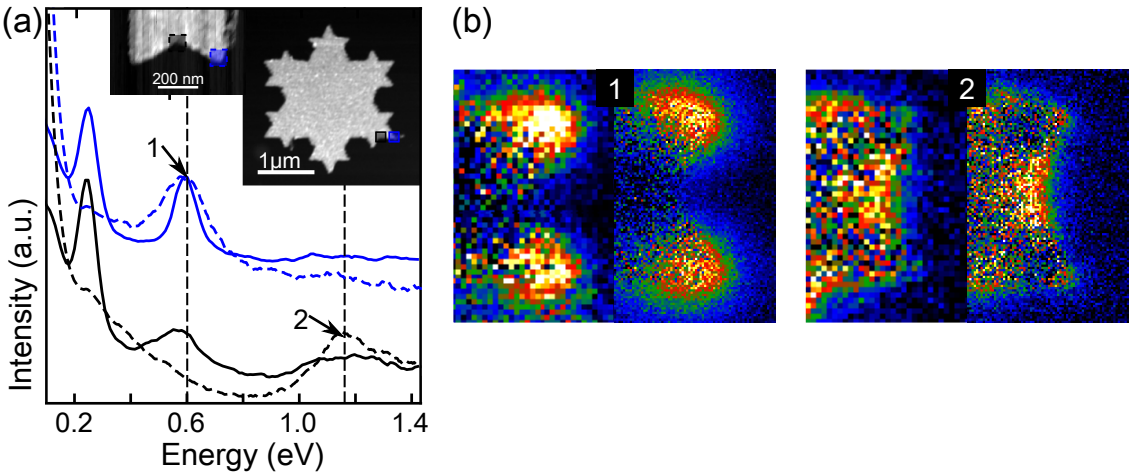

Figure 6.62: Side-to-side comparison of the modes in the isolated characteristic edge in the 50 μm silver strips (dashed lines) and in the full Koch snowflake fractals (solid lines) of iteration 2. (a) EELS spectra acquired at the positions marked on the insets. The spectra of the full Koch snowflake fractal is red shifted 70 meV to align the E_1 modes of both structures. (b) Comparison of the EELS energy filtered maps of the isolated edges (right) and of the full snowflake (left) showing that the modes on both structures are equivalent.

The same approach of edge isolation is taken to understand the modes present in the iteration 2 of the Koch fractal. We therefore divided the edges of the snowflake structure to find the characteristic shape of the structure, which is the same "V" shape

as for the iteration 1 but one-third smaller, as shown in Figure 6.57(d).In the EELS spectra and energy filtered maps of the isolated characteristic shape, shown in Figure 6.57(e-f), we are able to identify two resonant peaks that correspond to edge modes E_1 and E_2, similar to the ones found in the iteration 1 fractal, but at higher energies due to the shorter length of the edge. A comparison of these two modes, excited in the characteristic isolated shape with the modes present in the Koch snowflake fractal of Figure 6.55(c,f), we can identify mode four of the fractal as an edge mode order one (E_1) of the isolated edge (because of the same strong EELS signal on each small vertex) and mode seven of the fractal as an edge mode order two (E_2) of the isolated edge on the strip. To corroborate this argument, a side-to-side comparison of the maps and spectra of the isolated characteristic "V" shape and the snowflake fractal iteration 2 is shown in Figure 6.62 displaying the excellent nodal distribution agreement of the modes between the Koch fractal and the isolated edge. As we did in the comparison between the fractal iteration 1 and its characteristic isolated edge, for iteration 2 we also red shift the spectra in the Koch snowflake iteration 2 by 70 meV, as shown in Figure 6.62(a). We observe that after the shift the peaks corresponding to the E_1 and E_2 modes in the isolated edges in the 50 μm silver strips match in energy scale the peaks present in the Koch snowflake fractal.

For the fractal structure iteration 2, we also isolated and analyzed a larger portion of the structure, as shown in Figure 6.57(e-f), i.e. the characteristic shape of the Koch fractal iteration 1 after we apply an additional iteration of the fractal procedure to it. In this larger portion of the fractal, we can distinguish five peaks, as shown in Figure 6.57(e). The first peak at 0.27 ± 0.04 eV corresponds to a E_1 mode or dipolar mode, which is the same mode displayed in the silver strip of the Koch fractal iteration 1

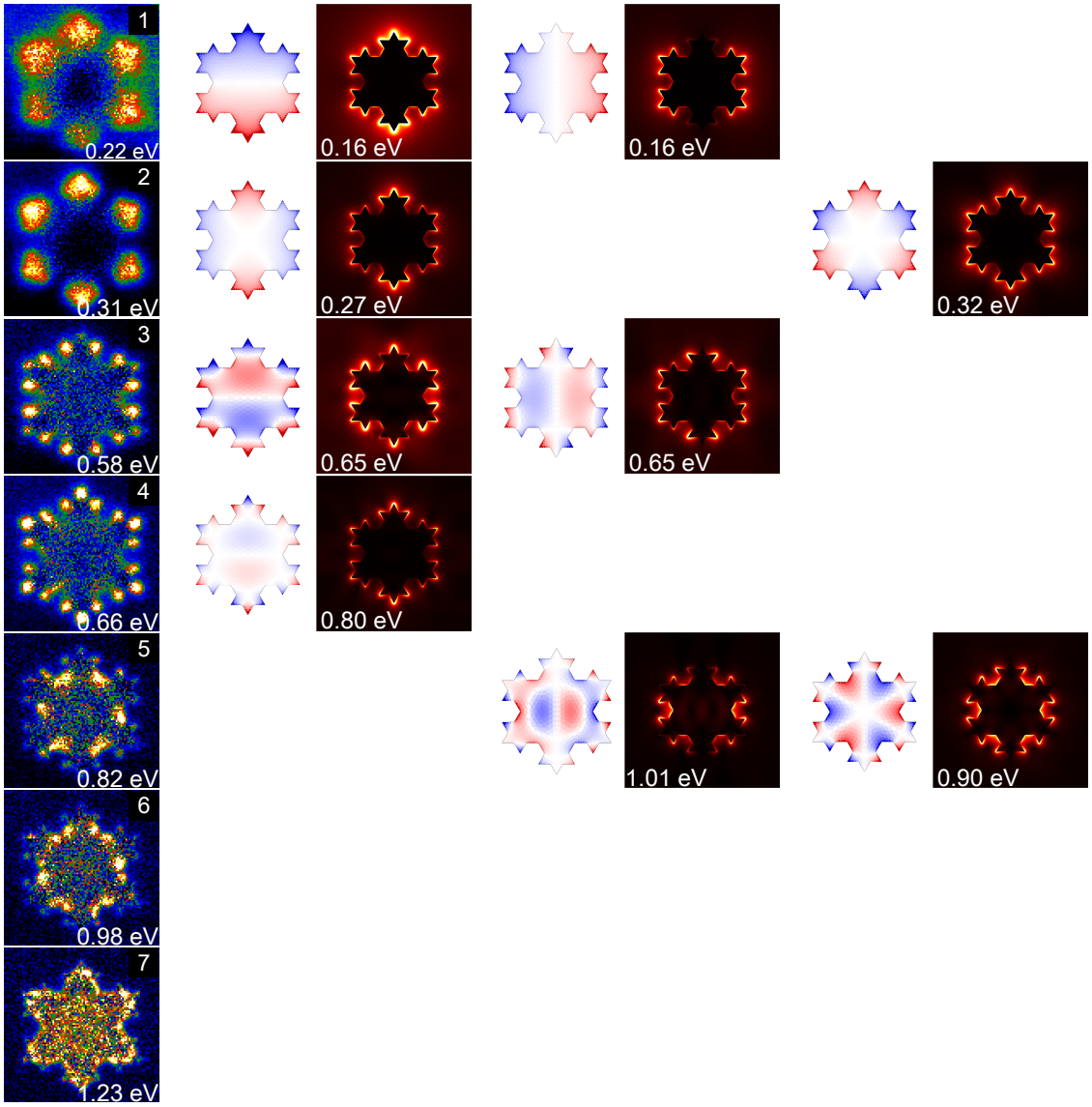

Figure 6.63: Measured energy filtered maps of the Koch snowflake fractal iteration 2 and their corresponding calculated eigenmodes and their near-field distribution. The numbers correspond to the EELS peaks in Figure 6.55c.

at 0.28 ± 0.04 eV. This result suggests that the dipolar mode of iteration 1 can still be excited in the next iteration of the fractal as the dipolar mode is the most global one (as seen in figure 6.63) and is thus expected to be minutely affected by the fine modification of the 2nd iteration. This effect is also observed in the Koch snowflake fractal iteration 1 (figure 6.55b), where the second mode, which is a dipolar edge mode (E_1) at 0.32 ± 0.04 eV also present in the Koch snowflake iteration 2 (Figure 6.55c) at 0.31 ± 0.04 eV.

The second peak in Figure 6.57e is labeled as "2, 3" because in the energy filtered maps we observed two dissimilar intensity localizations, one with the antinodes located in the inner vertices and the other located in all vertices, as shown in the maps two and three in Figure 6.57f respectively. To extract the EELS maps corresponding to each surface plasmon resonance, we isolate the contribution from each edge mode to the spectrum image using the non-linear least squares fitting tool of the "Digital Micrograph" software [120], which fits Gaussian peaks to a spectrum image. The separation two Gaussians to the peak at 0.55 eV yield the two EELS maps at 0.46 ± 0.07 eV and 0.58 ± 0.09 eV for the second and third mode respectively. The third and sixth modes of the isolated edges of fractal iteration 2 on the strip shown in figure 6.57(e-f) are the same two modes found in the isolated characteristic shape of Koch fractal iteration 2 shown in figure 6.57(c-d). Thus, the modes of the isolated edges can be described as edge modes order one (E_1) and two (E_2) and represent modes four and seven found in the Koch snowflake fractal iteration 2 in figure 6.55(c,f). These results confirm that the modes present in the strips are a good representation of modes present in the Koch snowflakes.

When two of the characteristic "V" shapes of Koch fractal iteration 2 are joined

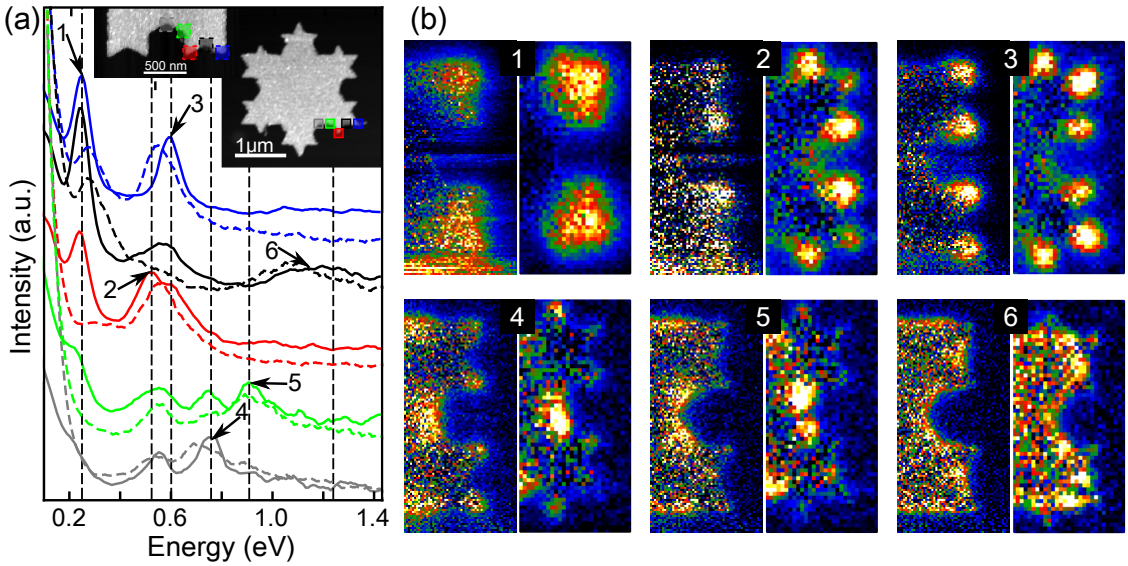

Figure 6.64: Side-to-side comparison of the modes in the isolated edges in the 50 μm silver strips and in the full Koch snowflake fractals of iteration 2. (a) EELS spectra acquired at the positions marked on the insets. The spectra of the full Koch snowflake fractal is red shifted 70 meV to align the E1 modes of both structures. (b) Comparison of the EELS energy filtered maps of the isolated edges (left) and of the full snowflake (right) showing that the modes on both structures are equivalent.

by a 120 degrees angle, we generate an inverted "U"-like shape as shown in the central area in the inset in Figure 6.57(e) and 6.67. This "U" shape, despite the multiple kinks, also sustains edge modes. Modes E_1 (dipolar edge mode), E_2, and E_3 can be identified at 0.46 $\pm$ 0.07, 0.72 $\pm$ 0.04, and 0.95 $\pm$ 0.04 eV as seen in Figure 6.57(f). The "U" shape is also present in the full Koch snowflake fractal iteration 2 in Figure 6.55(c,f), and by comparison it displays the same edge modes found in the isolated edge seen in Figure 6.57(e-f).The third, fifth and sixth peaks in the full Koch snowflake is a E_1, E_2, and E_3 modes respectively. To confirm this identification, Figure 6.64 shows the good match between the modes present in the Koch snowflake fractal iteration 2 and the modes isolated in the 50 μm silver strips. The spectra in

Figure 6.64a, also shows a good energy overlap between the modes in the isolated edges on the strip and the modes of the snowflakes after the latter is red-shifted by 70 meV. The energy shift can be mainly attributed to interaction of edge modes in the snowflake [77] and to a lower extent to the fabrication procedure that did not produce equal edges and sizes in both structures. This supports the evidence that the isolated modes on the silver strip are equivalent to the modes present in the Koch snowflake fractals. To support the proposed concept that a "U" characteristic edge structure can sustain plasmonic edge modes similar to the ones found in a straight edge, we draw a parallel and analyze the modes in a simulated "U" shape bent silver nanowire [67, 154]. Figure 6.65 shows the spectra and the energy-filtered maps of the bent nanowire, demonstrating that, despite the bending, the nanowire still supports one-dimensional modes.

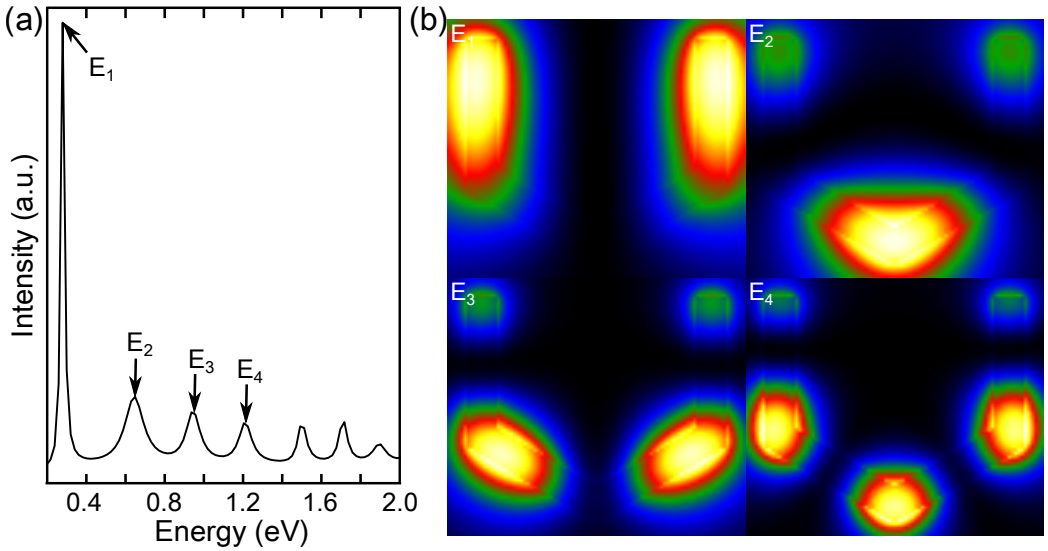

Figure 6.65: Simulated EELS spectra (a) and energy filtered maps (b) of a 444 x 44 x 30 nm^3 silver nanowire bent in a "U" shape formed by joining two 120 degrees bent nanowires. The maps (b) show that the nodal distribution of a straight nanowire is maintained in the "U" shaped nanowire.

6.5 Self-similarity of edge modes

Now that we have identified all the edge modes present in the Koch snowflake fractals, we can analyze the self-similarity or fractal character of the edge modes present in the structures as we increase the number of iterations. Due to the C_3 symmetry of the Koch snowflake fractal, each mode exists 3 times. As we explained above, in our analysis we ignore this "degeneracy". For each edge mode in the Koch snowflake fractal structure multiple eigenmodes can be found, however in our analysis of self-similarity of edge modes we will not consider these eigenmodes and we only focus on the modes found experimentally. Figure 6.66 shows a diagram depicting the formation of edge modes for each fractal iteration. In iteration 0, we have only one mode of a particular order for each edge. In Koch snowflake fractal iteration 1, we have two modes that originate from a dipolar/E_1 mode and only one mode for each higher order edge mode. As described above, the first mode is the same dipolar mode found in iteration 0, and the second mode is formed by the E_1 modes in the characteristic "V" edges in this iteration as shown in Figures 6.57(c) and 6.67. In the case of the Koch fractal iteration 2, we have four dipolar/E_1 modes, one coming from fractal iteration 0, one from the E_1 mode of fractal iteration 1, and two new E_1 modes. This structure presents two types of characteristic edges, one is the characteristic "V" shape and the other is the "U" shape as shown in Figures 6.57(e) and 6.67, and each one of these two edges can support an E_1 mode, thus two new modes are created in this iteration. As was the case for iteration 0 and 1, in iteration 2 also only one mode of higher order is supported. From this analysis we notice that the fractal character of the Koch snowflake is reflected in the number of dipolar/E_1 modes supported by the fractal structure. In addition, we can deduce that the total number of edge modes in

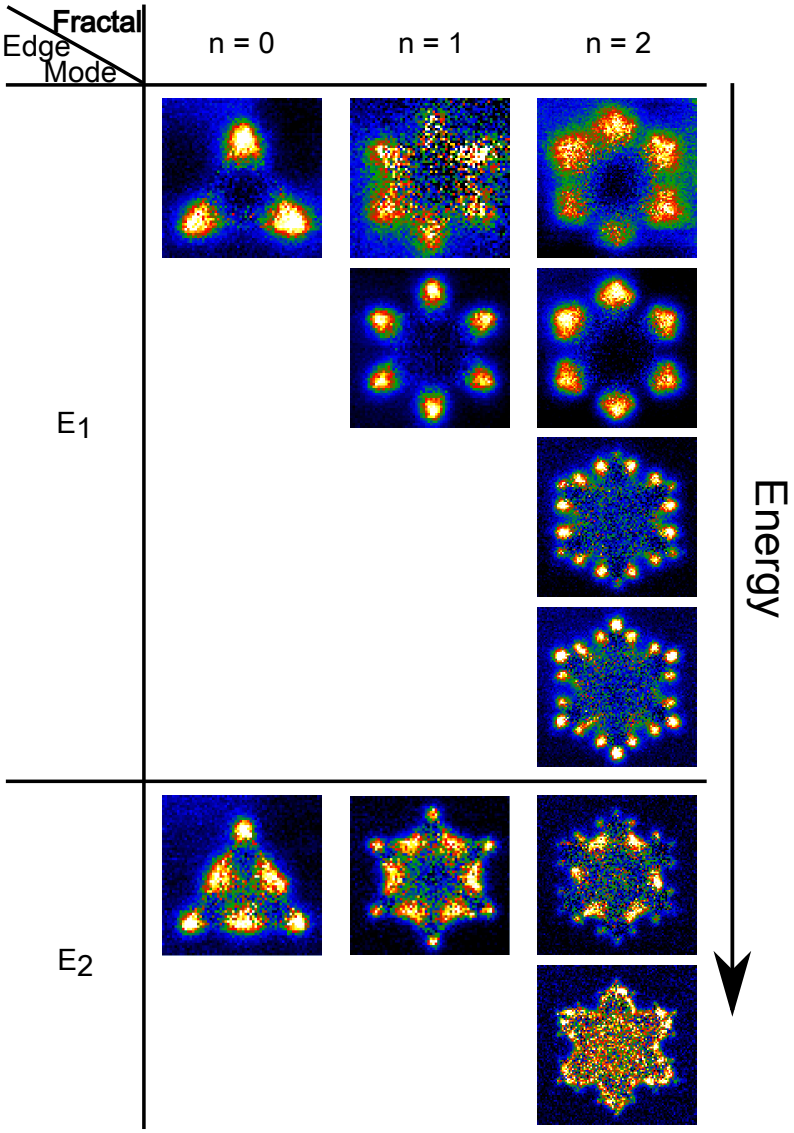

Figure 6.66: Diagram of the formation of the plasmon modes in Koch snowflake fractal antennas. The number of modes depends on the number of independent edges as described in the text.

a Koch snowflake is equal to the number of dipolar/E_1 modes in the previous fractal iteration plus the modes formed on the characteristic edges present in the fractal. Because the experimental results show that the modes in the fractal are governed by the modes in the characteristic edges, this analysis can be applied to other planar fractal structures.

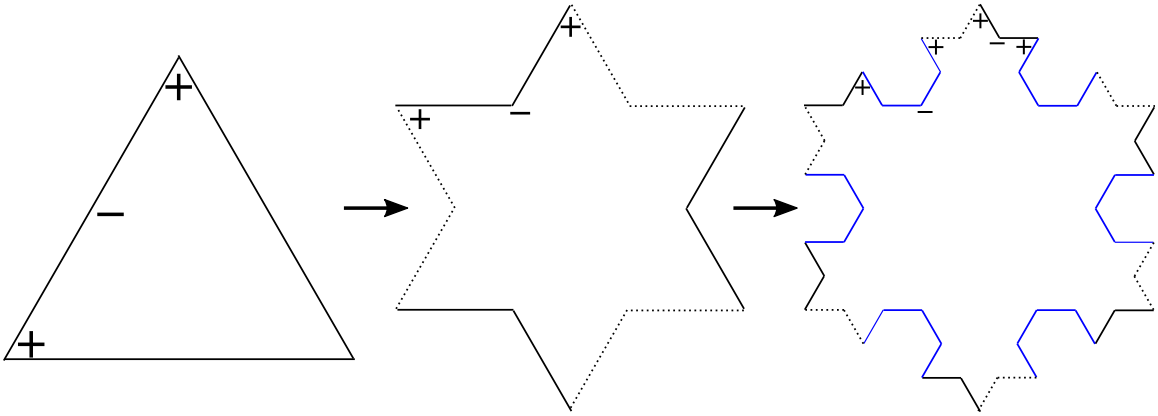

Figure 6.67: (Left) Equilateral triangle which is the iteration 0 of the Koch snowflake fractal. (Center) Koch snowflake fractal iteration 1 showing the characteristic "V" shape of the structure formed by two line segments at an 120 degrees angle. (Right) Koch snowflake fractal iteration 2 showing its two types of chracteristic edges: One type is the characteristic "V" shape (in black). The other type is the "U" shape (in blue) formed by two characteristic "V" shapes at 120 degrees angle. The figure shows the charge distribution of an edge mode that is supported in each one of the edges.

Now that we understand how the modes evolve as we increase the fractal iterations we can extend and quantify the number of dipolar/E_1 modes (N^{edges}) generated by the self-similarity in the Koch snowflake fractal. From our analysis, we can infer how many types of characteristic edges in the Koch fractal are produced after n iterations of the fractal. For $n = 0$, and 1 only one type of characteristic edge is produced, however for n $n > 1$, after each iteration two types of characteristic edges are produced, the "V" and the "U" edges. Therefore, $N_0^{edges} = 1$, and for $n > 0$,

$N_n^{edges} = 2n$. This results shows that the plasmons excited on Koch snowflake fractal structures shows a self-similar fractal response with the number of modes increasing after each iteration. This confirms that plasmonic fractal optical-antennas can exhibit multi-resonant or broadband behaviour while maintaining a compact structure similar to the ones found in macro-scale antennas.

6.6 Conclusions

We have analyzed and described the plasmon modes present in planar silver Koch snowflake fractal antennas. The lowest energy modes present in all the fractal structures were identified as dipolar modes. For the higher energy modes, insight into their origin was gained by measuring simplified geometries describing the basic building block segments of the fractal structures. Two types of basic segments were found and studied: a "V" characteristic shape, formed by two lines at 120 degrees angle, and a "U" shape formed joining two characteristic "V" shapes also at 120 degrees angle. We found that, in spite of the fact that these two geometries presented were not straight line segments, the modes sustained were quasi-one dimensional modes (E_i). From the analysis of the isolated characteristic edges, we identified all the edge modes supported in the Koch snowflake fractal. We determined that the total number of edge modes in a Koch snowflake of a given number of iterations depends on the number of characteristic edges created in the fractal. Following a simple rule we observed that the number of plasmon dipolar/E_1 edge modes increases by two after a fractal iteration, confirming that the plasmonic Koch snowflake fractal antennas can exhibit multi-resonant or broadband behaviour while maintaining a compact structure reflecting the characteristics of their macro-scale counterpart.

Chapter 7

Summary

7.1 Conclusions

In the work presented in this thesis, we have used EELS performed inside a STEM equipped with an electron monochromator, to characterize the plasmonic response of planar silver nanostructures fabricated by electron beam lithography. Theoretical modeling of the plasmon response supports and complements our findings.

As described in Chapter 3, EELS energy resolution is one of the limiting factors for the analysis of losses below 5 eV, region in which plasmon resonances lie. In this work, we implemented and tested the Richardson-Lucy algorithm. We showed that the algorithm could be used to obtain effective energy resolutions up to 10 meV. We also demonstrated that the deconvolution of EELS spectra enhances the contrast of the plasmon resonances EELS energy filtered maps by a factor of three. This implementation was used as a post-processing tool in the analysis of the resonances in nanostructures studied in this thesis.

Analyzing the surface plasmon resonances of planar nanostructures, we have found

that the supported resonances can be described as edge and cavity or film modes, with edge modes behaving as quasi-1D modes. Furthermore, taking advantage of the relatively large size of the analyzed structures, we were able to map, with a very high level of detail the presence of film or cavity modes. We have demonstrated that the modes supported by a nanowire are formed by the coupling of the edge modes in the nanowire. We also showed that the edge modes in bent edges are unaffected by the presence of bends up to the critical angle of 90° where the modes start self-interacting producing large energy shifts and the modes converge at small bending angles.

We have shown that coupling in planar nanostructures can be described by the coupling of their edge modes, and three coupling behaviors were identified.: 1) Coupling through the edge of a nanostructure, 2) coupling through a corner, and 3) a non-coupling behavior where the edge of the nanostructure behaves independently of the rest of the structure. We further explored the coupling through the edge in offset nanowire, and we found that by careful tuning of the nodal alignment and spectral overlap it is possible to promote or suppress the coupling of a particular mode. These studies prove that plasmonic coupling is a very versatile tool to modify the optical response of plasmonic systems.

Finally, we have analyzed and described the plasmon modes present in planar silver Koch snowflake fractal antennas by describing the modes present in the building segments of the fractal structures. We found that the fractal geometry can sustain quasi-1D edge modes, in spite of the fact that the edges of their building segments were not straight edges. The results showed that the total number of plasmon edge modes in the Koch fractal snowflake depends on the number of characteristic edges created after each iteration demonstrating that the plasmonic Koch snowflake fractal

antennas can exhibit multi-resonant behavior while maintaining a compact structure.

This thesis provides a comprehensive picture of the surface plasmon resonances in planar nanostructures and their coupling. Moreover, the studied coupling cases present simplified rules to aid in the design of future plasmonic devices compatible with planar industrial fabrication methods. The thesis results emphasize the power of EELS as a research tool to understand in depth the surface plasmon resonances and to improve the design of new nanostructures for nanophotonic applications.

7.2 Future work

As we showed in this thesis, the STEM-TEM system is a unique tool for the characterization of surface plasmon resonances. This equipment combined with the ability to fabricate structures with the use of electron beam lithography has the potential to further the understanding of plasmon resonances and its applications in a number of areas. In this section, I mention a few areas that are worth pursuing and where preliminary results were obtained.

7.2.1 Alternative methods for the characterization of surface plasmons resonances

To date, the predominant method of studying plasmon oscillations in a TEM has been EELS. In a non-relativistic approximation, this energy loss is produced by the component of the electric field along the optical axis of the excited plasmon resonance. Thus, it is impossible to gain any information about the electric field in the viewing plane (i.e., perpendicular to the optical axis). Precisely this component can, however, be studied using differential phase contrast (DPC) [155, 156].

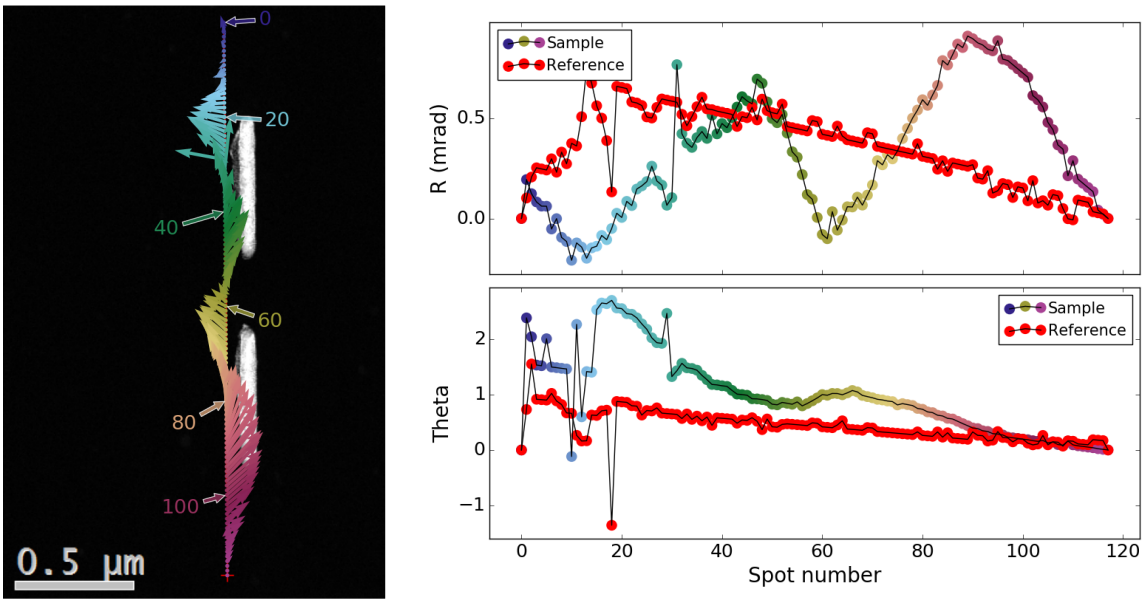

Figure 7.68: (Right) Deflections of the electron beam as it moves in a line-scan over a reference area and over the sample. (Left) ADF image showing the line-scan direction and the net deflections of the electron beam. In collaboration with Stefan Loffler and graduate student Isobel Bicket.

DPC exploits the fact that electrons subject to an electromagnetic field are deflected according to the Lorentz force. Any deflection along the optical axis gives rise to a change in kinetic energy and, hence, shows up in EELS. Any deflection perpendicular to the optical axis, however, changes the direction of the electron's momentum. This gives rise to a shift in the electron's momentum distribution. The final momentum distribution, after passing the nanostructure, can then conveniently be measured in the TEM's diffraction plane. Compared to a reference measured without field, the displacement of the transmitted beam shows a shift that is proportional to the field integrated along the electron trajectory.

To test this idea, We have performed preliminary experiments on two silver nanowires as shown in Figure 7.68. The right panel shows the deflections of the

electron beam as we line-scan the beam over the sample and over an area away from the nanowires and over the substrate which works as our reference. The reference line-scan also shows deflections (which are unwanted) that are probably coming from charging effects of the silicon nitride substrate. After subtraction of the reference we obtain the net deflections shown on the left panel of Figure 7.68. We observe that the largest deflections correspond to the tips of the nanowires where the dipolar mode it is expected to have high electric field intensities.

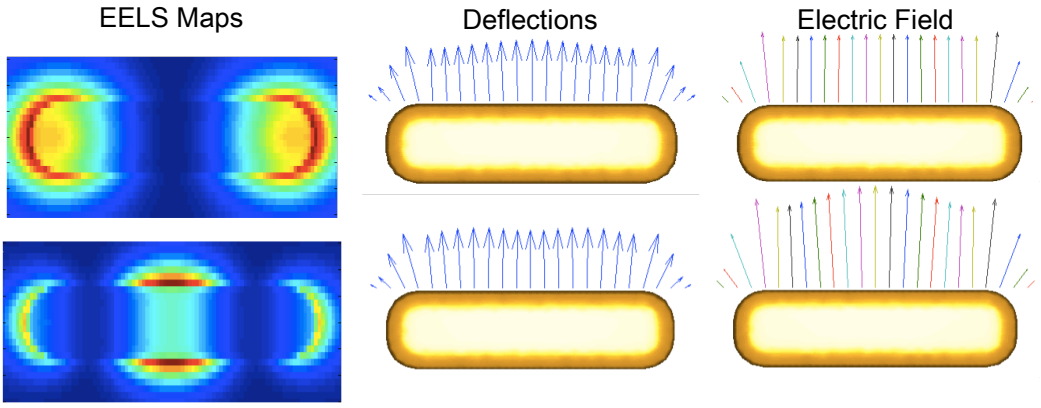

Figure 7.69: EELS maps of the first and second plasmon resonant modes (Left). DPC deflections (Center) and corresponding electrical in-plane components of the electrical field (Right) for the first and second modes. In collaboration with Stefan Loffler and graduate student Isobel Bicket.

Using the MNPBEM toolbox and a custom script done by Stefan Loffler, we have also simulated the plasmonic response of a 200x50x50 nm^3 Ag nanorod to the electron beam. We calculated the EELS maps and in-plane deflections along a line parallel to the nanorod, as shown in Figure 7.69, for two plasmonic modes. The EELS maps show the typical excitation probabilities for the first two modes, and the in-plane electric field components show a similar behavior in general, although the local extrema are less pronounced. The DPC deflections are found to be in good agreement with the

electric field with some small differences close to the center of the rod which can be attributed to the cumulative nature of the DPC deflections as well as retardation effects. The absolute magnitude of the DPC deflections in Figure 7.69 is of the order of 0.1 μrad at 300 keV, with a maximum deflection of 0.17 μrad for the first mode, and a 0.04 μrad deflection for the second mode. Albeit small, these deflections should be measurable with latest generation TEMs when using large camera lengths. In the experiments the deflections are in the range of a mrad and not in μrad as indicated in the simulations this apparent contradiction might indicate that there is a secondary effect that we are measuring in the experiments, further experiments and analysis it is needed to clarify this.

These preliminary results indicate that it might be feasible to determine all three components of the electromagnetic field caused by plasmons using a combination of DPC and EELS. Isobel Bicket, PhD student at Prof. Botton's group, is working on this topic to further understand this deflections and determine if it is possible to use DPC to characterize plasmonic devices.

7.2.2 3D plasmonic structures and their coupling

This thesis focuses entirely on the analysis of planar structures, however for some applications 3D structures might be desired. For this purpose it is possible to use multi-step electron beam lithography (EBL). Isobel Bicket, in Prof. Botton's group, is using this technique to fabricate the upright split ring resonators (SRRs) on TEM grids. A precise alignment of each EBL layer is required, this is done using pre-fabricated sacrificial alignment marks deposited in the first step. Using this fabrication process, we were able to fabricate three-dimensional upright SRRs with hollow pillars, as shown in Figure 7.70.

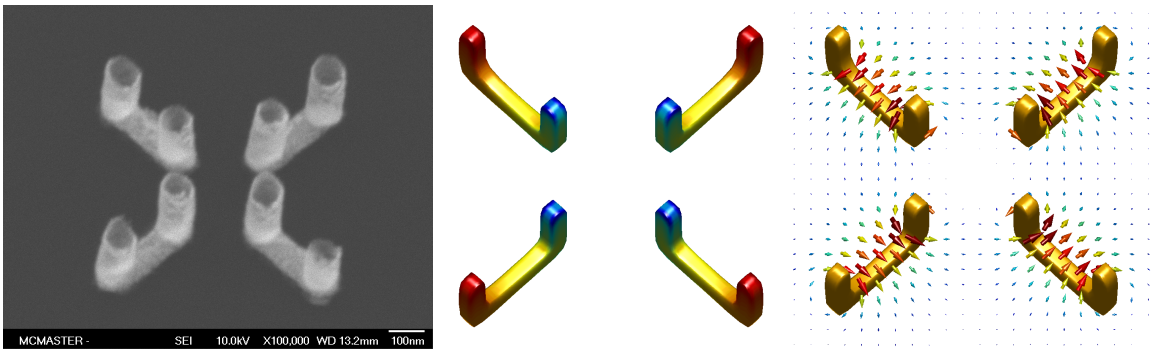

Figure 7.70: 3D upright SRRs fabricated by multi-step EBL (Left). Charge distribution of the toroidal mode formed by the coupling of the dipolar modes in each SRRs (Center). Magnetic field distribution of the toroidal mode (Right). In collaboration with graduate student Isobel Bicket.

Isobel is studying SRRs because of their possible applications as metamaterials to produce many unique properties when interacting with light, such as a negative refractive index, and dipole magnetic moments. Due to ease of fabrication most studies focused on planar SRRs, however with 3D fabrication, it is possible to fabricate upright SRRs, and study the coupling of these SRRs. As shown in the simulations in Figure 7.70, an array of SRRs with toroidal symmetry is expected to produce a toroidal magnetic moment. According to reported simulations [157], the toroidal dipole moment shows a high quality factor making the structure a good candidate for a nanoscale spaser system: the nanoscale surface plasmon analogue to the laser.

7.2.3 Alternative materials for plasmonic applicactions

The most common materials materials for plasmonic applications are silver, gold, and aluminium. Although these materials are used in most plasmonic applications to date, new alternative materials that will exhibit low plasmonic losses, have a response in the telecommunications electromagnetic range, and are CMOS compatibility are

required. Different material classes such as conventional semiconductors, transparent conducting oxides, perovskite oxides, metal nitrides, silicides, germanides, and 2D materials such as graphene, are being explored [158]. One of this materials is Indium Tin Oxide (ITO), which is a material commercially used as transparent electrode in application such as screens and photovoltaics. ITO has low optical losses and a optical response in the mid to near IR range [159], and because is a commercialized material it can be readily use in future commercial plasmonic devices.

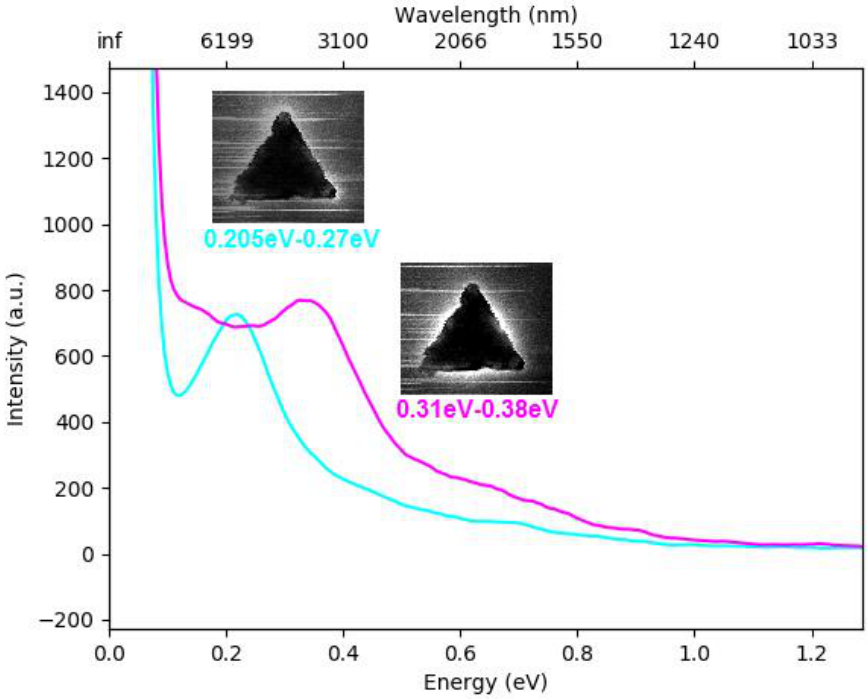

Figure 7.71: EELS spectrum of an ITO triangle with a thickness of 100nm and a side length of 650nm. The insets show the EELS maps of the first two plasmon resonances in the nano-triangle. In collaboration with graduate students Viktor Kapetanovic and Isobel Bicket.

Using STEM-EELS, Viktor Kapetanovic, master student at Prof. Botton's group,

has obtained some preliminary results of the plasmonic response of ITO nanostructures fabricated by EBL, as shown in Figure 7.71. We were able to observe surface plasmon resonances in ITO nano-triangles at energies below 0.5 eV, thanks to a combination of electron monochromation and deconvolution as we explained in Chapter 3. The crystallinity of ITO structures was important for the detection of the modes. The as fabricated ITO structure did not show plasmonic response in the EELS measurements. However, after an annealing treatment in a nitrogen atmosphere the ITO nanostructure formed larger crystalline grains, which decreases the number of electron scattering sites within the material, thus reducing plasmon losses, and allowing the detection of the plasmon resonances by EELS, as shown in Figure 7.71.

Bibliography

[1] E.D. Palik. *Handbook of Optical Constants of Solids*. Academic Press, Inc., New York, 1985.

[2] E Prodan, C Radloff, N J Halas, and P Nordlander. A hybridization model for the plasmon response of complex nanostructures. *Science (New York, N.Y.)*, 302(5644):419–22, oct 2003.

[3] T J Davis, D E Gómez, and K C Vernon. Simple model for the hybridization of surface plasmon resonances in metallic nanoparticles. *Nano letters*, 10(7):2618–25, jul 2010.

[4] Mario Hentschel, Michael Saliba, Ralf Vogelgesang, Harald Giessen, A. Paul Alivisatos, and Na Liu. Transition from isolated to collective modes in plasmonic oligomers. *Nano Letters*, 10(7):2721–2726, 2010. PMID: 20586409.

[5] FEI Company. *Titan on-line help*. FEI Company, Hillsboro, Oregon 97124 USA, 1.3 edition.

[6] Gerd Duscher. Electron energy loss spectroscopy. Accessed 2017-02-04.

[7] Gianluigi Botton. *Analytical Electron Microscopy*, pages 273–405. Springer New York, New York, NY, 2007.

[8] Mathieu Kociak and Odile Stéphan. Mapping plasmons at the nanometer scale in an electron microscope. *Chemical Society reviews*, 43(11):3865–83, jun 2014.

[9] F. J. García De Abajo and M Kociak. Probing the photonic local density of states with electron energy loss spectroscopy. *Physical Review Letters*, 100(10):1–5, 2008.

[10] Jaysen Nelayah, Mathieu Kociak, Odile Stéphan, F. Javier García de Abajo, Marcel Tencé, Luc Henrard, Dario Taverna, Isabel Pastoriza-Santos, Luis M. Liz-Marzán, and Christian Colliex. Mapping surface plasmons on a single metallic nanoparticle. *Nature Physics*, 3(5):348–353, apr 2007.

[11] David Rossouw and Gianluigi A. Botton. Plasmonic Response of Bent Silver Nanowires for Nanophotonic Subwavelength Waveguiding. *Physical Review Letters*, 110(6):066801, feb 2013.

[12] D Rossouw, M Couillard, J Vickery, E Kumacheva, and G A Botton. Multipolar plasmonic resonances in silver nanowire antennas imaged with a subnanometer electron probe. *Nano Letters*, 11(4):1499–1504, 2011.

[13] J Nelayah, M Kociak, O Stéphan, N Geuquet, L Henrard, F J García de Abajo, I Pastoriza-Santos, L M Liz-Marzán, and C Colliex. Two-dimensional quasistatic stationary short range surface plasmons in flat nanoprisms. *Nano letters*, 10(3):902–7, mar 2010.

[14] Franz-Philipp Schmidt, Harald Ditlbacher, Ulrich Hohenester, Andreas Hohenau, Ferdinand Hofer, and Joachim R Krenn. Universal dispersion of surface plasmons in flat nanostructures. *Nature communications*, 5:3604, 2014.

[15] Ai Leen Koh, Kui Bao, Imran Khan, W Ewen Smith, Gerald Kothleitner, Peter Nordlander, Stefan A Maier, and David W. Mccomb. Electron energy-loss spectroscopy (EELS) of surface plasmons in single silver nanoparticles and dimers:

Influence of beam damage and mapping of dark modes. *ACS Nano*, 3(10):3015–3022, oct 2009.

[16] Ina Alber, Wilfried Sigle, Sven Müller, Reinhard Neumann, Oliver Picht, Markus Rauber, Peter a van Aken, and Maria Eugenia Toimil-Molares. Visualization of multipolar longitudinal and transversal surface plasmon modes in nanowire dimers. *ACS nano*, 5(12):9845–53, dec 2011.

[17] Richard P. Feynman. There is plenty of room at the bottom, December 1959. Lecture given at an American Physical Society meeting at Caltech.

[18] Surface plasmon resurrection., November 2012.

[19] Harry a Atwater. The promise of plasmonics. *Scientific American*, 296(4):56–63, 2007.

[20] N. Yamamoto, K. Araya, and F. J. García de Abajo. Photon emission from silver particles induced by a high-energy electron beam. *Phys. Rev. B*, 64:205419, Nov 2001.

[21] Ming-Wen Chu, Viktor Myroshnychenko, Cheng Hsuan Chen, Jing-Pei Deng, Chung-Yuan Mou, and F Javier García de Abajo. Probing bright and dark surface-plasmon modes in individual and coupled noble metal nanoparticles using an electron beam. *Nano letters*, 9(1):399–404, jan 2009.

[22] Jeffrey N. Anker, W. Paige Hall, Olga Lyandres, Nilam C. Shah, Jing Zhao, and Richard P. Van Duyne. Biosensing with plasmonic nanosensors. *Nature materials*, 7(6):442–453, June 2008.

[23] Fenglin Liu, Erik J Luber, Lawrence a Huck, Brian C Olsen, and Jillian M Buriak. Nanoscale plasmonic stamp lithography on silicon. *ACS nano*, 9(2):2184–93, 2015.

[24] Hong Liu and Jinghua Teng. Plasmonic Nanolithography: Towards Next Generation Nanopatterning. *Journal of Molecular and Engineering Materials*, 01(01):1250005, jan 2013.

[25] Zhihua Xie, Weixing Yu, Taisheng Wang, Hongxin Zhang, Yongqi Fu, Hua Liu, Fengyou Li, Zhenwu Lu, and Qiang Sun. Plasmonic Nanolithography: A Review. *Plasmonics*, 6(3):565–580, 2011.

[26] Surbhi Lal, Susan E. Clare, and Naomi J. Halas. Nanoshell-Enabled Photothermal Cancer Therapy: Impending Clinical Impact. *Accounts of Chemical Research*, 41(12):1842–1851, 2008.

[27] Ivan H. El-Sayed, Xiaohua Huan, and Mostafa A. El-Sayed. Surface Plasmon Resonance Scattering and Absorption of anti-EGFR Antibody Conjugated Gold Nanoparticles in Cancer Diagnostics: Applications in Oral Cancer. *Nano Letters*, 5(5):829–834, 2005.

[28] Harry A Atwater and Albert Polman. Plasmonics for improved photovoltaic devices. *Nature materials*, 9(3):205–13, mar 2010.

[29] Henri J. Lezec, Jennifer A. Dionne, and Harry A. Atwater. Negative refraction at visible frequencies. *Science*, 316(5823):430–432, 2007.

[30] Nikolay I. Zheludev. A roadmap for metamaterials. *Opt. Photon. News*, 22(3):30–35, Mar 2011.

[31] J. B. Pendry. Negative refraction makes a perfect lens. *Phys. Rev. Lett.*, 85:3966–3969, Oct 2000.

[32] R.W. Wood. On a remarkable case of uneven distribution of light in a diffraction grating spectrum. *Philosophical Magazine Series 6*, 4(21):396–402, 1902.

[33] U. FANO. The theory of anomalous diffraction gratings and of quasi-stationary

waves on metallic surfaces (sommerfelds waves). *J. Opt. Soc. Am.*, 31(3):213–222, Mar 1941.

[34] C. J. Powell and J. B. Swan. Origin of the characteristic electron energy losses in magnesium. *Phys. Rev.*, 116:81–83, Oct 1959.

[35] C. J. Powell and J. B. Swan. Effect of oxidation on the characteristic loss spectra of aluminum and magnesium. *Phys. Rev.*, 118:640–643, May 1960.

[36] Andreas Otto. Excitation of nonradiative surface plasma waves in silver by the method of frustrated total reflection. *Zeitschrift für Physik A*, 216(4):398–410, 1968.

[37] D Heitmann. Radiative decay of surface plasmons excited by fast electrons on periodically modulated silver surfaces. *Journal of Physics C: Solid State Physics*, 10(3):397, 1977.

[38] T. W. Ebbesen, H. J. Lezec, H. F. Ghaemi, T. Thio, and P. A. Wolff. Extraordinary optical transmission through sub-wavelength hole arrays. *Nature*, 391:667–669, February 1998.

[39] Matthew Pelton and Garnett W Bryant. *Introduction to metal-nanoparticle plasmonics*. A Wiley-Science Wise Co-Publication. Wiley, Hoboken, NJ, 2013.

[40] P. Drude. Zur elektronentheorie der metalle. *Annalen der Physik*, 306(3):566–613, 1900.

[41] P. Drude. Zur elektronentheorie der metalle; ii. teil. galvanomagnetische und thermomagnetische effecte. *Annalen der Physik*, 308(11):369–402, 1900.

[42] SA Maier. *Plasmonics: Fundamentals and Applications*. Springer, 2007.

[43] Jacob B Khurgin. How to deal with the loss in plasmonics and metamaterials. *Nature Publishing Group*, 10(1):2–6, 2015.

[44] Gustav Mie. Beiträge zur optik trüber medien, speziell kolloidaler metalläsungen. *Annalen der Physik*, 330(3):377–445, 1908.

[45] P. E. Batson. Surface plasmon coupling in clusters of small spheres. *Phys. Rev. Lett.*, 49:936–940, Sep 1982.

[46] Prashant K. Jain and Mostafa A. El-Sayed. Plasmonic coupling in noble metal nanostructures. *Chemical Physics Letters*, 487(46):153 – 164, 2010.

[47] Beverly Z. Packard, Dmitri D. Toptygin, Akira Komoriya, and Ludwig Brand. Intramolecular resonance dipoledipole interactions in a profluorescent protease substrate. *The Journal of Physical Chemistry B*, 102(4):752–758, 1998.

[48] U. Fano. Effects of configuration interaction on intensities and phase shifts. *Phys. Rev.*, 124:1866–1878, Dec 1961.

[49] Boris Luk'yanchuk, Nikolay I Zheludev, Stefan a Maier, Naomi J Halas, Peter Nordlander, Harald Giessen, and Chong Tow Chong. The Fano resonance in plasmonic nanostructures and metamaterials. *Nature materials*, 9(9):707–15, sep 2010.

[50] Ulrich Hohenester and Andreas Trügler. MNPBEM A Matlab toolbox for the simulation of plasmonic nanoparticles. *Computer Physics Communications*, 183(2):370–381, feb 2012.

[51] Ulrich Hohenester. Simulating electron energy loss spectroscopy with the MNPBEM toolbox. *Computer Physics Communications*, 185(3):1177–1187, mar 2014.

[52] F. J. García de Abajo. Optical excitations in electron microscopy. *Reviews of Modern Physics*, 82(1):209–275, feb 2010.

[53] Ai Leen Koh, David W. McComb, Stefan a. Maier, H. Y. Low, and Joel K. W.

Yang. Sub-10 nm patterning of gold nanostructures on silicon-nitride membranes for plasmon mapping with electron energy-loss spectroscopy. *Journal of Vacuum Science & Technology B: Microelectronics and Nanometer Structures*, 28(6):C6O45, 2010.

[54] R. H. Ritchie. Plasma losses by fast electrons in thin films. *Phys. Rev.*, 106:874–881, Jun 1957.

[55] Arthur Losquin, Luiz F Zagonel, Viktor Myroshnychenko, Benito Rodríguez-González, Marcel Tencé, Leonardo Scarabelli, Jens Förstner, Luis M Liz-Marzán, F Javier García de Abajo, Odile Stéphan, and Mathieu Kociak. Unveiling nanometer scale extinction and scattering phenomena through combined electron energy loss spectroscopy and cathodoluminescence measurements. *Nano Letters*, 15(2):1229–1237, 2015. PMID: 25603194.

[56] Michel Bosman, Vicki J Keast, Masashi Watanabe, Abbas I Maaroof, and Michael B Cortie. Mapping surface plasmons at the nanometre scale with an electron beam. *Nanotechnology*, 18(16):165505, 2007.

[57] Lin Wu, Huigao Duan, Ping Bai, Michel Bosman, Joel K W Yang, and Erping Li. Fowler-Nordheim tunneling induced charge transfer plasmons between nearly touching nanoparticles. *ACS nano*, 7(1):707–16, jan 2013.

[58] Jonathan a Scholl, Ai Leen Koh, and Jennifer a Dionne. Quantum plasmon resonances of individual metallic nanoparticles. *Nature*, 483(7390):421–7, mar 2012.

[59] Shunping Zhang, Kui Bao, Naomi J Halas, Hongxing Xu, and Peter Nordlander. Substrate-induced Fano resonances of a plasmonic nanocube: a route to increased-sensitivity localized surface plasmon resonance sensors revealed. *Nano*

letters, 11(4):1657–63, apr 2011.

[60] Olivia Nicoletti, Francisco de la Peña, Rowan K Leary, Daniel J Holland, Caterina Ducati, and Paul a Midgley. Three-dimensional imaging of localized surface plasmon resonances of metal nanoparticles. *Nature*, 502(7469):80–4, oct 2013.

[61] Stefano Mazzucco, Nicolas Geuquet, Jian Ye, Odile Stéphan, Willem Van Roy, Pol Van Dorpe, Luc Henrard, and Mathieu Kociak. Ultralocal modification of surface plasmons properties in silver nanocubes. *Nano letters*, 12(3):1288–94, mar 2012.

[62] Shu Fen Tan, Lin Wu, Joel K. W. Yang, Ping Bai, Michel Bosman, and Christian a. Nijhuis. Quantum Plasmon Resonances Controlled by Molecular Tunnel Junctions. *Science*, 343(6178):1496–1499, mar 2014.

[63] Franz Philipp Schmidt, Harald Ditlbacher, Ulrich Hohenester, Andreas Hohenau, Ferdinand Hofer, and Joachim R. Krenn. Dark plasmonic breathing modes in silver nanodisks. *Nano Letters*, 12:5780–5783, 2012.

[64] Franz P Schmidt, Harald Ditlbacher, Ferdinand Hofer, Joachim R Krenn, and Ulrich Hohenester. Morphing a plasmonic nanodisk into a nanotriangle. *Nano letters*, 14(8):4810–5, aug 2014.

[65] Olivia Nicoletti, Martijn Wubs, N Asger Mortensen, Wilfried Sigle, Peter a van Aken, and Paul a Midgley. Surface plasmon modes of a single silver nanorod: an electron energy loss study. *Optics express*, 19(16):15371–9, aug 2011.

[66] Beth S Guiton, Vighter Iberi, Shuzhou Li, Donovan N Leonard, Chad M Parish, Paul G Kotula, Maria Varela, George C Schatz, Stephen J Pennycook, and Jon P Camden. Correlated optical measurements and plasmon mapping of silver nanorods. *Nano letters*, 11(8):3482–8, aug 2011.

[67] Guillaume Boudarham, Nils Feth, Viktor Myroshnychenko, Stefan Linden, Javier García de Abajo, Martin Wegener, and Mathieu Kociak. Spectral Imaging of Individual Split-Ring Resonators. *Physical Review Letters*, 105(25):255501, dec 2010.

[68] Michel Bosman, Geoffrey R Anstis, Vicki J Keast, Jackson D Clarke, and Michael B Cortie. Light splitting in nanoporous gold and silver. *ACS nano*, 6(1):319–26, jan 2012.

[69] Huigao Duan, Antonio I Fernández-Domínguez, Michel Bosman, Stefan a Maier, and Joel K W Yang. Nanoplasmonics: classical down to the nanometer scale. *Nano letters*, 12(3):1683–9, mar 2012.

[70] Wilfried Sigle, Jaysen Nelayah, Christoph T. Koch, and Peter A. van Aken. Electron energy losses in ag nanoholes—from localized surface plasmon resonances to rings of fire. *Opt. Lett.*, 34(14):2150–2152, Jul 2009.

[71] Nahid Talebi, Wilfried Sigle, Ralf Vogelgesang, Christoph T Koch, Cristina Fernández-López, Luis M Liz-Marzán, Burcu Ögüt, Melanie Rohm, and Peter a van Aken. Breaking the mode degeneracy of surface plasmon resonances in a triangular system. *Langmuir : the ACS journal of surfaces and colloids*, 28(24):8867–73, jun 2012.

[72] Viktor Myroshnychenko, Jaysen Nelayah, Giorgio Adamo, Nicolas Geuquet, Jessica Rodríguez-Fernández, Isabel Pastoriza-Santos, Kevin F. MacDonald, Luc Henrard, Luis M. Liz-Marzán, Nikolay I Zheludev, Mathieu Kociak, and F. Javier García De Abajo. Plasmon spectroscopy and imaging of individual gold nanodecahedra: A combined optical microscopy, cathodoluminescence, and electron energy-loss spectroscopy study. *Nano Letters*, 12(8):4172–4180, 2012.

[73] Lin Gu, Wilfried Sigle, Christoph T. Koch, Burcu Ögüt, Peter a. van Aken, Nahid Talebi, Ralf Vogelgesang, Jianlin Mu, Xiaogang Wen, and Jian Mao. Resonant wedge-plasmon modes in single-crystalline gold nanoplatelets. *Physical Review B*, 83(19):195433, may 2011.

[74] Judit Morla-Folch, Luca Guerrini, Nicolas Pazos-Perez, Raul Arenal, and Ramon A. Alvarez-Puebla. Synthesis and Optical Properties of Homogeneous Nanoshurikens. *ACS Photonics*, 1(11):1237–1244, nov 2014.

[75] David Rossouw and Gianluigi a Botton. Resonant optical excitations in complementary plasmonic nanostructures. *Optics express*, 20(7):6968–73, mar 2012.

[76] Edson P. Bellido, Alejandro Manjavacas, Yue Zhang, Yang Cao, Peter Nordlander, and Gianluigi A. Botton. Electron energy-loss spectroscopy of multipolar edge and cavity modes in silver nanosquares. *ACS Photonics*, 3(3):428–433, 2016.

[77] Franz-Philipp Schmidt, Harald Ditlbacher, Andreas Hohenau, Ulrich Hohenester, Ferdinand Hofer, and Joachim R. Krenn. Edge Mode Coupling within a Plasmonic Nanoparticle. *Nano letters*, 16(8):5152–5155, 2016.

[78] Bart Goris, Giulio Guzzinati, Cristina Fernández-López, Jorge Pérez-Juste, Luis M Liz-Marzán, Andreas Trügler, Ulrich Hohenester, Jo Verbeeck, Sara Bals, and Gustaaf Van Tendeloo. Plasmon Mapping in Au@Ag Nanocube Assemblies. *The journal of physical chemistry. C, Nanomaterials and interfaces*, 118(28):15356–15362, jul 2014.

[79] Steven J Barrow, David Rossouw, Alison M Funston, Gianluigi a Botton, and Paul Mulvaney. Mapping bright and dark modes in gold nanoparticle chains using electron energy loss spectroscopy. *Nano letters*, 14(7):3799–808, jul 2014.

[80] L Krivanek and M K Kundmann. Spatial resolution in EFTEM elemental maps. *Journal of Microscopy*, 180(April):277–287, 1995.

[81] R.F. Egerton. New techniques in electron energy-loss spectroscopy and energy-filtered imaging. *Micron*, 34(3-5):127–139, apr 2003.

[82] Ondrej L Krivanek, Tracy C Lovejoy, Niklas Dellby, and R W Carpenter. Monochromated STEM with a 30 meV-wide, atom-sized electron probe. *Microscopy (Oxford, England)*, 62(1):3–21, mar 2013.

[83] Maureen J. Lagos, Andreas Trügler, Ulrich Hohenester, and Philip E. Batson. Mapping vibrational surface and bulk modes in a single nanocube. *Nature*, 543(7646):529–532, Mar 2017. Letter.

[84] Ondrej L. Krivanek, Tracy C. Lovejoy, Niklas Dellby, Toshihiro Aoki, R. W. Carpenter, Peter Rez, Emmanuel Soignard, Jiangtao Zhu, Philip E. Batson, Maureen J. Lagos, Ray F. Egerton, and Peter A. Crozier. Vibrational spectroscopy in the electron microscope. *Nature*, 514(7521):209–212, Oct 2014. Letter.

[85] R F Egerton, H Qian, and M Malac. Improving the energy resolution of X-ray and electron energy-loss spectra. *Micron (Oxford, England : 1993)*, 37(4):310–5, jan 2006.

[86] Feng Wang, Ray Egerton, and Marek Malac. Fourier-ratio deconvolution techniques for electron energy-loss spectroscopy (EELS). *Ultramicroscopy*, 109(10):1245–9, sep 2009.

[87] M.H.F Overwijk and D Reefman. Maximum-entropy deconvolution applied to electron energy-loss spectroscopy. *Micron*, 31(4):325–331, aug 2000.

[88] Ryuichi Kuzuo and Michiyoshi Tanaka. Resolution Enhancement of Electron

Energy-Loss Spectra Using the Maximum Entropy Method. *Journal of Electron Microscopy*, 243:240–243, 1993.

[89] K. Ishizuka, K. Kimoto, and Y. Bando. Improving Energy Resolution of EELS Spectra by Deconvolution using Maximum-Entropy and Richardson-Lucy Algorithms. *Microscopy and Microanalysis*, 2(9):832–833, 2003.

[90] Koji Kimoto, Kazuo Ishizuka, Teruyasu Mizoguchi, Isao Tanaka, and Yoshio Matsui. The study of Al-L23 ELNES with resolution-enhancement software and first-principles calculation. *Journal of Electron Microscopy*, 52(3):299–303, 2003.

[91] William H. Richarson. Bayesian-Based Iterative Method of Image Restoration. *Journal of the Optical Society of America*, 62(1):55–59, 1972.

[92] L. H. Lucy. An iterative technique for the rectification of observed distributions. *Astronomical Journal*, 79(6):745–754, 1974.

[93] L a Shepp and Y Vardi. Maximum likelihood reconstruction for emission tomography. *IEEE transactions on medical imaging*, 1(2):113–22, jan 1982.

[94] G. M. P. Van Kempen, L. J. Van Vliet, P J Verveer, and H. T. M. Van Der Voort. A quantitative comparison of image restoration methods for confocal microscopy. *Journal of Microscopy*, 185(3):354–365, 1997.

[95] Sudhakar Prasad. Statistical-information-based performance criteria for Richardson-Lucy image deblurring. *Journal of the Optical Society of America. A, Optics, image science, and vision*, 19(7):1286–96, jul 2002.

[96] Donald L Snyder, Abed M Hammoud, and Richard L White. Image recovery from data acquired with a charge-coupled-device camera Array. *Journal of the Optical Society of America A*, 10(5):1014–1023, 1993.

[97] J M Zuo. Electron detection characteristics of a slow-scan CCD camera, imaging plates and film, and electron image restoration. *Microscopy research and technique*, 49(3):245–68, may 2000.

[98] a Gloter, a Douiri, M Tencé, and C Colliex. Improving energy resolution of EELS spectra: an alternative to the monochromator solution. *Ultramicroscopy*, 96(3-4):385–400, sep 2003.

[99] S Lazar, G a Botton, and H W Zandbergen. Enhancement of resolution in core-loss and low-loss spectroscopy in a monochromated microscope. *Ultramicroscopy*, 106(11-12):1091–103, 2006.

[100] Jeffery a Aguiar, Bryan W Reed, Quentin M Ramasse, Rolf Erni, and Nigel D Browning. Quantifying the low-energy limit and spectral resolution in valence electron energy loss spectroscopy. *Ultramicroscopy*, 124:130–8, jan 2013.

[101] J W L Eccles, U Bangert, M Bromfield, P Christian, a J Harvey, and P Thomas. UV-Vis plasmon studies of metal nanoparticles. *Journal of Physics: Conference Series*, 241:012090, jul 2010.

[102] Stefan a. Maier, Mark L. Brongersma, and Harry a. Atwater. Electromagnetic energy transport along arrays of closely spaced metal rods as an analogue to plasmonic devices. *Applied Physics Letters*, 78(1):16, 2001.

[103] P E Batson, N Dellby, and O L Krivanek. Sub-ångstrom resolution using aberration corrected electron optics. *Nature*, 418(6898):617–20, aug 2002.

[104] O.L. Krivanek, N. Dellby, and a.R. Lupini. Towards sub-Å electron beams. *Ultramicroscopy*, 78(1-4):1–11, jun 1999.

[105] R F Egerton. Limits to the spatial, energy and momentum resolution of electron energy-loss spectroscopy. *Ultramicroscopy*, 107(8):575–86, aug 2007.

[106] Edson P Bellido, David Rossouw, and Gianluigi a Botton. Toward 10 meV Electron Energy-Loss Spectroscopy Resolution for Plasmonics. *Microscopy and microanalysis : the official journal of Microscopy Society of America, Microbeam Analysis Society, Microscopical Society of Canada*, 20(2009):767–78, 2014.

[107] X. L. Zhu, Y. Ma, J. S. Zhang, J. Xu, X. F. Wu, Y. Zhang, X. B. Han, Q. Fu, Z. M. Liao, L. Chen, and D. P. Yu. Confined Three-Dimensional Plasmon Modes inside a Ring-Shaped Nanocavity on a Silver Film Imaged by Cathodoluminescence Microscopy. *Physical Review Letters*, 105(12):127402, sep 2010.

[108] Yang Cao, Alejandro Manjavacas, Nicolas Large, and Peter Nordlander. Electron Energy-Loss Spectroscopy Calculation in Finite-Difference Time-Domain Package. *ACS Photonics*, 2(3):369–375, mar 2015.

[109] Ulrich Hohenester, Harald Ditlbacher, and Joachim Krenn. Electron-Energy-Loss Spectra of Plasmonic Nanoparticles. *Physical Review Letters*, 103(10):106801, aug 2009.

[110] Markus K. Krug, Michael Reisecker, Andreas Hohenau, Harald Ditlbacher, Andreas Trügler, Ulrich Hohenester, and Joachim R. Krenn. Probing plasmonic breathing modes optically. *Applied Physics Letters*, 105(17):2014–2017, 2014.

[111] Alfredo Campos, Arnaud Arbouet, Jrme Martin, Davy Grard, Julien Proust, Jrme Plain, and Mathieu Kociak. Plasmonic breathing and edge modes in aluminum nanotriangles. *ACS Photonics*, 4(5):1257–1263, 2017.

[112] Edson P. Bellido, Yue Zhang, Alejandro Manjavacas, Peter Nordlander, and Gianluigi A. Botton. Plasmonic coupling of multipolar edge modes and the formation of gap modes. *ACS Photonics*, 4(6):1558–1565, 2017.

[113] Shaista Babar and J. H. Weaver. Optical constants of Cu, Ag, and Au revisited.

Applied Optics, 54(3):477, jan 2015.

[114] Jian Ye, Fangfang Wen, Heidar Sobhani, J Britt Lassiter, Pol Van Dorpe, Peter Nordlander, and Naomi J Halas. Plasmonic nanoclusters: near field properties of the Fano resonance interrogated with SERS. *Nano letters*, 12(3):1660–7, mar 2012.

[115] Shima Kadkhodazadeh, Jakob Rosenkrantz de Lasson, Marco Beleggia, Harald Kneipp, Jakob Birkedal Wagner, and Katrin Kneipp. Scaling of the Surface Plasmon Resonance in Gold and Silver Dimers Probed by EELS. *The Journal of Physical Chemistry C*, 118(10):5478–5485, mar 2014.

[116] Björn M Reinhard, Merek Siu, Harish Agarwal, A Paul Alivisatos, and Jan Liphardt. Calibration of dynamic molecular rulers based on plasmon coupling between gold nanoparticles. *Nano letters*, 5(11):2246–52, nov 2005.

[117] Carsten Sönnichsen, Björn M Reinhard, Jan Liphardt, and A Paul Alivisatos. A molecular ruler based on plasmon coupling of single gold and silver nanoparticles. *Nature biotechnology*, 23(6):741–5, jun 2005.

[118] Ina Schubert, Wilfried Sigle, Peter a. van Aken, Christina Trautmann, and Maria Eugenia Toimil-Molares. STEM-EELS analysis of multipole surface plasmon modes in symmetry-broken AuAg nanowire dimers. *Nanoscale*, 7(11):4935–4941, 2015.

[119] Søren Raza, Shima Kadkhodazadeh, Thomas Christensen, Di Vece, Martijn Wubs, N Asger Mortensen, and Nicolas Stenger. Multipole plasmons and their disappearance in few-nanometer silver nanoparticles. *Nature Communications*, 6:8788, 2015.

[120] R.D. Leapman and C.R. Swyt. Separation of overlapping core edges in electron

energy loss spectra by multiple-least-squares fitting. *Ultramicroscopy*, 26(4):393 – 403, 1988.

[121] Rubén Esteban, Garikoitz Aguirregabiria, Andrey G. Borisov, Yumin M. Wang, Peter Nordlander, Garnett W. Bryant, and Javier Aizpurua. The morphology of narrow gaps modifies the plasmonic response. *ACS Photonics*, 2(2):295–305, 2015.

[122] Dario Knebl, Anton Hörl, Andreas Trügler, Johannes Kern, Joachim R. Krenn, Peter Puschnig, and Ulrich Hohenester. Gap plasmonics of silver nanocube dimers. *Physical Review B - Condensed Matter and Materials Physics*, 93(8):1–5, 2016.

[123] Todd Brintlinger, Andrew A Herzing, James P Long, Igor Vurgaftman, Rhonda Stroud, and B S Simpkins. Optical Dark-Field and Electron Energy Loss Imaging and Spectroscopy of Symmetry-Forbidden Modes in Loaded Nanogap Antennas. *ACS Nano*, 9(6):6222–6232, 2015.

[124] J. A. Dionne, L. A. Sweatlock, H. A. Atwater, and A. Polman. Plasmon slot waveguides: Towards chip-scale propagation with subwavelength-scale localization. *Physical Review B - Condensed Matter and Materials Physics*, 73(3):1–9, 2006.

[125] Hikaru Saito and Hiroki Kurata. Direct measurement of dispersion relation for surface plasmon-polaritons on silver nanoantennas. *Microscopy (Oxford, England)*, 0(0):1–5, nov 2013.

[126] Mihail Bora, Benjamin J. Fasenfest, Elaine M. Behymer, Allan S-P Chang, Hoang T. Nguyen, Jerald A. Britten, Cindy C. Larson, James W. Chan, Robin R. Miles, and Tiziana C. Bond. Plasmon resonant cavities in vertical

nanowire arrays. *Nano Letters*, 10(8):2832–2837, 2010. PMID: 20698595.

[127] Valentin Flauraud, Gabriel D. Bernasconi, Jrmy Butet, Duncan T. L. Alexander, Olivier J. F. Martin, and Jrgen Brugger. Mode coupling in plasmonic heterodimers probed with electron energy loss spectroscopy. *ACS Nano*, 11(4):3485–3495, 2017. PMID: 28290663.

[128] D.H. Werner, Randy L. Haupt, and P.L. Werner. Fractal antenna engineering: the theory and design of fractal antenna arrays. *Antennas and Propagation Magazine, IEEE*, 41(5):37–58, Oct 1999.

[129] Benoit B. Mandelbrot. *The Fractal Geometry of Nature*. W. H. Freeman and Company, 1977.

[130] C. Puente-Baliarda, J. Romeu, R. Pous, and a. Cardama. On the behavior of the Sierpinski multiband fractal antenna. *IEEE Transactions on Antennas and Propagation*, 46(4):517–524, apr 1998.

[131] C.P. Baliarda, J. Romeu, and a. Cardama. The Koch monopole: a small fractal antenna. *IEEE Transactions on Antennas and Propagation*, 48(11):1773–1781, 2000.

[132] Subhrakanta Behera, K J Vinoy, and Senior Member. Multi-Port Network Approach for the Analysis of Dual Band Fractal Microstrip Antennas. *IEEE Transactions on Antennas and Propagation*, 60(11):5100–5106, 2012.

[133] A A Omar. Design of ultrawideband coplanar waveguide-fed Koch-fractal triangular antenna. *International Journal of RF and Microwave Computer-Aided Engineering*, 23(2):200–207, 2013.

[134] A Ismahayati, P J Soh, R. Hadibah, and G. A E Vandenbosch. Design and

analysis of a multiband koch fractal monopole antenna. In *2011 IEEE International RF and Microwave Conference, RFM 2011 - Proceedings*, volume 4, pages 58–62, 2011.

[135] MN A Karim, MKA Rahim, and HA Majid. Log periodic fractal Koch antenna for UHF band applications. *Progress In Electromagnetics Research*, 100:201–218, 2010.

[136] Jeffrey N Anker, W Paige Hall, Olga Lyandres, Nilam C Shah, Jing Zhao, and Richard P Van Duyne. Biosensing with plasmonic nanosensors. *Nature materials*, 7(6):442–53, jun 2008.

[137] S. Kawata, Y. Inouye, and P. Verma. Plasmonics for near-field nano-imaging and superlensing. *Nature Photonics*, 3(7):388–394, 2009.

[138] Surbhi Lal, Susan E Clare, and Naomi J Halas. Nanoshell-enabled photothermal cancer therapy: impending clinical impact. *Accounts of chemical research*, 41(12):1842–51, dec 2008.

[139] M. Schnell, A. García-Etxarri, a. J. Huber, K. Crozier, J. Aizpurua, and R. Hillenbrand. Controlling the near-field oscillations of loaded plasmonic nanoantennas. *Nature Photonics*, 3(5):287–291, 2009.

[140] Petru Ghenuche, Sudhir Cherukulappurath, Tim H. Taminiau, Niek F. Van Hulst, and Romain Quidant. Spectroscopic mode mapping of resonant plasmon nanoantennas. *Physical Review Letters*, 101(11):1–4, 2008.

[141] David P. Fromm, Arvind Sundaramurthy, P. James Schuck, Gordon Kino, and W. E. Moerner. Gap-dependent optical coupling of single "bowtie" nanoantennas resonant in the visible. *Nano Letters*, 4(5):957–961, 2004.

[142] Terukazu Kosako, Yutaka Kadoya, and Holger F. Hofmann. Directional control

of light by a nano-optical Yagi Uda antenna. *Nature Photonics*, 4(March):312–315, 2010.

[143] Ray F. Egerton. Electron energy-loss spectroscopy in the TEM. *Reports on Progress in Physics*, 72(1):016502, 2008.

[144] Hongyan Liang, Haiguang Zhao, David Rossouw, Wenzhong Wang, Hongxing Xu, Gianluigi a. Botton, and Dongling Ma. Silver Nanorice Structures: Oriented Attachment-Dominated Growth, High Environmental Sensitivity, and Real-Space Visualization of Multipolar Resonances. *Chemistry of Materials*, 24(12):2339–2346, jun 2012.

[145] Michel Bosman, Vicki J Keast, Masashi Watanabe, Abbas I Maaroof, and Michael B Cortie. Mapping surface plasmons at the nanometre scale with an electron beam. *Nanotechnology*, 18(16):165505, apr 2007.

[146] Samuel Gottheim, Hui Zhang, Alexander O Govorov, and Naomi J Halas. Fractal nanoparticle plasmonics: The cayley tree. *ACS Nano*, 9(3):3284–3292, 2015.

[147] Lorenzo Rosa, Kai Sun, and Saulius Juodkazis. Sierpiński fractal plasmonic nanoantennas. *Physica Status Solidi - Rapid Research Letters*, 5(5-6):175–177, 2011.

[148] Shawn Sederberg and A.Y. Elezzabi. Sierpiński fractal plasmonic antenna: a fractal abstraction of the plasmonic bowtie antenna. *Optics express*, 19(11):10456–10461, 2011.

[149] Giorgio Volpe, Giovanni Volpe, and Romain Quidant. Fractal plasmonics: subdiffraction focusing and broadband spectral response by a Sierpinski nanocarpet. *Optics express*, 19(4):3612–3618, 2011.

[150] Heykel Aouani, Mohsen Rahmani, Hana Šípová, Victor Torres, Kateina Hegnerová, Miguel Beruete, Jií Homola, Minghui Hong, Miguel Navarro-Cía, and Stefan A. Maier. Plasmonic nanoantennas for multispectral surface-enhanced spectroscopies. *Journal of Physical Chemistry C*, 117(36):18620–18626, 2013.

[151] Kuiru Li, Mark Stockman, and David Bergman. Self-Similar Chain of Metal Nanospheres as an Efficient Nanolens. *Physical Review Letters*, 91(22):227402, 2003.

[152] Gabriel D. Bernasconi, Jrmy Butet, Valentin Flauraud, Duncan Alexander, Juergen Brugger, and Olivier J. F. Martin. Where does energy go in electron energy loss spectroscopy of nanostructures? *ACS Photonics*, 4(1):156–164, 2017.

[153] Gabriel D. Bernasconi, Jérémy Butet, and Olivier J. F. Martin. Mode analysis of second-harmonic generation in plasmonic nanostructures. *J. Opt. Soc. Am. B*, 33(4):768–779, Apr 2016.

[154] Francisco J. Rodríguez-Fortuño, Carlos García-Meca, Rubén Ortuño, Javier Martí, and Alejandro Martínez. Modeling high-order plasmon resonances of a u-shaped nanowire used to build a negative-index metamaterial. *Phys. Rev. B*, 79:075103, Feb 2009.

[155] H. Rose. Nonstandard imaging methods in electron microscopy. *Ultramicroscopy*, 2:251 – 267, 1976.

[156] Matthias Lohr, Ralph Schregle, Michael Jetter, Clemens Wchter, Thomas Wunderer, Ferdinand Scholz, and Josef Zweck. Differential phase contrast 2.0 opening new fields for an established technique. *Ultramicroscopy*, 117:7 – 14, 2012.

[157] Yao-Wei Huang, Wei Ting Chen, Pin Chieh Wu, Vassili A. Fedotov, Nikolay I.

Zheludev, and Din Ping Tsai. Toroidal lasing spaser. *Scientific Reports*, 3:1237 EP –, Feb 2013. Article.

[158] Gururaj V. Naik, Vladimir M. Shalaev, and Alexandra Boltasseva. Alternative plasmonic materials: Beyond gold and silver. *Advanced Materials*, 25(24):3264–3294, 2013.

[159] Crissy Rhodes, Stefan Franzen, Jon-Paul Maria, Mark Losego, Donovan N. Leonard, Brian Laughlin, Gerd Duscher, and Stephen Weibel. Surface plasmon resonance in conducting metal oxides. *Journal of Applied Physics*, 100(5):054905, 2006.